

Viral DNA Packaging at Base Pair Resolution

by

Jeffrey Randolph Moffitt

B.A. (College of Wooster) 2003
M.A. (University of California, Berkeley) 2005

A dissertation submitted in partial satisfaction of the

requirements for the degree of

Doctor of Philosophy

in

Physics

in the

Graduate Division

of the

University of California, Berkeley

Committee in charge:

Professor Carlos Bustamante, Chair

Professor Jan Liphardt

Professor James Berger

Spring 2009

Viral DNA Packaging at Base Pair Resolution

© 2009

by Jeffrey Randolph Moffitt

Abstract

Viral DNA Packaging at Base Pair Resolution

By

Jeffrey Randolph Moffitt

Doctor of Philosophy in Physics

University of California, Berkeley

Professor Carlos Bustamante, Chair

During its lifecycle the bacterial virus φ 29 packages its genome into a preformed protein shell, compressing the genome to near-crystalline density and high macroscopic pressures against large elastic, electrostatic, and entropic forces. At the core of this process is a molecular DNA pump—a complex assembly of protein and nucleic acid which extracts the chemical energy stored in the gamma phosphate bond of adenosine triphosphate and converts this energy into the mechanical work necessary to overcome these large energetic barriers.

In this thesis, we construct an optical tweezers capable of observing single base pair length changes to molecules of DNA, distance changes of only 3.4 Å, and use this instrument to detect the discrete increments of DNA packaged each cycle of the packaging motor. We find that the full cycle involves the action of four of its five ATPase subunits, each of which binds ATP, delays the utilization of this molecule until the entire ring is loaded, and then packages the DNA in a 2.5-bp step, generating a collective burst of four steps each full cycle. Not only do these results indicate an intricate form of inter-subunit coordination novel for ring ATPases, they represent the

first time that a molecular motor has been observed to move in a non-integer repeat of the chemical periodicity of its substrate. Both observations have profound implications for the mechanism of the packaging motor and, perhaps, related ring ATPases.

In parallel, we develop a series of new theoretical tools to extract kinetic information from the statistical properties of the inherent fluctuations in the packaging motor dynamics. In particular, we show that there are multiple classes of enzymatic fluctuations, and we provide methods for identifying the class of fluctuations in both theoretical models and actual experimental data. In parallel, we derive a Michaelis-Menten-like expression for fluctuations. We then use this expression to reveal new mechanistic properties of the packaging motor from fluctuations in the data collected. With the combination of experimental and theoretical tools developed in this thesis, the door is now open to a detailed, Ångstrom-scale dissection of the mechanism of a wide variety of nucleic acid motors.

Carlos Bustamante, Chair

For my parents, Dennis and Nancy Moffitt

Table of Contents

Chapter 1. Introduction.....	1
1.1: The DNA Packaging Motor.....	3
1.2: Instrumentation Limitations.....	22
1.3: Theoretical Limitations.....	26
1.4: Thesis Organization	39
Chapter 2. Design and Construction of a High Resolution Optical Tweezers	43
2.1: Why do we Need Better Resolution?.....	44
2.2: The Dual Trap Optical Tweezers.....	45
2.3: Environmental Concerns.....	47
2.4: Instrument Design.....	53
2.5: Summary and Conclusions	80
Chapter 3. Brownian Fluctuations in Dual-Trap Optical Tweezers	82
3.1: How do Brownian Fluctuations Limit Resolution?	83
3.2: Equations of Motion	85
3.3: Derivation of Signal-to-Noise Ratios	88
3.4: The Spatial Resolution of Dual Trap Optical Tweezers	94
3.5: Experimental Verification.....	101
3.6: Single Base Pair Resolution.....	106

3.7: Summary and Conclusions	112
Chapter 4. The Packaging Mechanism of the Bacteriophage φ 29	115
4.1: Introduction.....	116
4.2: Packaging under Low Forces.....	118
4.3: Packaging at High Force.....	126
4.4: Inter-Subunit Coordination	138
4.5: Non-Integer Step Size Models.....	148
4.6: Conclusions.....	153
Chapter 5. Experimental Methods	155
5.1: Instrument Calibration	156
5.2: Packaging Experiments.....	169
5.3: Data Analysis	178
5.4: Summary and Conclusions	201
Chapter 6. Distinct Statistical Classes of Enzymatic Fluctuations	204
6.1: Introduction.....	205
6.2: Theoretical Results	208
6.3: Exact Solutions for Discrete Kinetic Models	223
6.4: Summary and Conclusions	234
6.5: Appendices.....	235
Chapter 7. A Michaelis-Menten Expression for Enzymatic Fluctuations	246

7.1: Introduction.....	247
7.2: Theoretical Results	252
7.3: Application to the Packaging Motor.....	260
7.4: Discussion and Conclusions	269
7.5: Appendices.....	273
Chapter 8. Work in Progress and Conclusions	292
8.1: DNA Contacts in the Packaging Motor.....	293
8.2: Completing the Mechanochemical Cycle	305
8.3: Dissecting a Molecular Throttle	313
8.4: Concluding Thoughts.....	319
Bibliography	327

List of Figures

Figure 1.1. φ 29 Assembly Pathway	5
Figure 1.2. The Packaging Motor	6
Figure 1.3. Previous Optical Tweezers Experiments.....	10
Figure 1.4. Inter-Subunit Coordination Models for Ring ATPases	17
Figure 1.5. The Additional Strand Conserved E Superfamily	19
Figure 1.6. Statistical Kinetics	30
Figure 2.1. Different Optical Tweezers Geometries	45
Figure 2.2. Air Fluctuations in Optical Tweezers.....	52
Figure 2.3. High Resolution Optical Tweezers.....	54
Figure 2.4. Optical Layout.....	55
Figure 2.5. Lasers Used in the High Resolution Optical Tweezers	56
Figure 2.6. The Power Stage.....	58
Figure 2.7. Beam Steering Stage.....	59
Figure 2.8. The Conjugate Planes of a Telescope.....	62
Figure 2.9. Objective Stage.....	65
Figure 2.10. Installed Sample Chamber.....	66
Figure 2.11. Microfluidics Chamber and Adaptors	67
Figure 2.12. Detection Stage.....	69
Figure 2.13. Instrument Noise	74
Figure 3.1. The Signal and Noise in a Two Trap System	83
Figure 3.2. Parameterization of the Two Trap System	86
Figure 3.3. Hydrodynamic Coupling	87
Figure 3.4. Measuring the Spatial Resolution.....	102

Figure 3.5. Spatial Resolution versus DNA Stiffness.....	103
Figure 3.6. Spatial Resolution versus Trap Stiffness.....	105
Figure 3.7. Observation of Single-Base-Pair-Length Changes.....	107
Figure 3.8. Improvement in Resolution with Force.....	108
Figure 4.1. Experimental Setup and Low Force Data.....	119
Figure 4.2. 10-bp Dwell Time Statistics	121
Figure 4.3. Interrupted Bursts	125
Figure 4.4. Temperature Dependence of Packaging Velocity	128
Figure 4.5. 2.5-bp Steps at High Force	129
Figure 4.6. Additional 2.5-bp Analysis.....	131
Figure 4.7. PWD for Alternative Stepping Models	133
Figure 4.8. DNA Distortions do not Effect Step Size Measurements	136
Figure 4.9. General Data Statistics	137
Figure 4.10. Two Phase Model of Packaging.....	139
Figure 4.11. Mechanism of ATP Binding.....	141
Figure 4.12. The Full Mechanochemical Cycle of the Packaging Motor.....	146
Figure 4.13. A Steric Drive Mechanism	149
Figure 4.14. Cracked, Dynamic Ring Model.....	150
Figure 4.15. Pitched Ring Model.....	152
Figure 5.1. Example Power Spectra Fits with Residuals	160
Figure 5.2. Voltage Offset Measurements	166
Figure 5.3. Tether Assembly Procedure in the Tweezers	174
Figure 5.4. Semi-Passive Mode	177

Figure 5.5. Internal Distance Standard	182
Figure 5.6. Measurement of Systematic Error	184
Figure 5.7. Pairwise Distance for all Data and Top 50%.....	189
Figure 5.8. <i>t</i> -Test Step Finder	194
Figure 6.1. Example Kinetic Models	209
Figure 6.2. Examples of Conditional and Non-Conditional Statistics.....	211
Figure 6.3. Dwell Time Distributions for a Reversible System.....	212
Figure 7.1. Dwell Time Statistics versus Substrate Concentration.....	255
Figure 7.2. Fitting the Measured Data	262
Figure 7.3. Restricting the Catalytic Efficiencies of the Different Subunits	267
Figure 8.1. Mapping the Phosphate Contacts	295
Figure 8.2. High Resolution Experiments with 5 bp of dsMeP	298
Figure 8.3. High Resolution Dynamics at Neutral DNA	301
Figure 8.4. Possible Locations for ATP Hydrolysis	307
Figure 8.5. Effect of Packaged DNA on Packaging Velocity.....	315
Figure 8.6. High Resolution Dynamics at High Internal Filling.....	316

List of Tables

Table 5.1. Estimates of Systematic Errors in Dwell Time Moments.....	201
Table 7.1. Parameter Fits to Packaging Data.....	262

Acknowledgements

This thesis is the result of the collaborative work of several very talented people. In particular, I am indebted to Yann Chemla who was involved in nearly all of the research described here. Always calm and rigorous in his thinking, he set the high standards I strive to achieve in my own work. I also owe much to Jason Choy and Stephan Grill. Many of the ideas in the instrumentation portion of this thesis had their origins in casual conversations over coffee with these talented individuals. Their openness and willingness to discuss ideas should be the model of free scientific thought. Jason will be missed by those who knew him.

I'm also indebted to Craig Hetherington, Ariel Kaplan, Gheorghe Chistol, Marta Kopaczyńska, Adam Politzer, Melania Strychar ska, Lacramioara Bintu, Yara Meija, Phillip Elms, Eric Galburt, Jeff Vieregg, Christian Kaiser, Wei Cheng, Aathavan Karunakaran, Courtney Hodges, Oren Levy, David Izhaky, and Nancy Forde for conversations and guidance, both scientific and personal, over the past six years. In addition, I must thank all of the other members of the Bustamante and Tinoco labs, past and present, for creating a great environment in which to balance work with foosball.

Finally, I owe a tremendous scientific and personal debt to my advisor, Carlos Bustamante. From him I have learned that the backbone of science is the people who conduct it. Ideas are worth little if they can't be clearly communicated to others.

1. Violine *f espr.e legato*

2. Violine *f espr.e legato*
div.

Bratsche *f espr.e legato*

Violoncell *f espr.e legato*

Kontrabass *f pesante*
Un poco sostenuto

1. Viol. *pizz.*

2. Viol. *f pizz.*

Br. *f unis. pizz.*

Vcl. *f pizz.*

K.-B. *f pizz.*

-Johannes Brahms, *Un poco sostenuto*, Symphony No. 1 in C minor, Op. 68, 1876

Chapter 1. Introduction

Our view of the cell and cellular dynamics has undergone a quiet but revolutionary shift over the last half of a century (1). During the fifties and sixties when molecular biology was born, it seemed clear that the driving force of cellular dynamics was thermal diffusion. If a metabolite and an enzyme needed to associate and bind, it was diffusion which brought them together. If a DNA binding protein needed to find its binding site, it was diffusion which facilitated its search. If cellular cargo was required in one portion of the cell, but produced in another, it was diffusion which carried this cargo from point A to point B.

While thermal diffusion is clearly an important player in cellular dynamics, this picture suggests an image of the cell (or at least the cytosol) which is homogeneous and isotropic. In the past fifty years it has become increasingly clear that this is simply not the case (1). When cellular cargo needs to be transported from one portion of the cell to the next, it isn't diffusion that accomplishes this task. Rather, the cargo is *physically carried* by an enzyme which *walks* along an intracellular highway established for that exact purpose. When DNA needs to be replicated, the DNA polymerase does not float along an untethered DNA molecule. Rather, a fixed polymerase *pulls* the DNA through a complex assembly of proteins (2). Moreover, when similar genes are expressed, distal regions of different chromosomes are physically transported to *fixed assemblies* which include all of the enzymes needed to create and process the mRNA (3, 4). In other

words, the cell is far from homogeneous and isotropic. And rather than being the exception, highly localized assemblies and large spatial gradients appear to be the norm.

At the core of these inherently mechanical processes is a class of enzymes known as molecular motors. These assemblies of protein and nucleic acid catalyze a chemical reaction—hydrolysis of a bond or transport of some chemical species along its chemical potential—and from the free energy released in this reaction catalyze the generation of directed motion. With directional motion comes the need for mechanical work and the generation of forces or torques. Thus, molecular motors are chemical to mechanical transducers, taking chemical energy and converting it into the physical motions needed to operate the cellular factory.

The list of enzymes which are molecular motors is expanding. Just ten years ago, when one said molecular motor, it was the cargo transport proteins or muscle proteins such as kinesin or myosin which came to mind. However, it is now clear that enzymes such as RNA and DNA polymerases (5-8), nucleic acid helicases (9, 10), ribosomes (11), and many others also move directionally on a substrate and are capable of working against and generating physical forces. Moreover, enzymes which produce rotations rather than linear motions, such as F1 ATP synthase (12) or DNA topoisomerases (13-15), can also be thought of as converting chemical energy into mechanical work (or vice versa in the case of F1 ATP synthase). And, once one starts down this road, it is clear that even metabolic enzymes involve at least internal motions, thus, they too must generate forces and torques (1). In short, rather than being a small, specialized class of enzymes, molecular motors are the core players in the cellular world.

In this thesis, we will directly probe the mechanism of one of these remarkable cellular machines—a molecular DNA pump used to package DNA in a bacterial virus. In this process, we will develop both the novel experimental tools that will permit us to observe the individual catalytic turnovers of a single copy of this motor and the novel theoretical tools needed to extract the mechanistic information from these new data. As we will see, biology has many surprises in store for us, and the dynamics of this machine are more subtle and elegant than anyone would have expected.

Portions of this thesis have been previously published in a variety of places, Refs. (16-21), and are reproduced with permission from the various publishers.

1.1: The DNA Packaging Motor

Of the many mechanical events that occur in the cellular world, perhaps one of the most amazing is the compaction of genomic DNA into preformed protein shells, a task accomplished during the self assembly of many bacterial and animal viruses (22-24). What is remarkable about this process is the degree to which the genome is compressed: it reaches near-crystalline densities and is pressurized to many times atmospheric pressure. At the heart of this phenomenon is a multimeric molecular motor which converts chemical energy harnessed from the hydrolysis of the gamma phosphate bond in adenosine triphosphate (ATP) into the necessary mechanical work needed to compact the genome. In this thesis, we will dissect the mechanochemical mechanism of such a motor—the packaging motor of the bacteriophage φ 29. In this section, we introduce the bacteriophage φ 29 and its packaging motor, review what is known of its function and the

function of related enzymes, and pose the questions that we will address directly in this thesis. These topics are reviewed in Refs. (21-25).

1.1.1: An Introduction to φ29

The bacteriophage φ29 is a double-stranded DNA (dsDNA) virus that infects the common soil bacteria, *B. subtilis*. With a genome of only 19.3 kb that encodes for only ~20 proteins, φ29 is perhaps one of the simplest known of the dsDNA bacteriophages (23). During its infection cycle, φ29 docks to an unknown receptor on the surface of *B. subtilis*. It then injects its genome, leaving behind all of the protein machinery needed to transport the genome from one host cell to the next. Early genes are expressed (25), and the process of capsid assembly starts. See Figure 1.1. In parallel, the genome is replicated and prepared for packaging. Once the genome is ready and the capsids are assembled, the phage DNA is packaged inside the capsid. This process continues with the assembly of the final infectious machinery—the tail assembly (26, 27). The infection completes with the lysis of the cell and the release of fully infectious particles. From start to finish, this process takes only ~40 minutes (23).

During the self-assembly process, the bacteriophage overcomes a rather remarkable problem. This problem is best illustrated by comparing the dimensions of the capsid, roughly 40 by 50 nm, to the size of the genome, ~7 microns. Thus, the DNA is a 100-fold larger than the capsid in which it needs to be packaged (23). In fact, a back-of-the-envelope calculation reveals that when packaged fully, the DNA fills nearly 50% of the free space in the capsid and is compressed to near-crystalline density and extremely large concentrations, ~500 mg/mL! This compaction is particular impressive when one recalls that DNA is a highly-charged, stiff polymer; thus, compressing it to such densities

requires overcoming large electrostatic, elastic, not to mention, entropic barriers. (The barriers to genome compaction have been extensively reviewed in Refs. (28-32)).

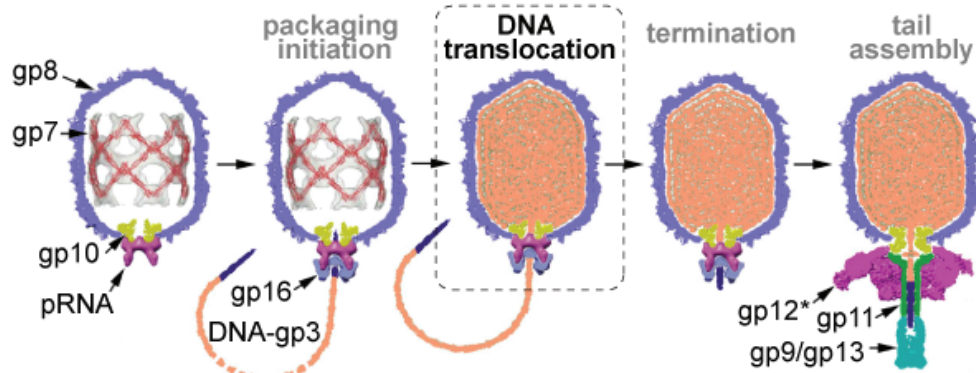


Figure 1.1. ϕ 29 Assembly Pathway

Gene products (gp) 7, 8, and 10 assemble the prohead—the empty shell which will protect the genome during transport from one host cell to the next. Once the pentameric pRNA assembles on the connector, gp10, the phage genome with the terminal protein gp3 and the pentameric ATPase gp16 assemble to form the full motor complex. After the packaging motor compresses the genome into the capsid, the packaging process is terminated with the disassembly of the pRNA and gp16 rings. The rest of the infectious machinery, gps 9, 11, 12* and 13, then attach and complete the self replication process. This thesis will focus on the process of DNA translocation—the step highlighted in the dashed box. Figure courtesy of P. Jardine and G. Chistol.

1.1.2: The Packaging Motor

Given the large energy costs associated with packaging the genome, it is clear that this process cannot occur spontaneously. The bacteriophage cannot wait for thermal fluctuations to drive the DNA into the capsid. To overcome these energy barriers, the bacteriophage has evolved a molecular DNA pump—a complex assembly of protein and nucleic acid known as the packaging motor (23). This molecular complex catalyzes the hydrolysis of the gamma phosphate bond in adenosine triphosphate (ATP) and somehow uses this chemical energy to overcome the large mechanical barriers to genome compaction.

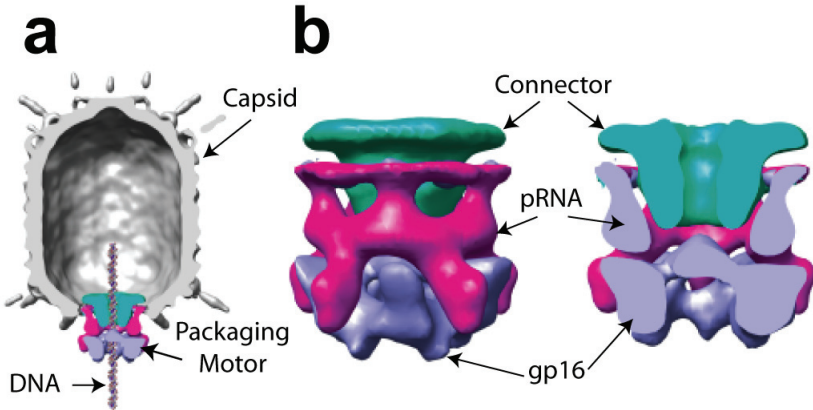


Figure 1.2. The Packaging Motor

(a) Cryo-electron microscopy (EM) reconstruction of the capsid with the packaging motor complex. The DNA is modeled here to set the relative scale. (b) Cyro-EM reconstruction of the different components of the packaging motor: the dodecameric connector, gene product 10 (gp10), the pentameric pRNA ring, and the pentameric ATPase ring, gp16. Adapted from Ref. (33) with permission from Elsevier, © 2008.

Structural, biochemical, and even single-molecule techniques have already revealed much about the packaging motor. The motor is composed of three major components. See Figure 1.2. The first component is the dodecameric connector (34, 35) (gene product 10), which provides a structural bridge between the capsid and the rest of the packaging motor (23). The connector is situated in one of the five-fold vertices along the prolate axis of the capsid (23), and the five-twelve symmetry mismatch that results from this location has been the subject of much discussion (36). A symmetry mismatch implies that there is no unique orientation of the connector and capsid, and, thus, no large barriers to rotation of the connector within the capsid (36). This observation, in turn, suggests packaging models which involve DNA translocation driven by rotation of the connector—much like a nut and a screw (23, 34, 36). For this reason, the connector was considered the central, active component of the packaging motor for many years. However, recent experiments have ruled out the active rotation of the

connector during packaging (37, 38). And sequence homology work, described below, now makes it seem likely that another component of the motor is the active translocase. (In Chapter 8, we will discuss preliminary experimental results which suggest that connector does play an important *regulatory* role in the packaging process, acting as a molecular throttle.)

Situated on top of the connector is the next component of the packaging motor, a novel RNA ring known as the prohead- or p-RNA ring (23, 33, 39). This ring is formed by exploiting normal intra-molecular kissing loop interactions used to form RNA pseudo knots in an inter-molecular fashion (23, 40, 41). Extensive mutational analyses (23, 39, 40, 42-46) have revealed crucial and dispensable portions of the 174 nucleotide monomers which form this ring, yet, aside from the recognition of viral genome during initiation (S. Grimes, unpublished), its exact role in packaging process remains elusive (23). (Single-molecule experiments aimed at understanding the role of the pRNA ring are underway but will not be discussed as a part of this thesis.)

There has been a lively debate over the multimeric state of this pRNA ring (33, 34, 39, 44, 47-49). Experiments in which the pseudo-knots of individual RNA molecules are mutated to support only specific combinations of mutant RNA molecules support the existence of trimers and dimers on the pRNA ring (44). This observation, in turn, suggests that the multimeric state of the entire ring is a common multiple of two and three, i.e. a hexamer. However, recent experiments designed to probe the role of the pRNA via mutations reveal that the pRNA ring can tolerate single mismatched pseudo-knots, clouding the interpretation of these genetic experiments (S. Grimes, unpublished). The hexamer hypothesis was also recently supported by single molecule photobleaching

experiments in which RNA molecules were tagged with a fluorophore and single bleaching events were counted to determine the number of RNA molecules that are bound to a single prohead (47, 50-52). Unfortunately, the labeling efficiency in these experiments was not 100%; thus, the number of observed photobleaching events was variable and the exact number of molecules subject to interpretation. Similar experiments were also conducted with pRNA labeled with ferritin and gold nanoparticles which could be imaged by electron-microscopy, but these studies suffer from the same issues with labeling efficiency (53). In parallel, cryo-electron-microscopy images of single capsid-connector-pRNA ring complexes has uniformly suggested that the pRNA ring is a pentamer (33, 34, 48, 49). The caveat to these experiments is that they assume symmetry to improve the signal-to-noise ratio in their multi-particle averages. Assuming a pentameric symmetry produces a clear pentameric ring (49) with density that is well described by models of the pRNA monomers (48) whereas assuming a hexameric symmetry produces a smooth density devoid of feature (49). In our opinion, the cryo-electron microscopy experiments are the most convincing, making it likely that the pRNA ring is a pentamer. Thus, throughout this thesis we will assume that this is the case.

Finally, the last component of the packaging motor is a ring of identical copies of gene product 16 (gp16), a 36 kDalton ATPase (54). Sequence analysis using sensitive profiles (55) built from the FtsK/HerA family of ATPases (56) identifies gp16 and analogous proteins from related phages as a recently divergent clade of the FtsK/HerA family. Members of this family are RecA-like ATPases, which commonly form homomeric ATPase rings, as is thought to be the case for gp16 (23, 33, 57). See Figure

1.2. Since FtsK and its relatives are capable of translocating nucleic acid polymers without structures analogous to the connector or pRNA ring, it seems likely that the gp16 ring is the core translocase in the packaging motor. For this reason, we will focus our discussion on the gp16 ring throughout this thesis, though it should be understood that this does not rule out important roles for the pRNA and connector in active translocation of DNA. Finally, while there remains some debate over the multimeric state of the gp16 ring (since it is believed that it shares the same multimeric state as the pRNA ring), cryo-electron microscopy has now imaged this ring directly, revealing that it is likely a pentamer (33). And, again, we will assume this multimeric state throughout this thesis. Aside from a few cosmetic differences in our packaging models, this assumption does little to change the interpretation of the data we will present.

1.1.3: Previous Single-Molecule Experiments

The packaging motor has been the subject of several single-molecule measurements aimed at addressing several basic features of its mechanism (37, 58-62). In the basic optical tweezers assay, depicted in Figure 1.3a, single prohead-motor-DNA complexes are attached via antibodies to polystyrene beads affixed to a micropipette while the other end of the DNA is held via a biotin-streptavidin linkage to a second polystyrene bead held in an optical tweezers (63) (we will further discuss optical tweezers below and in Chapter 2). By introducing an ATP containing buffer, the procapsid can be induced to package the DNA. The result is a shortening of the DNA tether remaining between the capsid and the streptavidin bead (the rest of the DNA is packaged into the capsid), and by following this length as a function of time, the rate at which DNA is packaged can be measured. See Figure 1.3b. This assay allows two basic questions to be asked. First,

how strong is the packaging motor, i.e. how does force affect its packaging rate? And, second, how is this force generated; what chemical transition, ATP binding or product release, corresponds to the actual conformational change that packages the DNA and generates force?

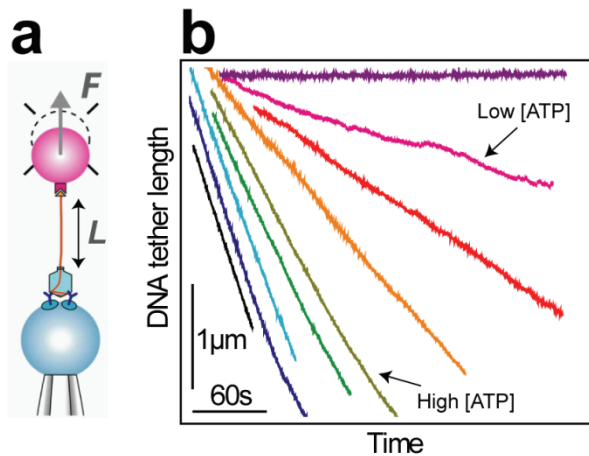


Figure 1.3. Previous Optical Tweezers Experiments

(a) Cartoon depiction of the optical tweezers packaging assay. A single prohead-motor-DNA complex is immobilized on a polystyrene bead fixed to a micropipette via antibodies to the major capsid protein, gp8. The other end of the DNA is affixed to a streptavidin-coated, polystyrene bead via a biotinylated nucleotide incorporated into the end of the DNA. This bead is held in an optical trap which allows both the application of an average tension to the DNA molecule, F , and the direct measurement of the response of the system. As the bacteriophage packages the DNA, its length, L , decreases in time. (b) Length of a single DNA tether as a function of time under different concentrations of ATP. The slopes of these traces are the average rate at which the motor packages the DNA, i.e. the packaging velocity. Adapted from Ref. (59) with permission from Elsevier, © 2005.

In the initial studies, Smith and Tans et al. (58) addressed the strength of the packaging motor by using the optical trap to play a molecular tug-of-war with the packaging motor and follow the average packaging velocity as a function of the applied force. They found that the packaging velocity decreased slowly with increasing force finally coming to a halt at an average force of ~60 pN (58). To understand the scale of this *stall force*, recall that muscle myosins—the proteins responsible for macroscopic

force generation—stall at a force of ~5 pN (64), 10-fold smaller than the packaging motor. Moreover, DNA undergoes a phase transition, unwinding and melting, under tensions of ~67 pN (65, 66). Thus, not only is the packaging motor one of the strongest known molecular motors, it is essentially as strong as the physical properties of its nucleic acid substrate permit it to be (21).

In addition, Smith and Tans et al. noticed that as packaging proceeds at a constant force the packaging velocity decreases naturally (58). They hypothesized that this was due to the increasing resistance of DNA already packaged within the capsid. Moreover, the force sensitivity of packaging complexes with different amounts of prepackaged DNA appeared to differ only by the addition of an *internal* force added to account for the prepackaged DNA. This analysis suggested that the internalized DNA generated an internal force opposing packaging which was *additive*, i.e. the effective force felt by the packaging motor is the sum of the external, optically applied force and this internal force. This observation allowed the internal force to be calibrated from the decrease in packaging velocity as a function of DNA filling. Dividing by the effective cross section of DNA turned this internal force into an estimate for the pressure of the fully packaged genome—a remarkable 60 atmospheres at the end of packaging (58). Recently, the measurements of the effect of the screening the DNA charge with different salts has supported a decrease in packaging velocity due to an internal force (60, 61). We will revisit these measurements in Chapter 8 using the techniques developed in this thesis, and we will argue that in addition to this internal force, the slowdown of the packaging velocity arises from a novel molecular function most likely in the connector: a pressure-sensitive allosteric switch.

Following these initial studies, Chemla et al. (59) set out to determine the chemical transition which generates the force in the packaging motor. The general ATP hydrolysis cycle contains several core kinetic events: the binding of ATP, its hydrolysis, and then the release of its products, inorganic phosphate (P_i) and adenosine diphosphate (ADP). In the normal enzymatic study, the fact that these kinetic events correspond to physical conformational changes of the enzyme is typically ignored, essentially because the exact nature of these conformational changes is not particularly relevant for the kinetic mechanism. However, in a molecular motor at least one of these chemical transitions (or a related transition) generates a physical motion which is very relevant: it is the conformational change which actually generates the motion the DNA. Because this transition involves a physical motion along the direction of the optically-applied force (along the direction of the DNA tether), the application of force requires the enzyme to generate additional work, which slows the rate of this process. (The effect of force on kinetic rates is well reviewed in Ref. (1)).

Chemla et al. (59) used the ability to slow down the translocation rate with applied force to determine how this rate is coupled to other kinetic events, such as the binding of ATP, ADP, or P_i . The authors performed an exhaustive set of measurements probing the coupling between force, [ATP], [ADP], and [P_i] on the packaging velocity. They found that at very low concentrations of [ATP], where the time it takes to dock an ATP molecule dominates the kinetic cycle, the packaging velocity was largely insensitive to force. In contrast, at saturating concentrations of [ATP], where ATP effectively binds instantly, the packaging velocity was force sensitive. Since one would expect conditions of limiting ATP to be highly force sensitive if ATP binding were the force generating

step, these results immediately implied that a different kinetic transition generates force. The authors supplemented these observations with a more detailed analysis (67) in which the force dependence of the Michaelis-Menten constants that described the ATP dependence of the packaging velocity was tabulated. From this measured behavior, it was shown that not only was the force generation step not the binding of ATP, this step could not be a kinetic transition which was connected via reversible transitions to ATP binding.

In parallel, the authors demonstrated that ADP acts as a competitive inhibitor while $[P_i]$ has no measurable effect on packaging velocity, indicating that ADP is capable of reversibly binding to the motor whereas P_i is not. This observation suggests that the release of product ADP is reversible while the release of product P_i is not. Thus, as an irreversible transition after binding, P_i release is a very likely candidate for the force generating step (59).

Finally, the authors performed a series of experiments in which they added trace amounts of non-hydrolyzable ATP analogs such as AMP-PNP or ATP- γ -S. They found that these analogs introduced long-lived pauses into the packaging process with a pause frequency linearly proportional to the relative concentration of analog and ATP. This observation suggests that the binding of a single non-hydrolyzable analog to a single motor subunit is sufficient to pause the entire motor, indicating that the identical ATPase subunits that compose the packaging motor cannot act independently. They must somehow coordinate their individual hydrolysis cycles.

1.1.4: Open Questions

While these studies provide an extensive set of constraints on the mechanism of the packaging motor, there remain several very interesting open questions. First of all, the studies observe only the average packaging velocity of the motor, yet it is likely that the DNA is not packaged in a smooth continuous fashion, but in discrete increments. Measurements of the force dependence of the packaging velocity can put limits on the size of these discrete increments—the step size of the motor—but cannot uniquely determine it. Second, the non-hydrolyzable ATP analog studies hint at a certain degree of coordination between the hydrolysis cycles of the individual subunits, but do not provide a clear picture of how the subunits are actually coordinated. Addressing these questions will be, in part, the subject of this thesis.

The cyclic nature of the enzymatic cycle and the clear chemical periodicity of DNA make it extremely likely that the packaging motor encapsidates discrete increments of DNA, and a quantitative measure of this step size is interesting for several reasons. First, it is a crucial mechanical property of the motor, providing constraints on the size of internal conformational changes which drive translocation. These measures will be crucial in interpreting atomic structures of the packaging motor when they are available. Second, by matching the step size with the chemical periodicity of DNA, it will be possible to infer properties of the motor-DNA interactions. Finally, a quantitative measure of the step size is crucial in understanding energy transduction in the packaging motor, e.g., translating the stall force into a measure of the thermodynamic efficiency at which chemical energy is converted into mechanical work.

Previous experimental results place limits on the possible values of the step size. In particular, the stall force can be used to place an upper limit on the amount of DNA packaged per ATP consumed. From an energetic perspective, a 60 pN stall force and a free energy of ATP hydrolysis of ~100 pNm indicate that the step size must be no greater than ~5 bp of DNA since applying 60 pN over a distance of 5 bp produces a mechanical work equal to the free energy of ATP hydrolysis. In parallel, a lower limit on the step size can be set using bulk techniques. Namely, by measuring the amount of DNA packaged into proheads and the amount of ATP consumed in this process, Guo and coworkers (54) determined that on average ~2 bp are packaged per ATP consumed, a measurement that was recently confirmed by Chemla et al. (59). This measurement is a lower limit on the step size because there are a variety of processes which could consume ATP without packaging DNA but few processes, if any, that can package DNA without consuming ATP. Thus, we expect a step size somewhere between 2 and 5 base pairs.

Essentially all molecular motors will have a step size; however, the multimeric nature of the packaging motor—the fact that it is a pentameric ring of identical ATPases—raises mechanistic questions that are unique to homomeric ring ATPases. In particular, like a multi-piston engine, the packaging motor must somehow coordinate the action of its individual subunits—the molecular analog of a timing belt—if it is to avoid competing one subunit with another. This inter-subunit coordination is of particular interest for two reasons. First and foremost, an understanding of how the individual subunits coordinate their cycle is crucial to a detailed picture of the mechanism of this enzyme. The basic results of Chemla et al.(59) provide a picture of the basic function of a single subunit—ATP binds, is hydrolyzed, and upon product release generates a ~2 bp

step—but these measurements say relatively little about how the individual cycles are interwoven to produce the mechanochemical cycle of the entire ring. This understanding is critical to determining how the packaging motor is capable of exerting the remarkably large forces needed to package the genome. Second, as discussed above and will be discussed further below, the packaging motor is but one member of a large superfamily of ring ATPases. In fact, homomeric ring ATPases are ubiquitous in the cellular factory. And in all cases, these proteins must address this same fundamental problem: the individual subunits in the ring must somehow coordinate their activity. Thus, an understanding of the mechanism by which the subunits in the packaging motor coordinate their hydrolysis cycles will shed light on the basic operating principles of these related ATPases.

While the inter-subunit coordination in the packaging motor is not yet known, there are several basic models for such coordination. The first type of model, and by far the most common in the literature, is known as a *sequential* model (68, 69). In such a model, see Figure 1.4a, a single ATP binds to a single subunit, this subunit hydrolyzes this ATP and then generates a step, before activating an adjacent subunit, which repeats this process. Thus, in a sequential model every translocation step is preceded by the binding of single ATP. (There are many variants on this model with different nucleotide states of the other subunits, but all sequential models share this one ATP, one step feature.) Such a model has been proposed from stopped-flow experiments with the hexameric ring ATPases, *E. coli* DnaB (70, 71), *E. coli* Rho (72), and T7 gp4 (73). In addition, x-ray crystal structures have captured what appear to be intermediates states in a sequential model for Rho (74), the bovine papilloma virus (BPV) helicase E1 (75), T7

gp4 (76), the RNA packaging motor, P4, of the bacteriophage ϕ 12 (77), and the DNA translocase FtsK (78). Finally, experiments in which mutant and wild type subunits are mixed to form heteromeric rings support such a model for FtsK (78) and T7 gp4 (79). Based on a variety of measurements, such a model has also been proposed for the packaging motor (43, 59).

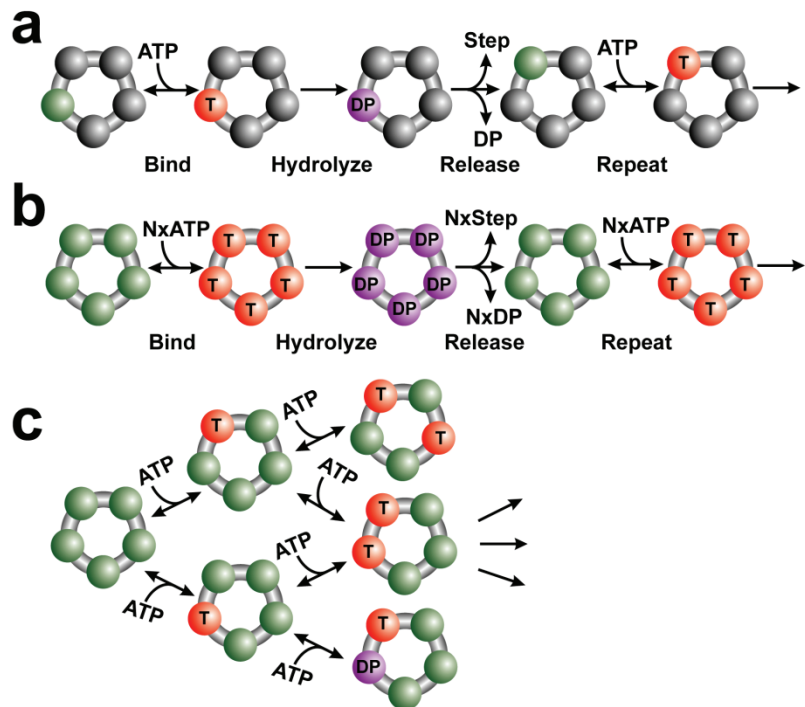


Figure 1.4. Inter-Subunit Coordination Models for Ring ATPases

(a) Cartoon depiction of a sequential model. One subunit binds ATP, hydrolyzes it, and generates a step upon product release. The next subunit then repeats this process. Sequential models can vary in the nucleotide state of the different subunits but all sequential models involve the binding of a single ATP before each single step. (b) Cartoon depiction of a concerted mechanism. This mechanism, proposed for the SV40 large tumor antigen, involves the simultaneous or consecutive binding of multiple ATPs to multiple subunits. This is followed by collective hydrolysis and one concerted step by all of the subunits. (c) Cartoon depiction of a random model. The individual hydrolysis cycles of the individual subunits are independent of one another, and binding, hydrolysis and stepping occur in a random order between the subunits. In all cartoons green represents a binding competent subunit, red (T) represents ATP bound, and purple (DP) represents the post hydrolysis state.

Crystal structures of the large tumor antigen from the simian virus, SV40, suggest a different inter-subunit coordination model. These structures suggest that all six of the ATP binding sites in this related hexameric ATPase are either empty, ATP bound, or ADP bound (80). This suggested to the authors that this motor functions via a *concerted* model in which all of the subunits bind nucleotides simultaneously and then move in synchrony to generate one large motion of the DNA (80). See Figure 1.4b. There has been no further support for this mechanism in the literature, and it is unclear how all six subunits can engage the DNA substrate simultaneously to generate one concerted translocation of the DNA. However, strictly speaking such a model is also consistent with the non-hydrolyzable analog induced pauses in the behavior of the packaging motor.

Finally, biochemical studies involving mixes of wild-type and mutant subunits for additional related ATPases, the bacterial ClpX protein translocase (81) and the archaeal MCM DNA translocase (82), suggest a limited degree of inter-subunit coordination in these systems. In the ClpX system it was shown that the rate of ATP hydrolysis and protein digestion decreased in linear proportion to the number of catalytically dead subunits in the ring, suggesting a *random* model in which each subunit is capable of driving peptide translocation independent of the state of the other subunits. See Figure 1.4c. Similar experiments in the MCM system showed that the ATP hydrolysis rates were more sensitive to the presence of mutant subunits than a fully random model, but less sensitive than one would predict for a coordinated mechanism such as that depicted in Figure 1.4a&b. The authors propose that the individual subunits are coordinated via a sequential model, but when this mechanism encounters catalytically dead subunits or

other catalytic barriers, it is capable of randomly restarting the sequential mechanism with another subunit (82).

1.1.5: Aside: The Related ASCE Motors

As discussed above, the packaging motor is member of a wide and diverse set of cellular ATPases. In this brief aside, we discuss this family in order to set the larger biological and mechanistic context of the detailed questions we will address for the packaging motor.

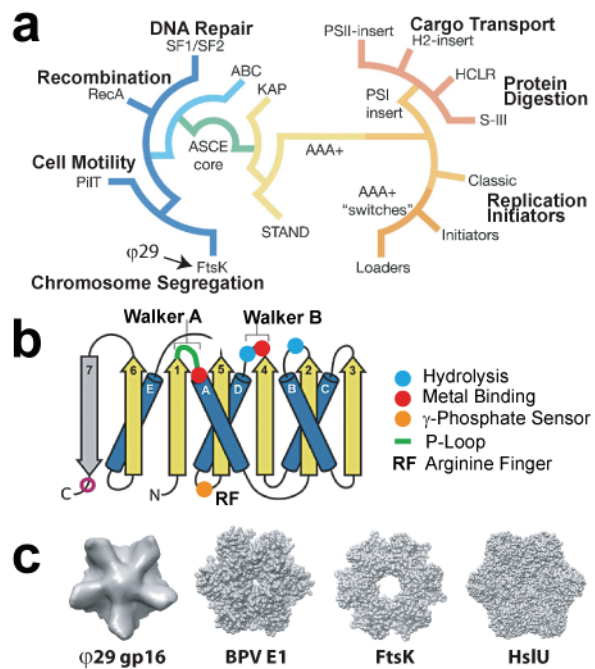


Figure 1.5. The Additional Strand Conserved E Superfamily

(a) A phylogenetic tree of the ASCE superfamily of cellular ATPases with functional annotations. (b) A cartoon depiction of the conserved ASCE fold in the context of the RecA family. The core ASCE domains correspond to beta sheets 1, 2, 4, 5, and 6 and the connecting helices. Conserved residues and motifs are labeled with their putative function in the hydrolysis cycle. (c) Cryo-electron microscopy or crystallographic images of representative members of the ASCE family which form homomeric rings. Cryo-EM map of gp16 courtesy of M. Morais (33). Panel (a) is adapted with permission from the Annual Reviews of Biophysics and Biomolecular Structure, © 2006 by Annual Reviews; Ref. (83). Panel (b) is adapted with permission from Molecular Microbiology, © 2008 by Blackwell Publishing; Ref. (84).

As discussed above, sequence homology identifies the packaging motor as a member of the FtsK/HerA family of ATPases (55). This family is itself a member of a much wider and diverse set of cellular ATPases, which has been collectively termed the Additional Strand Conserved glutamate (E) or ASCE superfamily (83, 85). See Figure 1.5. Members of this family play crucial roles in a remarkable diversity of cellular functions ranging from DNA replication and repair to protein transport and digestion and even to ATP synthesis and cell motility (83, 85-87). Figure 1.5 summarizes the different subfamilies or clades of the ASCE proteins, tabulates some of the cellular functions associated with members of each clade, and summarizes the basic structural features which are common to this family.

The core feature of the ASCE family—what makes a protein an ASCE protein—is a common structural motif composed of five parallel beta sheets connected by alpha helices. This structural motif is itself derived from an even more conserved structural domain known as the P-loop domain, a domain common to kinases and general NTPases among others (83-85). The distinction between these two domains is the addition of the fifth beta strand and a catalytic glutamate residue—the structural features which form the basis for the name of this family. While different clades and subfamilies of the ASCE superfamily have family specific additions to this core domain (83, 85), all ASCE proteins have this same structural core. See Figure 1.5b.

The likely reason that this core is so conserved is that it contains the residues responsible for the hydrolysis of nucleotide triphosphates. These important residues—which compose sequence motifs such as the Walker-A and Walker-B motifs—are contained on flexible loops between the beta sheets and alpha helices, and are responsible

for binding the phosphate backbone of the nucleotide triphosphate, positioning catalytic magnesium ions and water molecules, polarizing the backbone, and generally priming the system for hydrolysis (88). See Figure 1.5b. The majority of the conserved motifs occur on loops on the same side of the beta sheets; however, there are conserved residues distal to these domains. In particular, there is a highly conserved arginine residue (whose position does vary between families) which is believed to play an important role in the catalysis of NTPs (89).

How does a distal amino acid play an important role in the catalytic pocket? The answer is one of the core features of the ASCE proteins: they always occur in an oligomeric form with a competent catalytic pocket formed at the interface of *two* ASCE domains. The requirement to have two adjacent ASCE domains to form a competent catalytic pocket requires that in some form all ASCE proteins must multimerize. In general, this appears to occur in one of two fashions. In members of the superfamily I and superfamily II clades (SF1/SF2 in Figure 1.5a), this problem is often solved by fusing two ASCE domains into a single polypeptide. Alternatively, the ASCE proteins can form homomeric or heteromeric rings (or helical structures) in which the proteins are placed “front-to-back” to form competent ATPase pockets at the interface between subunits. This is an extremely common architecture shared by proteins from nearly all of the clades or sub-families, as demonstrated in Figure 1.5c. The implications of this domain architecture for the amplification of small conformational changes induced during ATP hydrolysis into large conformational changes needed for the function of these proteins should not go unnoticed.

Because the packaging motor shares a common structural core and a common oligomerization strategy with a wide and varied set of crucial cellular ATPases, an understanding of the mechanism of the packaging motor may be of more interest than just in deciphering the mystery of genome compaction. The same mechanistic problems which we will address in the packaging motor, discussed above, will arise in all multimeric rings ATPases of the ASCE family, and may to some degree arise in the so-called monomeric ATPases as well; thus, the answers we provide will lend some insight into both the conserved dynamics of the core ASCE structure and the ways in which its functional dynamics can be altered to lead to the observed diversity in biological function.

1.2: Instrumentation Limitations

It turns out that measurement of the step size and measurement of the inter-subunit coordination are related. If one can observe the discrete increments of DNA that are packaged each cycle of the motor, then one can determine not only the step size of the enzyme—from direct measurement of the size of these increments—but also the inter-subunit coordination—from the statistics of the stepping traces. However, the expected step size for the packaging motor is small, and at the beginning of this thesis, optical tweezers instruments were not sensitive enough to measure such a small step size. In this Section, we provide a brief introduction to biological measurements with optical tweezers and the limits to the resolution of these measurements, topics we will discuss in detail in Chapters 2 and 3.

1.2.1: The Basics of Optical Tweezers Measurements

Optical trapping works on a simple principle: light carries momentum, and if that light is bent or deflected, it will transfer some of that momentum to the object that does the bending or refracting (18, 90-92). And since momentum transfer per unit time is force, reflected or refracted light applies a force on the object interacting with the light. These optical forces are typically small, not noticeable in the everyday macroscopic world. But for small objectives—micron-sized polystyrene beads, for example—the applied force can be sizable and can produce meaningful motions. (The physics of optical trapping is extensively reviewed in Refs. (92-95)).

By focusing light to a diffraction limited spot, an optical tweezers exploits these principles to form an optical potential which stably traps small objects in three dimensions. This potential allows the manipulation of these objects and the application of optically applied forces. More importantly, these optical forces can be precisely calibrated through a variety of techniques (92, 96) and the response of the trapped object measured accurately with a resolution that is typically sub-Ångstrom on the millisecond time scale (18, 92). The instrumentation necessary to accomplish these tasks will be discussed in detail in Chapter 2 and has been reviewed extensively (16, 18, 19, 92).

The ability to apply forces and manipulate small polystyrene beads can be translated into the ability to apply forces and measure the response of smaller biological systems, such as single pieces of dsDNA, by attaching these systems to these beads. In this case, the bead acts as a molecular handle, serving both as a means of manipulating the system and measuring its response. See Figure 1.3a.

A single piece of DNA stretched in this fashion is continually under bombardment by solvent molecules and the thermal fluctuations induced into this molecule induce fluctuations perpendicular to the axis at which the DNA is pulled. These fluctuations are problematic because the distance between the optically trapped bead and the fixed bead, see Figure 1.3a, will not be a direct measure of the length of the DNA. Rather what is measured is the molecular extension—the projection of these fluctuations onto the axis along which the optically applied force acts. By increasing the average applied force, these fluctuations can be “squeezed” out, increasing the extension of the molecule. However, since the length of the DNA is not measured directly, changes to the length of this DNA molecule—due, for example, to a packaging bacteriophage—cannot be interpreted directly in terms of the physical movements of the enzyme. What is needed is a way to convert the end-to-end extension of the molecule at a particular force to its absolute contour length.

This problem was solved in the mid-90s by measuring the stretch properties of DNA—i.e. the degree to which the DNA would straighten and stretch under an applied force (65, 66, 97-102). These measurements allowed quantitative models to be built for how DNA responds under force, which in turn provided the ability to infer changes to the DNA directly from its measured extension under a given force. In particular, models such as the worm-like-chain interpolation formula (99) and its parameters have become a convenient way to “back out” the action of a biological system from the measured force and extension. Using this understanding of the polymer physics of DNA, and the typical optical tweezers setup shown in Figure 1.3a, a variety of biological dynamics has now been measured directly, ranging from the folding dynamics of nucleic acids and proteins

(103-106) to the action of polymerases, helicases, translocases, topoisomerases, and many others (5, 6, 18, 107).

1.2.2: Problems of Resolution

Continually bombarded by solvent molecules, the components of an optical tweezers measurement—the polystyrene beads, the DNA, and even the biological system itself—are never stationary, always fluctuating. And these fluctuations fundamentally limit our ability to infer small changes to the length of a piece of DNA with an optical tweezers. Fortunately, the physics of thermal fluctuations and diffusion is particularly well understood, and this fundamental limit can be calculated (6, 93, 108). The result is that if the biological system is sufficiently slowed, most of these fluctuations can be averaged away, and length changes as small as a single base pair should be observable. The distance between adjacent base pairs in B-form DNA is on average 3.4 Å (109), a distance roughly equivalent to three hydrogen atoms stacked one-on-top another. Thus, optical tweezers should have the ability to measure truly atomic-scale motions.

However, traditional optical tweezers measurements, as depicted in Figure 1.3a, were not able to reach this fundamental limit, and measurements were restricted to the several nanometer scale (63). The reason is obvious in retrospect. If one desires atomic-scale resolution, then all of the components in the measurement need to be stable relative to one another on the atomic scale. Given the dimensions of the experiment—micron sized beads attached to millimeter scale micropipettes—one part in a billion or better stability is required for atomic-scale stability in the measurement. Unfortunately, transient temperature variations cued by the heat produced by an operator in an instrument room, mechanical vibrations due to human movement through the building, or

acoustic vibrations due to quiet whispers can all generate instabilities larger than the width of a single hydrogen atom.

And without Ångstrom-scale stability, one cannot hope to measure the discrete steps of nucleic acid translocases such as the packaging motor. Thus, before we could begin to address the questions raised in the previous sections, it was first necessary to design and construct a novel optical tweezers, one insensitive to the multitude of noise sources which can easily obscure Ångstrom-scale motions. This is the issue which we tackle directly in Chapter 2. As we will show, it is now possible to achieve Ångstrom-scale stability in an optical tweezers and to reach the fundamental limits set by the unavoidable thermal fluctuations of the aqueous bath in which biological experiments must be conducted. In Chapter 3, we turn our attention to this fundamental limit itself and show that with a novel method of detecting motions in an optical tweezers, it is possible to actually lower this limit, making it that much easier to observe the fundamental motions of the packaging motor and other nucleic acid motors.

1.3: Theoretical Limitations

Dissecting the mechanism of the packaging motor from direct observation of its steps required solving not only the experimental challenges discussed above, but also significant theoretical problems as well. In particular, in the process of analyzing the high resolution stepping data described in this thesis, it became clear that a basic theoretical understanding of how to treat this data was lacking. The ability to observe the discrete steps of an enzyme allow the inherent fluctuations in its catalytic process to be measured directly, yet there was no clear and established method for extracting kinetic information from these fluctuations. In this section, we introduce the basic field of

statistical kinetics, a new and growing theoretical field concerned with extracting kinetic information from statistical measures of enzymatic fluctuations. And, we describe the theoretical problems we found it necessary to address in order to fully interpret the data collected in this thesis.

1.3.1: Fluctuating Enzyme Dynamics

Enzyme dynamics are naturally stochastic. While the directionality inherent in many catalyzed reactions is driven by the energy stored in chemical or electrochemical potentials, the internal conformational changes that compose the kinetic cycle of the enzyme often involve the crossing of kinetic barriers through thermally activated processes. As a result, the lifetime of each of the intermediate kinetic states is never the same. It is always fluctuating. Moreover, the trajectory of the enzyme through its kinetic cycle—the number of times it visits each kinetic state—is also variable, changing randomly each cycle of the enzyme. Thus, the time to complete one full enzymatic cycle, i.e. the sum of the individual lifetimes of each of the kinetic states visited, is naturally a stochastic quantity.

For much of the 20th century such fluctuations were ignored due simply to the difficulty of detecting them in large ensembles of unsynchronized copies of the enzyme; however, with the recent advances in single-molecule techniques and synchronized ensemble methods, it is now possible to observe these fluctuations directly (18, 107, 110). This powerful experimental advance necessarily raises new theoretical questions. In particular, what type of kinetic information is contained within fluctuations, and how do we extract this information in an unbiased fashion? Can fluctuations be classified—characterized, perhaps, by quantities in analogy to the Michaelis-Menten constants K_M

and k_{cat} ? And, if so, what are the implications of such classifications, and what do the new kinetic parameters tell us about possible mechanistic models?

These are the types of basic questions which face the new field of *statistical kinetics* (17, 111, 112)—the extension of enzyme kinetics from the mean rate of product formation to measures of the inherent fluctuations in this rate. If single-molecule studies are to realize their full potential, advances in experimental technique, such as those developed in this thesis, must be supplemented with advances in our theoretical understanding of the information content of fluctuations. In this Section, we will describe the foundational ideas of statistical kinetics, demonstrate the remarkable power of fluctuations to constrain kinetic models, and finally propose several outstanding theoretical questions that we will address in this thesis.

1.3.2: Steady-State Kinetics to Statistical Kinetics

How do traditional kinetic models produce fluctuations? To answer this question, let's consider the canonical kinetic model

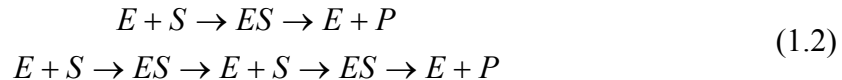


where an enzyme, E , binds substrate S at rate $k_1[S]$ to form the bound form ES . This bound form can then produce product P at a rate k_2 , or it can unbind the substrate unproductively at a rate k_{-1} . (For molecular motors product formation is equivalent to taking an observable step.)

In traditional steady-state kinetics, one would write out the set of coupled, first-order differential equations for the concentration of each of the species, E and ES —equations which describe how the concentration of one species changes continuously into

the next species—and then assume that concentrations have reached a steady-state, i.e. are constant in time. However, from a single-molecule perspective this picture is flawed. First of all, continuous changes are nonsensical; product formation is a discrete, punctate event. Secondly, the system can never be in steady-state: a single enzyme is either in one state or another, not some constant fraction of both.

Rather than considering continuous flows of one species to the next, it is more useful, on a single-molecule level, to think of a series of discrete paths through the kinetic cycle—paths which consist of consecutive and discrete transformations of one species into another (i.e. discrete hops between different kinetic states). For example, the above kinetic scheme implies that the following two diagrams represent valid microscopic paths to product formation



In the first path the enzyme binds substrate and then immediately forms product (depicted in the first step of Figure 1.6a) whereas in the second path it unbinds this substrate unproductively and has to rebind substrate before making product (depicted in the second step of Figure 1.6a). In this simple example, there are actually an infinite number of microscopic paths, representing the infinite number of times, in principle, that the enzyme could release substrate unproductively before completing a productive catalysis.

Now instead of thinking of the rate at which each species is transformed into the next, we consider the time the enzyme exists as each species. See Figure 1.6. The advantage of this subtle shift in thinking is that the lifetime for each of the above pathways is just the sum of the individual lifetimes of the states visited (113). For example, the total cycle completion time for the first pathway is $t = t_E + t_{ES}$, where t_E

and t_{ES} are the individual lifetimes of the empty and substrate bound states, respectively.

And the cycle completion time for the second pathway is $t = t_E + t_{ES} + t'_E + t'_{ES}$, where t'_E

and t'_{ES} are the distinct lifetimes of these states during the second visit. (The shift to a time view as opposed to a rate view is just a shift in perspective; a formal connection can be made between this picture and the first order differential equations that govern the concentrations of each species (17).)

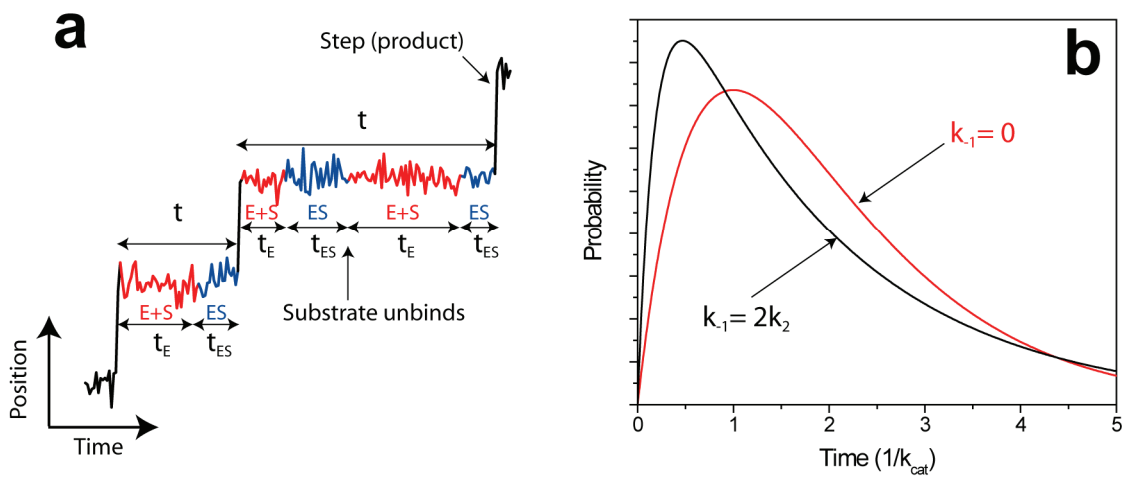


Figure 1.6. Statistical Kinetics

(a) A simulated molecular motor trace for the simple kinetic scheme considered in the text, where product formation is now the generation of an observable step, an increase in position. Each full dwell time or cycle completion time, t , can be divided into the lifetimes of the individual kinetic states, t_E and t_{ES} . Fluctuations in t come from both the variations in the individual lifetimes or in different number of visits to each state. (b) The probability of observing a dwell of a given duration t , the dwell time distribution, for the same kinetic model with a substrate concentration of K_M . The red trace corresponds to a model in which binding is irreversible, i.e. each cycle only visits E and ES once, while the black trace corresponds to reversible binding in which events like the second step in (a) are possible. Remarkably, these two models have exactly the same mean cycle completion times, and, thus, would be completely indistinguishable by traditional techniques. Yet the fluctuations clearly reveal the difference between the two mechanisms.

In this formalism, it is now clear that the statistical nature of this process arises in two fashions. First, the individual lifetimes of the states are themselves stochastic; thus,

their sum, the cycle completion time, will also be a random variable. In general, individual lifetimes are exponentially distributed via $\psi(t) = ke^{-kt}$ where k is the sum of all of the transition rates out of a specific state (114). (For the above example, $k_E = k_1[S]$ and $k_{ES} = k_{-1} + k_2$). The second type of stochastic behavior arises from the multiple microscopic paths that exist for product formation. Thus, not only are the individual lifetimes stochastic, so is the number of times that a given kinetic state is visited in a complete cycle (and thus the number of times that lifetime appears in the sum). Remarkably, as will show in Chapter 7, statistical measures of the fluctuations may be able to distinguish these two types of fluctuations.

1.3.3: Characterizing Fluctuations

We now arrive at the basic premise of statistical kinetics: since the inherent fluctuations in an enzymatic cycle completion time arise from the statistical properties of the kinetic states that compose the kinetic mechanism of the enzyme, measures of these statistical properties should constrain the properties of the underlying, *hidden* kinetic states. In other words, by measuring these fluctuations, it should be possible to infer properties of the kinetic mechanism of an enzyme. This brings us to perhaps the most fundamental outstanding question in statistical kinetics: how does one characterize enzymatic fluctuations in a way that provides information about the underlying kinetic mechanism of the enzymes?

Let us break this question down into two parts. First, how do we quantify and characterize these fluctuations, and, second, how do we extract information about kinetic mechanisms from these measures? Stochastic properties of enzymatic fluctuations can be measured and quantified just as one would quantify stochastic properties of any random

variable. One can calculate the statistical moments of this variable: its mean, its variance, its skew, etc. Alternatively, one can compute the full probability distribution of the random variable. These two methods are not completely independent since the probability distribution of a given random variable contains all of the information needed to compute its moments. (The converse is not true. A subset of the moments is typically not enough information to produce the full probability distribution.)

To illustrate this later method, let's again return to the simple enzymatic mechanism considered above (Eq. (1.1) and Figure 1.6a). In Figure 1.6b we plot the *dwell time distribution*—the probability of observing a cycle completion time of a given duration—for two different choices of kinetic rates in our enzymatic cycle. (The analytical form of these distributions was calculated with methods we discuss in Chapter 6.) In black we consider a system in which the probability of unbinding the substrate molecule unproductively is twice that of the probability of actually forming product with that molecule while in red we consider a system in which the enzyme *never* unbinds the substrate unproductively. Remarkably, through careful choice of the rate constants, it is possible for these two distributions to have the same mean and for this mean to have the same substrate dependence. Thus, measurements of the mean cycle completion time alone could not distinguish these two models. However, the dwell time distributions in Figure 1.6b are clearly different; thus, analysis of the fluctuations can discriminate between these two different mechanisms.

1.3.4: Multiple Pathways and Multiple Steps

As illustrated above, the dwell time distribution is an excellent way to characterize fluctuations for simple kinetic models. However, the above discussion makes an implicit

assumption: that each random dwell time is derived from the same kinetic mechanism, i.e. stochastic passage through the same kinetic states. This is an innocuous assumption when the enzyme takes a single type of step, e.g. forward steps of uniform size since it is likely that identical steps are produced by the same kinetic pathway. However, it is becoming increasingly clear that real enzymes display more complicated behaviors. For example, filament based cargo transport proteins such as kinesin, myosin, and dynein have now been observed to take both forward and *backward* steps and steps of varying size (115-123). Moreover, as we will show in Chapter 4, the stepping dynamics of the packaging motor are also more complicated than one simple class of step.

When there are multiple types of steps, there may also be multiple classes of dwell times, i.e. cycle completion times which come from very different kinetic pathways. Thus, before we can extract any kind of mechanistic information from fluctuations, we must be sure that we have properly sorted dwell times that are generated by the same kinetic mechanism and result in the same basic type of step. However, it is not immediately obvious how this should be done. Do we simply sort dwells based on the type of the following step? Or is possible that enzymatic dynamics may have some memory of more distant steps, perhaps the type of step before the dwell as well? Moreover, how do we distinguish between these possibilities; are there simple statistics that can be calculated directly from that data that allow these different possibilities to be addressed and the appropriate classification scheme to be determined?

These are the questions that we will address in Chapter 6. We will show that, in addition to the simple one-step statistics widely assumed in most kinetic models, enzymatic dynamics can display two additional classes of basic statistics: conditional

statistics and non-conditional statistics. Moreover, we will show how one can determine which type of statistics a given kinetic model will display and, in parallel, we will describe ways to determine the type of statistics displayed by actual enzymatic data. Finally, we conclude by demonstrating how these new classes of statistics modify a few common measures of enzymatic dynamics. As we will see in Chapter 4, an understanding of the type of statistics that arise in systems with multiple types of steps will prove useful in understanding the type of stepping behavior observed for the packaging motor.

1.3.5: Characterizing Fluctuations: Fitting Distributions

With a method for classifying dwell time dynamics correctly, even for the most complicated enzymatic behavior, we now return to the question of how to extract kinetic information from fluctuations. To illustrate this problem, consider again the simple example system above. In Figure 1.6b, we show that with the proper choice of rate constants, two different kinetic models (irreversible binding or reversible binding) can have the same mean time to complete the enzymatic cycle but very different fluctuations. The differences are clear in comparison, but imagine that we only had one of these distributions, as would be the case for real data. How do we then extract mechanistic information from this distribution?

One obvious possibility is to derive a function that describes the dwell time distribution and fit this expression to the measured distribution to extract information about the kinetic mechanism. This problem is complicated in two ways. First, it is very rare that the kinetic model is actually known *a priori*; thus, assumptions must be made about the specific kinetic model. For example, it is becoming increasingly common to

use the Poisson distribution to describe dwell time distributions. Since this distribution only has two free parameters, it is often quite well constrained by the data. The Poisson distribution is the correct functional form for the dwell time distribution when the underlying kinetic model has n states with equal lifetimes which are connected only via irreversible transitions. Unfortunately, it is often not the case that this feature can be assumed for an unknown kinetic model, and there is no well-established interpretation of fit values when the functional form of the distribution is simply not correct. Thus, in our opinion, despite being common in the literature, this technique should be avoided.

There is an alternative. It turns out that, under very general assumptions, it can be shown that a general kinetic model with n states will have a dwell time distribution that is described by a sum of n exponentials with different relative weights and decay rates (17); thus, in a very real sense we know exactly what function to fit to any distribution. However, this brings us to the second problem with fitting distributions. In practice, the general dwell time distribution has too many free parameters to be well constrained by typical amounts of data—especially when each data point is painstakingly gathered one at a time (17). Thus, it is often the case that there is simply not enough data to properly constrain dwell time distributions for accurate fitting.

The essential problem with the techniques above is that they are *model dependent*. The final kinetic information will be derived from the fit of a specific model to the data and, thus, this information will have little meaning outside of the context of the model used to fit the data. There is a recent method which attempts to extract rate information from dwell time distributions in a model-independent fashion. This method attempts to calculate a rate spectrum—the amplitude of exponentials at each decay rate—via direct

numerical manipulation of the distribution (124). This method is analogous to the Fourier method for disentangling different frequency components from complicated time series. While this method appears promising, it is only reported to perform well when the decay rates are separated by an order of magnitude, which is typically not the case in real experimental data (124). Moreover, this technique ultimately faces known and unsolved problems associated with the numerical stability of the Laplace transform; thus, we will not discuss this method further in this thesis.

1.3.6: Characterizing Fluctuations: Calculating Moments

Many of the problems associated with extracting information from the dwell time distribution directly can be relaxed by first calculating properties of this distribution such as its statistical moments. While it is clear that the moments of the distribution will contain a subset of the information contained in the full distribution, the advantage is that these moments are *model-independent*, i.e. a basic kinetic model or form for the distribution does not need to be assumed to calculate the mean dwell time or the variance in the dwell times. Moreover, calculation of these moments is simple and straightforward and there are well-established techniques to estimate the stochastic uncertainty in these moments directly from the measured data itself. And since the uncertainty in the moments can be easily calculated, one can use only the moments that are well constrained by the data, conveniently circumventing issues with unconstrained fits to distributions.

What can be learned with the moments of the dwell time distribution? In 1994, Schnitzer and Block (112, 125, 126) introduced a kinetic parameter related to the first and

second moments: the randomness parameter, $r = \frac{2D}{vd}$, where D is the effective diffusion constant of the enzyme, v is the average rate of the enzyme, and d is a normalization constant which determines the amount of product each cycle. For molecular motors, where this expression was first introduced, d is the step size. In this context, the diffusion constant is not the rate at which a molecular motor diffuses freely through solution, but a measure of how quickly two synchronized molecular motors will drift apart from one another.

Schnitzer and Block showed that under certain assumptions, the inverse of the randomness parameter is related to an additional quantity (112, 125),

$$n_{\min} = \frac{\langle \tau \rangle^2}{\langle \tau^2 \rangle - \langle \tau \rangle^2} \quad (1.3)$$

where $\langle \tau \rangle$ is the first moment of the dwell time distribution, its mean, and $\langle \tau^2 \rangle - \langle \tau \rangle^2$ is the second moment, its variance. Based on the analysis of a few example systems (112, 125), Schnitzer and Block conjectured that this dimensionless parameter provides a strict lower bound on the number of kinetic states that compose the underlying kinetic model, n_{actual} , i.e.

$$n_{\min} \leq n_{actual} \quad (1.4)$$

This is a remarkable conjecture which is worth a moment's inspection. Eq. (1.4) says that a weighted measure of enzymatic fluctuations places a *firm* limit on the number of kinetic states in the underlying kinetic model. The implication is that kinetic schemes with different numbers of kinetic states have *fundamentally different* statistical properties, and these properties can be used to discriminate between these models.

This conjecture was first proven rigorously by Koza in 2002 for an important class of kinetic models, nearest neighbor models, i.e. linear kinetic pathways with no parallel pathways, branches, or off-pathway events (127). (We provide an alternative proof in the Chapter 7.) However, no formal proof exists for this parameter for the general kinetic model. Despite this fact, no kinetic model has yet been found which violates this inequality, and its validity has been widely accepted.

1.3.7: A Michaelis-Menten Equation for Fluctuations

The remarkable inequality in Eq. (1.4) indicates that there is a tremendous amount of mechanistic information contained in the first two moments of the dwell time distribution and because these moments can be estimated in a model-independent fashion, the restrictions they place on the underlying kinetic mechanism are also model independent. We will use this inequality extensively in our study of the packaging motor, as described in Chapter 4.

However, as we will see, much of the informative power of this parameter comes from its limiting values at asymptotically low and high ATP concentration. We will argue in Chapter 4 that an understanding of what it means to be “limiting” or “saturating” in substrate concentration with respect to the mean dwell time is sufficient to insure that the measured concentrations are sufficiently high or low for n_{\min} to have reached its asymptotic values. Unfortunately, it is clear that this argument leaves much to be desired. How do we know that substrate concentrations are truly “limiting” or “saturating” with respect to n_{\min} ? Isn’t it possible that “limiting” and “saturating” have different functional meanings for measures of fluctuations and measures of the mean?

We can argue that a given substrate concentration is “saturating” or “limiting” for the mean dwell time because a substantial body of theoretical work has revealed that despite the near-infinite number of candidate kinetic models, there are only a few well-defined substrate dependencies for the mean rate of a reaction (the inverse of the mean dwell time), i.e. the Michaelis-Menten expression or the more general, but approximate, Hill-equation (128). Thus, in order for us to truly understand the properties of our fluctuation data, and to confirm that the conclusions we draw are based on valid assumptions, we need an analogous expression for the general substrate dependence of n_{\min} . We need a “Michaelis-Menten” equation for fluctuations.

In Chapter 7, we tackle this issue directly by deriving just such a function. We show that measurements of the second moment of enzymatic fluctuations and its dependence on substrate concentration yield three new kinetic parameters that classify the dynamics of enzymes (in addition to the two parameters typical of the Michaelis-Menten expression.) In addition, we demonstrate that, in contrast to the Michaelis-Menten parameters, these new kinetic constants have clear physical interpretations and place strict limits on possible kinetic models. Finally, we demonstrate that this general expression accurately describes the observed fluctuation data for the packaging motor. And in addition to confirming the conclusions we draw in Chapter 4, this analysis allows us to draw novel conclusions about the way in which the identical subunits within the ring ATPase bind ATP differently.

1.4: Thesis Organization

This thesis is organized in the following fashion. In Chapter 2, we discuss the novel instrumentation that we developed in order to perform quiet, Å-scale optical tweezers

measurements, a requirement for us to be able to observe the stepping dynamics of the bacteriophage packaging motor. The major advance in our instrument is the use of a second optical trap, allowing both ends of the biological system to be held optically. However, two optically trapped beads raise the possibility of additional thermal fluctuations in this system, fluctuations which might lower the resolution of the instrument and compromise the advances we have made in isolation. In Chapter 3, we address this question directly by solving the Brownian dynamics of two optically trapped beads coupled by a flexible DNA molecule. We use these solutions to derive the fundamental limit on spatial and temporal resolution in an optical tweezers and, remarkably, show that with clever detection methods, one can actually improve this limit. We demonstrate that the instruments described in Chapter 2 are capable of reaching this fundamental limit; thus, in a very real sense, these instruments are as quiet as they can be. We conclude by demonstrating that our instrument can observe length changes to a single piece of DNA of just one base pair, i.e. 3.4 Å.

With the ability to detect single-base-pair length changes, we turn our attention to the central mechanistic questions for the packaging motor. In Chapter 4, we describe the direct observation of the discrete increments of DNA packaged by this motor. Our measurements reveal that the identical subunits within the ATPase ring that drives packaging are highly coordinated in a fashion novel for ring ATPases. Moreover, we find that DNA is packaged in a fundamental step size that is *not* an integer number of base pairs. This result, in particular, has profound implications for the mechanism of the packaging motor, and we speculate on the implications for such a step size.

In Chapter 5, we describe the variety of experimental methods necessary to make the measurements described in Chapter 4. In some cases, we draw upon techniques that already exist in the literature, but in other cases, new methods were needed. Of particular interest is a novel way to determine systematic errors in our distance measurements. Using these methods, we can place firm uncertainties on our step size, which include not only the stochastic errors that naturally occur for finite measurements, but also firm estimates of the *systematic* errors in our measurements.

As we will show, the stepping behavior of the packaging motor turned out to be more complicated than initially expected; thus, to understand this data, we had to revisit basic assumptions about the type of stepping behaviors generated by simple kinetic models. In Chapter 6, we investigate the types of stepping statistics that are possible with generalized kinetic models. We derive two new classes of stepping statistics, demonstrate the practical effects of these classes on useful measures of enzymatic fluctuations, and finally describe methods by which actual stepping data can be easily classified. It is often useful to be able to calculate the expected properties of complicated kinetic models analytically; thus, we conclude this Chapter by describing a new method we have developed for performing these calculations.

In Chapter 7, we turn our attention to the fluctuations inherent in the mechanism of the packaging motor, and general enzymatic dynamics. In order to extract as much mechanistic information as we possibly can from this data, we develop a theoretical understanding of the general substrate dependence of enzymatic fluctuations. In essence, we derive a “Michaelis-Menten” equation for enzymatic fluctuations. We demonstrate that this expression accurately describes the measurements on the packaging motor. The

kinetic parameters from this fit not only confirm our previous interpretation of this data, they also provide quantitative constraints on the fashion in which ATP loads to the subunits within the ring.

Finally, we conclude this thesis in Chapter 8 by discussing the future avenues for research. In particular, we focus on several experiments that are currently underway and which promise to address missing features of the motor mechanism. Of particular interest is a set of measurements which hint at a novel role for the connector in the packaging dynamics as the capsid fills with DNA. We conclude this chapter with some brief speculation on the potential universality of our model of the packaging motor dynamics and the future of high resolution optical trapping techniques.

Chapter 2. Design and Construction of a High Resolution Optical Tweezers

For molecular motors which move along nucleic acid substrates, such as dsDNA, the base-pair scale is the expected spatial scale for the fundamental motions, or steps, of these enzymes. However, the base pair scale is small—the distance between adjacent base pairs along the contour length of dsDNA is just 3.4 Å, a distance roughly equivalent to three hydrogen atoms stacked one on top of another. Unfortunately, though perhaps unsurprisingly, such distances are smaller than the instabilities and noise sources that limit the spatial resolution in traditional optical tweezers measurements. Thus, the direct observation of the discrete steps of such motors is out of reach for the traditional instruments.

In this Chapter, we discuss the design and construction of an optical tweezers which is not limited by typical noise sources, an instrument which we will show in the following chapters permits the direct observation of base-pair-scale motions of single nucleic acid motors. The material for this chapter has been discussed previously, and some of the figures and discussions presented here have been drawn from Refs. (16, 18, 19) with minimal changes.

2.1: Why do we Need Better Resolution?

Many fundamental processes in the cell are mechanical in nature and occur by discrete physical movements—for example, the steps of molecular motors along cytoskeletal filaments, the incorporation of one nucleotide to a nascent nucleic acid chain in transcription or replication, or the unfolding and degradation of a protein domain by the proteasome. Often, the size of these displacements, the *step size*, is dictated by the inherent chemical periodicity of the track on which these systems move, e.g. the 8-nm repeat of microtubule monomers or the 3.4-Å distance between adjacent base pairs in double-stranded DNA (dsDNA). Thus, the chemical periodicity of this track can be used as a first approximation for estimates of the step size of a molecular motor.

Why is it interesting to measure the step size? First, the step size of a molecular motor is a crucial mechanical parameter, which characterizes the motor mechanism. The size of this step, its uniformity, and any potential variability in this size all provide crucial constraints on the mechanical mechanism of the enzyme, addressing questions related to how it engages its substrate and placing limits on the size of the internal conformational changes which generate mechanical work. Second, and perhaps more interestingly, the ability to measure the discrete steps of a molecular motor provide a clear indication of the beginning and end of a catalytic cycle. The ability to demarcate the exact times that the catalytic process begins and ends allows one to compute not just the mean cycle completion time but the full distribution of fluctuations inherent to this process. And, as we will discuss in great length in subsequent chapters, these fluctuations provide a wealth of mechanistic information that simply cannot be gleaned from measurements of the mean alone. Thus, the ability to measure the discrete steps of nucleic acid translocases

promises to allow fundamental mechanistic questions to be addressed through direct measurement.

2.2: The Dual Trap Optical Tweezers

In the traditional optical tweezers assay, see Figure 2.1, one end of the biological system, e.g. a packaging motor with its DNA substrate, is held with a polystyrene bead held in an optical trap. And the other end of the biological system is typically affixed to a static attachment point, e.g. the surface of a sample chamber or a second polystyrene bead attached to a micropipette. A single optically trapped attachment point is all that is needed to apply forces to the biological system and to monitor its response.

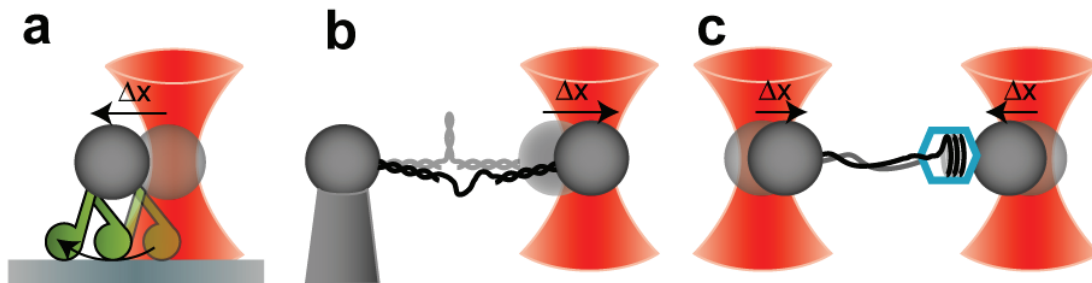


Figure 2.1. Different Optical Tweezers Geometries

- (a) Schematic diagram of the typical optical tweezers assay for following a single cytoskeletal motor such as kinesin (green). The motion of the bead reflects the motion of the enzyme, Δx , along its filament track.
- (b) Schematic diagram of the typical optical tweezers assay for nucleic acid dynamics, e.g. hairpin dynamics. The DNA substrate is held at one end by a bead affixed to a surface or a micropipette. The other end of the biological system is held by the enzyme attached to a bead in an optical trap.
- (c) Schematic diagram of a dual trap optical tweezers assay for studying motor dynamics. In this assay, two optical traps are used to hold each end of the biological system, e.g. a single DNA molecule being packaged by a bacteriophage. Adapted with permission from Ref. (18), Annual Review of Biochemistry, Volume 77, © 2008 Annual Reviews.

It is clear that if one desires Ångstrom-scale stability in the optical tweezers measurement, one must require that the relative distance between the optical trap and the

fixed attachment point must be stable to the Ångstrom-scale. This is a particularly hard task as it requires that the sample stage to which the micropipette or sample chamber is attached, the mounting to which the sample stage is attached, and, finally, the optical table to which this mounting is attached, all be stable to the Ångstrom-scale. In short, it requires that the entire optical apparatus be drift and fluctuation free on the level of a single Ångstrom. However, environmental noise sources—mechanical vibrations, acoustic vibrations, and temperature-cued expansion and contraction of mechanical components—typically produce drift and fluctuations on much larger scales. With no ability to discriminate biological signals from comparable movements introduced by these extraneous fluctuations, the ability to infer the action of the biological system will be limited to spatial scales larger than the typical fluctuations.

One solution to this problem is to monitor the fluctuations of the surrounding environment and then subtract the measured noise from the measured position of the optically trapped bead (129). Alternatively, active-feedback can be implemented, and the sample stage can be moved in a fashion that completely counteracts the fluctuations of the surrounding environment (130). Such an approach requires that the position of the fixed attachment point can be measured on the sub-Ångstrom scale. This typically requires that the position of fiducial marks, such as small microfabricated ridges or small polystyrene beads attached to the surface, be monitored with a second detection laser, using essentially the same detection methods that allow the position of optically trapped beads to be determined to this scale (129, 130).

There is an alternative approach. Instead of monitoring the environmental fluctuations and subtracting these motions from the measurement, one can isolate the

experiment from these fluctuations. This isolation can be accomplished by introducing a second optical trap, formed from the second orthogonal polarization of the same laser used to generate the first trap. In such a *dual trap optical tweezers*, the two optical traps are used to hold both ends of the biological system, as in Figure 2-1c. By decoupling the measurement from the fixed attachment point, i.e. the micropipette or sample stage, the effects of environmental fluctuations can be dramatically reduced. For example, if the position of the trapping objective drifts several nanometers with respect to the sample stage during the course of the measurement, this drift will have no effect on the measurement because the two traps will drift together and the distance between them, the experimental variable to which the measurement is sensitive, will not change. For this reason, we have adopted this two trap geometry for our high resolution optical tweezers.

The increased isolation and stability of the dual trap optical tweezers was first recognized by Shaevitz et al. (131) in 2003. Since then, this experimental geometry has provided the increased stability required to study prokaryotic (5, 131-133) and eukaryotic (134) RNA polymerases, nucleic acid hairpin dynamics (106, 135-138), the dynamics of DNA packaging motors in different bacteriophages (20, 60, 61, 139, 140), and even the motion of single ribosomes (11). Beyond the improved isolation, it turns out that dual trap optical tweezers also offer the ability to exploit correlations in the movements of the two beads to further improve the resolution of optical tweezers (18, 19). This topic is the subject of the following Chapter.

2.3: Environmental Concerns

Despite the large improvement in isolation imbued by the two trap geometry, we have found that it still important to house the instrument in a quiet environment. In particular,

care must be taken to choose a room that has low mechanical and acoustic vibrations, a high degree of temperature stability, and the instrument must be carefully isolated from atmospheric fluctuations.

2.3.1: Room Vibrations

Mechanical vibrations of the floor can introduce noise into the instrument by exciting differential movements of optical components. The amount of noise in a room can be characterized by using the vibration criterion (VC) introduced by The International Standards Organization (ISO) (141). The VC are a set of curves which define the frequency dependence of the root-mean-square floor vibration velocities and accelerations. The rankings range from the noisy workshop in which vibrations are noticeable, to the most stringent, VC-E, typically reserved for the most sensitive scanning or transmission electron microscopy measurements (141).

To illustrate the effect of mechanical vibrations, let's compare two environments: a busy office and the quiet basement space in which our instrument resides. Extrapolating from the ISO standards, a busy office environment displays $\sim 1000 \text{ } \mu\text{m/s}$ root-mean-squared vibrations at 2 Hz, a relevant frequency for optical trapping measurements. Below its resonance frequency f_0 , a damped harmonic oscillator is deflected by $\delta_{rms} = v_{rms} f / 2\pi f_0^2$ when driven by vibrations of velocity v_{rms} at a frequency f . Thus, an ideal optical component with a resonant frequency of 100 Hz—an mounted optic or a thin optical table—will fluctuate with a root-mean-squared amplitude of $\sim 30 \text{ nm}$ at 2 Hz. In contrast, our basement space exhibits vibrations less than 1 $\mu\text{m/s}$ at 2 Hz

(below the VC-E curve), corresponding to less than 0.1 Å root-mean-squared displacement.

Further isolation from the mechanical fluctuations of the floor is provided by a large optical table mounted on pneumatically isolated legs. Powered by the house pressure, the legs float the optical table, providing significant isolation from lateral and horizontal fluctuations for frequencies larger than ~10 Hz, the typical frequency range for mechanical fluctuations. In addition, we have selected a thick and relative short optical table, 4'x6' in length and width and 2' thick. The thicker and shorter the table, the higher the first mechanical resonance of the table. Thus, thicker and shorter tables resonate in a frequency range where the pneumatic isolators effectively remove all floor vibrations. Finally, it is typical for table manufacturers to measure the mechanical resonances of their tables and build in damping elements to remove these resonances. Our table, the TMC 790 Series (Technical Manufacturing Corporation, Peabody, MA), provides the highest degree of passive damping commercially available.

Vibrational noise couples to the instrument not only through the floor, but also through acoustic vibrations. In our experience, acoustical noise does not couple strongly into the instrument in a broad band of frequencies, but rather through the excitation of individual optical components and mounts at their respective resonance frequencies. As with floor vibrations, standards exist for the level of acoustic noise in a room. The Noise Criteria (NC) curves characterize acoustic noise based on human hearing and range from NC-15, a quiet recording studio, to NC-50, a noisy office (142). With the addition of acoustic absorbing foam to the walls of the instrument room and the removal of all fan-

cooled electronics, the noise in our room falls below NC-35, and we do not observe acoustically excited mechanical resonances.

2.3.2: Temperature Fluctuations

Changes in temperature can cue significant drift in an instrument due to differential thermal expansion and contraction of the various optical components. For example, stainless steel has a coefficient of thermal expansion of $\sim 2 \times 10^{-5}/\text{ }^{\circ}\text{C}$. This value implies that the typical 4"-high stainless steel optical post (~100 mm) will change in height by ~200 nm per $0.1\text{ }^{\circ}\text{C}$ change in temperature. It is not surprising, then, that ambient temperature changes will produce nanometer drift between two components that are mounted differently, such as a sample stage and a trap-forming objective. To combat the effects of temperature fluctuations, our instrument is housed in a custom-built room with temperature actively controlled to $\sim 0.1\text{ }^{\circ}\text{C}$.

Slow temperature changes are not of great concern if they occur on time scales much longer than that of the typical experiments; however, temperature variations on more relevant time scales can occur when heat is suddenly added to the instrument—when a laser is turned on or when an optical component is touched, for instance. Remarkably, there is enough heat deposited to an optical component with human contact that drifts lasting up to a half hour can be observed (data not shown). In addition, the human body produces roughly 100 W of heat; thus, even if the operator does not touch the instrument, his or her presence in the room can cue significant temperature changes. In parallel, absorption of the NIR trapping light by the microscope objectives can also have observable effects. With as little as 100 mW of incident light, thermal drifts of nanometers per minute in the focal length of the objective are observed.

To avoid thermal drift cued by heat from the user, our instrument is operated entirely remotely. There is no human contact with the instrument during the course of typical experiments, and the user controls these experiments from outside of the instrument room. Thermal drift due to heat deposited by the laser is more difficult to address. One solution is to turn on the laser and only perform experiments after the system has reached thermal steady-state, a process that typically takes \sim 1 hour. Fortunately, since the two traps are formed via the same objective, laser induced thermal drift affects the two traps in the same fashion, and we find that such drift has negligible effects on our measurements.

2.3.3: Atmospheric Fluctuations

The flow of air, like floor vibrations, can excite mechanical resonances in an instrument. More importantly, modest air flow can also cause significant fluctuations in the direction and position of the trapping beam. These are due to fluctuations in air density which lead to spatial and temporal variations in the refractive index. Similar phenomena are utilized in Schlieren photography to image convective flows, shock waves, and other atmospheric disturbances (143). Remarkably, this is essentially the same phenomenon that generates the twinkling of the stars, and when scaled-down appropriately to the size of an optical table, this twinkling can result in positional fluctuations of an optical trap by tens of nanometers at low frequencies. Figure 2.2a demonstrates that the fluctuations in the trapping beam position that generate these movements are systematically reduced by shielding the optics in plastic enclosures and further minimizing the air flow in the instrument room.

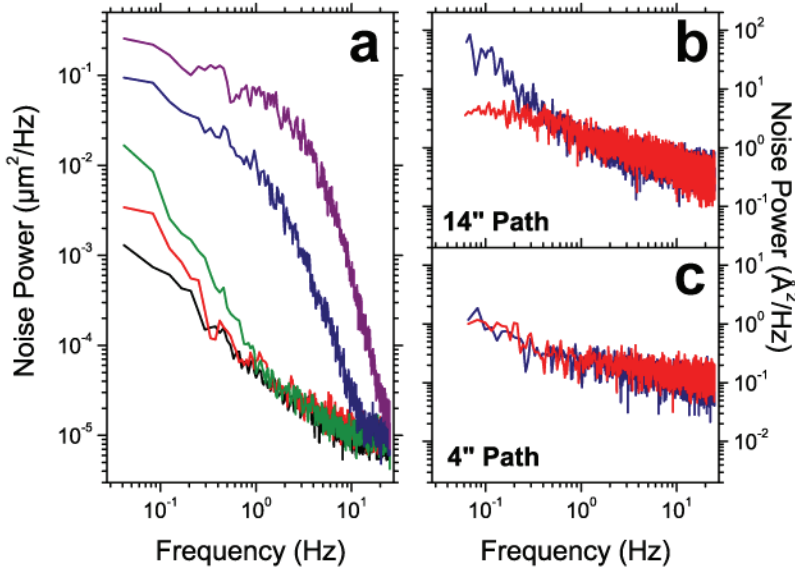


Figure 2.2. Air Fluctuations in Optical Tweezers

(a) Reduction of noise with covered optical paths. Displayed are detected positional fluctuations of the 845-nm trapping laser when different portions of the instrument are protected from the background air currents of a cooling fan. Traces correspond to: (purple) all beam paths exposed, (blue) only the objectives and detection path exposed, (green) all beam paths covered, (red) all beam paths covered with the air flow in the instrument room minimized, and (black) the background dark noise. (b) and (c) Noise reduction with helium and a short differential path. Relative movements of the two traps are measured by detecting the position of a strongly trapped bead with a weak monitor beam. (b) For a differential optical path of 14", the presence of Helium (red) removes additional low frequency fluctuations present in ambient atmosphere (blue). (c) In contrast, in an instrument with a 4" differential path, there is no improvement with Helium. See Section 2.4.11 for an introduction to noise power spectra. Adapted with permission from Ref. (16), © 2008 Cold Spring Harbor Laboratory Press.

However, we have observed and others have reported (132) that even when optics are completely enclosed, background air density fluctuations inside the optical enclosure can still have significant effects. One reported method to reduce this effect is to house the optics in a helium atmosphere (132). Since changes in refractive index, Δn , scale as $\Delta n = (n - 1)\Delta\rho/\rho$, where ρ is the air density (143), and $n - 1$ is about ten times smaller for helium than for air; therefore, atmospheric density fluctuations, $\Delta\rho/\rho$, produce ten times less variation in refractive index and thus positional fluctuations of trapping beams.

However, we have designed our instrument to be largely insensitive to this phenomenon, and a Helium atmosphere provides no additional improvement in our background noise. See Figure 2.2b & c. This will be discussed in detail below.

2.4: Instrument Design

In this section we discuss the basic features of the high resolution optical tweezers constructed. Images are provided throughout to illustrate the different components of the instrument. Readers interested in constructing a high resolution optical tweezers should consult, in addition to these sections, Refs. (16, 19, 92). In addition, the catalogs of various optical suppliers typically provide an excellent introduction to the basic optics that are required to build an optical tweezers. In particular, the optics introduction in the Melles Griot catalog is an excellent source both for beginners who need to learn the basics and for experts who need a quick reference.

2.4.1: Schematic Layout

The basic design of the high resolution optical tweezers we have constructed, see Figure 2.3, consists of 7 basic stages, see Figure 2.4. In the first stage, a single-mode laser provides the trapping light. In our system we have used two different lasers, a low power, high-stability, 845-nm, fiber-coupled laser, and a high-power, diode-pumped, 1064-nm, solid-state laser. Minor modifications were required to accommodate differences in these lasers, but the overall design of the instrument is essentially unchanged. In the second stage, we condition and control the power in this laser. In the third stage, the laser is split into two orthogonally polarized beams, each is manipulated individually, and then recombined into the same optical path. In the fourth stage, the

lasers are magnified to the final size, selected for efficiency in trapping, and the conjugate plane of the steerable mirror is mapped to the back-focal plane of the first objective. In the fifth stage, a microscope objective focus the trapping beams forming the two traps. A second, identical objective then collects the forward scattered light. In the sixth stage, this scattered light is separated via polarization and imaged onto a pair of position sensitive photodetectors. Finally, in the seventh stage, visible light is injected into the sample plane and imaged onto a CCD to provide a visible image of the plane in which the optical trapping experiments are conducted.

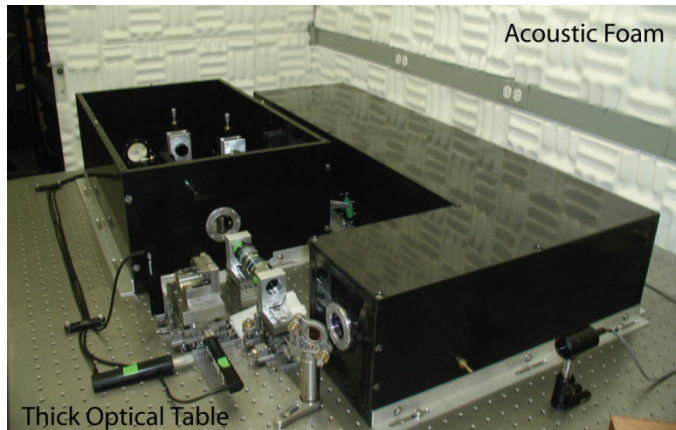


Figure 2.3. High Resolution Optical Tweezers

Image of the high resolution optical tweezers constructed built around the 845-nm laser. Nearly all of the optics are enclosed in black, plastic enclosures to protect them from transient air fluctuations. Also pictured is the 2' thick optical table on which the instrument is built and the acoustic foam added the separate instrument room. The lid to the detection system, upper right, is typically present during operation.

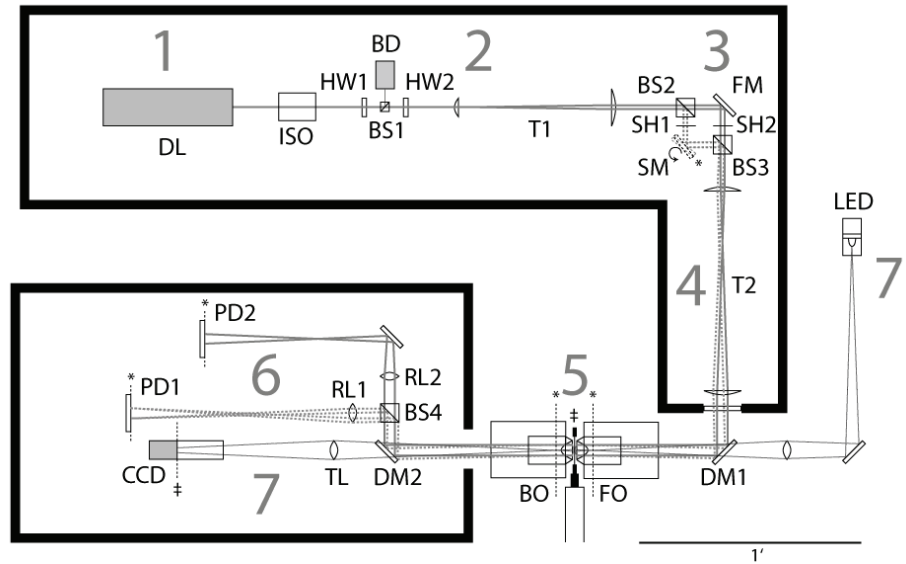


Figure 2.4. Optical Layout

Optical layout of the high resolution optical tweezers constructed around the 1064-nm diode-pumped, solid-state, YdVO₄ laser (DL). The instrument consists of 7 major sections which are numbered here and discussed in detail in the main text. This drawing is to scale. Solid dark lines correspond to the location of optical enclosures which protect the optics from stray air flow. Labels are defined throughout the text. Reproduced with permission from Ref. (16), © 2008 Cold Spring Harbor Laboratory Press.

2.4.2: Laser

In the instrument described here, we have used two different lasers (DL in Figure 2.4), a low power, 200 mW, 845-nm, fiber-coupled solid state laser (LU0845; Lumics, Berlin) and a higher power, 5 W, 1064-nm, diode-pumped solid state laser (J20I-BL-106C; Spectra Physics, Mountain View, CA). The pointing stability of a laser is the degree to which the angle at which the laser leaves the head is constant, and fiber-coupled lasers typically exhibit exceptionally high pointing stabilities since the light is effectively emitted from a cold source. However, optical transmission through the fiber is particularly sensitive to mechanical perturbations. By taking care to isolate the 845-nm fiber-coupled laser from mechanical vibrations, we find that its power and polarization stability are exceptional, < 0.01% on a 1 kHz bandwidth with < 0.1% drift over 15

minutes. Moreover, pointing instabilities are too small to be detected, < 1 nrad, see Figure 2.13 below.

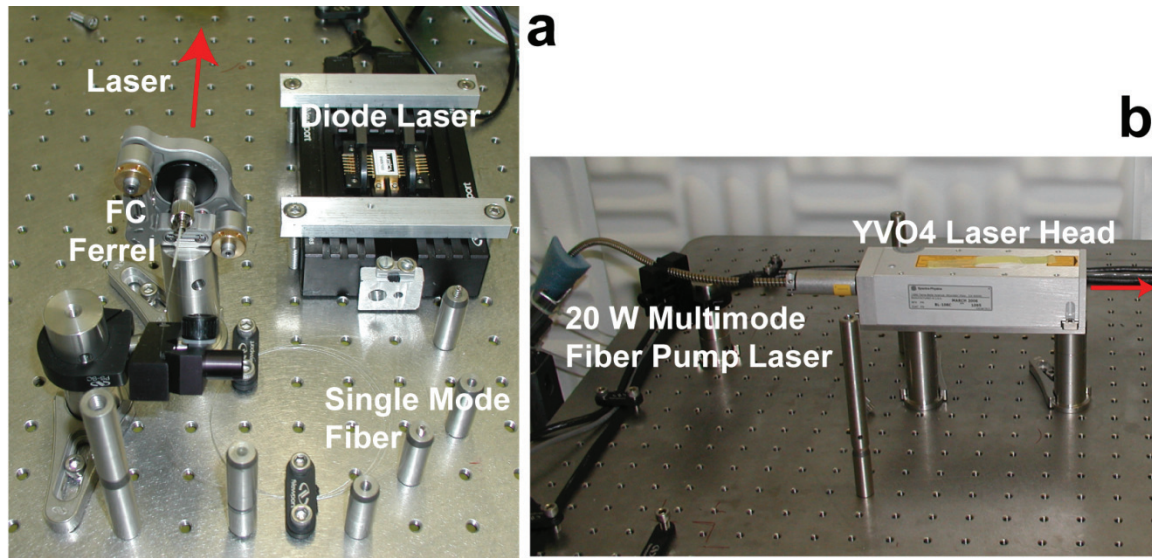


Figure 2.5. Lasers Used in the High Resolution Optical Tweezers

(a) Image of the solid-state, fiber-coupled, 845-nm, 200 mW diode laser used in the first high resolution optical tweezers. The 14-pin butterfly laser is pictured with the single-mode fiber. The laser was mounted using an FC ferrel and a collimator. (b) Image of the diode-pumped, 5 W, solid-state, YVO4 laser used in the second high resolution optical tweezers.

The pump laser for the 1064-nm laser is coupled to the laser head by an optical fiber; however, even with careful mechanical isolation of this fiber, we find that this laser is measurably less stable in power and polarization than the 845-nm laser. Power fluctuates typically by $\sim 0.1\%$ peak-to-peak over time scale of $\sim 10\text{-}15$ s. These power fluctuations have been traced to the temperature control feedback loop for the diode pump lasers. This loop is digitized on a scale *larger* than the instabilities in the laser; thus, discrete power fluctuations originate in the flipping of a single bit in the temperature controller. Furthermore, pointing instabilities are in this case large enough to be detected and are typically on the $\sim 1 \mu\text{rad}$ scale, see Figure 2.13. These instabilities have a similar spectral distribution as the power fluctuations, but no correlations have been observed

between the power and positional fluctuations. Despite the increased noise, the significant increase in power allows the application of much larger forces to smaller microspheres, (> 90 pN on ~ 800 nm diameter microspheres as opposed to < 15 pN for the same microspheres in the 845-nm system) resulting in a more versatile instrument.

2.4.3: Power Control Stage

Because there is ample power in the 5W, 1064-nm laser, it is possible to operate the laser below maximum power, at a level which optimizes stability (~ 2 W, for our laser). A half-wave plate on a remote-controlled rotary stage (Model 8401; New Focus, San Jose, CA) and a high-power polarizing beam splitter with a beam dump, allows us to run the laser at the most stable power and discard any additional, unneeded light. A second half-wave plate makes it possible to control the relative power in each polarization and, thus, each trap. See Figure 2.6. A Faraday isolator (IO-3-1064-VHP; Optics for Research, Caldwell, NJ), which allows the transmission of light in the forward but not the reverse direction, prevents stray light from being reflected back into the laser head, decreasing power fluctuations and increasing the life-time of the lasers.

A power control stage was not used for the 845-nm instrument, see Ref. (19), because the full 200 mW of laser power was always needed. However, an optical isolator (IO-845-HP; Optics for Research, Caldwell, NJ) was still used to prevent back reflections. In addition, a quarter-wave plate was added before the isolator. It is not uncommon for the polarization of light exiting an optical fiber to be elliptical. The quarter wave-plate converts this elliptical polarization into a pure linear polarization, maximizing the transmitted power through the optical isolator.

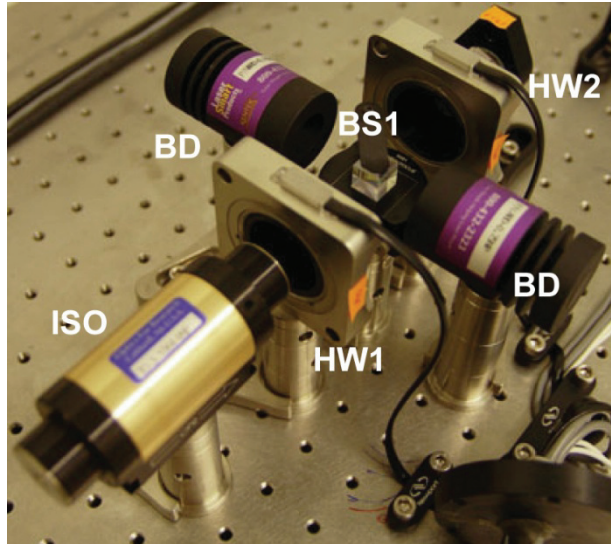


Figure 2.6. The Power Stage

The beam enters via the optical isolator (ISO) passes through a half-wave plate mounted on a remote control rotary stage (HW1). This allows the linear polarization of the laser to be rotated with respect to the following polarizing beam splitter cube (BS1). Excess power, determined by the angle of the polarization, is dumped into the top beam dump (BD). The bottom beam dump (BD) addresses the relatively large amount of power which can be reflected due to back reflections. The remaining power then enters a second half wave plate mounted on another rotary stage (HW2). This allows the polarization to be rotated with respect to the first beam splitter cube in the beam steering stage, allowing direct control over the relative amount power in the horizontal and vertical polarizations that from each trap. Picture courtesy of G. Chistol.

2.4.4: Beam Steering

Following the first telescope, the beam steering stage forms the two orthogonally-polarized beams that make the dual optical traps and steers one beam relative to the other. This stage has two important features (stage 3 in Figure 2.4). The first is the steerable mirror which allows us to move one optical trap with respect to the other. The second is the short differential path over which the two polarizations are formed, manipulated individually, and then recombined into the same optical path.

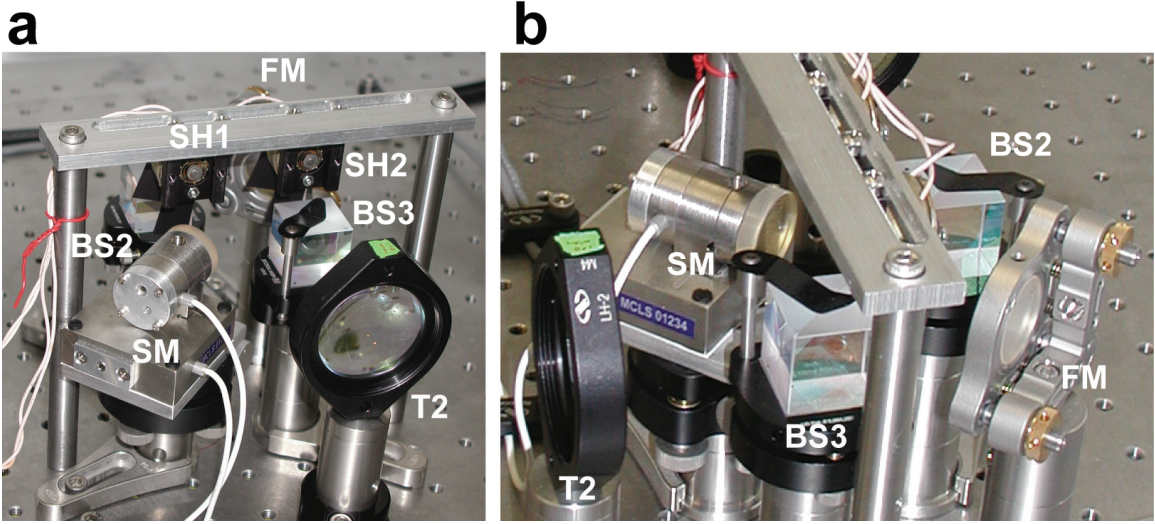


Figure 2.7. Beam Steering Stage

Two different views of the beam steering stage of the high resolution optical tweezers. The laser is split into two orthogonal polarizations by the polarizing beam splitter cube (BS2). One polarization is transmitted to the fixed mirror (FM) while the other is reflected to the steerable mirror (SM), whose angle can be varied via piezoelectric crystals over a range of ~ 2 mrad in both the horizontal and vertical direction. The two polarizations are then recombined to follow the same optical path with a second polarizing beam splitter cube (BS3). Servo controlled shutters (SH1 and SH2) allow each laser beam to be blocked separately. Also pictured is the first lens in the second telescope (T2).

The ability to manipulate the position of one optical trap with respect to another is a necessity of any dual trap optical tweezers. However, this degree of freedom is a liability if the method of steering this trap is not stable to the sub-Ångstrom scale. A physical translation of an optical trap in the sample plane corresponds to an angular change in the laser beam that enters the back-focal-plane of the trapping objective.¹ Thus, positional stability translates into angular stability for the beam steering stage. Given the focal length of our objective, 3.3 mm, a 1 Å movement corresponds to an angular motion of a trapping beam of just ~ 30 nano-radians (nrad). Just to provide a physical intuition for the nano-radian scale: 10 nano-radians corresponds to the angle

¹ Objectives convert angle, θ , into distance, d , via $d = f\theta$ where f is the focal length of the objective.

subtended by the dot on a 12 point letter “i” from a distance of ~25 miles. Thus, Ångstrom-scale stability in an optical tweezers requires a remarkably high degree of angular stability.

In our instrument, we steer our trap with a piezo-driven, tip-tilt mirror (Nano MTA-2; Mad City Labs, Madison, WI; SM in Figures 2.4 and 2.7). The mirror has an angular range of ~2 milli-radians (mrad) in two axes with a remarkable angular stability of ~20 nrad over a bandwidth of 200 Hz. Given the focal length of the objective, this implies that one trap can be moved over a ~6 micron range with a positional stability better than 0.6 Å. Thus, this mirror provides ample range for the typical experiment with the angular stability needed to perform Ångstrom-scale measurements.

Another important feature of the beam steering stage is its relatively compact size. As discussed in the previous section, the direction of propagation of a laser beam is sensitive to local changes in the refractive index of the air through which it travels due to minute density fluctuations. However, if the two trapping beams travel identical optical paths, they will be subject to the same fluctuations, and their angles will be equally perturbed. The result is that the two optical traps will be deflected by the same amount, and there will be no relative trap movements. In our instrument, the beams are recombined with a polarizing beam splitter immediately after manipulation, leaving only 4" of differential optical path. Since this is the only region of the instrument in which the two beams follow different optical paths, this is the only length in which air fluctuations can couple into the measurement. Alternatively, it has been shown that immersing the trapping optics in a low index of refraction atmosphere, such as Helium, can also reduce the effect of atmospheric fluctuations (132). Figure 2.2b & c shows that by decreasing

the length of the differential path between the formation of the two polarized beams and their recombination into the same optical path removes the need for Helium and all of the added complications that come with its use.

2.4.5: Beam Expansion and Conjugate Planes

To form efficient, strong optical traps it is necessary to carefully control the size of the laser beams that enter the back aperture of the trapping objective (92). In addition, it is also necessary to insure that rotations in the angle of propagation of the trapping beams, introduced by the beam steering stage, do not physically displace the trapping beams from the trapping objective. Both of these tasks are accomplished by the optics in stage 4 of Figure 2.4.

Beam magnification is accomplished in two steps. The first stage involves telescope 1 (T1) before the beam steering stage, see Figure 2.4. This telescope consists of two lenses, a 37.5 mm and a 175 mm, which provide a magnification of 4.7x. We use plano-convex lenses for all of our telescopes since these lenses are best suited to image collimated laser beams. Both of the lasers that we have used exit the laser head with very small beam waists, ~ 0.5 mm.² For such small beam waists, the concept of a collimated laser beam is no longer valid, and the beam quickly diverges. Thus, the exact distance between the laser head and the first telescope can change the size of the beam after the telescope. We adjust this distance so that the beam is 4-4.5 mm in diameter after T1. Exploiting the divergence of the beam provides an additional ~ 2 x magnification.

² Single-mode lasers typically have an intensity distribution which is described radially by a Gaussian, $I(r) \propto \exp(-r^2/2w^2)$, where w characterizes the radial decrease in intensity. w is the Gaussian beam waist—the effective diameter of the beam.

Optical traps are stronger and more efficient when the laser is focused to as small a spot as possible (16, 92). In general, the larger the beam waist with respect to the back aperture of the objective, the smaller the final focused laser spot. However, as the beam waist becomes comparable or larger than the back aperture of the objective, a significant portion of the trapping light is clipped by the mounting of the objective, and trapping power is lost. A good rule of thumb which balances these two competing effects is to make the beam waist roughly equal to the size of the back aperture. The back aperture of the trapping objectives that we use is 8 mm. Thus, after the beam steering stage, we use a second telescope, T2, to expand our beam an additional factor of 2, taking the beam waist from 4 – 4.5 mm to a final value of 8 – 9 mm. This is accomplished by a pair of lenses, 100 mm and 200 mm in focal length.

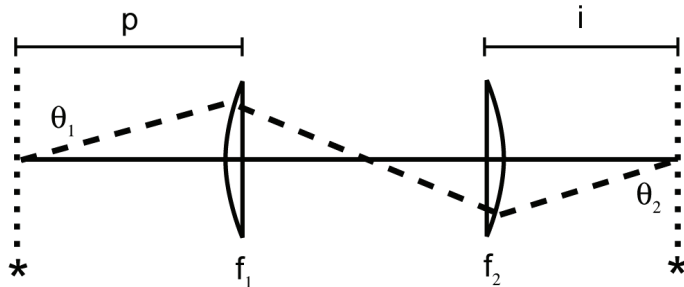


Figure 2.8. The Conjugate Planes of a Telescope

Given a telescope composed of lenses of focal lengths f_1 and f_2 , there are a family of conjugate planes (*) in which pure rotation in one plane results in pure rotation in the other plane. The distances between the planes p and i are constrained by Eq. (2.1).

In addition, the second telescope is responsible for imaging the optical plane of the steerable mirror onto the back focal plane of the trapping objective. Introducing an angular shift into a laser beam obviously produces deflections in the position of the laser spot at positions further along its optical path. Such motions are not desired since they may introduce asymmetric clipping of the trapping beam on the aperture of the trapping

objective, or worse, deflect it entirely off of the back objective. A telescope, however, can image a plane in which the beam does not translate but only rotates onto another plane, the *conjugate plane*, in which the beam also does not translate but only rotates. See Figure 2.8.

Thus, the second telescope also serves the purpose of imaging the plane of the steerable mirror, at which point angular changes are introduced into the laser beam which forms the movable trap, onto the back focal plane of the trapping objective, where we do not want rotation to introduce translation. Using thin lens optics (144) it is possible to show that the position of the two conjugate planes are related via

$$i = M(f_1 + f_2 - Mp) \quad (2.1)$$

where i is the distance from the last lens of the telescope to the conjugate plane, p is the distance from the first lens to the position of rotation, and f_1 and f_2 are the focal lengths of the two lenses that form the telescope. M , the magnification of the telescope is $M = f_2/f_1$. In addition, the angles are related via

$$\theta_2 = \theta_1/M \quad (2.2)$$

where θ_1 is the rotation angle before the telescope and θ_2 is the rotation angle at the conjugate plane. Thus, if the telescope magnifies the beam size by a factor M it *demagnifies* the rotation angle by the same factor. We decided to perform our magnification of the beam in two stages, specifically so that we could demagnify the angle with T2. While demagnifying the angle results in a smaller range for the movable trap, it increases the positional stability of this trap.

In theory, Eq. (2.1) can be used to position all of the optics correctly in the alignment of the conjugate planes. However, in practice, we find that it is much simpler

to use Eq. (2.1) to place the optics in approximate locations and then to find the conjugate plane by moving the steerable mirror and using a photodetector to find the plane at which the rotation does not produce a translation of the laser spot. Then the objective is aligned so that its back-focal plane is located at this plane.

2.4.6: Objectives and Sample Chamber

The principal optical component of any optical trap is a high quality, high numerical-aperture lens, responsible for focusing a collimated laser to as small a spot as possible. In our instrument, we utilize a water immersion, 60X, 1.2 numerical aperture (NA), infinity-corrected, differential-interference contrast (DIC) microscope objective (CFI Plan Apo VC 60X WI; Nikon, Melville, NY) with an 8 mm back aperture diameter. This objective has the highest degree of correction for spherical and chromatic aberrations (plan apo). In addition, it has the least amount of imperfections that scramble the polarization of incident light (DIC). The use of a water immersion lens, as opposed to the more common oil immersion, allows us to trap deep within a sample chamber. This choice further improves the isolation of the system from movements of the sample chamber surface (16).

The first objective in the objective stage is responsible for focusing the lasers to form the optical traps. The second objective is responsible for gathering the light from the optical traps after trapping. This light contains a portion that is scattered from the trapped bead and a portion which does not interact with the bead. There is a phase difference between these two portions of the trapping light due to interaction with the bead and with the optical physics of focused light (92). The phase difference results in an interference pattern between the scattered and unscattered light, and this pattern is

extremely sensitive to the position of the trapped bead with respect to the center of the trap (145, 146). Thus, by collecting this light with the second objective, the interference pattern can be transferred to the detection stage, discussed below, to extract information about the position of the optically trapped bead.

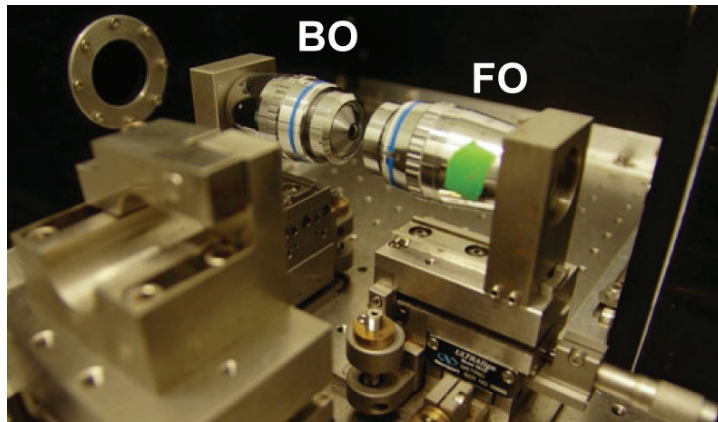


Figure 2.9. Objective Stage

The front objective (FO) is responsible for focusing the lasers to form the optical traps and collimating the visible illumination. The back objective (BO) is responsible for collecting the scattering light for the detection stage after trapping and forming the visible image of the sample plane. In the foreground is the mount used to hold and position the sample chamber. Picture courtesy of G. Chistol.

The objective stage also includes the sample chamber (147, 148). See Figures 2.10 and 2.11. The sample chamber is a pair of No. 1 cover slips fixed together by a piece of melted Nescofilm, a waxy, parafilm-like substance (Nescofilm; Karlan Research Products Corporation, Cottonwood, AZ). The Nescofilm is etched with a laser engraver to produce three distinct channels. One of the cover slips has also been etched with a laser engraver to produce six holes, two holes for each channel. These holes act as inlet and outlet ports for buffers. In the assembly of the chamber, two small capillary tubes with inner diameters of ~25 microns and outer diameters ~100 microns are placed between the top and middle channel and similarly between the bottom and the middle channel (Garner Glass Company, Claremont, CA). These capillaries provide a controlled

leak between the top and bottom channels into the middle channel. This allows the contents of these channels to be injected into the middle channel where experiments are conducted. (For the experimental assembly process see Figure 5.3.)

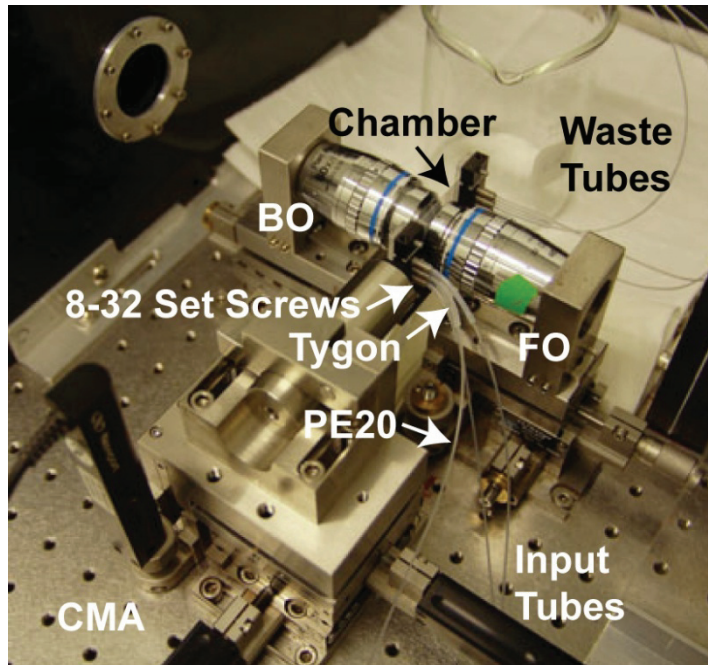


Figure 2.10. Installed Sample Chamber

Image of an installed sample chamber. The three plastic *input tubes* allow samples to be injected into the chamber while the three plastic *waste tubes* allow used buffer to be discarded. The black motors in the lower left, CMA, are the servo motors that allow the user to uniquely position the chamber with respect to the objectives. Picture courtesy of G. Chistol.

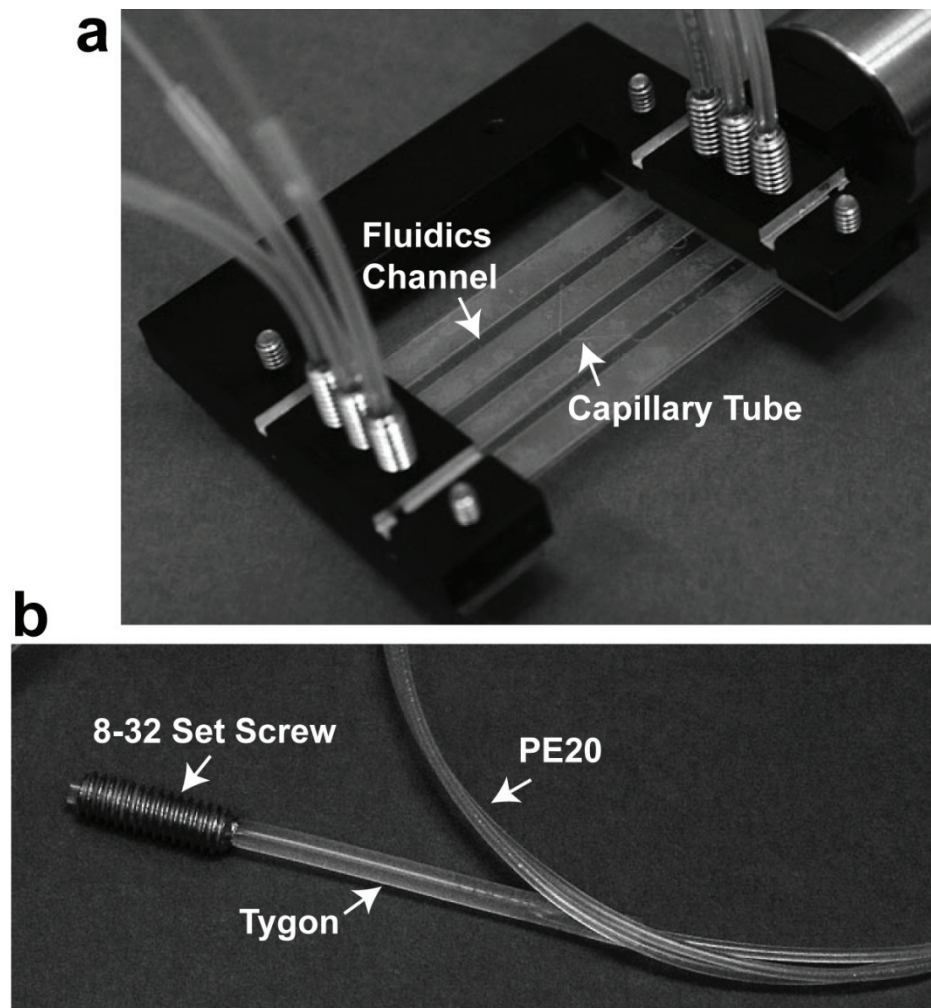


Figure 2.11. Microfluidics Chamber and Adaptors

(a) Image of a mounted microfluidics chamber. The three clear regions are the channels through which fluid injected through the displayed tubes flows. The hollow capillary tubes which provide controlled leaks between the top and bottom channel and the middle channel are also shown. (b) Fluid is injected into the microfluidics chambers via PE20 tubing inserted into a Tygon tubing adaptor which is itself inserted into a drilled 8-32 set screw. Carefully threading this screw into the mount shown in (a) provides the pressure needed to seal the Tygon tubing to the coverglass of the microfluidics channel. Pictures courtesy of G. Chistol.

These microfluidics chambers (147) are then placed in custom mounts that allow plastic tubing to be affixed to each of the six inlet/outlet ports. See Figure 2.11a. This attachment is accomplished with 8-32 set screws with clearance holes added to permit a plastic tubing to be inserted into the screws (Tygon 3350, Sanitary Silicon Tubing; inner

diameter 1/32"; outer diameter 3/32"; Saint-Gobain Performance Plastics, Beaverton, MI). See Figure 2.11b. Seals between the Tygon tubing and the drilled cover slip are formed by carefully twisting the set screws to apply a small pressure between the tubing and the cover slip. Tubing with a smaller inner diameter is then inserted into the Tygon adaptors (PE20; inner diameter 0.015"; outer diameter 0.043"; Intramedic, Becton Dickinson and Company, Sparks, MD). A smaller inner diameter decreases the dead-volume in the fluidics system, reducing the amount of sample used in a trapping session. Finally, this PE20 tubing can be adapted to a variety of different microfluidic control systems (148), or it can be directly attached to sample syringes via standard 26 gauge needles (26G1/2; Becton Dickinson and Company, Sparks, MD).

The position of the sample stage is controlled via three closed-loop, servo motors (CMA-12CCCL; Newport Corporation, Irvine, CA). These motors allow the user to remotely position the sample chamber. The motors have a 12.5 mm range with an accuracy of ~ 1 micron, making it possible to repeatably position the tips of the capillary tubes in close proximity to the optical traps, facilitating the capture of different types of beads—the typical contents of the top and bottom channels—and the quick assembly of experiments. As mentioned above, remote control of the sample stage is crucial for stability in the measurement since direct human contact with micro-positioning screws, for example, can introduce enough heat to cue noticeable drift for 10s of minutes.

2.4.7: Detection Stage

The detection stage immediately follows the objective stage and is shown in Figure 2.12. In this stage, the scattered light collected via the back objective is separated via polarization (BS4 in Figure 2.4), and then imaged onto two separate position sensitive

photodetectors (PD1 and PD2 in Figure 2.4; DL100-7PCBA3; Pacific Silicon Detectors, Westlake Village, CA). These photodetectors provide three voltages: one proportional to the position of the centroid in the x direction, one in the y direction, and a voltage proportional to the total amount of light incident on the detector. As discussed above, the presence of a trapped bead creates an interference pattern in the forward scattered light, and the centroid of this interference pattern is proportional to the position of the trapped bead (145, 149). Thus, once calibrated, the photodetectors allow us to measure the relative position of each bead in its own optical trap. There are definite advantages to measuring the deflections of both beads, which we will discuss in detail in the following chapter.

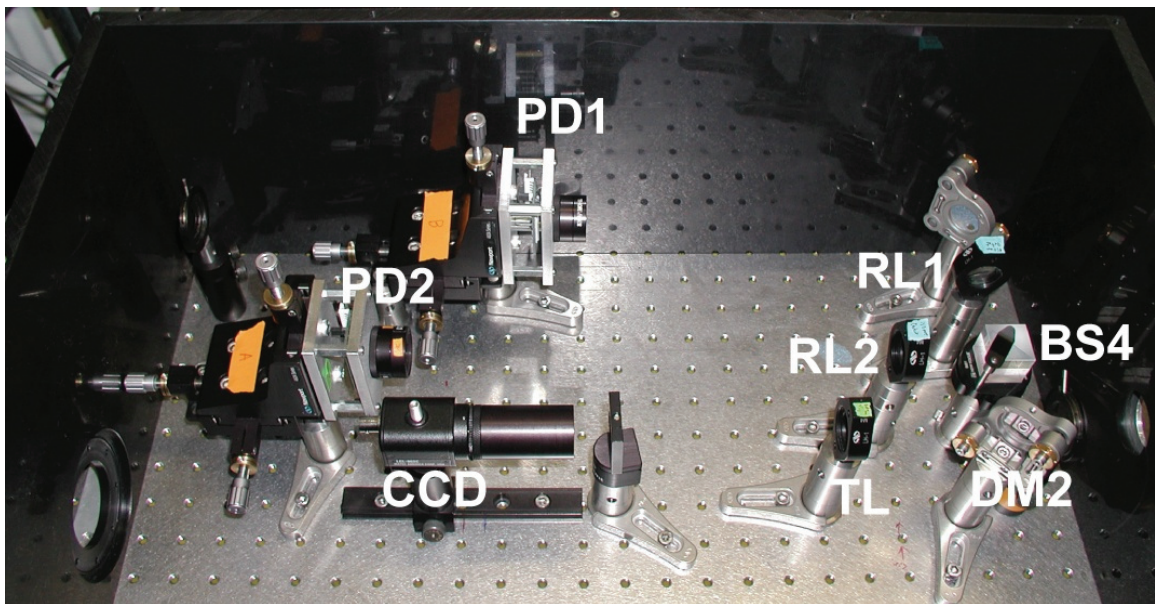


Figure 2.12. Detection Stage

Image of the detection stage with the lid of the optical enclosure removed. The different polarizations are separated via a polarizing beam splitter (BS4) and then imaged with relay lens (RL1/2) onto two positions sensitive photodetectors (PD1/2). Also pictured is the second portion of the visual stage which includes the tube lens (TL) which forms the visible image and focusing this onto a CCD camera (CCD). A dichroic mirror (DM2) separates the visible light from the trapping light.

Again, changes in the angle of the trapping beam may produce movements on the photodetectors, movements indistinguishable from changes in the centroid position due to bead motions. Thus, it is important that the photodetectors are in a plane that is conjugate to the steerable mirror. The second telescope makes the back-focal-plane of the front objective conjugate to the steerable mirror, as discussed above. Then the 1 to 1 telescope created from the two objectives maps the back-focal plane of the front objective onto the back-focal plane of the back objective. Finally, a set of 150 mm bi-convex *relay lenses* (RL1 and RL2) image this plane onto the photodetectors, ultimately making the photodetectors conjugate to the steerable mirror. Since there is no requirement to keep the collected light collimated for detection, we can use a single lens as opposed to a telescope, as discussed above. We use bi-convex lenses because this is the optimal lens shape when imaging objects at finite distances. Finally, we place the lenses at twice the focal length from the back objective and the same distance from the photodetectors since this is the distance which produces conjugate planes with unit magnification. The active area of the detectors is 10 mm and the back aperture of the objectives is 8 mm, so unit magnification insures that all of the collected light is imaged on the detectors with no clipping of this light.

2.4.8: Visual Stage

The final optical stage of the instrument is the visual stage. In order to efficiently assemble experiments, it is extremely useful to have a visible image of the sample plane. Fortunately, the microscope objectives required for trapping provide all the necessary optics to build a custom-built visible microscope around the trapping objectives. We start by injecting a visible light source. This is done with an ultra-bright, white LED, powered

by custom-built electronics. The LED is mounted behind a circular diffuser to smooth out irregularities in the light profile and a UV-filter to remove potentially damaging light. The visible light is combined with the optical path of the near-IR trapping light with a dichroic mirror that reflects near-IR light but transmits visible light (DM1 in Figure 2.4). The visible light is focused onto the back-focal-plane of the front objective to produce collimated light at the sample plane, i.e. a Köhler-style of illumination. The back objective forms the image of the sample plane. The visible and near-IR light are again separated using a dichroic mirror immediately after the objective stage (DM2 in Figure 2.4.). Finally, a tube lens, a 200 mm doublet, is used to focus the image onto an inexpensive black and white CCD camera (902-C; Watec, Orangeburg, NY). Because the objective is an infinity corrected objective, which implies that the image is formed at “infinity,” the distance to the tube lens from the back objective is not specified, but the tube lens must be one focal length away from the CCD camera. This portion of the visible system can be seen in Figure 2.12. The CCD image can then be displayed on inexpensive TV monitors or digitized using a video card (NI 1407; National Instruments, Austin, TX) and displayed on a computer monitor.

2.4.9: Back-end Electronics and Instrument Control

There are eight voltages that must be measured in our optical tweezers instrument. There are four voltages which give positional information of the beads: an x and y voltage for each of the two optical traps (x and y are defined as orthogonal to the optical axis). In addition, there are two voltages proportional to the total light intensity at each photodetector. And, finally, the exact position of the steerable mirror is measured with a set of strain gauges, one for each axis. Thus, there are two additional voltages which

report the exact position of the steerable mirror and, thus, the steerable trap. These voltages are digitized at a resolution of 18 bits and saved to disk directly using a National Instruments data acquisition card (PCI-6289; National Instruments, Austin, TX).

This card shares a single digital-to-analog converter between all eight channels with a switching rate of 500 kHz, or an interchannel delay of 2 μ s. Since it is possible for residual voltages from the previous channel to bias the measurement of a given channel, we sample channels in an order which groups signals of comparable magnitude. In addition, as we will discuss in detail in the following Chapter, it is important to preserve the correlations in the motion of the beads in different traps. Since large inter-channel delays will degrade these correlations, we also sample similar axes in order, bringing the sampling delay between the same axes of the different traps to just 2 μ s.

All of the software required to measure these voltages and to save them to disk is written in LabVIEW 7.1 (National Instruments, Austin, TX). 8 channels over 500 kHz produced an individual sampling rate of 62.5kHz for each channel. Data at this bandwidth can be saved directly to disk or averaged and decimated to a lower bandwidth with software and then saved to disk. Only raw voltages are saved to disk, and all calibration is done offline using custom Matlab software (The Mathworks, Inc., Natick, MA). This approach allows corrections to calibration to be applied to old data at any time.

The instrument is controlled through several different interfaces. The high power laser is controlled using a serial interface and software provided by the manufacturer (T20MON.exe; Spectra Physics, Irvine, CA). The remote-controlled rotary half-wave plates are controlled via Ethernet with custom software in LabVIEW. The piezo tip-tilt

mirror is controlled with analog outputs from the data acquisition card driven by custom LabVIEW software. The shutters are controlled with custom-built electronics and TTL outputs from the data acquisition card. Again, these are driven by custom LabVIEW software. The CMA motors which control the stage position are controlled with a Universal Motion Controller (ESP-300; Newport Corporation, Irvine, CA) which interfaces with the instrument computer via a serial interface. Control over the motor positions is often accomplished with a proprietary trackball driven by custom software. The motion controller interfaces with the user via custom LabVIEW software.

2.4.10: Instrument Noise

What distinguishes a high resolution optical tweezers from a low resolution instrument? The simple answer is noise, or lack thereof. Figure 2.13 characterizes the fluctuations of the different components of the instruments that we have constructed and compares this to the Brownian fluctuations of optically trapped microspheres.

In Figure 2.13, the black trace corresponds to the noise in the backend electronics, i.e. the photodetectors, the DAQ card, and all intermediate cables, etc, with no laser light. When converted into the apparent signal in Ångstroms that these voltages would produce, the resulting noise is remarkably small. The maximum value at 10^{-3} Å²/Hz is at least three orders of magnitude below the typical noise levels required for the most sensitive experiment (compare this to the fluctuations of the trapped beads in yellow and orange). Thus, the noise in the backend electronics will not limit our resolution.

The red and dark red traces in Figure 2.13 correspond to noise measured when the laser is turned on. The red trace measures the effective positional fluctuations in the 845-nm laser, and the dark red trace measures the same fluctuations with the 1064-nm laser.

Note that for much of its spectra, the 845-nm noise is identical to the black trace—the noise in the electronics. Since noise power from uncorrelated sources add, the noise we measure in this experiment is the sum of the laser positional fluctuations and the dark noise of the detector, the black trace. Since these curves are nearly identical, we conclude that the positional fluctuations in the 845-nm laser are much smaller than the noise in the back-end electronics. Thus, laser fluctuations will play no role in limiting the spatial resolution for instruments constructed with this laser.

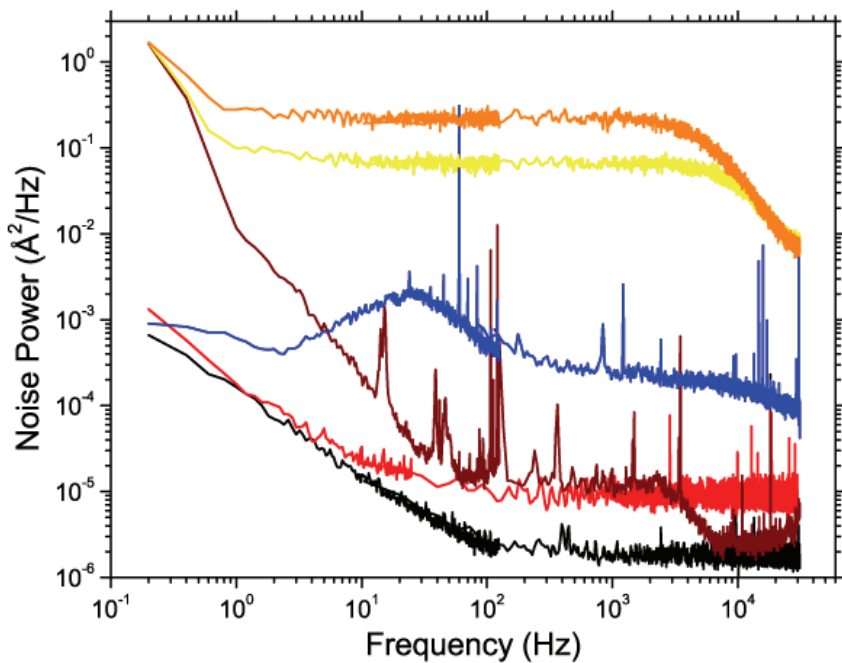


Figure 2.13. Instrument Noise

Noise power spectra for different conditions of the instrument: (black) background electronics noise; (red) background intensity noise with the 845-nm laser on but with no trapped beads; (dark red) background intensity noise with the 1064-nm laser on but with no trapped beads; (blue) background noise in the mirror position along the x-axis; (yellow) noise of a strongly trapped 860-nm diameter polystyrene bead; and (orange) noise of a weakly trapped 860-nm diameter polystyrene bead. All raw voltages have been scaled to the equivalent motion in Å in the sample plane. Adapted with permission from Ref. (16), © 2008 Cold Spring Harbor Laboratory Press.

In contrast, the 1064-nm laser positional fluctuations are nearly 3 orders of magnitude larger at low frequencies. In principle, positional fluctuations of the laser should produce identical motions in the two traps since they are formed from the same laser and since both traps have identical numbers of reflections; thus, this increase in noise should have no effect when differential measurements are performed (see Chapter 3). In practice, however, we find that subtraction of the positional fluctuations of one trap from the position of the other produces only an order of magnitude decrease in these fluctuations. Thus, differential measurement does not completely remove these additional fluctuations, a fact which has not yet been explained. Given their magnitude at low frequencies in Figure 2.13, it is these fluctuations which will ultimately limit the resolution of instruments constructed around this laser, as discussed in more detail below.

The blue trace in Figure 2.13 shows the residual positional fluctuations of the mirror in one of its two axes, scaled to estimate the positional fluctuations of the trap in the sample plane. This noise comes from the feedback electronics which control the mirror command voltage, i.e. the voltage which sets its position. The bandwidth of this feedback loop has been adjusted to lower this noise as much as possible while maintaining a relatively fast motion of the mirror. However, the fluctuations are small enough that they should not affect Ångstrom-scale measurements on typical experimental bandwidths.

Finally, the yellow and orange traces in Figure 2.13 show the Brownian fluctuations of a single trapped bead in the absence of a DNA tether. Both traces were collected with the 1064-nm laser system (the dark red trace). Note that these fluctuations have a large region where the noise power is independent of the frequency of the

fluctuations. This type of noise is known as *white* noise and is the expected Brownian fluctuations of an optically trapped bead at low frequencies. Above a certain critical frequency, the fluctuations of the trapped beads begin to drop with increasing frequency. This noise is known as *colored* or *red* noise, and, again, represents the expected behavior of an optically trapped bead.

Since the Brownian fluctuations provide the fundamental limit to the resolution of an optical tweezers (as discussed in detail in the following Chapter), these traces set the typical noise scale for an optical tweezers measurement. Only noise sources comparable to this scale should affect the resolution of the instrument. The fact that all of the other noise traces are several orders of magnitude lower for almost all frequencies indicates that these noise sources will have negligible effects on our resolution for measurements on these time scales. However, below ~ 1 Hz it is clear that there are additional fluctuations in the positions of the beads, which clearly originate in the positional fluctuations of the 1064-nm laser. These are the fluctuations which will ultimately limit the resolution of our measurement; nonetheless, the fact that the deviations start at such a low frequency, implies that for measurements of relatively fast processes, >1 s, our measurements will be limited only by Brownian noise. Since the Brownian fluctuations are the fundamental limit to spatial resolution in an optical tweezers measurement, no additional action can be taken to improve resolution above ~ 1 Hz. Thus, the optical tweezers instruments constructed here are as quiet as it is physically possible for them to be with the typical experimental parameters. It is this fact which makes these instruments *high resolution* optical tweezers. Perhaps, a better, less subjective term would be *Brownian-limited* optical tweezers.

2.4.11: Aside: Understanding Noise Power Spectra

The construction of a high resolution optical tweezers is nothing more than the identification and elimination of noise sources. In this process, there is no tool more powerful than the noise power spectra, e.g. Figures 2.2 and 2.13. In this brief aside, we provide a first introduction to this useful tool.

Formally, the noise power spectrum is the magnitude-squared of the Fourier transform of a time series, e.g. a series of voltages measured at different times. Mathematically, the noise power spectra is

$$S(f) = |\mathfrak{I}(x(t))|^2 = \mathfrak{I}^*(x(t))\mathfrak{I}(x(t)) \quad (2.3)$$

where $x(t)$ is the time series, $\mathfrak{I}(x(t))$ is the Fourier transform of $x(t)$, and \mathfrak{I}^* is its complex conjugate. Physically, any time series can be constructed from the sum of sine and cosines at all frequencies—this is known as the Fourier theorem—and the noise power spectra at a given frequency is nothing more than the measure of the amplitude of the sine wave at that frequency needed to reconstruct the time series (150). More formally, the noise power spectrum is the power contained in that sine wave, i.e. $\frac{1}{2}$ of the amplitude squared divided by the frequency division of the spectra. Thus, the noise power spectra of the backend electronics, the black trace in Figure 2.13, for example, shows that the observed fluctuations have greater amplitudes at lower frequencies than at higher frequencies.

This information immediately allows one to discriminate between different noise sources based on the distribution of fluctuations at different frequencies, information that would not have been immediately obvious from the time series. For example, it is very common to sort noise by the frequency dependence of the noise power. Noise that is

frequency independent is known as white noise and can only originate through a process that has no memory of its previous state—i.e. Brownian diffusion at low frequencies or digitization noise. Noise power that decreases as the frequency squared, i.e. $\propto 1/f^2$ is known as red noise or one-over-f-squared noise. This noise typically comes from a process that remembers its previous state, such as a directed drift at a constant velocity, or Brownian diffusion at high frequencies. For example, the fact that the 1064-nm laser noise at low frequencies decreases as $1/f^2$ immediately implies that this is not digitization noise or uncorrelated behavior. Ultimately, this observation led us to the discovery that this noise is caused by the random flipping of a single bit in the temperature controller of the laser, a process which has memory on the time-scale of the laser noise. Finally, noise power which decreases as $1/f$ is known as *pink* noise or one-over-f noise. There is no well-defined physical origin for such noise, but it is typical of physical systems which involve a large number of components or natural time scales, e.g. complicated electronic circuits. Thus, it is not unexpected to see $1/f$ at low frequencies for our back-end electronic noise, black trace in Figure 2.12.

In addition, to discriminating between noise sources, the noise power spectra also allows one to estimate the amount of noise remaining in a measurement after the time series has been averaged over a given time window. This result originates in a very useful theorem which relates noise power spectra to the variance of the time series. This theorem is known as Parseval’s theorem³, and it states that

³ Here we have limited the integration to positive frequencies. Technically, there is also power at negative frequencies, but for real signals, this power is identical in magnitude to the power at the comparable positive frequency. Thus, it is possible to make a *one-sided* spectra, by simply scaling the power at all positive frequencies by 2.

$$\int_0^{\infty} S(f) df = \langle x^2 \rangle - \langle x \rangle^2 \quad (2.4)$$

In other words, if one adds up the power at each frequency, the integral of the noise power spectra, then the result is the variance in the time series, $\langle x^2 \rangle - \langle x \rangle^2$. A very important corollary to Parseval's theorem is that if one integrates only over a portion of the spectra, then the result is the variance in the time series if that time series had been averaged down to the same frequency. For example, if one integrates the noise power spectra up to 100 Hz, this produces the variance in the time series that one would expect if the time series was averaged down to 1/100Hz, i.e. ~ 10 ms. This is an extremely important result because, practically speaking, optical tweezers measurements always involve some degree of temporal averaging, and this corollary allows us to infer from the noise power spectra exactly what noise will remain in the measurement after this averaging is performed.

Finally, it is important to know that the noise power spectra of uncorrelated noise sources add. Moreover, if the two noise spectra do not add—this indicates that the noise is correlated, another useful parameter in deciphering the origin of the fluctuations. Thus, for uncorrelated noise sources an experimenter can build up the noise in the final measurement through careful analysis of the noise from each major optical component, exactly as is done in Figure 2.13. When it comes to debugging a noisy instrument or finding the limiting component, there is no more powerful analysis technique.

2.5: Summary and Conclusions

In this Chapter, we have described the design and construction of a dual trap optical tweezers, an instrument built for the purpose of detecting the minute length changes introduced into a DNA tether by the fundamental steps of nucleic acid motors. Since the chemical periodicity of DNA is on the Ångstrom-scale, this is the length scale that we must be able to detect. Unfortunately, there are a multitude of environmentally-cued fluctuations in an instrument that produce movements a full magnitude larger than this scale. To decouple ourselves from these fluctuations, we have utilized a dual trap geometry, in which the two optical traps are formed from orthogonal polarizations of the same laser. Moreover, by keeping the instrument simple and compact, we can use many of the same optics for both traps, further decoupling the fluctuations of these optical components from the final measurement. And, by keeping the region in which the two lasers must travel different optical paths as short as possible, we minimize the minute effects of atmospheric turbulence and avoid the complications associated with immersing the optics in a Helium atmosphere. Finally, our design exploits a novel dual trap detection system, which allows the motions of the two independently trapped beads to be monitored essentially simultaneously. As we will see in the next Chapter, this ability offers significant benefits when the effect of Brownian fluctuations are considered.

Despite the fact that our measurements are limited only by Brownian fluctuations for frequencies larger than ~ 1 Hz, a significant number of biological processes occur on times scales of a second or longer. Thus, there is still room for improvement in our instrument. The measurements presented in Figure 2.13 clearly indicate that the first instrumental component that should be replaced in order to improve the behavior of the

instrument below 1 Hz is the 1064-nm laser. This laser was chosen because of its previously published (131, 132) ability to provide ample optical power relatively stably (though not stably enough as we have shown). However, there are other laser options available that may be worth trying. For example, a tapered amplifier system such as the DLX110 from Toptica Photonics (Toptica Photonics Inc, Victor, NY) or the TEC-300 Power Littrow Series (Tiger-300; Sacher Lasertechnik Group, Buena Park, CA) can provide ~1 W of single-mode light at a wavelength of 780 nm. Tapered amplifiers work by scaling up the same solid-state technology used in the extremely stable 845-nm laser that we used; thus, it seems possible that the excellent stability seen in the 845-nm system may also be present in these systems, but with large enough optical powers to allow large forces to be applied. Plus the use of a different wavelength than 1064-nm would avoid the generation of singlet oxygen and significant sample heating, problems discussed in Chapters 4 and 5.

With the Brownian-limited instrument that we have described here, it is possible to detect length changes of a single base pair to a piece of dsDNA, as we will show in the next Chapter. Thus, the door is open to the high resolution study of the fundamental steps of many nucleic acid motors.

Chapter 3. Brownian Fluctuations in Dual-Trap Optical Tweezers

The addition of a second optical trap to hold the other end of the biological system of interest is an excellent way to decouple the measurement from the wide variety of environmental and mechanical fluctuations which limit resolution in typical single trap optical tweezers instruments (18, 131, 132). However, such experimental sources of noise are not the only noise sources that limit spatial resolution. The fundamental Brownian fluctuations of the optically trapped beads also limit the ability to measure small length changes. Moreover, the addition of a second optical trap to better isolate the measurement actually introduces a second degree of freedom subject to its own independent fluctuations. Thus, it is not clear that the added stability and isolation imbued by the extra optical trap is not compromised by an increase in the Brownian fluctuations in this system.

In this chapter, we address this issue by developing a theoretical understanding of how Brownian fluctuations limit the resolution of optical tweezers measurements. We then verify this theory with experimental measurements of spatial resolution under a wide variety of experimental parameters. Finally, we conclude by demonstrating that the instruments described in Chapter 2 are capable of measuring length changes to a single piece of DNA of just 3.4 Å. Several figures in this chapter and some of the discussion have been taken with permission from Refs. (16, 18, 19).

3.1: How do Brownian Fluctuations Limit Resolution?

The typical dual optical trap experiment consists of two beads held in two optical traps tethered by a single molecule of contour length L , which, for illustrative purposes, we assume is double-stranded DNA. A small change ΔL in the contour length of the molecule—due to, for example, the action of a DNA-manipulating protein—deflects the microspheres away from their initial positions in their traps. These displacements partition the change in tether length between the spring constants of each trap, k_1 and k_2 , and that of the DNA tether, k_{DNA} . See Figure 3.1. These are the measured signals—the physical parameters that are used to estimate the length change of the DNA introduced by the biological system of interest.

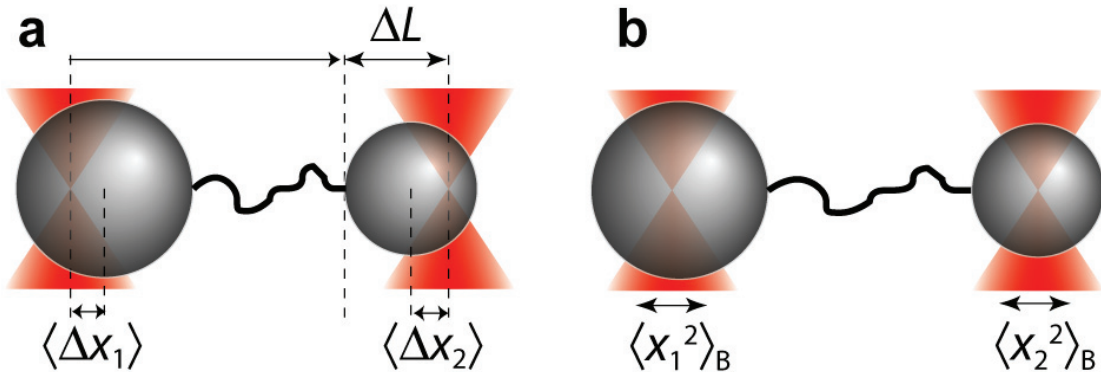


Figure 3.1. The Signal and Noise in a Two Trap System

(a) When the DNA is changed by a length ΔL , via the action of a biological system, the equilibrium positions of the two optically trapped beads will change. It is these changes in the average position of the beads, $\langle \Delta x_1 \rangle$ and $\langle \Delta x_2 \rangle$, which reveals the length change of the DNA. (b) However, the equilibrium position of the beads are fundamentally obscured by their Brownian fluctuations. The variance in these positions, $\langle x_1^2 \rangle_B$ and $\langle x_2^2 \rangle_B$, as a function of the averaging bandwidth, B , provide a measure of these fluctuations.

However, the ability to measure these signals is fundamentally limited. In addition to all of the extraneous sources of noise discussed in the previous Chapter, the ability to resolve these deflections is also limited by the fluctuating thermal force of the surrounding aqueous buffer, the same force that induces the Brownian motion of the trapped beads. To understand this phenomenon, consider the forces on each optically trapped bead. At every instant in time, each bead experiences the balance of three forces⁴: the restoring force of the optical trap, F_T , the tension of the tether, F_{DNA} , and the fluctuating Brownian force, F_B . Mathematically,

$$F_{DNA} + F_T + F_B = 0. \quad (3.1)$$

To determine the contour length of the DNA between the beads, one must know both the extension of the molecule, ξ , and its tension, F_T . Only then can models of the compliance of DNA, such as the worm-like-chain (98-101), be used to estimate the actual contour length of the DNA between the beads. In a perfect instrument, the instantaneous position of each bead, the separation of the traps, and, thus, the extension of the molecule, ξ , are known perfectly at all times⁵. However, the tension of the DNA is never determined directly, but inferred from the force on the optically trapped bead, F_T , using Eq. (3.1) with the assumption that on average $\langle F_B \rangle = 0$; thus, $\langle F_{DNA} \rangle = -\langle F_T \rangle$. This is a reasonable assumption for long time scales, as we will see below; however, at any given time, uncertainty in the magnitude and direction of the fluctuating Brownian force, F_B , provide an inherent uncertainty in the DNA tension. It is a common misconception that the thermal motion of the beads themselves are what limit the resolution of the optical

⁴ On the long time scales typical of measurements, the inertia of the system and the viscous drag forces can be neglected.

⁵ Typical instruments can easily resolve these distances to sub-Ångstrom levels.

tweezers—i.e. that positional fluctuations limit the ability to estimate the extension of the molecule—instead, it is actually the uncertainty in the instantaneous tension on the tether that fundamentally limits the spatial resolution attainable with an optical tweezers instrument. However, the positional fluctuations of the bead are a direct result of the fluctuating thermal forces, and we can determine the effect of these thermal fluctuations by calculating the size of the positional fluctuations caused by thermal forces, as we will show below.

3.2: Equations of Motion

Fortunately, the effect of thermal fluctuations on spatial resolution is a well-defined theoretical problem, conducive to analytic treatment. In this analysis, we describe the dynamics of two optically-trapped microspheres, attached via a single dsDNA molecule of contour length L , and held in a solvent bath at temperature T . In the interest of simplicity, we only consider displacements of the microspheres from equilibrium, x_1 and x_2 , along a direction parallel to the tether, and ignore orthogonal degrees of freedom including the Brownian rotation of each microsphere. Along this direction, we approximate the optical potential seen by each microsphere as harmonic with spring constants k_1 and k_2 . In the limit of small displacements, we treat the DNA as a linear spring with constant $k_{DNA}(\xi_{eq}) = dF_{DNA}/d\xi|_{\xi_{eq}}$, where we expand its force-extension behavior (98-101) about the equilibrium extension ξ_{eq} . The drag coefficient of each microsphere of radius r_i , in the absence of the other microsphere, is given by $\gamma_i = 6\pi\eta r_i$, where η is the viscosity of the solvent (9×10^{-10} pNs/nm² for water). See Figure 3-2 for a summary of this geometry.

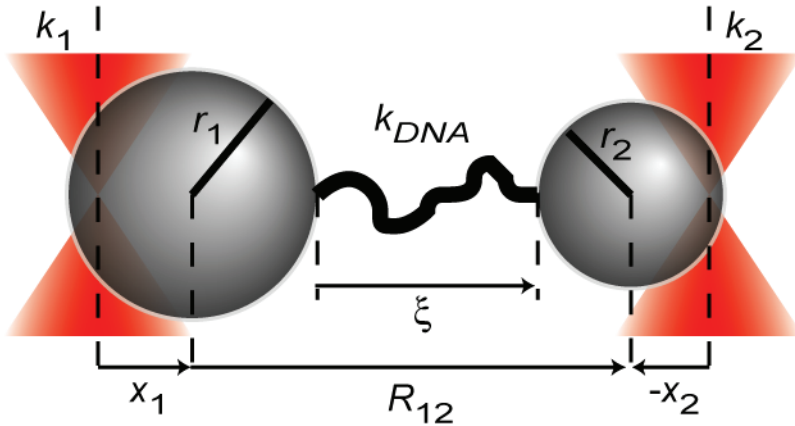


Figure 3.2. Parameterization of the Two Trap System

The two trap system consists of two optical traps of stiffnesses, k_1 and k_2 , containing two beads of radii, r_1 and r_2 , deflected by distances x_1 and x_2 from the center of their traps, and separated by an average distance R_{12} . These beads are tethered together via a piece of dsDNA of length L and average extension ξ . While the force-extension properties of DNA are highly non-linear, for small fluctuations, we can treat the DNA as a linear spring of stiffness, k_{DNA} . Reproduced with permission from Ref. (19), PNAS © 2006.

The drag coefficient assumed above is for an isolated bead far from any other beads or surfaces. In practice, we trap deep inside our sample chamber, thus, we can neglect hydrodynamic corrections due to nearby surfaces (96, 151). However, the relative proximity of the second microsphere introduces corrections that we cannot ignore. Physically, motions of one microsphere generate fluid flows which introduce motions in the second microsphere. See Figure 3.3. This hydrodynamic coupling is generally described by the Oseen tensor (152) which is approximately constant when the distance between the microspheres, R_{12} , is much greater than their positional fluctuations (152) and the time it takes the fluid to propagate between them is sufficiently short (153), both assumptions valid for most optical tweezers experiments. In addition, we will neglect the small effects of inertial terms (96), the finite relaxation time of the DNA tether (154), and the hydrodynamic interaction of this tether with the beads (155).

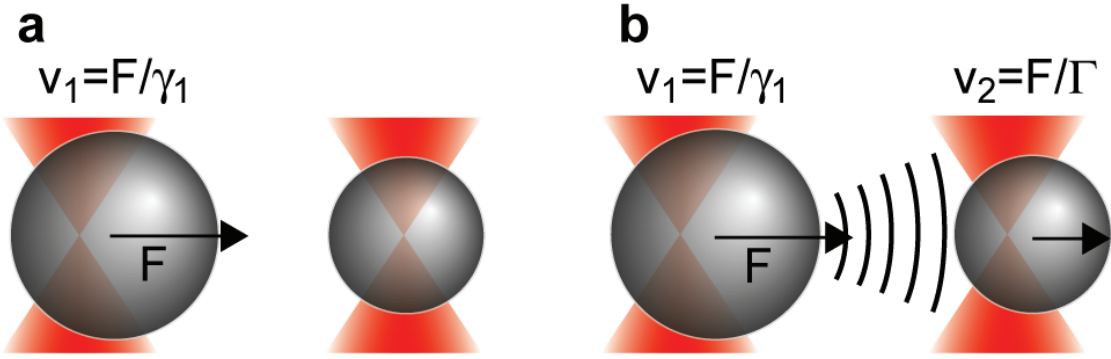


Figure 3.3. Hydrodynamic Coupling

(a) If a force, F , is applied to one optically trapped bead, the bead will respond with a proportional velocity, where the response is set by the drag coefficient of the bead, γ_1 . (b) The motion of the bead establishes a fluid field which exerts a force on neighboring beads. This bead responds with a velocity set by the strength of this hydrodynamic coupling, Γ .

Under these assumptions, the dynamics of the microspheres are governed by the balance between viscous, elastic, and stochastic Brownian forces, and are described by a set of linear, coupled Langevin equations:

$$-\boldsymbol{\mu}^{-1}\dot{\mathbf{x}} - \boldsymbol{\kappa}\mathbf{x} = \mathbf{F}(t), \quad (3.2)$$

where

$$\mathbf{x} = \begin{pmatrix} x_1 \\ x_2 \end{pmatrix}, \quad \boldsymbol{\mu} = \begin{pmatrix} 1/\gamma_1 & 1/\Gamma \\ 1/\Gamma & 1/\gamma_2 \end{pmatrix}, \quad \boldsymbol{\kappa} = \begin{pmatrix} k_1 + k_{DNA} & -k_{DNA} \\ -k_{DNA} & k_2 + k_{DNA} \end{pmatrix}, \quad \mathbf{F}(t) = \begin{pmatrix} F_1(t) \\ F_2(t) \end{pmatrix}. \quad (3.3)$$

\mathbf{x} is the position vector which describes the exact location of each bead with respect to the center of its trap, x_1 and x_2 . $\boldsymbol{\mu}$ is the hydrodynamic matrix which determines the viscous response of the system. Diagonal terms are simply the inverse of the drag coefficients of the isolated beads while the off-diagonal terms contain the static hydrodynamic coupling between the two beads. When the distance between the beads, R_{12} , is much greater than the radii of the microspheres, the hydrodynamic coupling

strength is $\Gamma = 4\pi\eta R_{12}$ (156). κ is the stiffness matrix which determines the elastic response of the system. The diagonal terms correspond to the stiffness which holds each bead in its trap—the sum of the stiffness of the trap and the DNA. Off-diagonal terms correspond to the elastic elements which couple the motion of the two beads, namely the stiffness of the DNA. Finally, $\mathbf{F}(t)$ is the vector of the random Brownian forces which act on each of the two trapped beads, $F_{1,2}(t)$. As first argued by Einstein and later by Uhlenbeck and Ornstein (152, 157), the fluctuating Brownian forces, $\mathbf{F}(t)$, have zero mean and are uncorrelated in time:

$$\langle \mathbf{F}(t) \rangle = 0, \quad \langle \mathbf{F}(t) \otimes \mathbf{F}(t') \rangle = 2k_B T \mu^{-1} \delta(t - t'), \quad (3.4)$$

where \otimes denotes the outer product of the force vectors, k_B is the Boltzmann constant, and $\delta(t - t')$ is the Dirac delta function. Physically, Eq. (3.4) reflects the facts that: i) the Brownian fluctuations do not have a preferred spatial direction, and ii) fluctuations at a given time have no memory of previous fluctuations.

3.3: Derivation of Signal-to-Noise Ratios

3.3.1: Schematic Derivation

The equations of motion specified in Eqs. (3.2) and (3.3) along with the statistical properties of the Brownian forces, Eq. (3.4), completely determine the fluctuating dynamics of this system and its response to biological activity. However, because these equations are coupled, via both the elasticity of the DNA and the hydrodynamic terms, calculating the dynamics of this system involves some complicated algebra. Our approach will be as follows: first we will transform our system to a set of coordinates, the

normal coordinates, in which the system appears uncoupled. In these normal coordinates, we can then determine exactly how the Brownian fluctuations translate into fluctuations in the normal coordinates. Next, by transforming back to the real coordinates, we can determine the statistical properties of the bead fluctuations. In particular, we are interested in the variance in the bead position and how this variance depends on the amount of temporal averaging that is done, i.e. the bandwidth of the measurement, and other experimental parameters. These quantities represent the noise in our measurement. In parallel, we will take the time average of Eq. (3.2) under the application of a force equivalent to that introduced when the DNA tether is changed in length. This will yield the change in equilibrium positions of the beads—the signals. The ratio of the signal to the noise yields the *signal-to-noise ratio* (SNR) which will be our measure of how Brownian fluctuations limit the spatial resolution of optical tweezers measurements as a function of experimental parameters.

We summarize the important results here. The noise in the position of a given trapped bead is

$$\langle x_1^2 \rangle_B = 4k_B T B \frac{\gamma_1 (k_2 + k_{DNA})^2 + \gamma_2 k_{DNA}^2 - 2 \frac{\gamma_1 \gamma_2}{\Gamma} k_{DNA} (k_2 + k_{DNA})}{\left(1 - \frac{\gamma_1 \gamma_2}{\Gamma^2}\right) (k_1 k_2 + k_2 k_{DNA} + k_1 k_{DNA})^2} \quad (3.5)$$

where the noise in the other trap can be calculated by exchanging indices. In addition, the fluctuations of the two beads are correlated with an average cross-correlation of

$$\langle x_1 x_2 \rangle_B = \frac{4k_B T B}{\left(1 - \frac{\gamma_1 \gamma_2}{\Gamma^2}\right)(k_1 k_2 + k_2 k_{DNA} + k_1 k_{DNA})^2} \times \left\{ \gamma_1 k_{DNA} (k_2 + k_{DNA}) + \gamma_2 k_{DNA} (k_1 + k_{DNA}) - \frac{\gamma_1 \gamma_2}{\Gamma} (k_1 k_2 + k_2 k_{DNA} + k_1 k_{DNA} + 2k_{DNA}^2) \right\}. \quad (3.6)$$

Finally, the signal for a given trap is

$$\langle \Delta x_1 \rangle = \Delta L \frac{\xi}{L} \frac{k_2 k_{DNA}}{k_1 k_2 + k_2 k_{DNA} + k_{DNA} k_1}, \quad (3.7)$$

where the signal from the second trap is again calculated by exchanging indices, $1 \leftrightarrow 2$.

With these three quantities, it is possible to calculate all of the SNR discussed in subsequent sections; thus, readers uninterested in the full derivation of these quantities can immediately skip to Section 3.4.

3.3.2: Noise Power Spectra

The fluctuations in $\mathbf{x}(t)$ are completely described by their correlation functions $\langle \mathbf{x}(t) \otimes \mathbf{x}(t') \rangle$ or the Fourier transform, $\mathbf{S}_x(f)$, of these correlation functions, the *noise power spectra*. We solve for these quantities by finding a suitable normal coordinate which diagonalizes Eq. (3.2). In particular, we assume that $\mathbf{x} = \mathbf{A}\boldsymbol{\eta}$, where the matrix \mathbf{A} is chosen to decouple these equations. Thus, $\boldsymbol{\eta}$ is governed by a simpler set of equations, $-\dot{\boldsymbol{\eta}} - \boldsymbol{\lambda}\boldsymbol{\eta} = \boldsymbol{\Phi}(t)$, where $\boldsymbol{\lambda} = \mathbf{A}^{-1}\boldsymbol{\mu}\boldsymbol{\kappa}\mathbf{A}$ is the diagonal matrix of the eigenvalues λ_{\pm} and $\boldsymbol{\Phi}(t) = \mathbf{A}^{-1}\boldsymbol{\mu}\mathbf{F}(t)$ are the transformed Langevin forces.

Once decoupled, $\boldsymbol{\eta}(t)$ can be formally solved by integrating the fluctuating force with the appropriate Green's function,

$$\boldsymbol{\eta}(t) = - \int_{-\infty}^t dt_1 e^{-\lambda(t-t_1)} \boldsymbol{\Phi}(t_1). \quad (3.8)$$

By taking the time average of the outer product of $\boldsymbol{\eta}(t)$ and $\boldsymbol{\eta}(t')$ and using Eq. (3.4), we derive the correlation functions of the experimental coordinates, $\langle \mathbf{x}(t) \otimes \mathbf{x}(t') \rangle$, from the known correlation functions of the Brownian forces. We find that

$$\begin{aligned} \langle \mathbf{x}(t) \otimes \mathbf{x}(t') \rangle &= \mathbf{A} \langle \boldsymbol{\eta}(t) \otimes \boldsymbol{\eta}(t') \rangle \mathbf{A}^T \\ &= \mathbf{A} \int_{-\infty}^t dt_1 \int_{-\infty}^{t'} dt_2 e^{-\lambda(t-t_1)} \langle \boldsymbol{\Phi}(t_1) \otimes \boldsymbol{\Phi}(t_2) \rangle e^{-\lambda(t'-t_2)} \mathbf{A}^T \\ &= \mathbf{A} \int_{-\infty}^t dt_1 \int_{-\infty}^{t'} dt_2 e^{-\lambda(t-t_1)} \mathbf{A}^{-1} \boldsymbol{\mu} \langle \mathbf{F}(t_1) \otimes \mathbf{F}(t_2) \rangle \boldsymbol{\mu}^T \mathbf{A}^{-1T} e^{-\lambda(t'-t_2)} \mathbf{A}^T, \\ &= 2k_B T \int_{-\infty}^{\min(t,t')} dt_1 \mathbf{A} e^{-\lambda(t-t_1)} \mathbf{A}^{-1} \boldsymbol{\mu}^T \mathbf{A}^{-1T} e^{-\lambda(t'-t_1)} \mathbf{A}^T \end{aligned} \quad (3.9)$$

where we use the facts that $\langle \mathbf{F}(t) \otimes \mathbf{F}(t') \rangle = 2k_B T \boldsymbol{\mu}^{-1} \delta(t-t')$ and that $\boldsymbol{\lambda} = \boldsymbol{\lambda}^T$. This expression can be further simplified by choosing a convenient normalization for the transformation matrix, $\mathbf{A} \mathbf{A}^T = \boldsymbol{\mu}$. Inserting the equivalent expression, $\mathbf{A}^{-1} \boldsymbol{\mu}^T \mathbf{A}^{-1T} = \mathbf{1}$, into Eq. (3.9) and performing the integral, we find that the correlation functions of the experimental coordinates are

$$\langle \mathbf{x}(t) \otimes \mathbf{x}(t') \rangle = k_B T \mathbf{A} \boldsymbol{\lambda}^{-1} e^{-\lambda|t-t'|} \mathbf{A}^T. \quad (3.10)$$

It follows from the definitions of $\boldsymbol{\lambda}$ and \mathbf{A} that when $t = t'$, $\langle \mathbf{x}(t) \otimes \mathbf{x}(t) \rangle = k_B T \boldsymbol{\kappa}^{-1}$, as expected from the equipartition theorem.

This specific choice of normalization for \mathbf{A} has an attractive physical interpretation. It corresponds to a set of normal coordinates that also decouples the degrees of freedom in the Hamiltonian. Since all inertial terms are neglected in this system, the Hamiltonian is simply $H = \frac{1}{2} \mathbf{x}^T \boldsymbol{\kappa} \mathbf{x}$, which transforms to $H = \frac{1}{2} \boldsymbol{\eta}^T \mathbf{A}^T \boldsymbol{\kappa} \mathbf{A} \boldsymbol{\eta}$ in

the normal coordinates and simplifies to $H = \frac{1}{2} \boldsymbol{\eta}^T \boldsymbol{\lambda} \boldsymbol{\eta} = \frac{1}{2} \lambda_+ \eta_+^2 + \frac{1}{2} \lambda_- \eta_-^2$, with the above normalization condition. From the equipartition theorem, each of these uncoupled modes contains an average of $\frac{1}{2} k_B T$ of energy. Furthermore, since each mode evolves independently of the other, their correlation functions are simply $\langle \boldsymbol{\eta}(t) \otimes \boldsymbol{\eta}(t') \rangle = k_B T \boldsymbol{\lambda}^{-1} e^{-\lambda|t'-t|}$. Transformation back to the experimental coordinates yields Eq. (3.10).

The correlation functions $\langle \mathbf{x}(t) \otimes \mathbf{x}(t') \rangle$ describe the Brownian motions of the coupled microspheres. The measured noise that results from these fluctuations is characterized by the noise power spectra, $\mathbf{S}_x(f)$, defined as the Fourier transforms of the correlation functions:

$$\begin{aligned} \mathbf{S}_x(f) &= \int_{-\infty}^{\infty} \langle \mathbf{x}(\tau) \otimes \mathbf{x}(0) \rangle e^{-i2\pi f \tau} d\tau \\ &= k_B T \int_{-\infty}^{\infty} \mathbf{A} \boldsymbol{\lambda}^{-1} e^{-\lambda|\tau|} \mathbf{A}^T e^{-i2\pi f \tau} d\tau, \\ &= 2k_B T \mathbf{A} (\boldsymbol{\lambda}^2 + (2\pi f)^2 \mathbf{1})^{-1} \mathbf{A}^T \end{aligned} \quad (3.11)$$

which have a characteristic Lorentzian form.

3.3.3: Low Frequency Noise

In a typical measurement, data are collected at a frequency higher than the highest characteristic frequency and then averaged to a frequency, f_{av} , lower than the lowest. Thus, the power spectra are white, i.e. frequency independent, over the measurement bandwidth, $B = f_{av}/2$, and the mean squared noise in microsphere position over this

bandwidth, $\langle \mathbf{x} \otimes \mathbf{x} \rangle_B$, is well approximated by the low-frequency power spectra $\mathbf{S}_x(0)$ multiplied by $2B$.

The total measured noise, $\langle \mathbf{x} \otimes \mathbf{x} \rangle_B$, is simply given by the integral of the noise power spectra calculated above over the bandwidth of the measurement, B , i.e.

$$\begin{aligned}\langle \mathbf{x} \otimes \mathbf{x} \rangle_B &= \int_{-B}^B \mathbf{S}_x(f) df \approx \int_{-B}^B \mathbf{S}_x(0) df \\ &\approx 4k_B T B \mathbf{A} \boldsymbol{\lambda}^{-2} \mathbf{A}^T.\end{aligned}\quad (3.12)$$

In explicit terms, the eigenvalues of Eq. (3.2) are

$$\begin{aligned}\lambda_{\pm} &= \frac{k_1 + k_{DNA}}{2\gamma_1} + \frac{k_2 + k_{DNA}}{2\gamma_2} - \frac{k_{DNA}}{\Gamma} \\ &\pm \sqrt{\left(\frac{k_1 + k_{DNA}}{2\gamma_1} - \frac{k_2 + k_{DNA}}{2\gamma_2} \right)^2 + \left(\frac{k_1 + k_{DNA}}{\Gamma} - \frac{k_{DNA}}{\gamma_2} \right) \left(\frac{k_2 + k_{DNA}}{\Gamma} - \frac{k_{DNA}}{\gamma_1} \right)}\end{aligned}\quad (3.13)$$

and the noise in the experimental coordinates over the measurement bandwidth B is given by Eqs. (3.5) and (3.6) above.

3.3.4: Measured Signals

We now turn our attention to the measured signal—the equilibrium response of the microspheres to a length change in the tether. We consider a process in which the contour length, L , of the DNA tether is changed by ΔL . In response to this change, the first microsphere experiences a force $k_{DNA}\Delta L\xi/L$, and the second microsphere a force $-k_{DNA}\Delta L\xi/L$. Solving the time-averaged equations of motion, Eq. (3.2), for the changes in the equilibrium positions of the microspheres, $\langle \Delta x_1 \rangle$ and $\langle \Delta x_2 \rangle$, under these forces,

$$-\mathbf{K} \langle \Delta \mathbf{x} \rangle + \Delta \mathbf{F} = 0, \quad (3.14)$$

where

$$\langle \Delta \mathbf{x} \rangle = \begin{pmatrix} \langle \Delta x_1 \rangle \\ \langle \Delta x_2 \rangle \end{pmatrix} \text{ and } \Delta \mathbf{F} = k_{DNA} \Delta L \frac{\xi}{L} \begin{pmatrix} 1 \\ -1 \end{pmatrix}, \quad (3.15)$$

we find the equilibrium signals listed in Eq. (3.7).

Note that, in the limit that $k_2 \rightarrow \infty$, $\langle \Delta x_2 \rangle$ approaches zero, and

$$\langle \Delta x_1 \rangle = \Delta L \frac{\xi}{L} \frac{k_{DNA}}{(k_1 + k_{DNA})}, \quad (3.16)$$

as expected for a single trap. Moreover, because the system has a finite compliance,

$$\langle \Delta x_{1,2} \rangle \leq \Delta L.$$

3.4: The Spatial Resolution of Dual Trap Optical Tweezers

3.4.1: The Spatial Resolution for a Single Trap

A DNA length change, ΔL , is revealed by the measured signal, i.e., the change in the equilibrium displacement of each microsphere from the center of its trap, and the noise in this measurement is given by the integrated fluctuations in each microsphere position over the measurement bandwidth. Thus, the spatial resolution of the instrument—its ability to resolve the change ΔL —is given by the ratio of the measured change in microsphere position to the root-mean-square of its fluctuations: the *signal-to-noise ratio* (SNR). For the microsphere in trap 1 this is

$$SNR_1 \equiv \frac{\langle \Delta x_1 \rangle}{\sqrt{\langle x_1^2 \rangle_B}} = \frac{k_{DNA} \Delta L}{\sqrt{4k_B T B}} \frac{k_2}{\sqrt{\gamma_1 (k_2 + k_{DNA})^2 + \gamma_2 k_{DNA}^2 - 2 \frac{\gamma_1 \gamma_2}{\Gamma} k_{DNA} (k_2 + k_{DNA})}} \sqrt{1 - \frac{\gamma_1 \gamma_2}{\Gamma^2}}. \quad (3.17)$$

SNR_2 is found by exchanging indices, $1 \leftrightarrow 2$.

To better understand Eq. (3.17), it is useful to compare it to the SNR for single trap optical tweezers, which can be derived from SNR_1 in the limit that $k_2 \rightarrow \infty$.

$$SNR_{single} = \frac{k_{DNA}\Delta L}{\sqrt{4k_B TB\gamma_1}} \sqrt{1 - \frac{\gamma_1\gamma_2}{\Gamma^2}}. \quad (3.18)$$

The expression derived previously in the literature (108) ignores hydrodynamic coupling and is recovered in the $\Gamma^{-1} \rightarrow 0$ limit. The hydrodynamic coupling that appears in this equation reflects the fact that the mobility of the first microsphere is modified by the presence of the second, stationary microsphere. Similar modifications to this mobility can occur in the presence of a nearby surface (96, 151).

Comparing Eqs. (3) and (4) for single and dual optical traps, one observes significant differences in behavior. SNR_{single} is, remarkably, independent of trap stiffness and grows linearly with DNA stiffness. On the other hand, for the dual optical trap, SNR_1 depends on the stiffness of the second trap, and becomes increasingly independent of DNA stiffness, asymptotically reaching the value

$$SNR_{max} = \frac{\Delta L}{\sqrt{4k_B TB}} \frac{k_2}{\sqrt{\gamma_1 + \gamma_2 - 2\frac{\gamma_1\gamma_2}{\Gamma}}} \sqrt{1 - \frac{\gamma_1\gamma_2}{\Gamma^2}} \quad (3.19)$$

for $k_{DNA} \gg k_2$. This corresponds to the expected SNR for a dumbbell consisting of two microspheres connected by a rigid rod with a total drag coefficient of $\gamma_1 + \gamma_2$. Further inspection shows that $SNR_{single} \geq SNR_1$ for all experimental parameters, only approaching the equality in the trivial limit $k_{DNA} \rightarrow 0$.

3.4.2: Differential Detection

The above result confirms our initial intuition: the addition of a second optically trapped bead, subject to its own fluctuations, does indeed degrade the resolution of an optical tweezers when the actions of a biological system are estimated from motions of a single bead. However, in only considering the displacements of the beads individually, we have ignored the correlations between them due to the coupling of the DNA tether. Significantly, this correlation $\langle x_1 x_2 \rangle_B$ increases with DNA stiffness, see Eq. (3.6). If the deflections of both microspheres are monitored simultaneously, a new coordinate may be formed from a linear combination of x_1 and x_2 that exploits these correlations to produce higher spatial resolution. The use of such a coordinate to measure the changes in the length of the DNA tether represents a significant advantage of a dual trap optical tweezers in which the displacements of *both* microspheres are monitored.

3.4.3: The Difference Coordinate

To illustrate this point, consider the *difference coordinate*, $x_- \equiv x_1 - x_2$, for which we compute the small bandwidth noise, $\langle x_-^2 \rangle_B = \langle x_1^2 \rangle_B + \langle x_2^2 \rangle_B - 2\langle x_1 x_2 \rangle_B$ and the signal $\langle \Delta x_- \rangle = \langle \Delta x_1 \rangle - \langle \Delta x_2 \rangle$. The coupling due to DNA leads to a positive correlation in the positions of the microspheres $\langle x_1 x_2 \rangle_B$ since one microsphere effectively pulls the other in the same direction via the DNA as it undergoes Brownian motion. Thus, the negative sign in the definition of x_- implies that the small bandwidth noise $\langle x_-^2 \rangle_B$ is decreased by this coupling. In contrast, the signal resulting from a change in DNA length corresponds

to motions of the microspheres in opposite directions, and thus the negative sign in x_- increases the signal $\langle \Delta x_- \rangle$. The SNR in this coordinate is given by

$$SNR_{diff} = \frac{k_{DNA}\Delta L}{\sqrt{4k_B TB}} \frac{k_1 + k_2}{\sqrt{\gamma_1 k_2^2 + \gamma_2 k_1^2 + 2k_1 k_2 \frac{\gamma_1 \gamma_2}{\Gamma}}} \sqrt{1 - \frac{\gamma_1 \gamma_2}{\Gamma^2}}, \quad (3.20)$$

which, unlike SNR_l , is linear in DNA stiffness and, thus, does not saturate with increasing k_{DNA} . Unlike SNR_{single} , however, SNR_{diff} depends on both trap stiffnesses, and reaches a maximum under the condition

$$\frac{k_2}{k_1} = \frac{\gamma_2}{\gamma_1} \frac{1 - \gamma_1/\Gamma}{1 - \gamma_2/\Gamma}, \quad (3.21)$$

in which case the SNR is optimal and given by the simple expression

$$SNR_{opt} = \frac{k_{DNA}\Delta L}{\sqrt{4k_B TB \gamma_{eff}}} \sqrt{1 - 2 \frac{\gamma_{eff}}{\Gamma}}, \quad (3.22)$$

where $\gamma_{eff} = \gamma_1 \gamma_2 / (\gamma_1 + \gamma_2)$. For a given DNA stiffness and bandwidth, the best possible resolution is achieved with identical microspheres of the smallest possible size in traps of identical stiffness; however, even for two microspheres of unequal size, the resolution in the difference coordinate can be maximized by tuning the trap stiffnesses according to Eq. (3.21).

3.4.4: The Optimal Coordinate

The argument outlined above is valid for any arbitrary linear combination of x_1 and x_2 , $\psi \equiv \alpha_1 x_1 - \alpha_2 x_2$. However, in contrast to the SNR in the difference coordinate, the arbitrary amplitudes $\alpha_{1,2}$ can be chosen such that the SNR is maximized for *all* values of the trap stiffnesses.

Computing the small bandwidth noise

$$\langle \psi^2 \rangle_B = \alpha_1^2 \langle x_1^2 \rangle_B + \alpha_2^2 \langle x_2^2 \rangle_B - 2\alpha_1\alpha_2 \langle x_1 x_2 \rangle_B \text{ and the signal } \langle \Delta\psi \rangle = \alpha_1 \langle \Delta x_1 \rangle - \alpha_2 \langle \Delta x_2 \rangle,$$

we maximize the SNR in this coordinate, SNR_ψ , with respect to the amplitudes $\alpha_{1,2}$.

Since the SNR is independent of overall scaling, SNR_ψ only depends on the ratio of the amplitudes α_2/α_1 ; thus, the condition which maximizes SNR_ψ is

$$\frac{\alpha_2}{\alpha_1} = \frac{\gamma_1(k_2 + k_{DNA}) + \gamma_2 k_{DNA} - \frac{\gamma_1\gamma_2}{\Gamma}(k_2 + 2k_{DNA})}{\gamma_2(k_1 + k_{DNA}) + \gamma_1 k_{DNA} - \frac{\gamma_1\gamma_2}{\Gamma}(k_1 + 2k_{DNA})}. \quad (3.23)$$

Under this condition, SNR_ψ is equal to SNR_{opt} , Eq. (3.22). For any set of experimental parameters, Eq. (3.23) defines an optimal coordinate in which the ability to resolve changes in the tether length is maximized. However, a drawback compared to the difference coordinate is that this optimal coordinate requires knowledge of parameters that may change during the course of an experiment, most notably k_{DNA} and Γ . An exception to this situation occurs when the experimental parameters obey the condition in Eq. (3.21), in which case the optimal coordinate becomes the difference coordinate, Eq. (3.20). Thus, Eq. (3.21) suggests that, for simplicity in analysis, the traps should be of equal stiffness and the beads should be of equal size since the difference coordinate, as opposed to the more general coordinate defined above, does not depend on the stiffness of the DNA or on the strength of the hydrodynamic coupling Γ , both parameters that will change as a function of the DNA length.

3.4.5: Implications of the Theory

By exploiting the correlations between the microspheres, we have derived an SNR, SNR_{opt} , that does not saturate with DNA stiffness and that is remarkably similar in form

to SNR_{single} . However, because SNR_{opt} depends on an effective drag coefficient γ_{eff} which is always smaller than either drag coefficient individually, it can be shown that $SNR_{opt} \geq SNR_{single} \geq SNR_1$ for all values of the experimental parameters. (The proof is included in the Supporting Text of Ref. (19)). The improvement of SNR_{opt} over SNR_1 reflects the fact that despite the added Brownian noise due to the second trapped microsphere, only a fraction of the noise is relevant to the resolution of the signal. Since the microspheres move in a highly antisymmetric manner in response to change in the DNA length, only fluctuations that are similarly antisymmetric limit the resolution of this signal. By monitoring the motion of both microspheres, we can partition the symmetric and antisymmetric motions of the microspheres to improve the resolution. However, it may still seem surprising that the resolution of a system with two fluctuating degrees of freedom, SNR_{opt} , is higher than that of a system with only one degree of freedom, SNR_{single} . The reason is that resolution-limiting fluctuations relax faster in a system with two fluctuating microspheres, where both are involved in the dissipation of thermal energy, than in a system with only one fluctuating microsphere. The smaller effective drag coefficient γ_{eff} that results from the tether-mediated collective motion of the two microspheres reflects this faster relaxation mechanism.

Hydrodynamic coupling introduces correction terms as seen in Eqs. (3.17) – (3.23). Significantly, these corrections lower the spatial resolution in the difference and optimal coordinate. As demonstrated by Meiners and Quake (152), antisymmetric motions of two hydrodynamically coupled microspheres are longer-lived than symmetric motions. Thus, more noise power is contained in antisymmetric fluctuations and the net

effect is to reduce the correlation $\langle x_1 x_2 \rangle_B$ and the SNR in the difference and optimal coordinates relative to that expected in the absence of coupling. Even for reasonable experimental parameters, the hydrodynamic coupling correction can be important and should not be ignored. In spite of this fact, the optimal coordinate, in which the symmetric and antisymmetric fluctuations of the microspheres are best partitioned, continues to yield a higher spatial resolution than all other coordinates.

The fact that the trap stiffnesses do not appear in the optimal spatial resolution, Eq. (3.22), is significant and hints at the generality of this analysis. For example, it is common to run optical traps in force feedback—displacing the position of one trap relative to the other to maintain a constant force (158) or exploiting non-linear trapping regimes where the stiffness of the trap disappears (135). We expect, by the independence of SNR_{opt} on the trap stiffnesses, that these systems should have identical spatial resolution to those derived above. It is possible to verify this prediction directly by replacing the position of one of the microspheres with the position of the feedback trap, setting the stiffness of that trap to zero in Eq. (3.2), and deriving the appropriate coupled Langevin equations. An identical analysis yields the same SNR as derived above with the feedback trap stiffness set to zero, as expected. Thus, the best resolution, SNR_{opt} , is still achieved by monitoring the movements of both microspheres, with no improvement to spatial resolution provided by force feedback.

3.5: Experimental Verification

3.5.1: Experimental Setup

In order to test the above theory, a single flexible tether of dsDNA either ~ 5 kb or ~ 3.4 kb in length is formed between two polystyrene microspheres held in traps of variable stiffness. The observed noise spectra for these tethers are well described by the expected Lorentzian power spectra above ~ 1 Hz for a large range of DNA tensions. See the Supporting Text of Ref. (19), the main text of Ref. (16), and Figure 2.13 in Chapter 2. This result indicates that the predicted spatial resolution can be directly tested on bandwidths larger than ~ 1 Hz. To measure the spatial resolution in each coordinate, we then increase the separation of the optical traps by 3.5 nm increments. Because we know exactly when the separation is done, we can measure the change in the equilibrium position of the beads between steps and the standard deviation within a single step. Moreover, these measurements can be done for any of the coordinates discussed above. See Figure 3.4. It is possible to show that the change in equilibrium positions in each coordinate when the traps are separated is identical to the expected change if the DNA were to shorten by the same contour length. Thus, by directly measuring these equilibrium changes and comparing them to measured noise values on a given bandwidth, we can compute the SNR one would expect to see if an enzyme changed the DNA length by the same amount. To facilitate comparison to movements of different sizes and durations, we scale these SNR to that of a 1 nm step in a 1 Hz bandwidth.

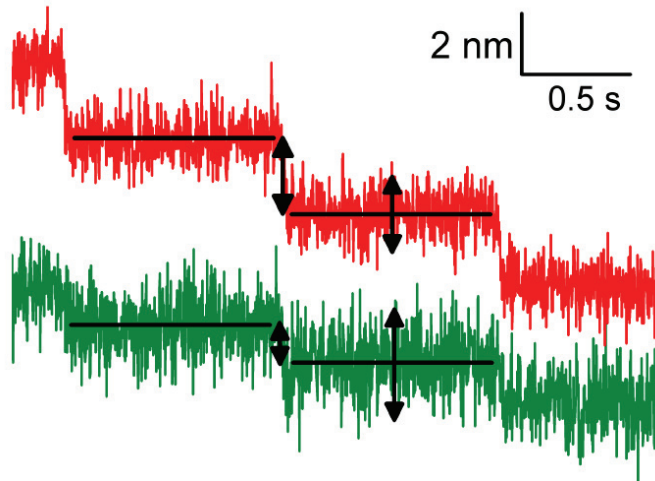


Figure 3.4. Measuring the Spatial Resolution

Equilibrium position of the trapped beads estimated via the optimal (red) or single trap coordinates (green) as the separation between the optical traps is increased in 3.5 nm increments every 1 s. The signal is measured from the difference between the mean positions of the coordinate within adjacent steps. The noise is calculated directly from the standard deviation in the coordinate within a single step. The SNR can then be measured directly from the ratio of the measured signal to the measure noise. Data are displayed with a 500 Hz bandwidth.

3.5.2: Spatial Resolution versus DNA Stiffness

In the first test of the predicted SNR, a DNA tether \sim 3.4 kb in length is formed between two 860 nm microspheres in traps of equal but variable stiffness. By stretching the tether to different tensions, thereby increasing its stiffness, we probe directly the dependence of the different SNRs on k_{DNA} . In Figure 3.5, we plot this dependence for the measured SNR for a single trap and the optimal coordinate (also the difference coordinate for a symmetric system). Figure 3.5 also contains the predicted values for SNR_i and SNR_{opt} plotted as one sigma confidence intervals to reflect the uncertainties in the experimental parameters (shaded and hashed regions). The measured values of SNR support the above predictions in both the single trap and the optimal coordinate for low values of DNA stiffness and demonstrate the improvement in SNR with the latter coordinate. As the

tether is pulled to higher forces, and thus, higher stiffness, these measurements become increasingly sensitive to non-linearity in the force and light deflection from each trap; thus, even the optimal coordinate effectively saturates to a maximum resolution. The range of DNA stiffnesses over which the measured values agree with the predicted values increases with trap stiffness, supporting the conclusion that the deviations are due to nonlinearities in the trapping potential⁶.

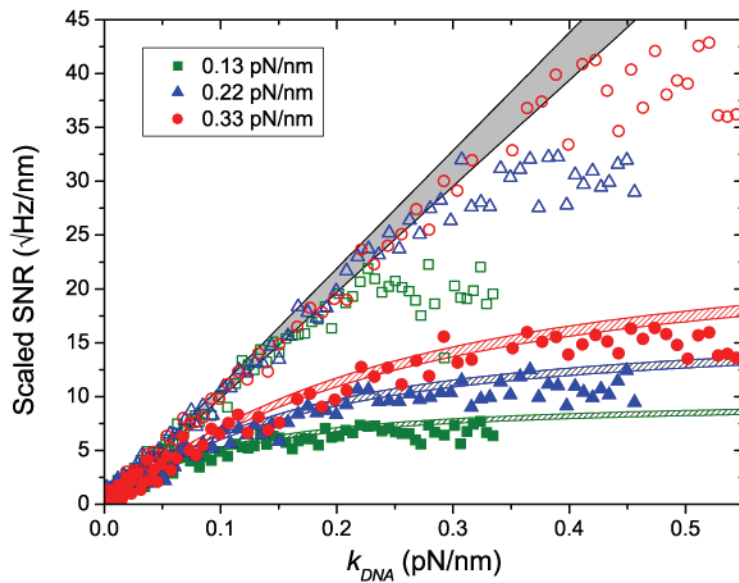


Figure 3.5. Spatial Resolution versus DNA Stiffness

Spatial resolution as a function of DNA stiffness at three different trap stiffnesses. Solid symbols corresponds to the spatial resolution for a single trap while open symbols correspond to the spatial resolution for the difference coordinate. The hashed regions correspond to the predicted spatial resolution for each trap stiffness while the solid gray region corresponds to the predicted spatial resolution for the optimal coordinate. The regions correspond to the uncertainty in the theoretical predictions due to uncertainties in the experimental parameters. Adapted with permission from Ref. (16), Cold Spring Harbor Laboratory Press © 2008.

⁶ Non-linearities scale as the distance displaced from the center of the trap; thus, with higher trap stiffnesses, higher DNA tensions and higher DNA stiffnesses can be reached with smaller displacements of the trapped beads.

3.5.3: Spatial Resolution versus Trap Stiffness

To test the ability of the optimal coordinate to extract a higher spatial resolution when the stiffnesses of the traps are not equal, we repeat the above experiment with a range of trap stiffnesses. A DNA tether of ~ 5 kb in length is attached between two identical 860 nm microspheres and pulled to a specified tension, corresponding to the desired DNA stiffness. The spatial resolution is then measured as above. A half-wave plate mounted on a rotary stage is then used to change the relative stiffness between the traps, and the measurement is repeated. Figure 3.6a shows the measured values of SNR_1 , SNR_2 , SNR_{diff} , SNR_{opt} for 6 DNA tethers at a DNA stiffness of 0.05 ± 0.005 pN/nm as a function of k_1 and the corresponding k_2 . The range of stiffnesses that can be accurately probed is limited by the nonlinearities in stiffness and displacement conversions that become prominent at lower forces in the weaker traps; thus, the distinction between the optimal coordinate and the difference coordinate is only noticeable at the edge points where the difference in trap stiffness is large.

To further test the predicted SNR, we form tethers between two microspheres of different diameters, 800 nm in trap 1 and 997 nm in trap 2. Again, we pull these tethers to a specified tension and measure the spatial resolution as a function of relative stiffness between the traps. Figure 3.6b shows the results for 4 different DNA tethers. The agreement between the predicted and observed values is not quite as good as for equal microspheres, Figure 3.6a. This effect is most likely due to slight imperfections in the sphericity of the 997 nm microspheres, which introduce additional noise. The power spectra for tethers made from two 997 nm microspheres have noticeable deviations from the predicted white noise on a larger frequency range (data not shown) for comparable

tensions, confirming this possibility. If the origin of the additional noise were the imperfection of the 997 nm microsphere, the agreement between measured SNR and theory should improve for the optimal coordinate when the movements of the 800 nm microsphere are weighted more, i.e., for higher stiffness in trap 1. See Eq. (3.23). As k_1 increases, the measured SNR for the optimal coordinate agrees better with the predicted values. See Figure 3.6b.

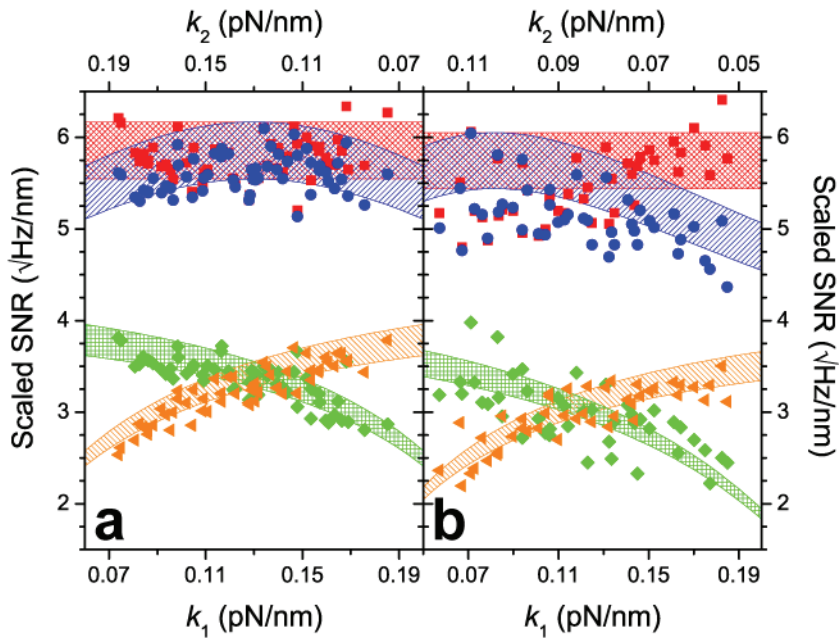


Figure 3.6. Spatial Resolution versus Trap Stiffness

- (a) Spatial resolution using the various coordinates when the two optically trapped bead are equal in size.
- (b) Spatial resolution for the various coordinates when the two optically trapped beads are different in size. Hashed regions correspond to the predicted values from the calculated SNR with the propagated uncertainty in the experimental parameters. Red corresponds to the optimal coordinate; blue corresponds to the difference coordinate; green corresponds to the SNR from trap 1; and orange corresponds to the SNR from trap 2. The solid points are measured values. The SNR have been scaled to 1 nm steps with a bandwidth of 1 Hz. Reproduced from Ref. (19), PNAS © 2006.

3.6: Single Base Pair Resolution

3.6.1: Experimental Demonstration of Single Base Pair Resolution

Dual trap detection should make it possible to detect smaller steps at larger bandwidths and lower DNA tensions than would be possible by only monitoring the motions of one microsphere. To demonstrate this point, we pull a ~3.4 kb molecule of DNA tethered between two 860 nm microspheres in traps of equal stiffness to a tension of 7.3 ± 0.1 pN. The distance between the traps is then increased by ~ 3.4 Å every 2 s, corresponding to a length change of dsDNA by 1 base pair. Figure 3.7a shows the displacements for a single trap and the optimal coordinate on a bandwidth of 100 Hz and 2 Hz. Whereas each of the 7 steps can be seen clearly in the optimal coordinate, the presence of steps is not apparent in the displacements of a single microsphere. The pairwise distributions⁷ for the optimal coordinate and the single microsphere coordinate on a 2 Hz bandwidth, Figure 3.7b and c, confirm this result. While a peak for all seven steps can be seen clearly for the optimal coordinate, there is no clear evidence of such peaks for the single microsphere. Due to finite trap stiffness, the peaks in Figure 3.7b are separated by only 2.3 Å, the expected signal in the optimal coordinate for a 3.4 Å change in trap separation with the above experimental parameters.

⁷ The pairwise distance distribution is a statistically objective way of probing for the presence of steps in noisy data. This technique is discussed in detail in Chapter 5.

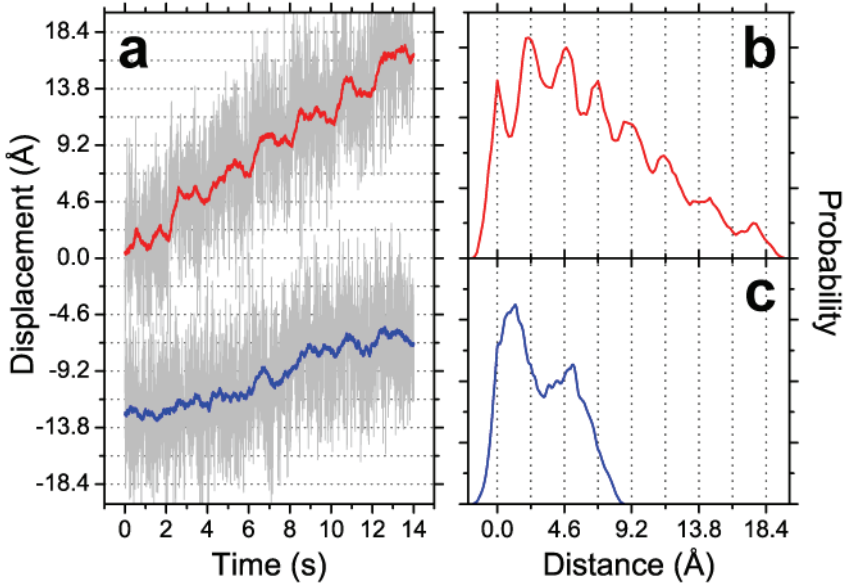


Figure 3.7. Observation of Single-Base-Pair-Length Changes

(a) Displacement as a function of time as the traps are separated in increments of just 3.4 Å. Light gray corresponds to data collected at 500 Hz and color to data averaged to 2 Hz with a sliding boxcar filter. Blue corresponds to the signal from one trap while red is the differential, optimal coordinate. Pairwise distance distribution of the data at 2 Hz for (b) the optical coordinate and (c) the difference coordinate. Seven peaks are clear in (b) indicating that all seven 3.4 Å steps have been observed. Reproduced with permission from Ref. (19), PNAS © 2006.

To demonstrate the improvement in resolution with increased DNA tension and stiffness, we performed the same stepping experiments in the high resolution instrument built around the high power 1064-nm laser. Figure 3.8 shows the single base pair traces collected under a tension of ~7 pN (as in Figure 3.7) and with a larger tension of ~27 pN. Under this increased tension, single base pair steps can be clearly detected even when the steps are faster, 1 s instead of 2 s in duration, and there is a factor of two less temporal averaging. The pairwise distribution in Figure 3.8b shows that these steps are clearly detectable with a higher SNR than the previous steps, indicating that even less temporal

averaging would be needed to observe these steps and permitting resolution of single base pair steps with shorter durations.

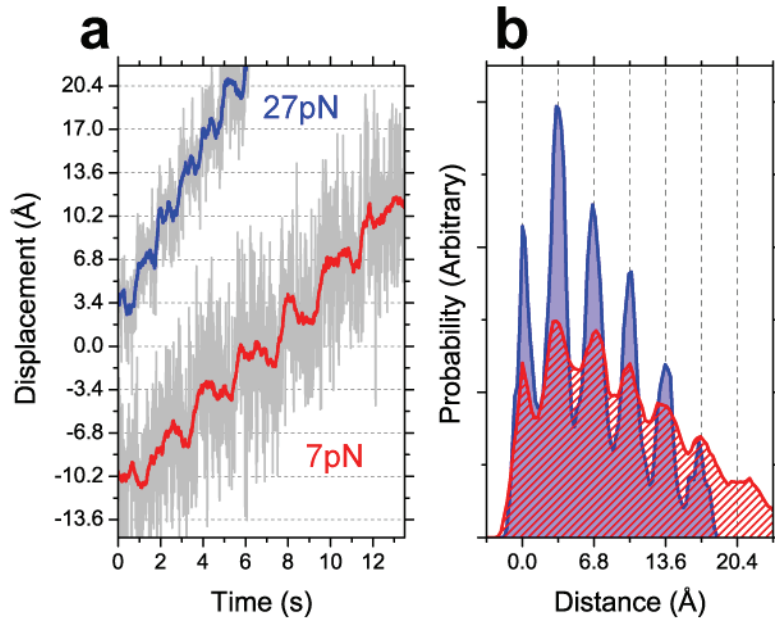


Figure 3.8. Improvement in Resolution with Force

(a) Single base pair steps measured with the optimal coordinate as at two different tensions: 7 pN in red and 27 pN in blue. Data in gray are averaged to 500 Hz while data in color are averaged to 2 Hz for red and 4 Hz in blue. (b) Pairwise distance distributions for the data in (a). Notice the increased clarity in the peaks for the higher DNA tension. Data in red are reproduced from Figure 3.7. Distances have been scaled in (a) to correct for the different compliances at the different tensions. Adapted with permission from Refs. (19) and (16), Cold Spring Harbor Laboratory Press, © 2008 and PNAS © 2006.

Comparable demonstrations of high spatial resolution have already been reported for dual trap optical tweezers (132) although only one microsphere was monitored. In those studies, large DNA tensions \sim 20 pN allowed single base pair steps to be observed with a 1.25 Hz bandwidth. The results presented here show, however, that by detecting the motion of both beads and performing a differential measurement, it is possible to resolve single base pair length changes with larger microspheres, longer DNA, and \sim 2.5 times less DNA tension than previously reported. The steps displayed in Figure 3.8

represent the current record for spatial and temporal resolution in an optical tweezers, single base pair steps with a temporal resolution of 250 ms.

3.6.2: Prescriptions for Base-Pair Resolution

The discussions in this Chapter and in the previous Chapter outline the basic principles by which single base pair resolution can be achieved with an optical tweezers. However, for convenience we summarize the crucial points here.

Instrument Isolation

1. *Operate the instrument in a quiet environment.* To house our high-resolution instrument, we use a room in the first basement of our building which displays floor vibration levels well below the Vibration Criterion E curve (141). To guard against acoustical noise, this room contains a separate sound-insulated enclosure into which only the optical trap and a rack of quiet electronics are located. All fanned electronics, such as computers, are placed outside.
2. *Maximize the resonance frequencies of the optical table and components.* We use a 4'x6', 24"-thick optical table (790 Series; Technical Manufacturing Corporation, Peabody, MA) which displays resonances above ~250 Hz, and levitate the table on four pneumatic isolators (Gimbal Piston Isolators; Technical Manufacturing Corporation, Peabody, MA) with a resonance frequency below ~2 Hz. In addition, all our optical components are mounted on 1"-diameter posts.
3. *Control the temperature of the instrument room.* We achieve this with a custom HVAC air handling system, maintaining the room temperature to within 0.1°C root-mean-square of the set value. Inside the instrument room, the air flow is quite diffuse to minimize air noise.

4. *Minimize human contact with the instrument.* All moving parts to the instrument, such as the sample stage, are operated by motorized actuators controlled by the user outside the instrument room. Other than during the loading of samples, the user does not enter the instrument room during the course of an experiment, eliminating transient temperature variations.
5. *Cover as much of the optical paths as possible.* To reduce the effects of air flow on the trap position stability, we cover the optical paths of the laser beams (except near the sample chamber which needs to be accessible) with enclosures made of 1/2"-thick plastic panels. Thinner panels can oscillate like a drum membrane, converting acoustical noise into mechanical vibrations directly coupled into the instrument.

Instrument Design

1. *Use a dual trap optical tweezers in which the same laser is used to form both traps.* There is a tremendous benefit to holding both ends of a tether optically as this geometry greatly decouples the instrument from mechanical drift of the stage and other optical components. In addition, using the same laser to form both traps minimizes the effect from pointing fluctuations in the laser.
2. *Minimize the path length after the polarized beams are separated and before they are recombined.* Keeping the optical paths as common as possible reduces the effects of air fluctuations on the relative position of the two traps. In our design, a low refractive index medium such as helium is not needed.
3. *Detect the motion of both trapped microspheres.* A dual-trap detection system that uses polarized back-focal-plane interferometry provides the sensitivity

needed to observe sub-Ångstrom movements of both microspheres. The detection of both microspheres further decreases sensitivity to background drift.

Experimental Design

1. *Estimate motions using the optimal coordinate.* As defined in Eq. (3.23), this linear combination of microsphere displacements maximizes the resolution of the instrument. For a symmetric system with identical trap stiffnesses and microsphere diameters, the optimal coordinate is simply the difference coordinate which has the added benefit of not depending on system parameters.
2. *Sample data synchronously and average to the lowest bandwidth possible.* Smaller bandwidths average more fluctuations, and, thus, lead to higher resolution. In addition, small time delays in the collection of the bead displacement signals preserve the correlations that optimize resolution.
3. *Use the smallest microspheres possible.* Resolution increases as microsphere size decreases. If, due to some experimental constraint, one microsphere must be of a fixed size, the other should still be as small as possible to maximize resolution. There is no advantage to equally sized microspheres, other than the convenience of a simple optimal coordinate.
4. *Maximize the tether stiffness.* Resolution scales linearly with tether stiffness, which can be increased by decreasing tether length or increasing tension. Practically, tethers that are too short introduce measurements errors and additional fluctuations while the tether tension is typically limited by the sensitivity of the biological system to force.

5. *Select the trap stiffness such that the applied forces fall within the linear range of the trap.* Weak traps result in additional noise from the coupling of axial fluctuations into lateral signals for relatively weaker forces. However, excessively strong traps should also be avoided as they increase the relative importance of instrumental noise sources.

3.7: Summary and Conclusions

In this Chapter, we calculate the degree to which Brownian fluctuations limit the ability to resolve equilibrium changes in the length of a flexible polymer held between two microspheres in two separate optical traps. By solving the equations of motion of each microsphere, we derive estimators for the spatial resolution of the system, i.e., the signal-to-noise ratios. Remarkably, we find that despite the addition of a second noisy degree of freedom, dual trap optical tweezers actually have higher spatial resolution than single trap systems, provided that the motions of *both* microspheres are monitored. Furthermore, we verify these predicted SNR by directly measuring the spatial resolution of a Brownian noise-limited dual trap optical tweezers.

Despite the good agreement between theory and experiment in the parameter range studied, it is useful to remember that several higher order effects are ignored in the derivation of the above SNR. First, the DNA has a finite relaxation time, degrading the instantaneous correlation between microspheres that gives rise to the improvement in SNR_{opt} . Using a simple Rouse model (154) with a drag coefficient extrapolated from experimental measurements (159), we estimate that this effect contributes no more than a 1% correction to the predicted SNR in Figure 3.6. However, as the length of the DNA increases, this relaxation time increases and corrections due to DNA dynamics should

become more important. Second, fluctuations of the microspheres in directions orthogonal to the DNA tether are coupled into the tether direction and become increasingly important as the DNA length decreases. The Brownian rotation of the microspheres also couple noise into this direction and become increasingly important as the microsphere diameter increases and DNA length decreases. We estimate that orthogonal movements and Brownian rotation degrade the SNR in Figure 3.6 by \sim 0.1% and \sim 1% respectively. Finally, we see no evidence in our measurements for partial shielding of the hydrodynamic coupling between the microspheres by the DNA as reported by Meiners and Quake (159). Our data agree well with the full \sim 14% hydrodynamic correction in the predicted SNR, as given by Eq. (3.22). The absence of noticeable shielding is not surprising since the measurements of Meiners and Quake (159) are conducted with DNA \sim 10 times longer than that used here, and we expect this effect to increase as the DNA length increases.

Practically, it has been shown that the greatest improvement provided by the addition of a second optical trap is the dramatic increase in isolation from the macroscopic environment (131, 132). Beyond this point, we have shown that there is a significant added benefit to monitoring the motions of both microspheres. In particular, the ability of the optimal coordinate to maximize the spatial resolution for a range of experimental parameters represents a significant increase in versatility of dual trap systems. For example, the freedom to modulate the stiffnesses of the traps without adversely affecting the spatial resolution may be useful in certain applications that require smaller laser fluxes to minimize photo-induced damage or laser heating. Furthermore, many of the biological systems which manipulate nucleic acids or proteins on the sub-

nanometer scale only operate in a limited range of forces. By exploiting correlations in the fluctuations of the microspheres, we have achieved sub-nanometer resolution at lower forces than previously reported, allowing the study of such systems under more permissive conditions.

Chapter 4. The Packaging Mechanism of the Bacteriophage φ29

During its lifecycle, the bacteriophage φ29 packages its ~19 kb genome into a proteinaceous capsid nearly 100-fold smaller in dimension than the genome, compressing this genome to near-crystalline density. This process is opposed by the large electrostatic, elastic, and entropic energy barriers associated with compressing a stiff, highly charged polymer into a small confining space. At the heart of this remarkable feat is a pentameric ring of identical ATPases that drive a complex assembly of protein and nucleic acid known as the packaging motor. While previous studies have delineated the basic mechanochemistry of this motor, several questions remain open. First, how is the motor geared—i.e. how much DNA does it package each chemical cycle? And, with multiple identical subunits comes the question: how are the activities of these individual subunits coordinated? Finally, the packaging motor is a member of a wide and diverse set of cellular ATPases, known as the ASCE superfamily; thus, by addressing these questions for the homomeric ring ATPase which drives packaging in the bacteriophage φ29, we can shed some light on the basic operating principles of this important family of enzymes.

In this chapter, we address these questions by using the high resolution optical tweezers discussed in the previous chapters to directly measure the discrete increments of DNA packaged by this motor each cycle. These measurements not only reveal the step

size of the motor, they also reveal the intricate coordination between the subunits that drive packaging. And on both fronts, these measurements yield surprises. First, a single mechanochemical cycle of the motor involves not one subunit and not five subunits, but the coordinated action of four subunits. This type of inter-subunit coordination is novel for ring ATPases. Second, the fundamental step size of the motor appears to be a non-integer number of base pairs—the chemical repeat of DNA. This is the first time that a molecular motor has been observed to move in distances that are not integer repeats of its molecular track, and a non-integer step size has rather profound implications for the mechanism of the motor. Materials for this chapter have been drawn with some revisions from Refs. (20, 21) with permission.

4.1: Introduction

Multimeric ring ATPases of the ASCE (Additional Strand, Conserved E) superfamily represent a structurally homologous yet functionally diverse group of proteins involved in such varied tasks as ATP synthesis, protein unfolding and degradation, and DNA translocation (68, 83, 85-87). Despite their importance, the coordination mechanism between the hydrolysis cycles of the individual and often identical subunits that compose these ringed-proteins is poorly understood. Recent crystallographic and bulk biochemical studies (68, 86) suggest various models of coordination in which subunits act sequentially and in order (12, 72-77, 79, 160), simultaneously and in concert (80), or independently and at random (81). Unfortunately, direct observation of subunit dynamics has only been reported for a heteromeric system, the F1 ring of ATP synthase (12), whose heterodimers function in a sequential manner.

The DNA packaging motor in the *Bacillus subtilis* bacteriophage φ 29 provides a model system to investigate the inter-subunit coordination in homomeric ring ATPases because it can be fully reconstituted *in vitro* (161), has a relatively slow translocation rate (58, 59), and has been extensively characterized by bulk (23) and single-molecule (37, 58-61) methods. Packaging of the double-stranded DNA genome of φ 29 into its proteinaceous precursor capsid (prohead) is driven by a powerful molecular machine (58) which consists of three multimeric rings organized coaxially around the point of DNA entry (23): a dodecameric (162) ring of gene product 10 (gp10) known as the head-tail connector, a pentameric (33, 49, 162) ring of RNA molecules known as the prohead-RNA (pRNA), and a pentameric (33, 162) ring of the ATPase gp16. See Figure 4.1a. Sequence homology (55) places gp16 in the FtsK/HerA family of dsDNA translocases (56). This family is itself a member of the large ASCE superfamily; thus, the packaging motor is related to the ubiquitous AAA+ and RecA-like proteins (83, 85).

Recent studies of the packaging motor have suggested a mechanism in which the subunits operate sequentially (59), each binding ATP, hydrolyzing it, and translocating the DNA by 2 bp (54, 59), before the next subunit repeats this cycle. While this scheme is consistent with the observed data (43, 59, 162) and with sequential models proposed for other ring ATPases (12, 68, 72-77, 79, 86, 160), direct observation of the coordination of the mechanochemical cycles of the individual subunits in the packaging motor has been lacking. In this article, we report the first measurements of the individual packaging steps of the φ 29 motor, which reveal both its step size and the novel coordination between its subunits. Because of its relation to the ASCE superfamily (55), the

mechanism for the packaging motor we propose here may have implications for the function of a diverse set of ring ATPases.

4.2: Packaging under Low Forces

4.2.1: Experimental Setup

To probe the dynamics of the packaging motor of φ 29, single prohead-motor-DNA complexes are tethered between two 860-nm diameter polystyrene beads held in two optical traps as in Figure 4.1a. Packaging is initiated *in situ* (60, 61) or by restarting stalled complexes (58, 59) in an ATP packaging buffer and monitored in a semi-passive mode in which the tension applied to the motor is kept within a narrow range by periodically changing the distance between the two traps. Motor translocation is determined from the decrease in the contour length of the DNA tether and is followed with base pair scale resolution (16, 18, 19). A detailed description of the experimental methods is presented in the following Chapter.

4.2.2: DNA is Packaged in 10-bp Increments

In our first experiments, we probe packaging at an average low external tension of ~ 8 pN and at ATP concentrations ([ATP]) above and below the K_M of the motor, ~ 30 μM (59).

Figure 4.1b shows representative packaging traces collected under these conditions. Across the full range of [ATP], packaging of DNA occurs in a stepwise manner consisting of *dwells*, in which the DNA length remains constant, followed by *bursts*, in which DNA is translocated in ~ 10 -bp increments. We determine the average length of DNA encapsidated in these packaging bursts for each [ATP] from the periodicity in the average pairwise distance distribution (PWD) as seen in Figure 4.1c. No statistically

significant trend is observed in the size of these bursts as a function of [ATP] (see Figure 4.1d); thus, the average of these values, 10.0 ± 0.2 bp (s.d.), is the best estimate for the burst size. This value and the values reported in Figures 4.1c and d have been corrected for small systematic errors in our distance measurement, as discussed in Chapter 5. Error bars include the uncertainty in this systematic error.

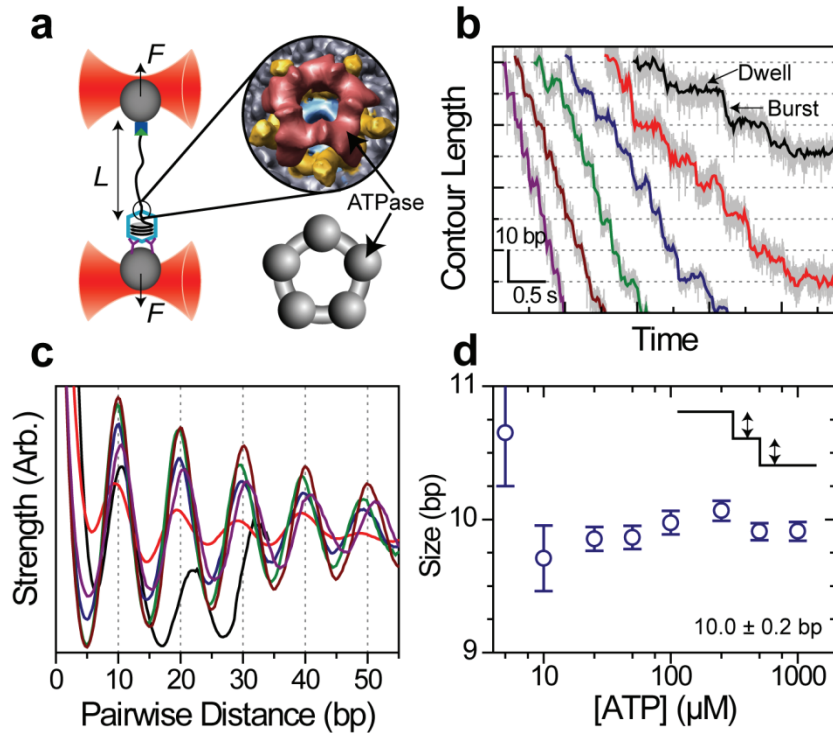


Figure 4.1. Experimental Setup and Low Force Data

(a) A single packaging bacteriophage prohead-motor complex and its dsDNA substrate are tethered between two beads each held in an optical trap. Inset: cryo-EM reconstruction of the full motor complex (33) (Courtesy of M. Morais), ATPase in red, pRNA in yellow, connector in cyan, and capsid in gray with a top view cartoon of the ATPase ring alone (below, gray). (b) Representative packaging traces collected under low external load, ~ 8 pN, and different [ATP]: 250 μM , 100 μM , 50 μM , 25 μM , 10 μM , and 5 μM in purple, brown, green, blue, red, and black, respectively, all boxcar-filtered and decimated to 50 Hz. Data at 1.25 kHz are plotted in light gray. (c) Average pairwise distributions of packaging traces selected for low noise levels (50% of all packaging data; Chapter 5, Section 5.3.4). Color scheme as in (b). (d) The average size of the packaging burst versus [ATP] determined from the periodicity in (c). Error bars are the error in the slope from a linear fit to the peak position. Data collected at 500 μM and 1 mM [ATP] are not shown in (b) and (c) for clarity. Reproduced with permission from Ref. (20), Macmillan publishers Ltd: Nature © 2009.

4.2.3: Dwell Time Distributions

To elucidate the mechanism by which the motor translocates in 10-bp increments, we analyze the time the motor spends in the dwell before each burst and the time it takes to complete each burst as a function of [ATP]. In order to measure these dwell times, we developed a step finding algorithm based on the Student's *t*-test. This algorithm is discussed in detail in Chapter 5.

The first striking feature of these dwells times is that, even under constant [ATP], the time the motor pauses before packaging is variable. This inherent stochasticity is a reflection of the hidden, thermally-activated, kinetic transitions which govern each intermediate kinetic state, and this variability implies that a single number cannot completely characterize the behavior of the motor at a given [ATP]. Instead, we compute the full probability distributions of observing a dwell of a given duration. These *dwell time distributions* as shown in Figure 4.2a completely characterize the dwell times at a given [ATP].

In principle, it is possible to fit these distributions to extract information about the kinetic mechanism of the dwell; however, fitting distributions requires knowledge of the functional form of the distribution. To avoid making such assumptions, we instead calculate the moments of the distribution. (This issue is discussed in greater detail in Chapters 6 and 7). The mean dwell time, seen in Figure 4.2b, shows a strong dependence on [ATP] that follows an inverse hyperbolic expression, $\langle \tau \rangle = (K_{1/2} + [T]) / (k_{\max}[T])$, with a $K_{1/2}$ of $23 \pm 7 \mu\text{M}$ (s.d.) and a k_{\max} of $8.7 \pm 0.7 \text{ s}^{-1}$ (s.d.). A fit to the more general Hill equation returns a Hill coefficient consistent with 1, 0.7 ± 0.3 (s.d.). In addition, the time the motor takes to complete the packaging of ~10 bp is finite and longer than our

averaging bandwidth. Figure 4.2b shows that these durations are largely insensitive to [ATP] and have a global mean of 10 ± 6 ms (s.e.m.). Taken together these observations produce a packaging velocity with a Michaelis-Menten [ATP] dependence consistent with previous measurements (59).

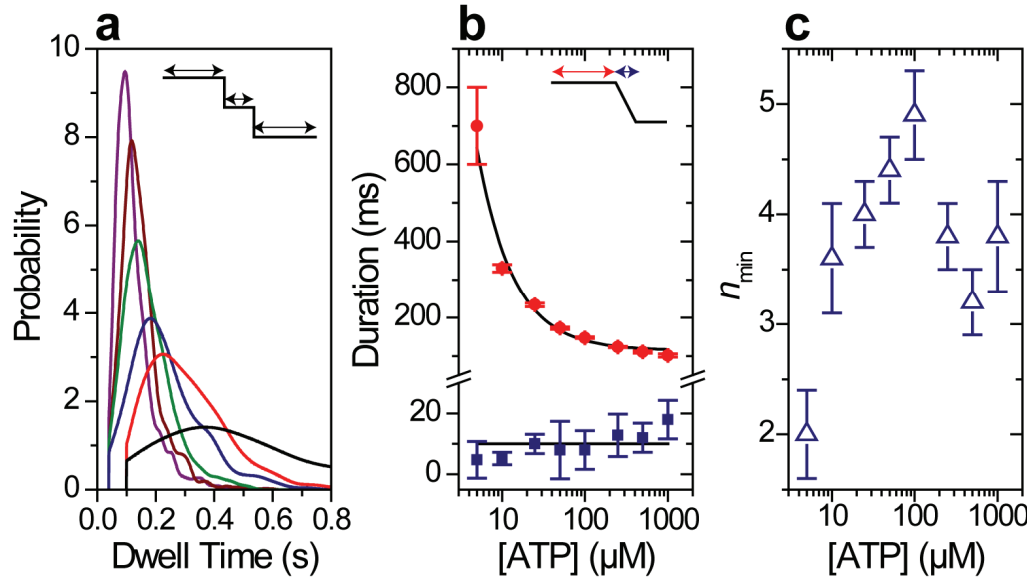


Figure 4.2. 10-bp Dwell Time Statistics

(a) Probability distributions for the dwell times preceding a 10-bp burst under low external load, ~ 8 pN, and different [ATP]: color scheme as in Figure 4.1. Figure 4.9 contains the number of observed bursts for each [ATP]. Distributions for 500 μM and 1 mM [ATP] are not shown for clarity. (b) The mean dwell time before the 10-bp bursts (red circles) for all [ATP] with an inverse hyperbolic fit (black) and the mean duration of all bursts (blue squares, average denoted by black line). (c) The minimum number of rate-limiting kinetic events during the dwell before the 10-bp bursts, n_{\min} , for all [ATP]. Error bars are the standard error. Reproduced with permission from Ref. (20), Macmillan publishers Ltd: Nature © 2009.

4.2.4: Limiting the Number of Kinetic Events

The specific shape of the dwell time distributions seen in Figure 4.2a provides further information on the kinetic transitions within a single dwell. For example, if the dwell time is governed by a single rate-limiting kinetic event, then one would expect a dwell time distribution that follows a single exponential dependence, i.e. the kinetic process has

no memory of when it started—it is a Markov process. If the dwell time is governed by two rate-limiting kinetic events, then the dwell time distribution is the convolution of the individual exponential decays for each process, and the resulting distribution is a peaked distribution, which does have a memory of when it started. In particular, the more rate-limiting kinetic transitions that compose the dwell, the more sharply peaked the distribution (112).

We can formalize these arguments with a new kinetic parameter which is calculated from the moments of the dwell time distribution. In particular, we define

$$n_{\min} = \frac{\langle t \rangle^2}{\langle t^2 \rangle - \langle t \rangle^2}, \quad (4.1)$$

where $\langle t \rangle$ is the mean dwell time and $\langle t^2 \rangle - \langle t \rangle^2$ is the variance in the dwell times.

Inspection of this kinetic parameter—which we will call n_{\min} or the minimum number of kinetic events, for reasons that will be obvious below—reveals that it is a measure of how “peaked” a distribution is. For example, a more sharply peaked distribution has a smaller variance and, thus, a larger n_{\min} , while a less peaked distribution, such as an exponential distribution, has a larger variance and, thus, a smaller n_{\min} . n_{\min} is related to another useful measure of enzymatic fluctuations, the randomness parameter, r , via $1/r = n_{\min}$. However, as we will show in Chapter 6, this equality is only true in certain circumstances, and when it is not true, n_{\min} is the more informative parameter.

As we will discuss in detail in later chapters, n_{\min} appears to have the remarkable property (112, 127) that it provides a *strict* lower bound on the number of kinetic events that occur in a given kinetic process. Namely,

$$n_{\min} \leq n_{actual}, \quad (4.2)$$

where n_{actual} is the number of intermediate kinetic states in a given process, such as the dwell before the 10-bp bursts. Thus measurements of the degree to which a distribution is “peaked” can provide strict limits on the number of hidden kinetic events which must occur within a single dwell.

Figure 4.2c plots the calculated n_{\min} for the measured dwell times for all [ATP]. At limiting [ATP], $5 \mu\text{M} \ll K_M$, we measure an n_{\min} of 2.0 ± 0.4 (s.e.m.), indicating that there are at least two rate-limiting transitions in each dwell. Since ATP binding must be rate-limiting under these conditions, i.e. the time it takes to bind ATP dominates the dwell, we conclude that no less than 2 ATP molecules bind to the motor before each 10-bp burst. In contrast, if a single ATP were to bind during each dwell, one would expect the dwell time distribution to be a single exponential and n_{\min} to be 1 (17, 112). At saturating [ATP], $1 \text{ mM} \gg K_M$, we measure an n_{\min} of 3.8 ± 0.5 (s.e.m.). Since binding is no longer rate-limiting, this indicates that at least 4 additional non-binding transitions must occur in each dwell. For intermediate [ATP], both binding and non-binding transitions can be rate-limiting; thus, we expect n_{\min} to peak to a value greater than either of the extreme values, exactly as is observed. Thus, Figure 4.2c indicates that, in total, no less than 6 kinetic transitions must occur in the dwell before each 10-bp burst—at least 2 ATP binding events and at least 4 non-binding transitions. In Chapter 7 we will formalize these arguments even further and rigorously show that the inferred values of n_{\min} at low and high [ATP] are indeed good estimates of the asymptotic limits of this parameter.

4.2.5: Interrupted Bursts

The findings that packaging occurs in 10-bp increments—five times larger than the 2-bp value proposed from bulk measurements (54, 59)—and that the preceding dwells contain multiple ATP binding transitions suggest that the 10-bp bursts may be composed of multiple smaller steps that in general may be too fast to resolve under the above conditions. This inference is supported by the observation that many bursts have durations larger than the measurement bandwidth (Figure 4.1b and Figure 4.2b), indicative of intermediate kinetic transitions. Moreover, Figure 4.3a shows that occasionally these intermediate transitions can be resolved, appearing as short micro-dwells that split the 10-bp burst into smaller steps.

While these smaller steps are not detected by a pairwise distance analysis, the t -test step finding algorithm identifies a significant subpopulation of steps smaller than 10 bp, Figure 4.3b-d. The two dimensional probability distribution, step size versus dwell time, shown in Figure 4.3b shows that this subpopulation has an average size of \sim 5 bp and a dwell time distribution that appears to have two components, a peaked distribution similar to the dwell time distribution observed for the 10-bp events and an exponential component which becomes prominent at short times. If the 5-bp events represent interrupted 10-bp bursts, then we would expect that the first 5-bp step of an interrupted burst should have a dwell time that is identically distributed to those observed for the 10-bp events since it would involve all of the same kinetic events. Moreover, we would expect that the second \sim 5-bp step in an interrupted burst should have a distinct dwell time since it likely involves different kinetic events than the dwells before 10-bp events. And, we would expect that these dwell times should be relatively short since they are typically

too fast to observe, i.e. not every burst is interrupted. Thus, we would expect that the ~5-bp events should display a dwell time distribution which is the sum of two distributions, the same distribution as the 10-bp events and a faster, distinct distribution. This expectation is exactly what is observed in Figure 4.3b-c.

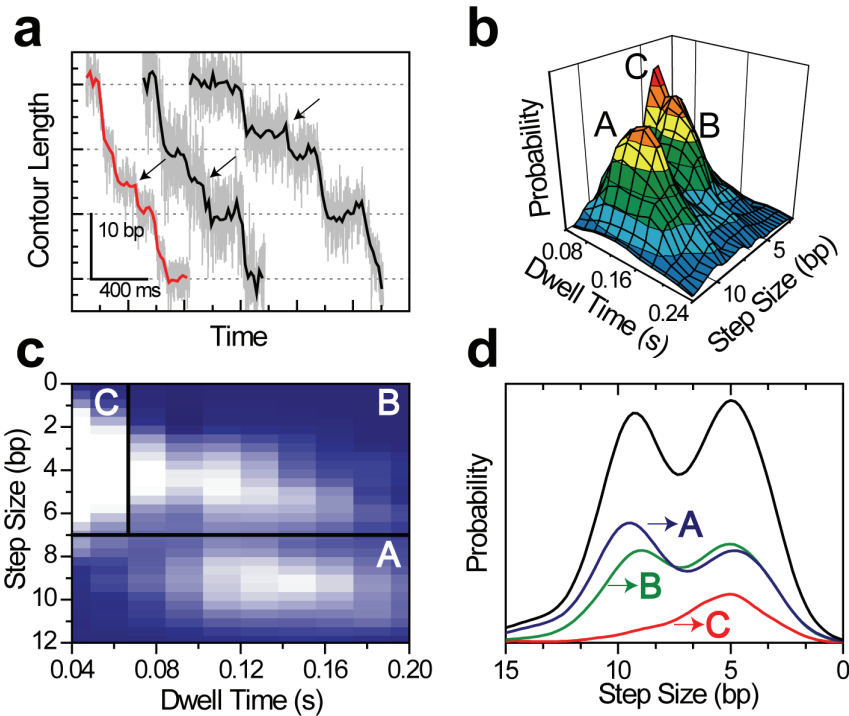


Figure 4.3. Interrupted Bursts

(a) Representative packaging traces at low external load show 10-bp packaging bursts are interrupted by brief micro-dwells, highlighted by arrows. Plotted are traces collected at 25 μM (red) and 10 μM (black) [ATP] at 1.25 kHz in gray and filtered and decimated to 50 Hz in color. Similar events can be observed for all [ATP]. (b) Two dimensional probability distribution for the step sizes and dwell times found using the t-test step finder for low external load at 100 μM [ATP], smoothed with a 2x2 boxcar kernel. Similar distributions are observed for all [ATP]. (c) Image plot of the same two dimensional distribution shown in (b) with the boundaries used to define three distinct events, labeled A, B, and C. (d) Conditional step size distributions for steps that precede events in regions A, B, and C, weighted by the probability of each type of event and plotted in blue, green, and red, respectively. The non-conditional step size distribution is shown in black. Reproduced with permission from Ref. (20), Macmillan publishers Ltd: Nature © 2009.

An additional prediction of the interrupted burst model is that the ~5-bp steps should tend to occur in pairs with ~5-bp events with a short dwell time following ~5-bp

events with a long dwell time. To test this prediction, we divide the \sim 5-bp events into two categories, fast and slow events. These are labeled C and B, respectively, and the \sim 10-bp events are labeled step type A. The divisions between step types are set to minimize the misidentification of one type with the other and are shown in Figure 4.3c. In Figure 4.3d we display the *conditional* step size distribution given a following step of a given type—i.e. a measure of the sizes of steps that precede each step type. We find that there is little preference for \sim 5-bp or \sim 10-bp events to precede a 10-bp event or a \sim 5-bp event with a *long* duration. However, we find that there is a dramatic increase in the fraction of \sim 5-bp events that precede \sim 5-bp events with short dwell times, exactly as predicted by the interrupted burst model. Thus, the smaller events do indeed cluster together to form 10-bp events, indicating that the population of smaller steps represent interrupted bursts and not a variable step size. The \sim 5-bp steps should not be interpreted as the fundamental step size of the packaging motor, as there may be a selection bias for 5-bp events since they represent the largest transition from the preceding and succeeding dwells.

4.3: Packaging at High Force

4.3.1: The Need for High Force

Under the experimental conditions above, the steps that compose the 10-bp bursts have dwell times that are typically too short for us to resolve. Thus, their detection is not frequent enough to allow proper statistical determination of both the number of steps within a single 10-bp burst or the size of these steps. Moreover, because the burst duration is insensitive to [ATP], lowering the concentration of ATP will not slow these

steps. However, these steps correspond to the actual translocation of DNA and the preceding dwell times correspond to kinetic events which generate force; thus, these dwells must be force sensitive (1). Therefore, we should be able to slow these steps with the application of high opposing loads.

This approach was initially complicated by the fact that the first optical tweezers that we constructed could not exert forces higher than ~15 pN which, given the strength of the packaging motor, was not sufficient to appreciably slow the bursts. Thus, to exert the necessary opposing forces, it was first necessary to build a new instrument around a much more powerful laser (Chapter 2). Unfortunately, with additional laser power, comes additional heating of the sample. And, in the course of our initial experiments, it was determined that the minor sample heating, ~2-3 °C, due to the high laser powers needed to apply appreciable loads to packaging motor resulted in a temperature-dependent increase in the packaging velocity. Remarkably, the temperature-dependent increase in packaging velocity effectively compensated for its force-dependent decrease, and we found that at ~40 pN the motor packaged the DNA much too quickly to observe the small steps that compose the burst.

The solution to this problem was to perform our experiments in a medium which does not absorb the trapping light as readily (163) yet still supports active packaging. In particular, we remade our packaging buffers by diluting a 10X buffer with 90% D₂O (Sigma-Aldrich, Ipswich, MA) as opposed to H₂O. The increased mass of deuterium reduces the absorption of D₂O relative to H₂O at our trapping wavelength, and laser heating tests confirm that a heavy water buffer displays negligible sample heating over all probed laser powers (data not shown). Moreover, control experiments at low force and

saturating [ATP] show that the packaging motor continues to take 10-bp bursts with dwell times distributed in a similar fashion as in H₂O when the motor operates in heavy water though the average duration of the dwell is increased, likely due to an isotope effect (data not shown but included in Ref. (20)). To avoid issues with slow hydrogen exchange and buffer density differences, all beads, including the beads with the stalled motor complexes, were suspended in heavy water buffers and allowed to incubate for several hours.

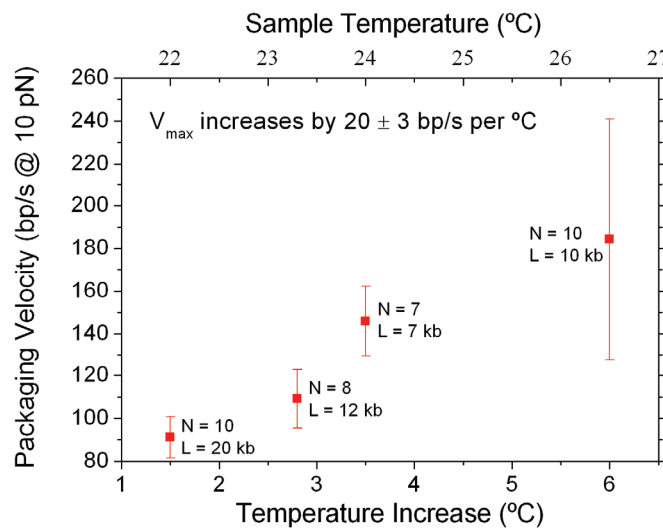


Figure 4.4. Temperature Dependence of Packaging Velocity

The packaging velocity at saturating [ATP], 1 mM, and low forces, ~10 pN, as a function of the temperature increase cued by increased 1064-nm laser power. The number of packaging phages under each condition and the total contour length of DNA packaged during all measurements is listed next to each point. The error bars represent the standard deviation of the velocity and are a measure of the spread in the population velocity. Temperature was measured by determining the change in the viscosity at each laser power (164).

4.3.2: DNA is Packaged in Four 2.5-bp Increments

As a direct demonstration of the composition of the 10-bp bursts, we follow packaging against high external loads, ~35-45 pN, at near-saturating [ATP] (250 μM) in a heavy water buffer. Figure 4.5a shows that, under 40 pN of average load, smaller steps of ~2.5

bp and integer multiples thereof can be clearly and frequently observed. The PWD for this data, shown in Figure 4.5b, reveals a periodicity of 2.4 ± 0.1 bp (s.e.m.). To determine if this periodicity is sensitive to force, we collected the PWD from regions of different opposing loads, and recalculated the periodicity. The inset to Figure 4.5b shows that the observed periodicity is independent of force, strongly suggesting that the 2.5-bp step size is a force-independent feature of the motor and that the 10-bp bursts observed at low force are, therefore, composed of four 2.5-bp steps. This conclusion is further supported by the prominent fourth peak observed in the PWD which is consistent with the corresponding 10-bp periodicity observed at low force.

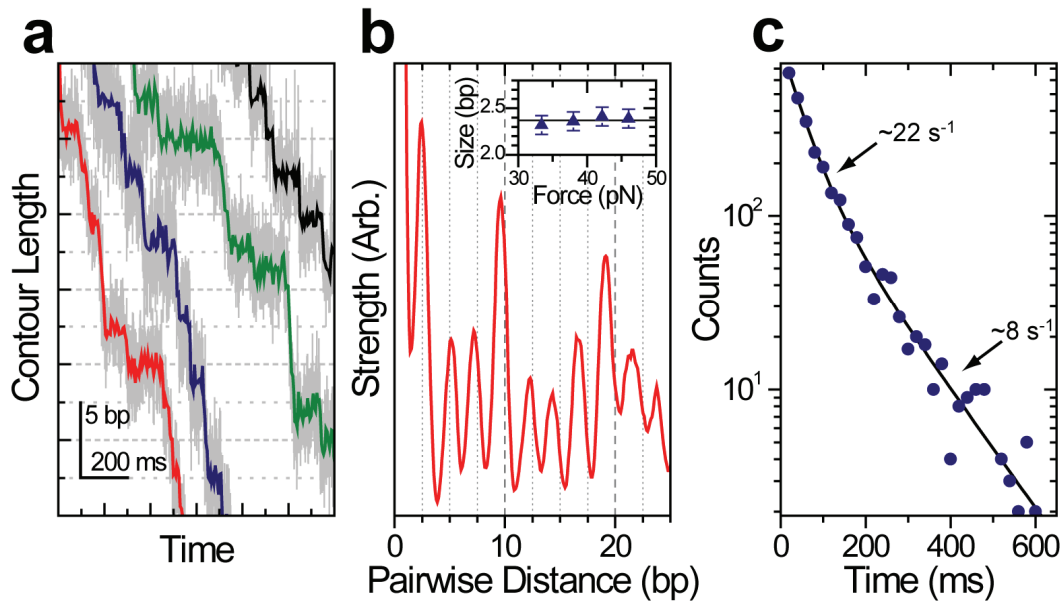


Figure 4.5. 2.5-bp Steps at High Force

(a) Representative packaging traces collected with external loads of ~ 40 pN and $250 \mu\text{M}$ [ATP]. Data in light gray are plotted at 1.25 kHz while data in color are boxcar-filtered and decimated to 100 Hz. (b) Average pairwise distribution of packaging traces selected for low noise levels (50% of all packaging data; see Figure 5.7). Inset: Force dependence of the observed spatial periodicity. The solid line is the mean for all forces 2.4 ± 0.1 bp (s.e.m.). (c) Dwell time histogram for the 2.5-bp steps observed under the packaging conditions seen in (a) plotted in blue circles with a bi-exponential fit in black ($N=2,662$). Reproduced with permission from Ref. (20), Macmillan publishers Ltd: Nature © 2009.

The dwell time distribution associated with the 2.5-bp steps (Figure 4.5c) is well described by a weighted sum of two exponential decays, with a fast rate of $22 \pm 2 \text{ s}^{-1}$ (s.d.) and a slow rate of $8 \pm 1 \text{ s}^{-1}$ (s.d.). The fast rate in the dwell time rationalizes the fact that many of the steps observed in Figure 4.5a appear as multiples of 2.5-bp since this rate indicates that many of the 2.5-bp dwells will be faster than our measurement dead-time, $\sim 20 \text{ ms}$.

We can make this observation quantitative by investigating the step size distribution determined from the *t*-test step finder. This distribution, Figure 4.6a, shows a clear peak at $2.48 \pm 0.03 \text{ bp}$ (s.e.m.), confirming the periodicity in the PWD. It also has a broad tail representing the many steps observed to be multiples of $\sim 2.5 \text{ bp}$. If our *t*-test analysis misses dwells, because they are shorter than the dead time of the measurement, for example, then we would predict that the step finder would identify a fraction of steps that are integer multiples of the fundamental step size. If the only events that are missed come from dwells that are shorter than our dwell time, we can predict the relative frequency of each higher order step size.

Quantitatively, we would predict that the step size distribution should be described by a series of Gaussian distributions of equal width, σ , separated by integer multiples of a fundamental step size, d , and with geometrically decreasing amplitude p , where p is the probability of missing a single 2.5-bp dwell. (The amplitudes decrease geometrically because missing two 2.5-bp dwells is required to produce a 7.5-bp step, which should occur with a probability p^2). Mathematically, the probability of observing a step size of x is:

$$p(x) = A \left(e^{-(x-d)^2/2\sigma^2} + pe^{-(x-2d)^2/2\sigma^2} + p^2 e^{-(x-3d)^2/2\sigma^2} + p^3 e^{-(x-4d)^2/2\sigma^2} \right) \quad (4.3)$$

where A is an arbitrary normalization constant related to the total number of counts in the distribution.

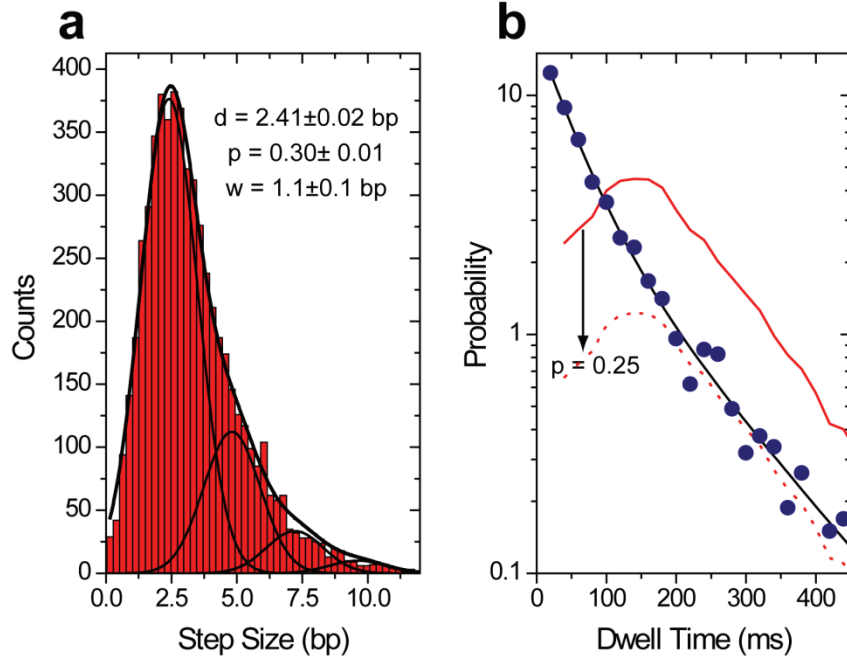


Figure 4.6. Additional 2.5-bp Analysis

(a) Step size histogram for the high force stepping data derived from the *t*-test analysis ($N=5,754$.) This distribution has a peak at 2.48 ± 0.03 bp (s.e.m.) and is well described by the sum of four Gaussians equally spaced by a step size d , with equal widths w , and with geometrically decreasing amplitude p . The step size derived from this fit is consistent with a step size inferred from Figure 4.5b and the amplitude is consistent with the kinetics observed in Figure 4.5c and the dead-time of the measurement, 20 ms. Error bars are the standard deviation. (b) The dwell time distribution measured for the 2.5-bp steps at high external force, 250 μ M [ATP], and an 80% D₂O packaging buffer is plotted in blue circles with the bi-exponential fit to this distribution in black. Plotted in red is the dwell time distribution observed for the 10-bp bursts under the same packaging conditions but low external force. See Figure 4.9. The dashed line is this distribution scaled by 0.25, a value consistent with one out of four steps having dwell time distributions drawn from the peaked distribution seen in solid red. Reproduced with permission from Ref. (20), Macmillan publishers Ltd: Nature © 2009.

Fitting Eq. (4.3) to the step size distribution in Figure 4.6a produces a step size, d , of 2.41 ± 0.02 bp, a width, σ , of 1.1 ± 0.1 bp and a probability of missing a dwell, p , of

0.30 ± 0.01 (all error bars are standard deviations). The step size and width are remarkably consistent with the values determined independently from the PWD in Figure 4.5b. Moreover, the predicted probability of missing a given dwell given the kinetics observed in Figure 4.5c is $p = \int_0^{t_0} k e^{-kt} dt = 1 - e^{-kt_0} \approx 0.35$ where t_0 is the dead-time of the *t*-test step finder, 20 ms, and k is the exponential decay rate, 22 s^{-1} . Thus, the measured value of p , 0.3, is remarkably consistent with the predicted value from the observed kinetics. This analysis indicates that the step size distribution, the measured PWD, and the measured dwell time distribution are all internally consistent, lending significant support to these measurements.

4.3.3: The Dwell-Burst Structure is Maintained at High Force

If the burst structure is maintained at high force, then one would expect that the dwell before every fourth 2.5-bp step would be distributed via a distinct dwell time distribution. And, since the dwell before the 10-bp burst involves many kinetic events that do not generate motion of the DNA, it should be largely insensitive to force, and we would predict that this distribution should be the same distribution observed at low force under the same buffer conditions. Figure 4.6b shows that the long exponential decay observed in the dwell time distribution for the 2.5-bp steps at high force decays with a similar time scale to the distribution measured for the 10-bp dwells under the same experimental conditions but low force. Scaling this distribution by one in four, to represent the expected frequency of a long dwell, remarkably reproduces the amplitude of this tail. Moreover, with this amplitude, the expected peak in the distribution would be obscured by the large fast exponential decay. Taken together, these observations suggest that the

dwell time distribution observed for the 2.5-bp steps is composed of two distributions, a fast exponential distribution and a slow peaked distribution, with three short dwells for every long dwell. While not conclusive, these arguments strongly suggest that the dwell-burst structure observed at low force is maintained at high force.

4.3.4: 2.5 bp is 2.5 bp

A step size that is a non-integer repeat of the fundamental chemical repeat of the motor substrate has never before been observed and, as we will discuss in detail below, this observation has profound implications for the mechanism of the packaging motor. Thus, it is worth ruling out the possibility that this measured step size is an artifact of either the motor behavior or our measurement.

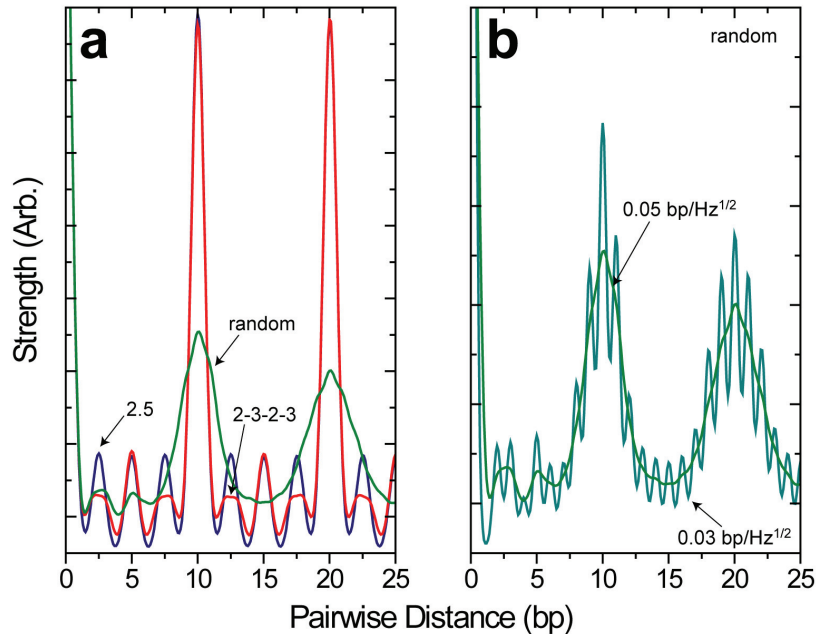


Figure 4.7. PWD for Alternative Stepping Models

- (a) Pairwise distance distributions (PWD) for a model with a uniform 2.5-bp step size (blue), a model in which integer steps of 2 and 3 bp alternate (red), and a model in which 2- or 3-bp steps are taken randomly but with equal probability (green), all calculated from simulated data with Gaussian noise of $0.05 \text{ bp/Hz}^{1/2}$. Plotted in (b) are the PWD for the random model with $0.05 \text{ bp/Hz}^{1/2}$ noise in green or $0.03 \text{ bp/Hz}^{1/2}$ noise in cyan. Reproduced with permission from Ref. (20), Macmillan publishers Ltd: Nature © 2009.

First, one might imagine that the motor takes integer-sized steps but that these steps vary in size, say from 2 to 3 bp, so that the average step size is 2.5 bp. There are two basic models for such a mechanism: a *deterministic model*, in which 3-bp steps always follow 2-bp steps and vice versa, and a *random model*, in which the steps occur in a random order but with equal probability. To test these models, we generated a series of simulated data traces with realistic noise values and performed the same PWD analysis as done in Figure 4.5b. The results are shown in Figure 4.7.

This figure shows that these alternative stepping models predict clear signatures for the PWD which are not observed in Figure 4.5b. For the deterministic model, one expects an oscillating amplitude for each peak, with odd-numbered (1st, 3rd, etc.) peaks smaller than even-numbered peaks (2nd, 4th, etc.). This amplitude modulation arises because every odd-numbered peak is actually the average of two peaks (2 or 3; or 2+3+2=7 and 3+2+3=8) whereas each even-numbered peak represents a single peak size (2+3=5). This type of oscillation is not seen in the higher order peaks in Figure 4.5b, suggesting that the packaging motor does not behave in this fashion. In contrast, Figure 4.7 shows that the signature of a random model is even more distinct. Rather than having an oscillating amplitude, the peaks in the random model eventually disappear, with no higher-order peaks above ~5 bp. Figure 4.7b shows that lowering the noise in the measurement does not allow these peaks to be resolved. These higher-order peaks do not exist because each successive peak involves an increased range of possible step sizes (the third peak can be 2+2+2=6, 2+2+3=7, 3+3+2=8, or 3+3+3=9). Again, this signature is clearly not observed in Figure 4.5b, ruling out a random integer step size model. Finally, it is worth noting that our experimental PWD does not perfectly match the uniform 2.5-

bp step size, rather is shows signs of the “dephasing” of peaks characteristic of a model with a random step size. This suggests that there is some variability in the step size, but that it is less than 0.5-bp. It is worth noting that the rise of DNA is sequence specific with variation on the ~0.1-0.3 bp level (109); thus, such variability in the step size may be expected.

An alternative source of error might be the assumption of B-form helical properties for the DNA being packaged. In particular, one might imagine that within the motor complex or even for a few base pairs in front of it, the DNA might be distorted and the B-form rise per base pair may not be an accurate measure of the distance between adjacent base pairs. However, it turns out that this scenario does not affect our ability to infer the number of base pairs that are inserted into the motor-capsid complex each step.

Figure 4.8 provides an illustration of this point. Imagine that the motor binds the DNA, distorting a constant number of base pairs in front of the motor contact N_d and leaving the remaining N_B base pairs in undistorted B-form. If the motor steps in increments of N_{step} base pairs, then the required conformation change of the motor will be $\Delta x' = \beta' N_{step}$, where β' is the average rise of the distorted DNA, an unknown quantity. However, once the motor finishes the step, returning to its original mechanochemical state, by translational symmetry, it must again distort N_d base pairs in front of it, resulting in a loss of N_{step} base pairs from the B-form region of the DNA. The net change for the mechanochemical cycle, the value that determines the observed step size, is N_{step} base pairs of B-form DNA and zero base pairs of the distorted DNA. Thus, the presence of distorted DNA does not affect our ability to infer the number of base pairs of

DNA packaged from the observed extension changes. We are not measuring the distance moved by the motor, but rather the number of B-form base pairs that are removed from the predominantly B-form DNA tether outside of the packaging-motor complex.

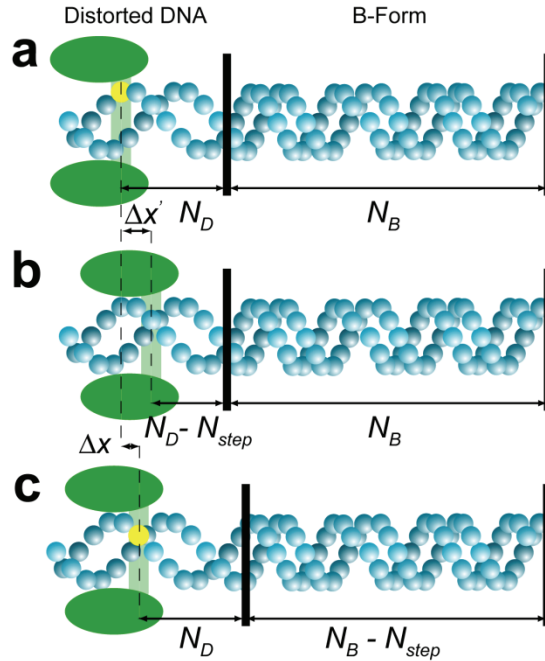


Figure 4.8. DNA Distortions do not Effect Step Size Measurements

(a) A molecular motor (green) engages the DNA at a specific phosphate (yellow) distorting the DNA out of B-form within the motor and potentially for N_D base pairs in front of the motor. (b) When the motor steps forward, its motion $\Delta x'$ is equal to the number of base pairs per step N_{step} times the rise of the distorted DNA, an unknown quantity. (c) Upon reengagement of the next phosphate, the same distortion is introduced locally into the DNA, distorting B-form base pairs to replace the N_{step} distorted base pairs that were translocated. Thus, it is the B-form region of the DNA that is shortened each mechanochemical cycle. The steps observed in (b) and (c) most likely occur simultaneously on the time scale of measurement. Reproduced with permission from Ref. (20), Macmillan publishers Ltd: Nature © 2009.

This argument does not require a discrete number of distorted base pairs of DNA nor a discrete transition from distorted DNA to undistorted DNA. It only requires that the distortion propagates over a distance much smaller than the total length of the DNA tether. Such an assumption is valid for two reasons. The first reason is that our DNA

tethers are not torsionally constrained, so any twist applied by the motor—a non-local deformation—will be dissipated from the molecule much faster than our measurement time, ~ 10 ms. The second reason is that structural evidence suggests distortions to DNA are highly local. For example, the crystal structure of a B-Z DNA transition shows that B-form is reestablished only a few base pairs after the highly distorted Z region (165).

4.3.5: Data Statistics

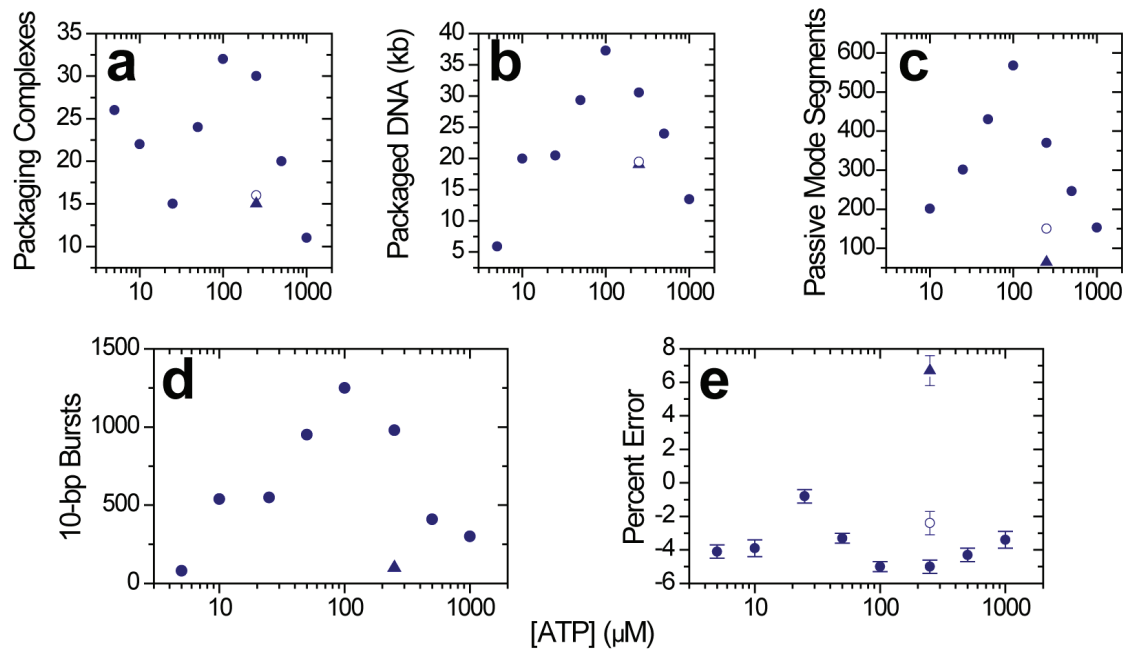


Figure 4.9. General Data Statistics

(a) The number of packaging complexes as a function of [ATP] and under different packaging conditions, low external load (solid circles), high external load (open circles), and low external load but in an 80% D₂O buffer (solid triangles). (b) The total length of packaged DNA under each condition. (c) The total number of semi-passive mode segments under each condition. (d) The number of 10-bp increments used for the distributions in Figure 4.2a and Figure 4.6b. (e) The fractional error estimated from the internal distance standard between semi-passive mode segments. Error bars represent the standard error of the mean. A negative percent error indicates that the passive mode calculation of the contour length from the observed force and extension underestimates the actual contour length change. The systematic error plotted for 5 μM [ATP] was estimated from the average value observed for all other low external force values, except for the outlier at 25 μM , since the low processivity of the motor at this low [ATP] prevented direct estimation. Reproduced with permission from Ref. (20), Macmillan publishers Ltd: Nature © 2009.

For completeness we include here some basic statistics on the data discussed above. Figure 4.9a-d shows the number of packaging complexes, the total length of DNA packaged, the number of semi-passive mode segments, and the number of 10-bp bursts observed as a function of [ATP] and force. Figure 4.9e lists the systematic errors estimated with our internal distance standard (discussed in detail in Chapter 5) as a function of experimental conditions. All reported distances have been corrected by the systematic error at the appropriate conditions. As discussed in the following chapter, the fact that these errors cluster around a value of ~-4% in a H₂O buffer suggests that the systematic error arises in a error in the drag coefficient of the bead, likely the result of errors in the bead radius quoted by the manufacturer. This conjecture is supported by the large discrepancy between the systematic errors in H₂O and D₂O, where there is a large change in the viscosity of the buffer.

4.4: Inter-Subunit Coordination

4.4.1: Dwell-Burst Model

Taken together our results indicate that the individual mechanochemical cycles of the identical subunits of the packaging motor of φ29 are highly coordinated, with the loading of ATP and the translocation of DNA segregated into two distinct phases that comprise the mechanochemical cycle of the entire ring (Figure 4.10). During the initial, “dwell,” phase the DNA is held at constant length while multiple ATPs are loaded, giving this dwell its observed [ATP] dependence (Figure 4.2b). This process is followed by the “burst” phase in which DNA is packaged in four increments of 2.5 bp, totaling 10 bp of

DNA translocated per cycle (Figures 4.1d and 4.5b). Thus, this phase has an average duration that is independent of [ATP] but dependent on force.

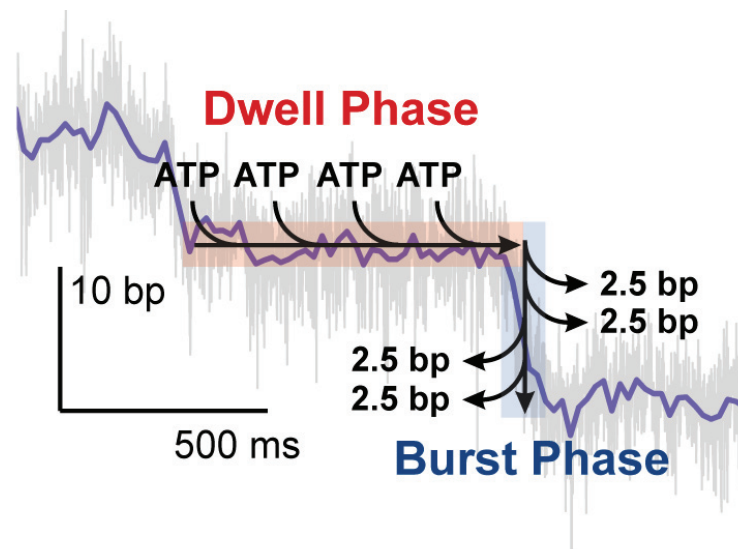


Figure 4.10. Two Phase Model of Packaging

Packaging occurs in two phases. During the dwell phase, the DNA is held at constant length while multiple ATPs load to the ring, likely four. The dwell phase is followed by the burst phase in which DNA is packaged in a burst of four 2.5-bp steps which add to 10 bp. Data displayed are collected at 10 μ M [ATP] and low force. Adapted with permission from Ref. (20), Macmillan publishers Ltd: Nature © 2009.

4.4.2: Four ATPs Bind During the Dwell Phase

The observation of four translocation steps per burst strongly suggests that four ATPs bind to the ring each dwell, one for each of the subsequent steps in the burst phase. This inference is consistent with the measured value of n_{\min} at limiting [ATP] since differences in binding rates will decrease the observed value of n_{\min} from the actual number of binding events (112). (This point will be discussed in greater detail in Chapter 7). It is also consistent with the 10-bp burst size since a single ATP provides insufficient free energy to package 10-bp against the high forces tested previously (1, 58, 59). Moreover, the binding of four ATPs predicts a coupling constant between ATP

consumption and packaging of 2.5 bp/ATP, in reasonable agreement with the ~2 bp/ATP value estimated from bulk measurements (54, 59). The ~25% discrepancy may be explained by additional processes that consume ATP in bulk measurements, such as the repackaging of DNA that slips from the capsid (58, 59). However, it is also possible that a regulatory fifth ATP is bound each cycle and hydrolyzed futilely.

4.4.3: ATP Binding Mechanism

In addition, our data place strict limits on the possible mechanisms by which these ATPs load to the ring. Interestingly, these restrictions arise out of efforts to resolve an apparent contradiction in our data. In our measurements of the mean dwell time as a function of [ATP] (Figure 4.2b), we found that the [ATP] dependence of the mean dwell time was well described by a Hill coefficient of 1, i.e. this data displayed a simple Michaelis-Menten-like [ATP] dependence. However, the requirement that multiple ATPs bind before the formation of product (as required by our n_{\min} measurements) is the classic textbook (128) example of binding cooperativity and is generally expected to produce an [ATP] dependence of the mean dwell time with a Hill coefficient greater than 1. How do we reconcile these contradictory observations? It turns out that by requiring that the ATP bind to the ring not in one but in two kinetic events, that one of these transitions be essentially irreversible, and that the ATPs bind sequentially in time, the binding cooperativity inherent to a scheme with multiple ATP binding events can be effectively hidden, producing an [ATP] dependence of the mean dwell time with a Hill coefficient of 1, consistent with our data. See Figure 4.11.

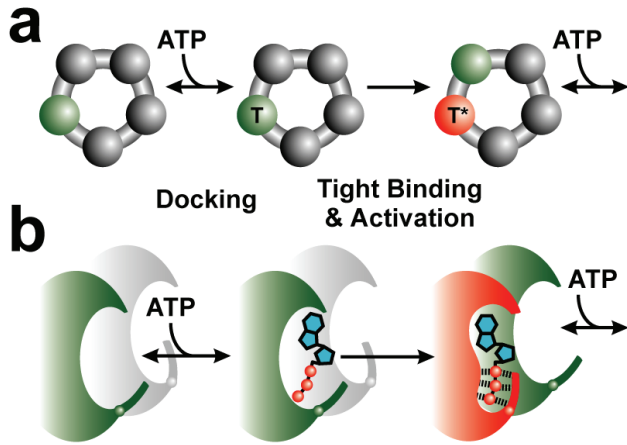


Figure 4.11. Mechanism of ATP Binding

Cartoon depiction of the ATP loading process. (a) ATP binding occurs in two steps, ATP docking (green, T) followed by tight-binding (red, T*). (b) Upon tight-binding of an ATP, the binding pocket of the next subunit, formerly inactive (gray), is activated for docking (green). Thus, only a single subunit is capable of docking ATP at a time. Adapted with permission from Ref. (20), Macmillan publishers Ltd: Nature © 2009.

To illustrate how these restrictions arise, consider the following kinetic scheme for a simplified two binding-pocket system:



where E denotes the empty or apo state, T the docking or loosely bound ATP state, and T^* a second ATP binding state, the “tightly bound” ATP state. The k_i denote the forward rates while the \bar{k}_i denote the reverse rates. The docking rates are expressed as pseudo-first order rates, i.e. $k_1[ATP]$. The mean dwell time for this simplified two binding pocket system can be calculated by a variety of techniques (17, 128), and can be shown to be

$$\langle t \rangle = (b_0 + b_1[ATP] + b_2[ATP]^2) / (a_0[ATP]^2) \quad (4.5)$$

where the individual coefficients, a_i and b_i , are functions of the individual rates. Note that this expression has [ATP] terms to a higher power than 1, and, thus, would display a Hill coefficient greater than 1, as expected for a system which requires the binding of multiple substrates (128).

To understand how the [ATP] dependence can be simplified and the binding cooperativity of the system hidden, it is particularly instructive to consider the coefficient

$$b_0 = \bar{k}_1 \bar{k}_2 (k_4 k_5 + k_5 \bar{k}_3 + \bar{k}_3 \bar{k}_4) \quad (4.6)$$

Remarkably, if b_0 is zero, then the [ATP] dependence of the above expression will simplify to

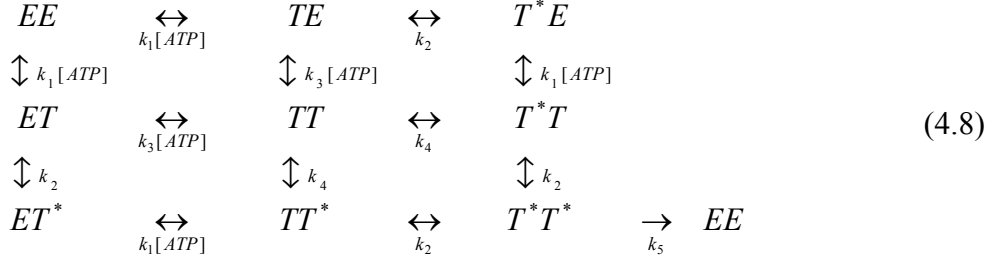
$$\langle t \rangle = (b_1 + b_2[ATP]) / (a_0[ATP]) \quad (4.7)$$

i.e. to a simple Michaelis-Menten-like [ATP] dependence—an [ATP] dependence typical of systems that do not exhibit binding cooperativity. (The specific values of the other parameters are included in the Supporting Text of Ref. (20)).

Note that b_0 will go to zero if one of just two rates is zero, \bar{k}_1 or \bar{k}_2 , i.e. if either the docking of ATP or the second binding transition, the tight binding, is irreversible. By setting one of these rates to zero, the binding of the first ATP is separated from the binding of the second ATP by at least one irreversible transition; thus, the binding events are effectively decoupled. What are the physical implications of setting either of these two rates to zero? First of all, if \bar{k}_1 were zero, this would imply that as soon as an ATP docks to the motor, this ATP is committed to the hydrolysis cycle. This seems unlikely from theoretical studies of similar ATPases (166) and the experimental observation that

ADP readily binds and unbinds from the packaging motor (59). Since we cannot set this rate to zero, we must introduce the second binding state, the tight-binding state, to introduce the necessary irreversible transition. Physically, this choice implies that a single ATP can dock and undock to the motor reversibly, but eventually the catalytic pocket undergoes a second conformational change that is irreversible and which commits the bound ATP to the hydrolysis cycle. Such a tight binding transition has been proposed to explain previous experimental observations (59) and has also been suggested by theoretical studies of ATP binding (166). In particular, these theoretical studies suggest that during the tight binding transition a series of hydrogen bonds form, or “zipper,” around the phosphate backbone of ATP (166). Such an extensive set of hydrogen bonds would provide the necessary free energy to make this transition effectively irreversible. While it is possible that there are additional intermediate kinetic states in the ATP binding process, no additional states are required to resolve and rationalize the apparent contradiction in the data.

However, there is one additional restriction imposed by our data implicit in the model assumed above. In this model, the ATP binding events within the ring occur sequentially in time. In other words, one ATP docks, then tight binds, and only then can the next ATP dock. However, given that the individual subunits are identical, it is unclear that such an assumption is reasonable. Why can’t several subunits be involved in the simultaneous docking of ATP, each docking ATP independently of the binding state of the other subunits? We can relax the assumption that the individual subunits bind ATP in a time-ordered fashion, and, for the sake of argument, consider the following simplified two-pocket system:



Here all of the ATP docking events have a rate of $k_1[ATP]$ and all tight binding transitions have a rate k_2 . All reverse rates (not shown) are again denoted with an overbar. By allowing a second ATP to dock before the first ATP is tightly bound (the TT state), we now permit both subunits to dock ATP independently of one another. To facilitate analysis, we assume different forward rates for these additional docking reactions and tight binding reactions, i.e. $k_3[ATP]$ and k_4 , and for their reverse rates, \bar{k}_3 and \bar{k}_4 . The mean dwell time for this system can again be calculated via some tedious algebra. It is described by the expression

$$\langle t \rangle = (b_0 + b_1[ATP] + b_2[ATP]^2 + b_3[ATP]^3) / (a_2[ATP]^2 + a_3[ATP]^3) \tag{4.9}$$

which again contains terms with [ATP] to a higher power than 1, indicative of binding cooperativity. Inspection of a few coefficients

$$\begin{aligned}
b_0 &= \bar{k}_1 \bar{k}_2 (k_2 k_5 (k_4 + \bar{k}_3) + (k_5 + 2\bar{k}_2)(k_4 \bar{k}_1 + \bar{k}_1 \bar{k}_3 + \bar{k}_1 \bar{k}_4)) \\
b_3 &= k_3 k_1^2 (k_2 (2k_4 + k_5) + (2\bar{k}_2 + k_5)(2k_4 + \bar{k}_4)) \\
a_3 &= 2k_3 k_1^2 k_2 k_4 k_5
\end{aligned} \tag{4.10}$$

reveals that this [ATP] dependence can again be reduced to a simple Michaelis-Menten-like expression by setting just two rate constants to zero, \bar{k}_2 and k_3 . Setting the first rate to zero simply satisfies the tight binding condition discussed above. Setting the second rate to zero, k_3 , effectively prohibits the simultaneous docking of ATP to multiple sites since this is the rate at which the system can dock a second ATP after the first ATP has

docked but before it has been tightly bound. It can be confirmed that such a choice for the rate coefficients is the only way to convert the above expression into a simple Michaelis-Menten-type equation, with a Hill coefficient of 1.

Physically this result implies that the identical subunits within the motor cannot all be active for ATP docking simultaneously. Rather, only a single subunit can be active at a time. And, only after it has committed its bound ATP, can another subunit start the docking process. Given the large free energy change required to make the tight binding transition irreversible, this transition is a likely candidate for the kinetic transition that is responsible for activating another subunit for docking. While our data cannot uniquely determine the order of activation within the subunits, the large conformational changes required for such an activation in combination with the known interactions between adjacent subunits in similar rings (56, 68, 83, 85) suggests that ATP binding occurs in an *ordinal* fashion, proceeding in the two step process depicted in Figure 4.11 in a sequential manner around the ring, as depicted in Figure 4.12.

4.4.4: The Full Mechanochemical Cycle

Figure 4.12 summarizes the kinetic transitions that occur during a complete mechanochemical cycle of the packaging motor. During the binding phase, four ATPs bind to the ring in the two-step process depicted in Figure 4.10. Previous work has shown that the release of phosphate precedes or coincides with translocation (59). Thus, after the ring has bound four ATPs, the burst phase is triggered, the first phosphate is released, and the first 2.5-bp step is taken. The burst phase then proceeds with three additional 2.5-bp steps preceded by three force-dependent micro-dwells.

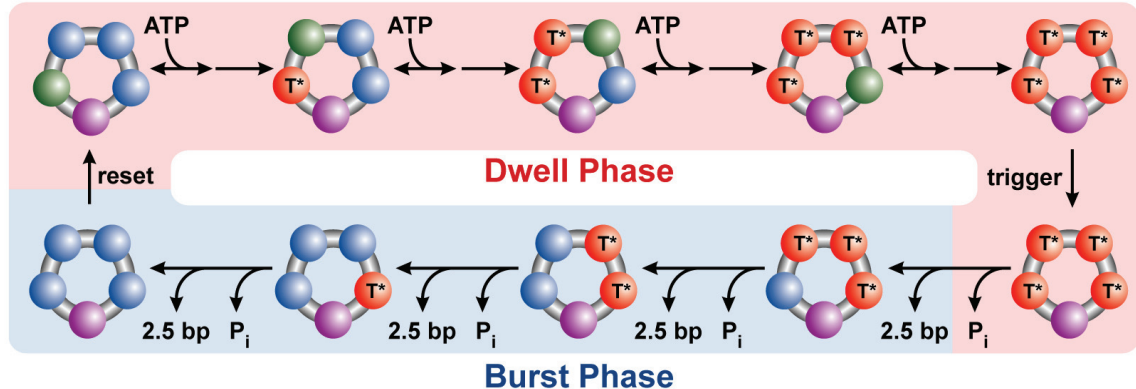


Figure 4.12. The Full Mechanochemical Cycle of the Packaging Motor

Schematic depiction of the full mechanochemical cycle of $\varphi29$. During the burst phase, ADP may remain on the ring (blue) to be released in the dwell phase. One subunit must be distinct from the others (purple) in order to break the symmetry of the motor and generate only 4 steps per cycle. The identity of this subunit may change each cycle. The subunit coloring scheme is the same as in Figure 4.11. Adapted with permission from Ref. (20), Macmillan publishers Ltd: Nature © 2009.

There are several notable kinetic transitions which are not clearly depicted in Figure 4.12. In particular, the exact locations of ATP hydrolysis and ADP release are not uniquely determined by our data. In a simple, single-subunit ATPase, causality orders these events, e.g. hydrolysis must occur *after* ATP binding and *before* ADP release. However, this need not be true between subunits in a multimeric enzyme. For example, one might imagine that each ATP is hydrolyzed immediately before the next subunit binds an ATP, or perhaps, all ATPs are bound and the hydrolyzed together in a cooperative wave of hydrolysis, or, perhaps, each ATP is only hydrolyzed immediately before that subunit generates a step. Moreover, it is possible that hydrolysis occurs asynchronously between the subunits in an uncoordinated fashion. Similar arguments can be made for the location of ADP release. (Methods for discriminating these possibilities will be discussed in Chapter 8).

The number of rate-limiting steps, n_{\min} , at saturating ATP (Figure 4.2c) does provide some clues as to the location of these events. This number indicates that in addition to binding, there must be at least four additional kinetic events that occur during the dwell phase. While it is possible that these events correspond to the ATP tight binding transitions, this seems unlikely since these transitions are believed to occur quite quickly (59). Thus, it is likely that these transitions correspond to either the hydrolysis of four ATPs or the release of four ADPs from the previous cycle or, perhaps, both. These transitions may occur together either as trigger or reset processes (Figure 4.12) or interspersed between ATP binding events.

In addition, the observation that the dwell-burst structure appears to be maintained at high forces argues against a model in which these rate-limiting kinetic events occur in an uncoordinated fashion. For example, imagine a scenario in which ADP release is uncoordinated and corresponds to the rate-limiting events during the dwell under saturating [ATP]. In this scenario, ADP can be released at any point after a given subunit has stepped but must occur before that subunit can bind ATP. At low forces, the burst phase might occur quickly enough that the ADPs remain bound to the ring throughout the burst, and, thus, the release of ADP would typically occur in the next dwell. However, if these events are not coordinated, one might imagine that at high forces, the burst phase could be extended to durations in which ADP release now will occur before the motor is finished stepping. The result would be that the dwell phase would not involve the release of ADP and, thus, would have fewer constituent kinetic states. If these events were rate-limiting under saturating [ATP], then we would expect to see substantial changes to the dwell time distribution under high force. Figure 4.6b suggests that this is not the case,

which in turn suggests that whatever kinetic state is rate-limiting at low forces, under saturating [ATP], also occurs in a coordinated fashion, just as binding and stepping.

4.5: Non-Integer Step Size Models

Our finding that packaging occurs in four 2.5-bp translocation steps raises two notable questions on the motor mechanism. First, how does a dsDNA translocase move in a non-integer number of base pairs? And, second, how is the pentameric symmetry (33, 49, 162) of the motor broken, generating only four steps per cycle? A step size that is a non-integer number of base pairs prohibits any mechanism in which every motor subunit within a *closed, planar* ring makes *specific* and *identical* chemical contacts with one strand of the DNA. Under this constraint, we can speculate on several alternative mechanisms that would produce a 2.5-bp step size and the implications these models have for a pentameric motor.

4.5.1: Closed, Planar Ring

Let us first consider a planar, closed ring. In this case, a non-integer step size could be generated if each subunit is capable of binding two or more alternating chemical moieties, which may or may not be on the same strand. Alternatively, the motor may make no specific contacts, but rather drive translocation via steric interactions, in which case the step size would be set not by the chemical periodicity of the DNA but by the size of the internal conformational changes that generate the power stroke. One example of such a mechanism is depicted in Figure 4.13 where each subunit makes non-specific contacts with the major groove of the DNA. In such a model, generation of four translocation steps requires that one of the five subunits is not equivalent to the other

four, breaking the symmetry of the pentameric ring. Since the nucleotide-free state is disengaged from the DNA (59), one subunit may be required to retain nucleotide at the end of the previous cycle, ensuring that a strong contact with the DNA is maintained while the remaining subunits load ATP during the subsequent dwell phase.

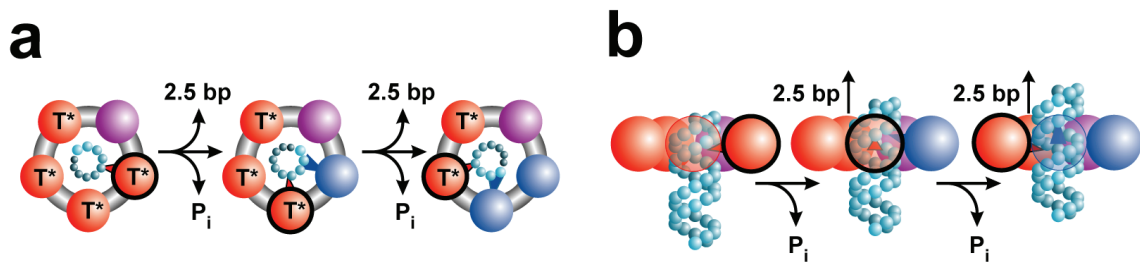


Figure 4.13. A Steric Drive Mechanism

(a) Top view of the packaging motor as DNA is handed from one subunit to the next as 2.5-bp steps are generated. (b) Side view of the packaging motor. If the ring is closed and planar, then the 2.5-bp step size requires that the motor either make multiple chemical contacts with the DNA, set by the local context, or perhaps, non-specific, steric contacts. The subunit color scheme is the same as in Figure 4.12. Adapted with permission from Ref. (20), Macmillan publishers Ltd: Nature © 2009.

4.5.2: Cracked, Dynamic Ring

However, we can require that specific DNA contacts are made by the motor as long as we relax the assumption that the ring is planar. In one such class of models, the *cracked, dynamic ring models*, only a subset of the subunits interact with the DNA and relative motion between these subunits is what drives translocation. Figure 4.14 depicts an example of such a mechanism in which only two subunits make specific contact with the DNA. Translocation is achieved via an “inchworm-like” movement of these two subunits driven by distortions in the ring. One appeal of this mechanism is that because a single specific contact is made with the DNA, it produces an integer burst size, yet because the DNA-binding subunit (the lever in Figure 4.14) is retracted by conformational changes induced into the ring by the other subunits, this burst can be

divided into non-integer steps. Moreover, this model also explains naturally the observation of four steps by a pentameric motor since one subunit interface must bear the accumulated distortion of the other four subunits, perhaps inactivating one of the five binding pockets. The relative motion between adjacent subunits needed to accommodate such a mechanism has been observed in the crystal structures of other ring ATPases (76, 167) but has not been implicated as part of the translocation mechanism (168).

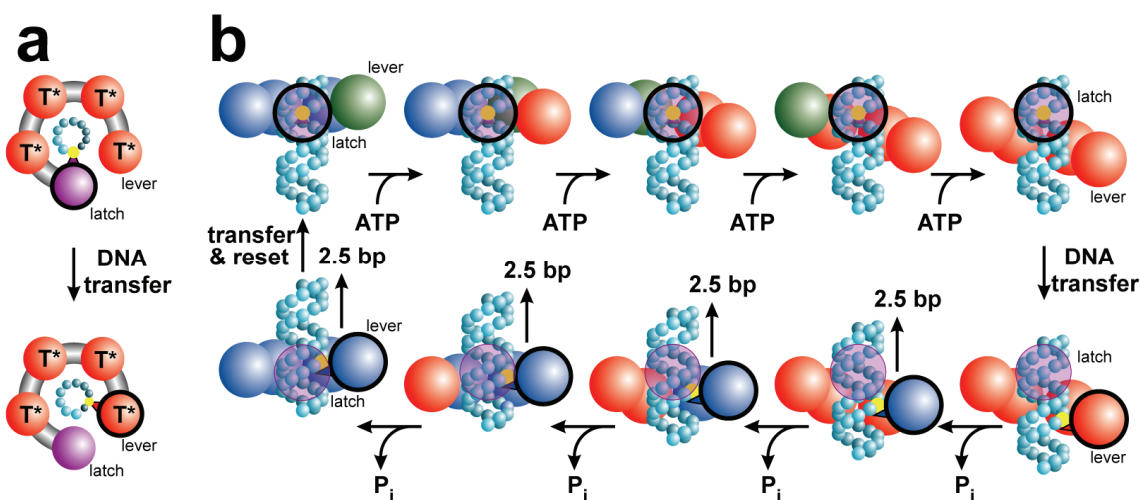


Figure 4.14. Cracked, Dynamic Ring Model

Depiction of a translocation model in which only two subunits contact the DNA (black outline.) (a) Top view. (b) Side view. In such a model, one subunit maintains contact with the DNA (the latch) while the loading of each ATP introduces relative subunit-subunit rotations which distort the ring. This distortion extends one subunit (the lever) along the DNA by ~10 bp. The DNA contact point is then transferred from the latch to the lever, and the release of hydrolysis products relaxes the ring, retracting the lever and the DNA. The DNA contact is then transferred back to the latch, the ring resets, and the cycle begins again. Because there are four subunits, the ring is retracted in four steps, dividing a 10-bp step into four ~2.5-bp substeps. The subunit color scheme is the same as in Figure 4. Adapted with permission from Ref. (20), Macmillan publishers Ltd: Nature © 2009.

4.5.3: Pitched, Static Ring

Finally, there is one additional class of model which can produce a non-integer step size. In this class of models, we again relax the assumption that the motor forms a symmetric

planar ring. However, in contrast to the cracked, dynamic ring model, in this model, *the static, pitched ring*, the motor subunits form a static asymmetric ring in which each subunit is slightly displaced along the axis of the DNA. In this class of model, each of the subunits eventually make contact with the DNA, just as in the steric drive model discussed above; however, since these subunits are displaced with respect to one another they can make *identical* chemical contacts. Thus, the actual “power stroke” of each subunit is a non-integer number of base pairs, yet since the subunits are displaced with respect to one another, these non-integer motions correctly position the DNA in register with the next subunit. For example, Figure 4.15 shows one model in which each subunit packages the DNA in 2.5 bp increments; however, since the subunits are each displaced by ~0.5-bp along the DNA axis with respect to the previous subunit, the subunits can make identical contacts with the DNA every 2 bp.

If the subunits are displaced with respect to one another, how does the motor overcome the necessary small break in the ring that must accumulate with four distorted interfaces? Remarkably, a pitch of 0.5-bp per subunit in a pentameric ring positions the original subunit perfectly in register with the 10th base pair; thus, one could imagine that there is a transfer from the last subunit to the first, which produces no net translocation of the DNA, yet resets the motor such that after one full cycle it is positioned 10 base pairs downstream of where it started (the final step in Figure 4.15b). Again, this relatively small distortion between the first and last subunit in the ring, <1 nm, would naturally explain the presence of only four steps per cycle in a pentameric ring since this large distortion might disrupt the binding pocket between these subunits, abrogating productive catalysis with this pocket. Finally, the degree to which the subunits would have to be

pitched to produce a 0.5-bp augmentation is remarkably small, \sim 1.7 Å. And, provocatively, such asymmetries have been observed for members of the ASCE family. For example, this is roughly the degree to which the DNA binding loops are staggered in the hexameric helicase, BPV E1 (75, 169).

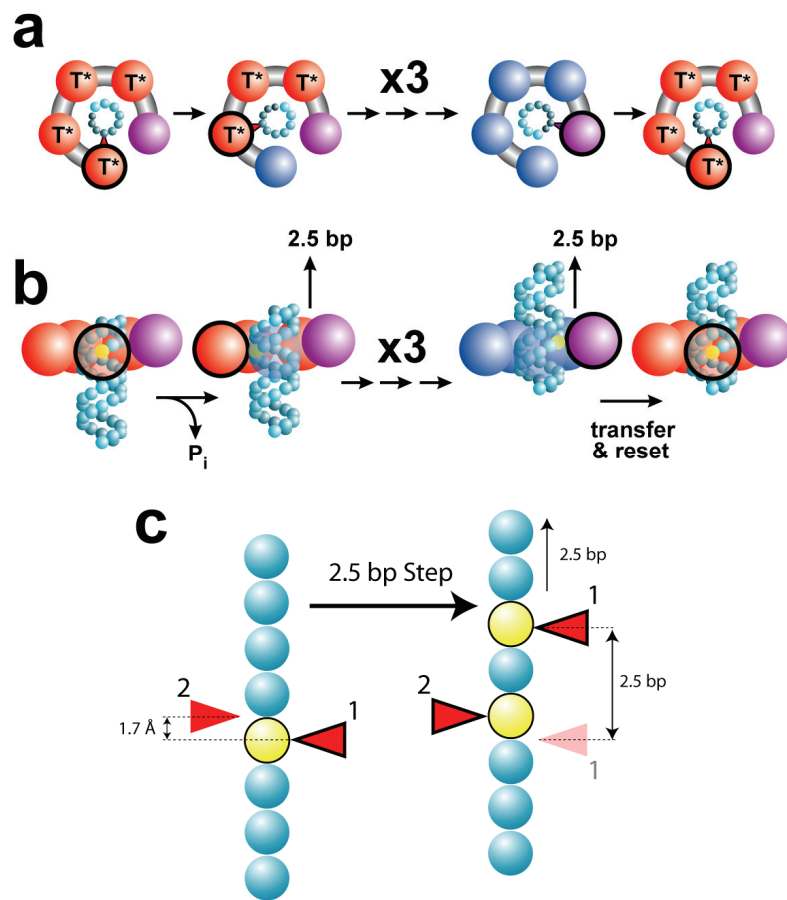


Figure 4.15. Pitched Ring Model

Cartoon depiction of a pitched ring model for a non-integer step size. (a) Top view. (b) Side view. In this model, the ring adopts a static conformation in which each subunit is displaced along the DNA by small amount, giving the ring a slight, 0.5-bp per subunit, pitch. Each subunit interacts with the DNA via the same chemical contacts, generating 2.5-bp power strokes. However, because the next subunit is located 0.5-bp further along the DNA, the contacts are actually separated by 2-bp increments. After four steps, the DNA is perfectly situated for the original subunit to reengage the DNA, completing the 10-bp cycle. (c) Schematic depiction of two subunits interacting (red triangles) with phosphates (blue). Subunit 2 is displaced from subunit 1 by a slight asymmetry, 1.7 Å or \sim 0.5 bp. Subunit 1 interacts with a specific chemical moiety (yellow phosphate), and upon its power stroke moves the DNA 2.5-bp. This positions subunit 2 *in register* with the same chemical group 2 bp downstream.

4.6: Conclusions

We have presented here the first high-resolution measurements of the stepping dynamics of the ring ATPase of the packaging motor of bacteriophage φ 29. Our results indicate a highly coordinated two-phase mechanism in which the binding of ATP and the translocation of DNA by multiple subunits are organized into two distinct and temporally segregated portions of the mechanochemical cycle of the ring. Our observation of a 2.5-bp step size challenges the long-held view that DNA translocation must occur in integer base pair increments, making it necessary to devise new and more complex models for motor-DNA interactions. In addition, while the inter-subunit coordination we observe is reminiscent of aspects of both the concerted-action model of the large tumor antigen of SV40 (80) and the sequential models proposed for the translocases BPV E1, T7 gp4, ϕ 12 P4, *E. coli* Rho, and FtsK (72-77, 79, 160), our mechanism represents a novel type of coordination not previously proposed for ring ATPases. Significantly, while a two-phase mechanism contrasts with these other models, it appears to be consistent with many of the biochemical (72, 73, 79, 160) and structural (74-77, 160) observations made on these related systems. One notable exception is the ClpX protease for which biochemical data clearly suggest a limited degree of subunit coordination (81). However, recent work on a related system, the archaeal MCM, suggests that coordinated systems can take alternative pathways when overcoming functional barriers such as catalytically inactive subunits (82).

Ring ATPases of the ASCE superfamily support a large and remarkably diverse set of cellular functions by drawing upon a comparatively small set of common structural features. Direct measurements of the inter-subunit dynamics in these systems, such as

those presented here, promise to reveal if these diverse cellular functions arise from a similarly small set of common structural dynamics.

Chapter 5. Experimental Methods

There are a variety of experimental methods that go into the successful measurement of the base-pair-scale dynamics of a single packaging motor, in addition to the careful instrumentation described in the previous chapters. In this chapter, we discuss in detail the protocols and methods used for the experiments discussed in this thesis. In the first section, we discuss how the instrument is calibrated, i.e. how raw voltages are converted into meaningful measures of force and distance. In the second section, we discuss how the bacteriophage system is assembled, how it is introduced into the tweezers, and how measurements are conducted. Finally, we finish with a discussion of the different techniques we have used to analyze our data and determine the systematic errors in our measurement. The description of the techniques and methods provided here are taken in part from the main text and supplemental sections of Refs. (16, 19-21) with permission.

5.1: Instrument Calibration

5.1.1: Trap Calibration

For each axis of each trap, there are two quantities that must be calibrated. First, the photodetectors measure a voltage proportional to both the light intensity and the centroid position. To remove the sensitivity to total intensity, we divide this voltage by the voltage proportional to the total light intensity, leaving a dimensionless quantity that measures the deflection of the centroid of the light. This unit-less deflection must be converted into the nanometer displacement of the bead in the optical trap; thus, our first calibration parameter is the conversion ratio α —the number of nanometers of bead motion per deflection or *deflection unit* (DU) measured on the detector. Second, to a good approximation, the potential of the optical trap is harmonic and linear displacements of the trapped bead result in a force proportional to the distance displaced. To convert the calibrated displacement of the bead into an optically applied force, we must also know this proportionality constant, the stiffness of the optical trap, k . These parameters need to be calibrated for each optical trap and each axis, so in practice we calibrate four conversion ratios and four stiffnesses.

The most direct way to calibrate the system is to apply a known, calibrated force to an optically trapped bead, and measure its response. These known forces may be drag forces generated from carefully calibrated fluid flows (92) or even the force required to stretch single DNA molecules (170) or unfold single nucleic acid hairpins (171). Unfortunately, the accuracy of these techniques is limited by the accuracy to which the behavior of the fluid flow or of the biological system is known, which in some cases can be relatively low. We, instead, take advantage of the fact that the thermal forces which

drive diffusion are extremely well understood (96) and use these forces to apply our calibration forces.

The Brownian dynamics of the system vary as a function of the time scale of the measurement; thus, instead of simply measuring the total response of the system to Brownian forces, we measure the full frequency dependence of these fluctuations, the *noise power spectra* (see Section 2.4.11). By fitting these spectra, we can extract our calibration parameters. Extracting high precision fits from noise power spectra is a complicated task which involves attention to a wide variety of details. First, accurate fits require a more complete description of diffusional physics than that provided in Chapter 3, including subtle frequency dependent viscous phenomenon and also inertial effects of both the bead and the fluid it entrains. Second, sampling thermal noise at finite frequencies introduces known artifacts into the spectra that must be incorporated into the fit. Third, the noise in power spectra is exponentially distributed not Gaussian distributed, as is assumed for most non-linear least squares fitting programs. And, finally, it is not uncommon for photodetectors to be partially transparent to the near-IR light used for trapping, resulting in a partial delay in the response of the detector to fast changes in light intensity. These issues have been discussed in detail in Refs. (96, 172-174) and interested readers should consult these papers in addition to the discussion below.

To collect the noise power spectra, we measure the Brownian fluctuations of two optical trapped beads at 62.5 kHz for 10 s. We separate the beads by the full range of the mirror to neglect hydrodynamic coupling (152). These fluctuations are then divided into one hundred 0.1 s bins or one thousand 0.01 s bins, the noise power spectra of each bin is

calculated, and the resulting spectra are averaged together. Binning and averaging reduces the inherent fluctuations in these spectra, permitting more constrained fits at the expense of low frequency fluctuations which contain little information. Moreover, via the central limit theorem, the noise remaining in the average spectra is better approximated by a Gaussian distribution; thus, most non-linear least squares fitting routines can be used to fit this data with minor bias. Figure 5.1 contains sample power spectra.

To fit these spectra, we use a diffusional theory which includes a series of minor physical corrections (96), which are not discussed in Chapter 3. In particular, an oscillating bead entrails a region of fluid surrounding it, forcing this fluid to oscillate with it. The size of this fluid region decreases with increasing frequency with a characteristic frequency captured by the parameter

$$f_v = \frac{\nu}{\pi r^2} \quad (5.1)$$

where ν is the kinematic friction coefficient of water, and r is the radius of the trapped bead. In addition, the volume of fluid entrained by the bead has some mass, and thus, some inertia. An additional frequency parameter

$$f_m = \frac{\gamma}{2\pi} \left(m + 2\pi\rho r^3 / 3 \right)^{-1} \quad (5.2)$$

describes the time-scale over which friction dissipates the energy associated with this mass of moving fluid. Here m is the mass of the bead and ρ is the density of water. For most conditions, these physical phenomena are minor, and the corrections they introduce into the thermal spectra are small. Yet, including their effects can dramatically improve the precision of fits to the thermal spectra (96). Fortunately, these parameters are

completely determined by properties of the system, i.e. viscosity, density, and bead radius, so they need not be added as fitting parameters.

With these corrections the power spectra of an optically trapped bead is described by

$$S(f) = \frac{D}{\pi^2} \frac{1 + (f/f_v)^{1/2}}{\left(f_c - f^{3/2}/f_v^{1/2} - f^2/f_m\right)^2 + \left(f + f^{3/2}/f_v^{1/2}\right)^2}. \quad (5.3)$$

where there are two free parameters: f_c , the corner frequency and D , the diffusion constant (96). We will discuss these parameters in greater detail below. In practice, noise power spectra are always sampled at a finite sampling frequency, f_{samp} . However, the bead physically fluctuates on all time scales, including frequencies faster than what is measured. These faster fluctuations cannot be neglected, rather they show up as noise in the frequency range measured due to a phenomenon known as *aliasing* (96, 150). To address this issue we do not fit our measured spectra with Eq. (5.3), but rather a modified equation that accounts for this aliasing effect. The modified form is generated by the infinite sum

$$S_{fit}(f) = \sum_{i=-n}^n S(f + nf_{samp}). \quad (5.4)$$

In practice, we find that $n=10$ is a reasonable approximation to the infinite sum (96).

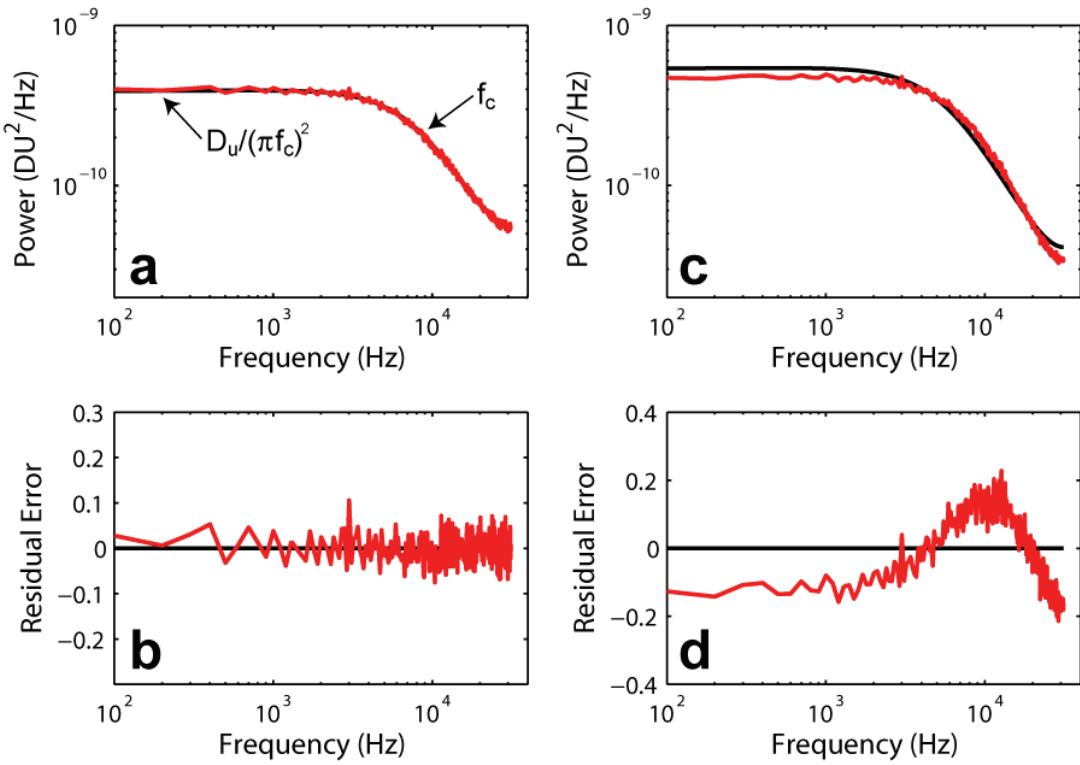


Figure 5.1. Example Power Spectra Fits with Residuals

(a) In red is the average of 1000 power spectra from 10 s of fluctuations of an 860-nm polystyrene bead in a trap formed by the 845-nm laser. In black is the fit to the expected spectra including all of the corrections mentioned. The corner frequency and the uncalibrated diffusion constant are labeled here. (b) The fractional difference between the fit and the spectra in (a). The fact that the residual is flat and distributed around zero indicates that this is an excellent fit to the data. (c) The same spectra and fit but with the 1064-nm laser system. (d) The fractional difference between the fit and the spectra in (c). Here there is a large discrepancy between fit and spectra. This is due to a parasitic filtering effect with the 1064-nm wavelength (172, 174). This problem is fixed by fitting over a smaller frequency range.

Each fit to the power spectra along a single axis returns two fit parameters: the corner frequency of the system, f_c , and the uncalibrated diffusion constant, D_u . See Figure 5.1. The corner frequency is the frequency at which the viscous and elastic responses of the system are equal in magnitude, and it is this frequency that sets the scale at which Brownian fluctuations transition from white noise (independent of frequency) to

red noise (decreasing as $1/f^2$). The corner frequency is determined from the drag coefficient of the bead, $\gamma = 6\pi\eta r$, and the stiffness of the optical trap along that axis, k , via

$$f_c = k/(2\pi\gamma) \quad (5.5)$$

The diffusion constant characterizes the strength of the coupling between the thermal bath and the bead and is determined by

$$D = k_B T / \gamma \quad (5.6)$$

where $k_B T$ is the thermal energy in the bath. The diffusion constant has units of nm²/s; however, the power spectrum of the uncalibrated fluctuations of the bead will not have units of nm; rather, it will have units of uncalibrated deflection (DU). It is the conversion ratio which relates the uncalibrated diffusion constant, D_u , with units of DU²/s to the theoretical value of the diffusion constant via

$$D = \alpha^2 D_u. \quad (5.7)$$

Eqs. (5.5)-(5.7) define three unknowns based on the two parameters determined from fits. To fully determine this system, we must assume one of the unknowns. The obvious candidate is $\gamma = 6\pi\eta r$ since its value is well determined from known quantities, i.e. the viscosity of water and the bead radii determined from the manufacturer⁸. Once γ is assumed the stiffness of the trap can be determined from the fit value of f_c using

$$k = 2\pi\gamma f_c \quad (5.8)$$

and the conversion ratio between DU and nm can be determined by

⁸ In practice, we find that the bead radii are very uniform, varying typically no more than 1-2%. However, the actual value of the bead radii can vary from the manufacturer's value by 5-10%. Thus, it is always important to confirm the assumed drag coefficient with direct measurement, as discussed below.

$$\alpha = \sqrt{\frac{D}{D_u}} = \sqrt{\frac{k_B T}{\gamma D_u}}. \quad (5.9)$$

For the 845-nm system, Figures 5.1a&b indicate that the thermal spectra are well fit with the full hydrodynamic expression with the aliasing corrections, Eqs. (5.3) and (5.4). This result indicates that the detector is capable of accurately measuring fluctuations over the entire frequency range, as has been reported for these detectors (92, 175). However, for the 1064-nm system, minor residuals became apparent when fitting across the full range of the detector. See Figure 3 5.1c&d. This discrepancy arises because the detector cannot respond fast enough to faithfully measure the fastest fluctuations of the system. Such an effect is known as parasitic filtering and is caused by the partial transparency of silicon to this wavelength (172, 174).

To address this problem, we measured the response function of the detector—i.e. its ability to measure fluctuations at different frequencies—for the 1064-nm light. In principle, the measured response function could be used to correct the spectra or, if the physics is well understood, the response function could be modeled, included in the expected shape of the spectra, and determined accurately from fits to the data (172, 174). However, we found that the response function for our detectors could not be accurately modeled and was dependent on too many free parameters—laser power and fluctuation amplitude—to permit correction with previously measured response functions (data not shown). Fortunately, we found that the detectors do respond faithfully over a limited frequency range, < 12 kHz, for all parameter studied. Thus, this problem could be circumvented by simply fitting the spectra over this limited range. For the high force packaging experiments described in Chapter 4 very stiff traps were needed, and the corner frequency was outside of this fitting range. In this case, the trap stiffness was

calibrated by exploiting the known linear relationship between trap stiffness and trapping power and extrapolating the stiffness from measurements of this behavior at low trapping powers and trap stiffnesses.

5.1.2: Video Calibration

The visual image of the sample plane is typically only used to direct the assembly of single molecule experiments and to visually inspect all of the components before measurements are conducted. (Multiple beads may be stuck together—something that can easily be identified by eye.) However, a calibrated video image of the sample plane is needed when calibrating the motion of the steerable mirror or for confirming positional calibrations of the system. For example, the conversion ratio can be directly checked via video microscopy of a bead displaced under force.

We calibrate the video by imaging two different types of calibration grids (16): a 10 μm grid provided with the objective (Nikon, Melville, NY) and a separate 2 μm reticule (Graticules, London) purchased independently. The grids are mounted using the same sample stage used to mount micro-fluidics chambers. The front objective provides uniform illumination while the back objective acts as a normal microscope objective, forming a visible image of the grid. Images can be captured using the National Instruments video card, and the number of pixels per division can be determined. By moving the grids throughout the full visual area of the sample plane, it is possible to place limits on the parallax in the system.

Each distance standard allowed the calibration of the video system to 0.2%. Moreover, the calibrations from each standard agreed to 0.3%, placing a limit on the amount of systematic error associated with the video calibration. Finally, these

calibration values are very sensitive to the relative position of the tube lens and the back objective as well as the position of the correction collar on the objective (a collar used to correct for imperfections in the thickness of cover slips). Thus, once the video system is calibrated, care must be taken not to change these parameters.

5.1.3: Mirror Calibration

In addition to the conversion ratio and the stiffness for each of the axes of each of the traps, it is also necessary to know the relative positions of the two traps. Since only one trap is moved in our setup, we need only calibrate its relative position with respect to the fixed trap. This involves both a slope, α_M —nanometer moved per control voltage—and the mirror voltage at which the two traps are overlapping, V_O , for each axis.

We calibrate the slope of the mirror motion, α_M , by trapping a bead in the movable trap and using video microscopy to follow its position as a function of the voltage measured by the strain gauge on the mirror. Through careful measurement, we routinely determine this slope to $\sim 0.3\%$, a limit largely determined by our error in calibrating the visual system.

We determine the voltage at which the two traps overlap, V_O , by trapping two beads and measuring the mirror voltage which aligns the centers of these beads in one dimension when they are spatially separated in the other dimension. By eye, it is not uncommon to determine the overlap position to better than ~ 40 nm, a value not much worse than the limit of video microscopy. Ultimately, it is this uncertainty in the overlap voltage which limits our ability to determine the *exact* length of a DNA molecule. Thus, if absolute distances are needed for an experiment, better calibration of this number

should be the first improvement made to our calibration protocols. Fortunately, measurements of the step size are inherently a differential measurement, so an uncertainty in the absolute length of the DNA tether has little effect on the uncertainty in the measurements described here.

As we will show below, the mirror calibration, in particular the slope, is crucial in the interpretation of the distance scale in our final data. Since its calibration relies heavily on one method—video microscopy—it may be prone to systematic errors. Thus, to provide an estimate of these systematic errors and to confirm the mirror calibration, we developed a second independent calibration technique. In this technique, we use DNA as a length standard since its length can be determined to the Ångstrom scale simply by specifying its sequence. Four different DNA molecules were created via PCR with approximate lengths of ~1, 2, 3 and 5.6 kb. We then measured the average extension of these molecules at several different forces. In particular, at high forces, >15 pN, the DNA is essentially fully extended, and our measurements are, thus, largely insensitive to the stretch properties of short DNA molecules (176). By measuring the change in mirror position required to fully extend each molecule as a function of the change in molecule length, we could confirm the calibration described above to better than 1%.

5.1.4: Offset Correction

Despite the high degree of polarization correction, the objectives still slightly scramble polarization (177). The result is that a small component of the opposite polarization is present in each trap⁹. These contaminant polarizations can interfere with one another, producing small variations in the centroid position of the light spot as a function of the

⁹ The bleed through intensity from one trap places a limit on this scrambling of less than 2% of the intensity which forms each trap.

trap separation, even when there is no force applied to the beads. To address this issue we measure the centroid position that corresponds to zero applied force for each trap as a function of the separation between the two beads, as seen in Figure 5.2. In practice, these offsets are typically quite small compared to the average deflection of the bead, and are, thus, largely negligible. However, to avoid any potential artifacts in our data, we subtract these position-dependence, zero-force deflections from actual data.

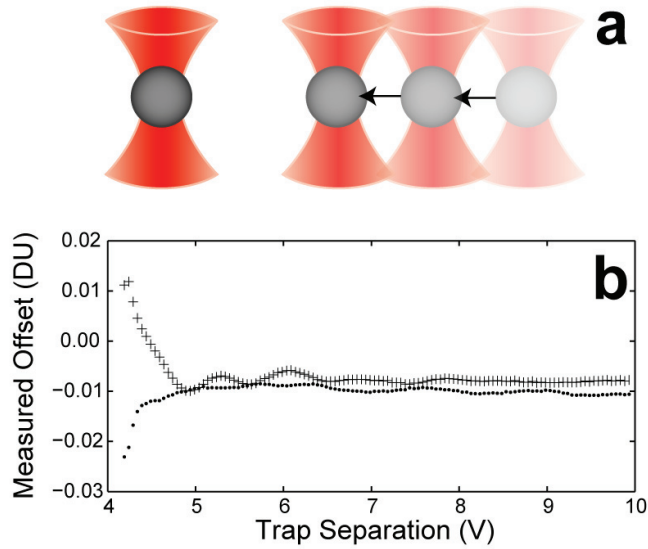


Figure 5.2. Voltage Offset Measurements

(a) Two untethered beads are held in two optical traps and the deflection corresponding to an average zero force is measured for each trap as they are progressively brought closer together. (b) Measured deflection in the x axis for the movable trap (crosses) and the static trap (dots) for different trap separations measured in the strain gauge voltage on the steerable mirror (b). The beads are nearly touching at a separation of ~4V.

These interference patterns can vary as the objective warms during the course of extended trapping sessions. Moreover, the interference pattern is somewhat dependent on the specific beads used for trapping. Thus, to minimize systematic errors, an offset measurement is taken for each set of beads used for experiments. Typically after the experiment is completed, high forces are applied to the tether to break it. Once broken,

the beads are separated, and the offset is measured as in Figure 5.2. While it is possible to eliminate this effect through additional instrumentation (177), we find that measurement and subtraction is quite effective at removing these minor artifacts.

5.1.5: Checking the Drag Coefficient

In the power spectra calibration above, the drag coefficient of the bead is assumed. To measure the actual drag coefficient, we implemented a technique inspired by a method developed by Tolic-Norrellykke et al. (173). In this paper, the authors demonstrate that by shaking their microfluidic chamber at a known frequency and amplitude, they could generate an oscillating fluid flow which would force the bead to oscillate at that frequency. By measuring the response of the bead to the known fluid flow, they could measure the drag coefficient directly, relaxing the need to assume it as discussed above.

However, shaking the microfluidics chamber does not always establish the expected fluid flow, as Tolic-Norrellykke et al. point out (173). To avoid this complication, we instead wiggle our optical trap. From the perspective of the optically trapped bead, this oscillation creates an equivalent fluid flow, without any of the complications associated with shaking the entire chamber. With some algebra it is possible to show that if one wiggles an optical trap at a frequency f , then the bead will respond at that frequency with a theoretical power, P_{th} , set by

$$P_{th}(f) = \frac{\xi^2}{1 + (f_c/f)^2} df \quad (5.10)$$

where ξ is the oscillation amplitude of the trap position, f_c is the corner frequency of the bead, and df corresponds to the discrete frequency interval of the measurement, i.e. the inverse of the total time of the measurement. The power that is actually measured

will be the sum of the power induced by wiggling the trap and the power due to thermal fluctuations (173). Once the latter is removed, the measured power, P_m can be compared to the expected power to determine the conversion ratio, α , via

$$\alpha = \sqrt{P_{th}/P_m}. \quad (5.11)$$

(Again this is because uncalibrated power will be measured in units of DU² while the theoretical power will be in units of nm²). With α constrained via a different measurement, the uncalibrated diffusion constant determined from a fit to the noise power spectra when the bead is not wiggled, as above, can now be used to determine the drag coefficient via

$$\gamma = \frac{k_B T}{\alpha^2 D_u}. \quad (5.12)$$

We performed these measurements on the same beads used for optical trapping measurements. The trap was wiggled at either 10 or 20 Hz and 10 – 100 s of data at 2.5 kHz were collected. During these experiments, we trapped a bead in the movable trap only and the static trap was shuttered. This eliminated modest signals due to the interference between the two traps as discussed above. Various oscillation amplitudes were used, and it was found that larger amplitudes better constrained the measured value of γ with no apparent systematic dependence of the measured γ on the drive amplitude. These measurements suggest that our assumed drag coefficients are systematically larger than the actual drag coefficients by ~5%. Given that the viscosity of water is extremely temperature dependent, changing ~2.5% per °C (178), this discrepancy could be a combination of temperature uncertainties in our sample plane and systematic errors in the bead radii.

Recalibrating a test set of stepping data with the corrected drag coefficients did not produce a change in the size of the observed bursts different from that imposed by the internal distance standard described below (data not shown). This result suggests that the systematic errors in our measurement arise from errors in the assumed drag coefficient.

5.2: Packaging Experiments

5.2.1: Sample Preparation

The components of the *in vitro* bacteriophage φ 29 packaging system—proheads, gp16, and genomic DNA—were isolated as described previously (57) by our collaborators, Shelley Grimes and Paul Jardine in the lab of Dwight Anderson at the University of Minnesota. All other materials—packaging buffers, ATP stocks, genomic digestions, PCR DNA, etc.—were made at Berkeley.

There are several buffers used for packaging experiments. The main buffer is 1/2x TMS (50 mM Tris; 50 mM NaCl; 5 mM MgCl₂, pH 7.8; Sigma Aldrich, St. Louis, MO) and is made in a 10x stock with the appropriate amounts of Trizma base and acid such that the pH needs little adjustment with NaOH or HCl. We also use 10x and 1x TM, another common buffer, which is identical in its composition to TMS but does not include NaCl. In addition, we occasionally use 1x PBS, phosphate-buffered-saline (179). Nucleotide stocks are made directly from dry stocks (Sigma Aldrich, St. Louis, MO) in 100 mM Tris, pH 7.8 with final concentrations set by absorbance measurements. 100 mg/ml stock concentrations of bovine serum albumin (Sigma Aldrich, St. Louis, MO) were made by diluting dry protein into 100 mM Tris, pH 7.8.

Two different DNA templates were used for packaging experiments. The first DNA template used was a 4,277 bp DNA tether PCR amplified from lambda phage DNA (140). One of the PCR primers (IDT, San Jose, CA) contains a 5'-terminal biotin, allowing these molecules to be bound to streptavidin-coated beads. The length of this DNA molecule was chosen to minimize the amount of packaged DNA present inside the capsid during the experiments while maintaining a reasonable length of DNA to insure good stepping statistics for each packaging trace. φ 29 packaging *in vivo* and *in vitro* typically require a covalently-linked, terminal protein, gp3. Thus, assembly procedures that start in the test tube require the DNA to have this terminal protein. To this end, we also generated a second, short DNA template from restriction digestion of genomic DNA, which includes the terminal protein. A ClaI (New England Biolabs, Ipswich, MA) digest produced a left-end fragment, 6,149 bp in length, which is preferentially packaged by φ 29 (23, 180). The restriction overhang left by ClaI was then filled-in with biotinylated nucleotides using the Klenow exo- DNA polymerase (New England Biolabs, Ipswich, MA). The digestion and fill-in reactions were performed according to the instructions from the manufacturer. After heat inactivation of Klenow exo-, the reaction was dialyzed (0.025 μ m; VSWP; Millipore) against 50 mL of 10 mM Tris pH 7.8 for one hour.

We used two types of functionalized polystyrene beads. Streptavidin-coated polystyrene beads, 800 or 860-nm in diameter, are purchased pre-functionalized from the manufacturer (Spherotech, Libertyville, IL). Before use, these beads were washed¹⁰ three times in 1xPBS and then resuspended in 1/2xTMS. Beads coated with antibodies to the major capsid protein, gp8, were made by binding polyclonal antibodies to gp8 to protein-

¹⁰ Washing protocol: 1) 60 uL of beads + 140 uL 1x PBS; 2) spin in a tabletop centrifuge at 10,000 rpm for 1 minute; 3) remove supernatant and discard; 4) add 200 uL 1x PBS and resuspend the beads in the pellet by vortexing for 1 minute; 5) repeat 2 through 4.

G-coated, polystyrene beads, 860-nm in diameter (Spherotech, Libertyville, IL). The protein G-beads were first washed three times in PBS as above. Then resuspended in 60 μ L of 1x PBS with 20 μ L of antibody (\sim 2 μ g/ μ L). The solution was vortexed on low for 2 hours at room temperature to allow the antibodies to bind. Then the beads were washed three more times with 1xPBS and resuspended in 1/2x TMS. Stock solutions of beads were kept at 4 °C for 6 – 12 months.

Before daily use, both streptavidin and antibody coated beads were passivated extensively. 1 μ L of stock bead solution and 1 μ L of 100 mg/mL BSA were added for every 20 μ L of 1/2xTMS. The final solution was then vortexed on high for 30 minutes to promote the separation of aggregated beads. Alternatively, this solution was also ultrasonicated on very low power though this technique required the use of particularly low-power sonicators to maintain the integrity of the beads. Passivation was found to be necessary to prevent nonspecific sticking of the beads and to also improve the quality of the data, presumably by forcing the unbinding of “dirt”—small non-specifically bound filaments and sub-micron objects of unknown origin.

ϕ 29 prohead-motor complexes were prepared in two different fashions depending on the method used to initiate packaging in the tweezers. In the *stalled complex method* of initiation (37, 58, 59), the following components were mixed in order: 9 μ L ddH₂O; 2 μ L 5xTMS; 4 μ L of ClaI digested genomic DNA (300 ng/ μ L); 2 μ L 1/10 dilution of gp16 (\sim 500 ng/ μ L) in 1xTM; and 2 μ L 1/10 dilution of proheads (\sim 4 μ g/ μ L) in 1/2xTMS. This mixture was vortexed briefly, then 1 μ L of 5 mM ATP was added to initiate packaging *in vitro*. Packaging was allowed to proceed for 30-45 s, then 4 μ L of 5 mM ATP- γ -S was added to stall packaging. Packaging complexes prepared in this

fashion can be stored for ~1 day at 4 °C. To prepare these complexes for tweezers work, 1 µL of this stalled-complex mix was added to 10 µL of passivated antibody beads and mixed well. After 30 minutes of incubation at room temperature this mixture was diluted with 1 mL of syringe filtered¹¹ 1/2x TMS. The residual nucleotides from the stall mixture are sufficient to maintain stable complexes at this dilution, and these complexes can be stored on ice for ~1 day. In parallel, 10 µL of passivated streptavidin beads were diluted in 1 mL 1/2x TMS. These 1 mL samples were then loaded into 1 mL syringes and injected directly into the top and bottom microfluidics channels of the sample chamber mounted in the optical tweezers as in Chapter 2.

For the *in situ* method of initiation (60, 61), “prestall” complexes were made by mixing the following components in order: 6 µL ddH₂O; 2 µL 5xTMS; 0.5 µL gp16 (~500 ng/µL); 0.5 µL proheads (~4 µg/µL); and 1 µL mM ATP-γ-S. The solution is then vortexed briefly and incubated on ice or at 4 °C for at least 45 minutes to permit assembly of the motor-prohead complexes. 1 – 2 µL of this prestall mixture was added to 10 µL of the passivated antibody beads. This mixture was then incubated at room temperature for 30 minutes before being diluted with syringe filtered 1 mL 1/2xTMS. Again, the amount of nucleotide present in the initial stall mix is sufficient to keep the complexes stably assembled. Prestall mix can be reused for many days if stored at 4 °C, with the activity typically highest on the second day. In parallel, 10 - 100 pg of 4.2 kb PCR DNA (typically 1 -2 µL of various dilutions) was incubated with passivated streptavidin beads. After 30 minutes, the binding reaction was quenched by dilution with 1 mL of syringe filtered 1/2x TMS. These 1 mL mixtures were then injected into the top

¹¹ We have found that cleanliness is extremely important in high resolution experiments; thus, all materials introduced into the tweezers are syringe filtered. Since one cannot filter a bead solution, we filter the buffer used to dilute the beads to the final working concentration. We use a 0.25 µm syringe filter.

and bottom channels of the microfluidics chamber. The requirement for the terminal protein, gp3, is relaxed in this method of assembly presumably because the local concentration of DNA is much higher when beads are bumped in the tweezers than *in vitro*. See Figure 5.3.

1 mL aliquots of packaging buffer were made from 1/2x TMS supplemented with enough ATP to form the final desired concentration in 1 mL and 0.5 μ L of 100 mg/mL BSA. For experiments conducted in the 1064-nm system, the packaging buffer was supplemented with an oxygen scavenging system similar to those used in single molecule fluorescence experiments (37). The scavenging system consists of 12.5 μ L of 400 mg/ml dextrose, 2 μ L of 50 mg/ml glucose oxidase (dry powder dissolved in 2 parts 1xTMS and 1 part glycerol), and 1 μ L 200 mg/ml catalase (Sigma-Aldrich, St. Louis, MO). 1 mL of packaging buffer was then loaded into a 1 mL syringe with a syringe filter and injected directly into the center channel.

5.2.2: Tweezers Operation

Tether assembly in the tweezers proceeds as illustrated in Figure 5.3. First, the microfluidics channel is moved to bring the traps within \sim 10 μ m of the capillary tube connecting the bottom channel to the middle channel. See Figure 5.3a-A. A small but steady flow through this capillary produces a small flow of beads from the top channel. Once one of these beads is trapped in one of the optical traps, the microfluidics channel is moved to position the traps close to the capillary tube that connected the top and central channels. See Figure 5.3a-B. Again, a small but steady flow produces a constant flow of antibody-prohead-coated beads. When one of these beads is captured in the second trap, the microfluidics chamber is then moved so that the traps are positioned 1-2 mm

upstream from the capillary tubes. See Figure 5.3a-C. We work at this distance to reduce the dilution of the packaging buffer in the central channel due to the small by steady leaks from the top and bottom channels.

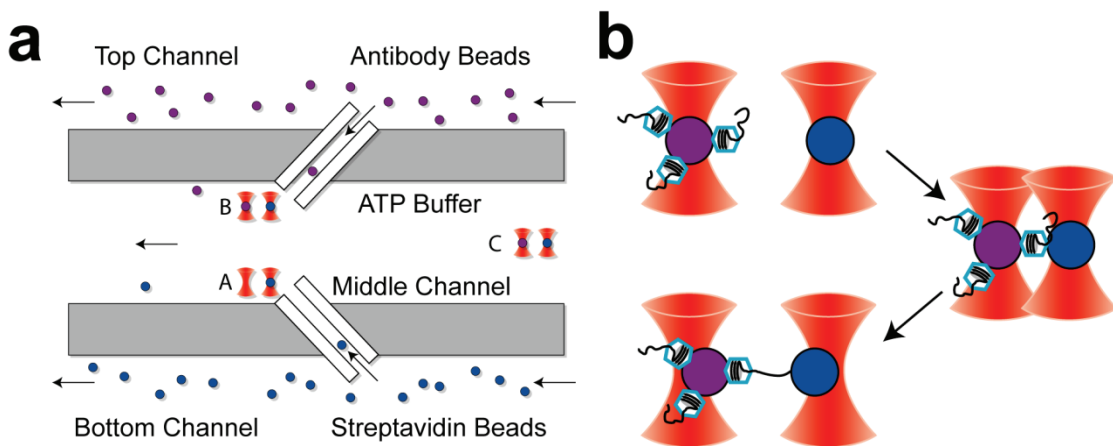


Figure 5.3. Tether Assembly Procedure in the Tweezers

(a) Cartoon diagram of the sample chamber. In the top channel we introduce antibody beads coated with prohead-motor complexes (purple) in a stall buffer. In the bottom channel we introduce streptavidin coated beads (blue) with or without DNA bound depending on the initiation method. We first move the chamber to position the traps near the bottom capillary tube to catch a streptavidin bead (A). Then we move to the top capillary tube to catch an antibody bead (B). Finally, we move upstream of the capillary tubes by 1-2 mm (C) so that minor dilution effects due to the leaks into the central channel can be neglected. (b) Once the two beads are trapped, we physically bump the beads to favor the formation of a tether. Depicted here is the stalled-complex method of initiation, where we are “fishing” for the biotinylated end of the genomic DNA held by a stalled prohead-motor complex. The presence of a tether is indicated by a mutual force between the two beads when the traps are separated. Proheads and DNA are not drawn to scale.

Once the two beads are trapped, the experimenter must move quickly to form a tether since the prohead-motor complexes have a finite lifetime in the packaging buffer in the central channel. To form a tether, with either initiation method, the two beads are physically bumped together. In the case of a stalled complex initiation method, the prohead-motor complex has already started packaging the DNA, so we are “fishing” only for the biotinylated end of this DNA. However, for the *in situ* method of initiation, the

DNA is on one bead while the stalled motor complexes are on the other. In this case, we bring the beads together in the hope that one of the prohead-motor complexes will spontaneously initiate packaging. After anywhere from 5-45 seconds, the beads are separated to determine if a tether has formed. The presence of a tether is indicated by a force exerted between the two beads. See Figure 5.3b.

There are a variety of methods for establishing steady fluid flows in the microfluidics chambers that we use. The more complicated methods involve extensive automated pneumatic systems to vary pressure on different fluid reservoirs (147). While we have constructed such a system for our instrument, we find that in practice there are much simpler methods for establishing constant fluid flows. For example, the most common method that we have used is to rely on the residual amount of compression that remains on a 1 mL syringe after ~100 μ L of fluid has been injected into the system. This residual compression maintains a small positive pressure on the contents of the syringes that supply the beads to the top and bottom channels. To reduce the background flow in the central channel, we physically clamp the PE20 tubing after the syringe containing the packaging buffer to prevent fluid flow through this tube. By then lowering the end of the waste tubing for the central channel with respect to the waste tubes for the top and bottom channel, we can magnify the pressure differences and establish a small but steady flow through the top and bottom capillary tubes into the central channel and out the waste tube for this channel. In practice, the residual pressure generated by compression of the syringe can establish fluid flows that last 30 minutes to an hour, more than enough time to conduct several packaging experiments.

5.2.3: Semi-Passive Mode

If the tether is being actively packaged, then the DNA between the two beads will shorten, pulling the beads further out of the traps and increasing the optically applied force. If nothing is done, the bacteriophage will continue to package, increasing the force, until either the tether breaks or the bacteriophage physically pulls the beads out of the optical trap. One common solution to this problem is to operate an optical tweezers in a “force-feedback” mode (58, 59, 158), in which the instrument dynamically moves either the trap or a fixed attachment point so that the optically applied force remains constant. Unless this feedback is instantaneous (135), or at least much faster than relevant dynamics of this system, active feedback will introduce additional noise. Moreover, especially slow feedback can actually mask fast motions of the biological system since the feedback acts as a low-pass filter.

To avoid these problems, we have developed a different mode of operation which we term “semi-passive” mode. See Figure 5.4 and also Figure 5.5 below. During a measurement, the traps are held at fixed separation while the tether is packaged. This is a “passive” mode measurement because the optical tweezers act passively, doing nothing to respond to the dynamics of the system. In such a measurement, the resolution is limited only by the thermal fluctuations discussed in Chapter 2, and the response of the system to fast biological motions is set by the diffusional physics of the bead-DNA-bead system—the fundamental “speed limit” of an optical tweezers measurement.

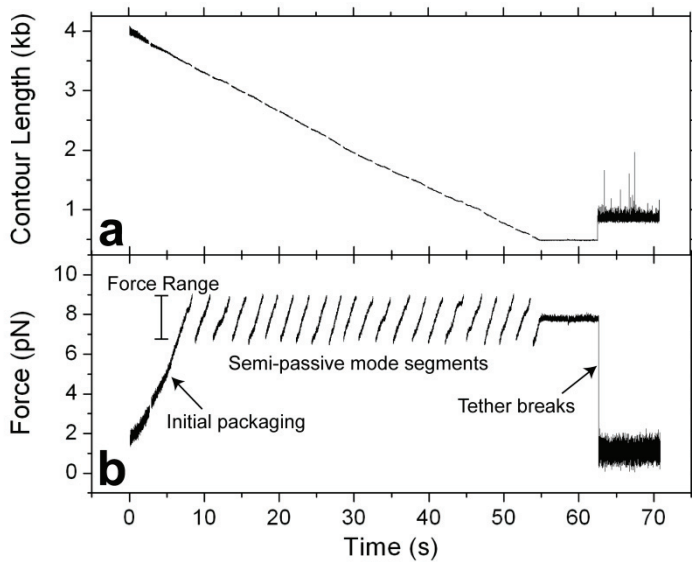


Figure 5.4. Semi-Passive Mode

(a) Contour length as a function of time as a single bacteriophage packages a 4.2 kb DNA tether. (b) Force as a function of time. As the DNA is packaged, the tension increases. Once it reaches a constant value, ~9 pN, the traps are moved together to lower the force, ~7 pN. The process repeats until the tether is completely packaged. Data during the period when one trap is moving are not analyzed.

Because the traps are held at a fixed separation, packaging of the DNA tether will increase the tension on the DNA tether. To maintain this tension in a preset force window, we simply move the traps together whenever the tension crosses an upper threshold. The distance moved by the traps is adjusted dynamically to bring the force to a preset lower threshold. Once the tension reaches the lower threshold, the separation of the traps is again fixed, and another “passive” measurement is conducted. Because we monitor the exact separation of the traps dynamically during a measurement, it is trivial to separate these “passive” and “active” regions in the data saved to disk. Regions where one trap is moving are discarded from subsequent analysis.

For all low force experiments, the semi-passive mode force range was 6 to 9 pN. Because the distance to transition state is small in $\varphi 29$, ~1 Å (59), the effect of this

varying force on the velocity of the system is minor, $\sim\pm 5\%$. For the high force data, the force range was 33 to 46 pN. This wider range was necessary to keep the run lengths of each passive mode segment long enough to perform proper pairwise distance analysis (as described below). However, due to the exponential nature of the force dependence, the expected velocity variation is again small, $\sim\pm 5\%$.

5.3: Data Analysis

5.3.1: Calculation of DNA Contour Length

To calculate the contour length of the DNA remaining between the beads, we must determine the average tension on the molecule, F , and its average end-to-end extension ξ . With these values, we can then use a model for the elasticity of the DNA to determine what contour length, L , would correspond to the measured values of F and ξ . In terms of the explicit raw deflections and calibration values discussed above the extension of the DNA molecule is determined via

$$\xi = \alpha_M(V_M - V_O) - r_1 - r_2 - \alpha_1(D_1 - O_1(V_M)) + \alpha_2(D_2 - O_2(V_M)) \quad (5.13)$$

where α_M is the mirror conversion ratio which converts the command voltage V_M into the position in nanometers, V_O is the voltage at which the traps overlap (Section 5.1.3), $r_{1,2}$ are the radii of the two beads, $\alpha_{1,2}$ is the conversion ratios for the first and second traps, $D_{1,2}$ is the measured deflection of the bead from the center of its trap (Section 5.1.1), and $O_{1,2}(V_M)$ are the measured offset deflections as a function of the mirror command voltage (Section 5.1.4). The final two terms represent the difference between the displacements of the two beads, i.e. the *differential coordinate* discussed in Chapter 3.

Thus, as long as the traps are nearly equal in stiffness and the beads are nearly equal in diameter, as is in the case for all of our experiments, our measured extension will be estimated by the optimal coordinate, and the resolution of our experiment will be maximized.

To determine the average tension on the molecule, we average the optical force experienced by each optically trapped bead. Again in explicit terms this is

$$F = \frac{1}{2} \{k_1 \alpha_1 (D_1 - O_1(V_M)) - k_2 \alpha_2 (D_2 - O_2(V_M))\} \quad (5.14)$$

where $k_{1,2}$ are the trap stiffnesses determined from the fits to the noise power spectra (Section 5.1.1). Eqs. (5.13) and (5.14) have been suppressed to a single dimension here for clarity. In practice, we work only along a single optical axis, so this approximation is appropriate.

With the extension of the molecule and the applied tension, one can now use the known stretch properties of DNA to determine the exact length of DNA between the two beads. It has been widely accepted that the elastic properties of DNA are well described by the extensible-worm-like chain model (100),

$$F = \frac{k_B T}{4P} \left(\frac{1}{(1 - \xi/L + F/S)^2} - 1 + 4(\xi/L - F/S) \right) \quad (5.15)$$

where F is the tension on the DNA molecule, ξ is its extensions, L is its contour length, and P and S are parameters which describe its stretch properties. P is the persistence length, ~ 53 nm (65, 97-99, 101, 181), which determines the entropic response to force, and S is the stretch modulus, ~ 1200 pN (181), which determines the enthalpic response to force, i.e. the amount the contour length, L , stretches under force.

For every force, F , and extension, ξ , Eq. (5.15) defines a unique contour length, L . In practice, it is possible to invert Eq. (5.15) numerically to determine L . While this calculation is straight-forward, it is slow, and converting large amounts of calibrated, 2.5 kHz data can take a significant amount of time, \sim hours. However, we have discovered that there are analytical solutions to this process which allow calculations to be done much more quickly, \sim minutes. In particular, one can show that the inextensible-worm-like-chain model,

$$F(u) = \frac{k_B T}{4P} \left(\frac{1}{(1 - \xi/L)^2} - 1 + 4 \frac{\xi}{L} \right), \quad (5.16)$$

determines a cubic polynomial, whose roots provide a unique solution to the inversion problem. The solution to the roots of a cubic equation are standard (182) and with some manipulation one can show that

$$\frac{\xi}{L} = 1 + \frac{1}{m \cos(q/3 + s 2\pi/3)} + \frac{F}{S} \quad (5.17)$$

where

$$a = -4 \left(F \frac{P}{k_B T} - \frac{3}{4} \right), \quad b = 4, \quad m = 2\sqrt{-a/3}, \quad q = \arccos \left(3 \frac{b}{m a} \right), \quad \text{and} \quad s = \begin{cases} 1 & a \leq 0 \\ -1 & a > 0 \end{cases}. \quad (5.18)$$

The first two terms in Eq. (5.17) are the solution to the inverse problem while the final term is the standard correction to the inextensible worm-like chain model to allow for the slight extensibility of the contour length over the typical force ranges probed (65, 100). The sign term, s , determines which of the two solutions is valid, depending on the value of the force. Contour length can be calculated quickly using Eq. (5.17) by simply dividing the measured extension by Eq. (5.17) evaluated at the measured force.

In this calculation, contour length has units of nanometers. However, it is typically more useful to think of the number of base pairs remaining in the DNA tether, so we often divide this length by the average distance along the contour length between adjacent base pairs in B-form dsDNA, 3.4 Å/bp (109).

5.3.2: Internal Distance Standard

A semi-passive mode, as shown in Figures 5.4 and 5.5, provides a means by which the above contour length calculation can be checked. In an “active” mode measurement the separation of the system is controlled dynamically to maintain a constant optically applied force (158). In such a measurement, the packaged contour length is determined directly from this change in separation and the elastic behavior of the tether at the known force. In a “passive” mode measurement, in which the trap separation is constant, the contour length is calculated from the change in displacement of each bead, the force change, the change in the absolute extension of the molecule, and the elastic behavior of the tether. Thus, the passive measurement, since it depends on many more parameters, is much more sensitive to calibration errors than an active mode measurement. However, since each packaging segment in a semi-passive mode measurement will pass through the same optically applied tensions as the previous segment, effectively a series of two point active mode measurements are embedded in our data. And, by comparing the contour length calculated in passive mode to that calculated using these two point active mode measurements, we can estimate the systematic errors in our passive mode measurements.

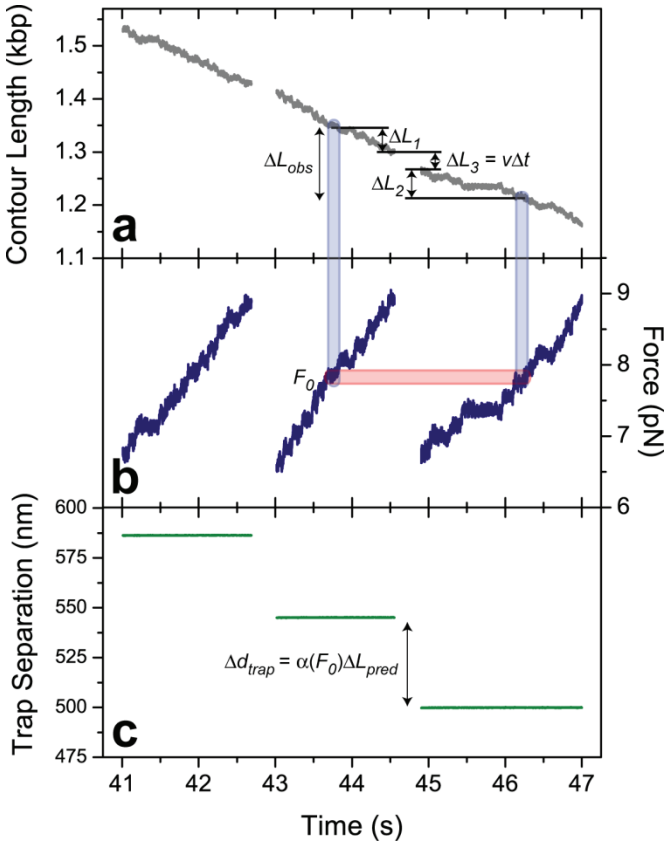


Figure 5.5. Internal Distance Standard

(a) Contour length versus time in semi-passive mode. (b) Force versus time for the same data as in (a). (c) Trap separation versus time for the data in (a). Note that at some point adjacent “semi-passive” mode segments pass through the same force, F_0 . At this point in time, the beads are displaced identical amounts out of the traps and the same tension is applied to the tether; thus, any errors in these quantities will be common to the two systems. Moreover, at this point in time the difference in contour length packaged must be related to the distance between the trap separations in a simple fashion. Thus, we can check the calibration of “passive” mode data by adding the contour lengths of DNA packaged between these two times and comparing this to the distance between the two trap positions. Reproduced with permission from Ref. (20), Macmillan publishers Ltd: Nature © 2009.

As shown in Figure 5.5, the observed change in contour length ΔL_{obs} between the points at which the applied tension reaches a value F_0 in two adjacent passive mode segments is determined by adding three contour length changes: ΔL_1 , the observed contour length change from the force set point to the end of the packaging segment; ΔL_2 , the observed contour length from the beginning of the next segment to the contour length

at which the tension reaches the same force value; and ΔL_3 , the contour length packaged during the reset time, Δt , estimated from the observed velocity of the initial segment, i.e. $\Delta L_3 = v\Delta t$. This sum, reflecting contour lengths calculated in the passive mode fashion, should be equal to the contour length change ΔL_{pred} predicted from the change in trap separation Δd between segments, which is calculated directly via $\Delta L_{pred} = \Delta d/\alpha(F_0)$. $\alpha(F_0)$ is the ratio of the extension to the contour length at the force F_0 calculated from the extensible-worm-like-chain model. See Eq. (5.17). The relative error between these values is calculated by $\delta = (\Delta L_{obs} - \Delta L_{pred})/\Delta L_{pred}$.

Because the motion of the steerable mirror is calibrated to <1% and stable to < 1 Å (see above and Chapter 2) and errors in the force result in minor errors in the parameter $\alpha(F_0)$ for forces above ~6 pN (at 6 pN a 10% error in the force results in <1% error in the value $\alpha(F_0)$), the predicted contour length can be determined with very high precision and accuracy, ~1%. In practice, stochastic errors in ΔL_{obs} are much larger than 1%; however, since the measured value of δ for each semi-passive mode segment is largely independent of the contour length of DNA packaged (data not shown), the values of δ from all packaging segments under a given set of conditions are averaged to produce an estimate of systematic errors. See Figure 5.6 for an example of this calculation for all data collected under 100 μM [ATP] and low forces.

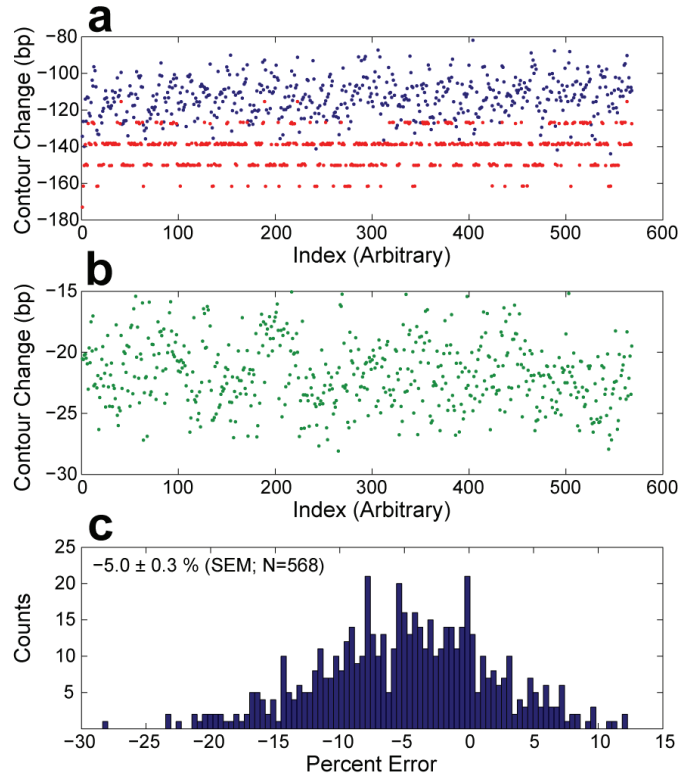


Figure 5.6. Measurement of Systematic Error

(a) Measured contour length ($\Delta L_1 + \Delta L_2$) and predicted contour length (ΔL_{pred}) from the measured trap separation (red) for all semi-passive mode segments collected at low force and 100 μM [ATP]. The index corresponds to the order in which the semi-passive mode was analyzed and is arbitrary. (b) Estimated contour length missed during the reset time calculated from the average velocity of the previous segment (ΔL_3). (c) Histogram of the measured percent error [(predicted-measured)/predicted]. While this distribution is broad due to the large noise inherent in these measurements, the standard error of the mean is quite low, so the mean is very well determined, $-5.0 \pm 0.3\%$. Negative contour change corresponds to the decrease in contour length that occurs during packaging.

The systematic error produced in this fashion was used to correct all reported distance values in Chapter 4. Moreover, given the unexpected step size measurements reported in this Chapter, a firm technique for estimating the systematic error in our measurement was absolutely necessary. Remarkably, rather than shifting our measurements away from 2.5-bp, these corrections actually brought our measurements in better agreement with this value. Similarly, our estimate for the burst size was 9.6 ± 0.2

bp before correction. The stochastic error on this value would have indicated that the motor also has a burst size that is a non-integer number of base pairs. However, by including the corrections due to our systematic errors, the burst size was shifted to 10.0 ± 0.2 bp, a value statistically consistent with an integer number of base pairs. It is clear that the distinction between a burst size that is an integer number of base pairs and one that is not has profound mechanistic implications for the packaging motor. This example should only reemphasize the need for methods for accurately calibrating an optical tweezers. While decidedly less exciting or flashy, these techniques are crucial if high resolution measurements are to be as informative as they can be.

5.3.3: Pairwise Distance Distributions

The objective of the high resolution optical tweezers studies described here is to observe the discrete steps of the packaging motor. To this end, it is extremely useful to have an objective measure of the presence of steps. One such measure is the pairwise distance distribution (PWD) or periodogram (183-186). This distribution is the probability distribution of observing a given spatial distance between any two points in a data set. If there is an underlying spatial periodicity in the data, due to the presence of steps of uniform size, then one would expect that certain inter-point distances would be more probable than others, and there should be peaks in the distribution. See Figures 3.7, 4.1, 4.5, and 5.7 below.

To calculate this distribution, we first compute a histogram of spatial positions with bins of uniform size on data that has been averaged with a sliding boxcar filter. Filtering removes extraneous noise, sharpening the histograms. Moreover, by using a sliding boxcar and not decimating this data, correlated data are left in the histogram,

effectively smoothing this distribution. A Fourier transform of this histogram is then calculated. An inverse Fourier transform of the power in the original transformation yields the autocorrelation function, via the Weiner-Khinchin theorem (150). While not obvious, it turns out that this autocorrelation is identical to the histogram of the distances between every two points (186). To summarize the mathematically operations, if $p(d)$ is the spatial histogram of a filtered stepping trace, then the PWD is

$$PWD(x) = \mathfrak{I}^{-1}(\mathfrak{I}(p)^2) \quad (5.19)$$

where \mathfrak{I} represents the Fourier transform and \mathfrak{I}^{-1} the inverse transform.

The pairwise distributions for single semi-passive mode segments are often quite noisy with peaks dominated by the distance between the steps with the largest average duration. Thus, to produce clear estimators of the periodicity in the data, we average the PWD from a selection of passive mode segments. The PWD reported in the previous chapter represented the average of the best 50% of the semi-passive mode collected under each experimental condition. (We will formally define “best” below).

For the low force data, we used a boxcar filter of 50 Hz and a bin size for the positional histogram of 0.25-bp. Before averaging, we normalized each PWD by the total counts and subtracted the mean. For high force data, the PWD was calculated for 50-bp windows of each passive mode segment. Contour length data were again boxcar-filtered to 50 Hz, a position histogram was calculated with 0.1-bp bins, and the autocorrelation was calculated. Each distribution was normalized as above. The 50-bp window was shifted by 25 bp to insure that all portions of each passive mode segment were included in this calculation.

The presence of peaks in an average PWD is an objective measure of the presence of steps in noisy data. However, we can also extract information about the size of these steps by measuring the periodicity in these peaks. The most common method to determine this spatial periodicity is to perform a spatial Fourier transform and use peaks in this spectra to determine the spatial periodicity in the data (132, 186). However, in our experience, this technique is quite limited when the length of the PWD is only a few times the fundamental step size. The reason is that the distance between points in a discrete Fourier transform is determined by the length of the PWD (150). For example, if a PWD is 50-bp long, then the points in the Fourier transform will be separated by $1/50 \text{ bp}^{-1}$. A step size of 10-bp will produce a peak at 0.1 bp^{-1} , and the two adjacent points in the power spectra will be at $1/10 \pm 1/50 \text{ bp}^{-1}$. These two points, 0.12 and 0.08 bp^{-1} correspond to step sizes of 8.3 and 12.5 bp, respectively; thus, the discrete nature of the distribution implies that the uncertainty in positioning this peak will be $\sim \pm 2\text{bp}$ when estimated from the position and width of the spectral density. This is remarkably large when compared to the fact that the PWD will have a spacing equal to the histogram spacing, 0.25-bp for the low force data in Chapter 4. This represents an inherent limitation of the power spectra method for determining spatial periodicity. This limitation is often addressed by padding data or interpolating between points in the discrete spectra (132). However, this adds only the appearance of new information to the spectra; thus, these approaches are at best deceptive and at worst dishonest.

We take a different approach. We estimate the underlying periodicity in our PWD by finding the peak position for each of the peaks in the distribution. We then investigate how the peak position scales with the peak number (first: 1; second: 2; etc.).

By fitting these peak positions versus number to a straight line, we can estimate the periodicity in the underlying data. And since the peak position can be determined from the position of higher order peaks, the step size can be determined to a precision better than the bin width of the PWD (or the spatial resolution of the Fourier transform). For example, at 100 μM [ATP], we find that the spatial periodicity in the PWD is well described by a step size of 9.98 ± 0.09 bp. The error bar includes the uncertainty in the slope of the peak position as a function of peak number, the uncertainty in the peak positions, and also the uncertainty in the estimates of the systematic errors, since this reported value was corrected by the systematic error (Section 5.3.2).

5.3.4: Data Selection

It is often the case that each bead-DNA-bead tether has distinct noise characteristics from other tethers. A reasonable fraction of these tethers are often quiet and well-behaved, with noise that is well-described by the expected Brownian fluctuations discussed in Chapter 3. However, a surprisingly large fraction of tethers display additional fluctuations that cannot entirely be explained. Some of this noise can be directly linked to excess DNA molecules on the surface of these beads. In particular, by increasing the amount of DNA on the streptavidin beads in the *in situ* initiation method, the “quality” of the packaging data can be degraded substantially. And, direct measurement of the power spectra of these beads shows additional noise at low frequencies which increases with the amount of DNA incubated with the beads (data not shown.) However, even with very low quantities of DNA, the noise level and “quality” of data between tethers can vary substantially. This is not a phenomenon contained to our experiments; rather, it has been

observed by other groups doing high resolution optical trapping (129, 132) though these issues are not widely discussed in the literature.

Previous work has separated “noisy” traces and “clean” traces by eye. In an effort to avoid such arbitrary analysis protocols, we have developed a different technique. A pairwise distance distribution (PWD) is calculated for each semi-passive mode packaging trace. We then average together *all* PWD, including traces that are obviously of poor quality, to produce an estimate of the dominant spatial periodicity in the data. See Figure 5.7. Once this periodicity is determined, the individual semi-passive mode traces are ranked based on the strength of this periodicity in their individual PWD. This strength is calculated by integrating a specified region in the Fourier transform of each PWD. All PWD analysis and dwell time analysis presented in Chapter 4 is done on the top 50% of the semi-passive mode traces ranked in this fashion.

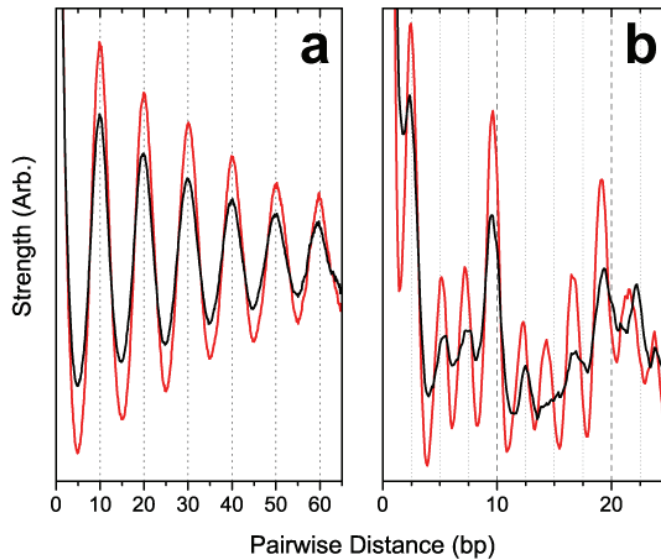


Figure 5.7. Pairwise Distance for all Data and Top 50%

- (a) Average PWD for *all* data at 100 μM [ATP] and low force in red and for the top 50% of data in black.
 - (b) Average PWD for *all* data at 250 μM [ATP] and high force and for the top 50% of data in black. Note that the periodicity observed in the top 50% of traces is the dominant periodicity observed in *all* of the data.
- Reproduced with permission from Ref. (20), Macmillan publishers Ltd: Nature © 2009.

The advantage of this technique is that even if there are subpopulations of different stepping behaviors in our data, we analyze the population that dominates the stepping behavior on average. However, it is clear that this technique leaves much to be desired. One might imagine performing a more rigorous noise spectral analysis on each semi-passive mode and using some measure of the features of this spectra to discriminate between “quite” and “noisy” traces. Moreover, it might be possible to tailor the filtering and analysis for each semi-passive mode trace based on its individual noise characteristics. Of course, the ideal solution would be to determine the physical differences between “noisy” and “quiet” tethers and develop the system such that only “quiet” tethers are formed. Determining the physical origin of this extra noise should be a high priority in future high resolution trapping efforts.

5.3.5: T-Test Transition Finding

While the PWD does an excellent job of finding the underlying spatial periodicity in a data set, it does not find the exact times at which stepping transitions occur. And, in order to analyze the time domain of these traces, these transitions must be uncovered. There is now a wide variety of such step finding algorithms being employed in the literature. (These are reviewed and contrasted in Ref. (187)). However, in our opinion, many of these step finding algorithms leave much to be desired. In particular, there are two limitations that we would like to avoid. First, many step finding algorithms involve a thresholding operation to define transitions. The specific value of the threshold can have significant effects on the performance of the step finder, yet the relationship between the threshold choice and the performance of the step finder is typically unclear. Second, many step finders are sensitive to the bandwidth of the data since the amount of

averaging determines the amount of noise in the data. However, on a fundamental level, the information content of the data should be unchanged if only Brownian noise is averaged away; thus, one expects that the ability to find steps should not depend on the amount of temporal averaging that has been conducted.

To address these issues we have developed a step finder based on the Student's t-test, a statistical test that determines whether two normally distributed samples with the same variance have the same mean (150). Since we expect that data before and after a transition will have the same variance, but different means, the t-test represent the best statistical formulation of the question: is there a step in the data? Moreover, what it means to "pass" or "fail" the t-test, i.e. the absence or presence of a transition, can be formally defined in terms of the probability of observing a given t-value.

Formally, we consider two windows of data consisting of N points before a given time and N points after that time. The data in the first window have a mean of μ_1 and a standard deviation of σ_1 and the data in the second window have a mean of μ_2 and a standard deviation of σ_2 . In this case, the t value at the central time point is defined as

$$t = \frac{\mu_1 - \mu_2}{\sqrt{\sigma_1^2/N + \sigma_2^2/N}}. \quad (5.20)$$

Thus, the t value is simply the difference in the mean for each window weighted by the sum of the standard error for each mean. Since the t value is weighted by the standard error of the mean, it is largely independent of bandwidth. To see this, recall that uncorrelated noise decrease in amplitude by the square-root of the number of points averaged together. If the data are collected at twice the sampling rate, there will be $\sqrt{2}$ more noise, but 2 times more samples per unit time. And, if the size of the t window

corresponds to the same duration in time, N will be twice as large for the larger bandwidth. Thus, the t value will be *identical* for both sampling rates. This is why the t test is largely independent of the bandwidth of the data, one of our desired step finder properties.

Once the t value is calculated for the data, we need a way to determine what values correspond to transitions. This can be done formally by calculating the probability of observing a given t value assuming the *null hypothesis*, i.e. that no transition occurred between the windows. This probability is

$$P(t, N) = I_{N/N+t^2}(N/2, 1/2), \quad (5.21)$$

where $I_x(a, b)$ is the incomplete beta function,

$$I_x(a, b) = \frac{\int_0^x s^{a-1} (1-s)^{b-1} ds}{\int_0^1 r^{a-1} (1-r)^{b-1} dr}. \quad (5.22)$$

Since a transition will violate this null hypothesis—the mean will change—we expect that transitions should produce t values that are entirely unlikely to be produced via fluctuations. To find these values, we must choose a probability threshold. The difference between this threshold and the arbitrary threshold used in most step finding algorithms is that this value, since it is related to a well-defined probability, has a physical meaning. For example, for all packaging data we used a threshold of 10^{-4} , which indicates that fluctuations will only produce a t value that suggests a transition in the absence of an actual step once out of 10,000 independent measurements. Thus, the probability threshold has a well-defined physical interpretation—it is the *false positive rate* for the step finding algorithm.

Figure 5.8 displays an example of the performance of the t-test step finding algorithm on real packaging data. We run a sliding t-test window across the data, calculating the value for N points before and after a given time point, Figure 5.8b. We then calculate the probability of observing each t value. The number of consecutive points that fall below a probability of 10^{-4} , i.e. a false positive rate of 1 in 10,000, determine the duration of a stepping transition. And, the local minima in each contiguous block of t values which violate the threshold is used to determine the exact time of the transition. The time between transitions determines the duration of a given dwell, τ_i , and the difference between the mean position during a given dwell and the previous dwell determine the observed step size, d_i . With the steps delineated in time, it is now possible to calculate a variety of additional useful parameters, such as the average force during a dwell, the variance in the dwell position (useful for propagating uncertainties in the measured step sizes), and the goodness of fit—the difference between the staircase fit determined by the t-test and the actual data. In this thesis, we have not made use of these useful parameters, but there are many advances in this analysis that could be done with this information.

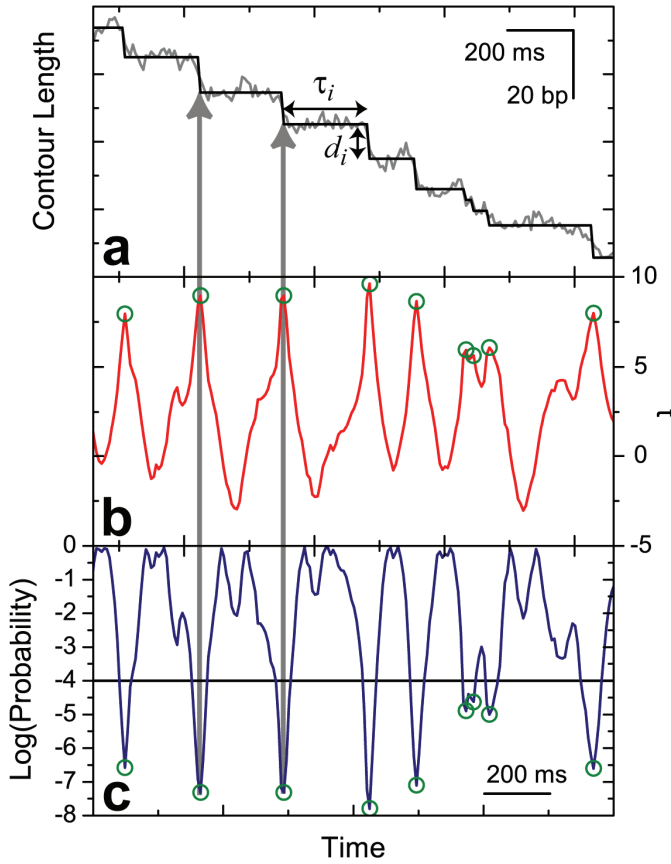


Figure 5.8. *t*-Test Step Finder

(a) Sample stepping trace, contour length of the DNA as a function of time, in gray. In black is the staircase fit based on the transitions found with the *t*-test. (b) The *t* value for the stepping trace in (a) as a function of time. (c) The log base 10 of the probability of observing the *t* value in (b) assuming that there was no transition. Transitions (green circles) are identified from the local minimum in probability for regions of probability under the threshold, 10^{-4} .

To demonstrate that the *t*-test step finder does not introduce any bias into the detection of dwell times—e.g. perhaps short dwell times are properly identified less frequently than long dwell times, etc.—we have performed extensive simulations to test the step finder (data not shown). These simulations reveal that the step finder introduces no bias into the detection of dwell times as long as these dwell times are equal or larger in duration than the duration of the *t*-test window, i.e. the number of points N in the window times the sampling rate. However, we find that the *t*-test is actually remarkably effective

at identifying transitions with dwells shorter than this window as well. In fact, the only systematic error we observe is a small artifact just below the duration of the *t*-test window. Yet, below this duration, it appears that the step finder is able to accurately find and identify dwells with no apparent bias. Because we do not understand why the step finder performs well when there are multiple transitions within a single window, we discard these dwells from our data.

5.3.6: Dwell Time Distributions and Moments

The *t*-test step finder described above provides a list of step sizes and the associated dwell times. There are several steps that must be taken to extract information from these dwell times and to insure that this information is unbiased.

The first complication that arises in analyzing this data is that there are multiple types of step sizes observed in the packaging data. This is readily demonstrated by the interrupted bursts observed at low force, as described in Chapter 4. To extract kinetic information we must first sort dwells into similar classes, long dwells and micro-dwells. This emergent complexity in the stepping behavior is what motivated the theoretical developments we will discuss in Chapter 6. As we will show in this chapter, for the general multi-step molecular motor, one must sort dwell times based on the size of the step both *before* and *after* the dwell. However, for the stepping observed in Chapter 4, it turns out that it is sufficient to sort dwells via the size of the step that follows the dwell time only (discussed in Chapter 6). Fortunately, the distinction between step populations is clear, so the proper choice of size thresholds to categorize steps was straightforward.

Once dwells were sorted by the size of the following step, we used these dwells to estimate the dwell time distribution—the probability distribution for observing a dwell of

a given duration—for all of the different experiment conditions. One common method for estimating a probability distribution is to calculate the histogram of the data. Histograms have a few well known problems, however. For example, the choice of the bin size is often arbitrary and can have dramatic effects on the appearance of the final distribution. Moreover, histograms throw away information smaller than the bin size. To avoid these problems we use an alternative technique known as *kernel density estimation*. In this method, the distribution is built from a functional kernel placed at each data point (188). In our case, we used a Gaussian distribution centered on the data point with a uniform width. Remarkably, there is a well-defined optimal width for this Gaussian, which is determined by statistical features of the data itself (188). In general, kernel density estimation converges to the true distribution for less data than the histogram since it maintains all of the information in the data. One limitation to this technique, is that the Gaussian distribution assumes that all possible times are possible whereas dwell time distributions are not defined for negative time. This is not a problem for the dwell time distributions for the dwells before the 10-bp bursts since these distributions appear to smoothly go to zero at zero time; however, we had to resort to the more traditional histogram in estimating the distribution for the high force data where a large exponential component to this distribution made the probability finite at zero time.

In general, the dwell time distribution contains the most kinetic information in the system; however, as we will argue in later chapters, fitting these distributions has several limitations and offers the risk of significant bias. Instead, we calculate the moments of the data, the mean and a measure of the variance, n_{\min} . The calculation of these moments is extremely straightforward. However, estimating the stochastic errors associated with

these moments is more subtle. To estimate these errors, we perform a modified form of the general bootstrap analysis. We divide our data into 10 random samples of equal size and calculate the moments for these sub-samples. The mean of the sub-sample means is the value reported while the standard error of this mean between the sub-samples is our best estimate of the uncertainty in these moments.

5.3.7: Estimating Systematic Errors in the Moments

While a bootstrap method works well for estimating the stochastic errors, it is not well-suited to estimate systematic errors in our moments. And, we expect that there should be such systematic errors because the t -test has a finite dead-time, i.e. a minimum dwell time duration that it can detect. Fortunately, these systematic errors can be estimated analytically.

We start by recognizing that the introduction of a finite dead-time t_0 produces a modified dwell time distribution,

$$\varphi'(t) = \begin{cases} 0 & t < t_0 \\ \alpha\varphi(t) & t \geq t_0 \end{cases} \quad (5.23)$$

where $\varphi(t)$ is the actual dwell time distribution, $\varphi'(t)$ is the modified distribution, and α is a normalization constant defined by the condition

$$\int_0^\infty \varphi'(t)dt = 1 \Rightarrow \alpha \int_{t_0}^\infty \varphi(t)dt = 1 \Rightarrow \alpha = \left(\int_{t_0}^\infty \varphi(t)dt \right)^{-1}. \quad (5.24)$$

The moments that we measure with a given dead time are the moments of this modified distribution and are determined by

$$\langle t' \rangle = \int_0^\infty t \varphi'(t) dt \text{ and } \langle t'^2 \rangle = \int_0^\infty t^2 \varphi'(t) dt. \quad (5.25)$$

In principle, we do not know the actual dwell time distribution *a priori*; thus, we cannot know the errors associated with measuring moments in the presence of a dead time. However, since this dead time is typically small compared to the range of times over which the distribution is distributed, we can assume a form for the distribution in the dead-time region and introduce only small errors with this assumption. One obvious distribution to assume is the Poisson distribution, a peaked dwell time distribution which corresponds to the time it takes to complete n identical processes of characteristic lifetime $1/k$. The Poisson distribution is given by

$$\varphi(t) = \frac{k^n t^{n-1}}{\Gamma(n)} e^{-kt} \quad (5.26)$$

where $\Gamma(n-1)$ is the gamma function, i.e. the continuous form of the factorial. Moreover, since we are only using this distribution for a small region of time, we can estimate its parameters from the measured parameters, again, without introducing significant errors into our estimates. Namely, we will use

$$n \approx \frac{\langle t' \rangle^2}{\langle t'^2 \rangle - \langle t' \rangle^2} \text{ and } k \approx \frac{n}{\langle t' \rangle}. \quad (5.27)$$

We now show that the errors in our estimation of the moments can be related to integrals of the Poisson function over the dead-time. First, we calculate α

$$\alpha = \left(\int_{t_0}^\infty \varphi(t) dt \right)^{-1} = \left(1 - \int_0^{t_0} \varphi(t) dt \right)^{-1} = \frac{\Gamma(n)}{\Gamma(n, kt_0)}, \quad (5.28)$$

where $\Gamma(n, kt_0)$ is the incomplete gamma function. Now we calculate the error in our estimation of the moments. Recalling that the real moments are

$$\langle t \rangle = \int_0^\infty t \varphi(t) dt \text{ and } \langle t^2 \rangle = \int_0^\infty t^2 \varphi(t) dt . \quad (5.29)$$

We can use this to calculate the error in our estimation of the mean

$$\begin{aligned} \langle t \rangle - \langle t' \rangle &= \int_0^\infty t \varphi(t) dt - \int_0^\infty t \varphi'(t) dt = \int_0^{t_0} t \varphi(t) dt + (1-\alpha) \int_{t_0}^\infty t \varphi'(t) dt \\ &= \int_0^{t_0} t \varphi(t) dt + \frac{(1-\alpha)}{\alpha} \langle t' \rangle \end{aligned} , \quad (5.30)$$

where in the last step we recognized that the final term is simply $\langle t' \rangle / \alpha$. This expression involves only integrals over the small region of the dead time and parameters that have already been measured, i.e. $\langle t' \rangle$. Since we have assumed the distribution, we can perform the first integral in Eq. (5.30). This yields

$$\int_0^{t_0} t \varphi(t) dt = \frac{\Gamma(n+1) - \Gamma(n+1, kt_0)}{k \Gamma(n)} . \quad (5.31)$$

If we add $\langle t' \rangle$ to Eq. (5.30), we can estimate the actual mean using only quantities that we have measured. We find that

$$\begin{aligned} \langle t \rangle &= \int_0^{t_0} t \varphi(t) dt + \frac{(1-\alpha)}{\alpha} \langle t' \rangle + \langle t' \rangle \\ &= \frac{\Gamma(n+1) - \Gamma(n+1, kt_0)}{k \Gamma(n)} + \frac{1}{\alpha} \langle t' \rangle . \end{aligned} \quad (5.32)$$

Similar arguments apply for the second moment. Namely, we find that

$$\begin{aligned} \langle t^2 \rangle - \langle t'^2 \rangle &= \int_0^\infty t^2 \varphi(t) dt - \int_0^\infty t^2 \varphi'(t) dt = \int_0^{t_0} t^2 \varphi(t) dt + (1-\alpha) \int_{t_0}^\infty t^2 \varphi'(t) dt \\ &= \int_0^{t_0} t^2 \varphi(t) dt + \frac{(1-\alpha)}{\alpha} \langle t'^2 \rangle \end{aligned} \quad (5.33)$$

and

$$\int_0^{t_0} t^2 \varphi(t) dt = \frac{\Gamma(n+2) - \Gamma(n+2, kt_0)}{k^2 \Gamma(n)}. \quad (5.34)$$

Again, adding back $\langle t'^2 \rangle$ yields our estimate for the actual second moment of the distribution

$$\langle t^2 \rangle = \frac{\Gamma(n+2) - \Gamma(n+2, kt_0)}{k^2 \Gamma(n)} + \frac{1}{\alpha} \langle t'^2 \rangle. \quad (5.35)$$

We can use the true moments estimated from Eqs. (5.26) and (5.29) to estimate the systematic errors introduced into the moments we measure by the finite dead-time of our measurement. Table 5.1 lists the measured moments from the data presented in Chapter 4 along with the systematic errors calculated using these moments. (A negative error represents an overestimate of the actual value.) All of the systematic errors associated with the mean dwell time are small; however, some of the systematic errors for the parameter n_{\min} —a measure of the variance of the dwell times—are relatively large, $\sim 10\%$. However, when compared to the stochastic errors (listed with the moments), these systematic errors are relatively small. The fact that these systematic errors are relatively small validities the various assumptions made above. If we had found that the errors were large, then these estimates would be less reliable, but would still indicate that not much weight should be given to the measured moments. Finally, the variable dead-time for different [ATP] correspond to a balance between systematic errors in the moments, which increase with dead-time, and the number of detected steps, which also increased with dead time. These systematic errors in the moments were used to determine what dead-times could be tolerated.

Table 5.1. Estimates of Systematic Errors in Dwell Time Moments

[ATP]	t_0	$\langle t' \rangle$	$\delta \langle t' \rangle$	n'	$\delta n'$
1 mM	20 ms	102 ± 4 ms	-1 %	3.8 ± 0.5	-4 %
500 μ M	20 ms	111 ± 3 ms	-2 %	3.2 ± 0.3	-6 %
250 μ M	40 ms	124 ± 2 ms	-4 %	3.8 ± 0.3	-12 %
100 μ M	40 ms	148 ± 2 ms	-1 %	4.9 ± 0.4	-4 %
50 μ M	40 ms	173 ± 3 ms	-1 %	4.4 ± 0.3	-4 %
25 μ M	40 ms	234 ± 5 ms	-0.5 %	4.0 ± 0.3	-2 %
10 μ M	100 ms	330 ± 10 ms	-4 %	3.6 ± 0.5	-11 %
5 μ M	100 ms	0.7 ± 0.1 s	-3 %	2.0 ± 0.4	-8 %

5.4: Summary and Conclusions

In this chapter, we have described in detail the various experimental methods that were utilized to make the measurements described in the previous chapters. First, we discussed the extensive calibration techniques required to convert raw instrument voltages into accurate estimates of the contour length of DNA remaining between the two beads. Then we detailed the experimental methods that go into preparing prohead-motor complexes, introducing these into the optical tweezers, and performing the measurements. Finally, we discussed, in detail, the various techniques we used to take raw DNA length versus time data and convert this into the various statistical measures which allow us to actually infer something from this data.

Many of the techniques described here are standard techniques, developed for other applications and described in detail many places in the literature. However, there are some techniques that are novel and were developed to address specific aspects of the experiments conducted in this thesis. In particular, the measurement of a step size that is a *non-integer* number of base pairs placed a much higher burden of proof on our measurements. Since such a measurement is unexpected and has clear and profound

implications for the motor mechanism, we felt it was necessary to do more than estimate stochastic errors. We had to place firm limits on our systematic errors and rule out any fleeting possibility of $\sim 20\%$ systematic errors. This work culminated in the realization that our data contain an internal distance standard which can be exquisitely well calibrated. Comparison of this distance standard to the actual data allowed us to calculate systematic errors exactly and to correct our data for these errors. Measurements of the drag coefficient of the beads confirmed that these systematic errors likely arise in the errors associated with assuming a bead radius which is actually smaller than quoted by the manufacturer. To the best of our knowledge, this represents the first time that systematic errors have been estimated for an optical tweezers measurement. Moreover, in our opinion, it is only with these careful estimates of experimental error that a non-integer step size can be taken seriously.

In parallel, we have developed methods for extracting step statistics from noisy stepping data. The *t*-test method (115) that we employ has many advantages over other step finders. Namely, the performance of this step finder is largely independent of the bandwidth of the data and the threshold that we use to separate transitions from non-transitions has a clear, physical meaning. However, it is plain that this step finder is not ideal. First, it draws only on local properties of the data. In other words, the step finder only knows features of the data within a single *t*-window. Yet, it is obvious that for long dwells, it would be better for the step finder to have a more global context in which to decide if a transition has occurred. Moreover, there are situations in which the *t*-test fails to find a transition that is actually present. And, it would be useful to have statistical tests that could be performed on individual dwells to determine if they are indeed statistically

consistent with a single uninterrupted dwell. Quantitative measures of the “quality” or “certainty” of such dwells would allow distributions to be built from only the most certain dwells and steps, lowering error and bias in the final distributions.

As high resolution optical trapping techniques are applied to the study of more varied systems, we expect that the limits of the current methodologies will be better determined. And, in many cases, new, better methodologies will need to be developed. However, as demonstrated by the work presented in Chapter 4, the current methodologies provide the ability to detect the fundamental steps of a nucleic acid translocase and extract from noisy stepping traces properties which limit the possible motor mechanisms. Thus, while there should always be a push towards better methodology, the current techniques, described here, should provide an excellent start to researchers investigating the fundamental dynamics of nucleic acid based molecular motors.

Chapter 6. Distinct Statistical Classes of Enzymatic Fluctuations

Moving stochastically through the underlying and hidden kinetic states that compose their kinetic mechanism, enzymes never complete their kinetic cycle in exactly the same time even when experimental conditions are identical. Since these natural fluctuations arise from the kinetic mechanism itself, it should be possible to extract mechanistic information from statistical measures of these fluctuations. And, as we have discussed throughout this thesis, experimental methods now exist that allow these fluctuations to be measured directly. With this new experimental ability come new theoretical challenges. In particular, when enzymatic dynamics are more complicated than the typical one outcome cycle, how does one address the possibility that different kinetic mechanisms might control each of the different outcomes?

In this Chapter, we address this question directly by determining the basic classes of statistics that can arise in enzymatic reactions which have multiple outcomes, e.g. molecular motors that take steps of different sizes or directions. We provide rigorous methods to classify both the statistical classes of theoretical models and actual experimental data. Finally, in the process of developing these basic statistics, we have laid the foundation for a particularly simple method for calculating the measurable properties of essentially any complicated discrete-state, kinetic model. We finish this Chapter by describing this method.

Materials for this Chapter have been reproduced from Ref. (17) with permission, © 2008 American Chemical Society.

6.1: Introduction

In recent years, single-molecule techniques have evolved into a powerful toolset for studying the dynamical behavior of many biological processes. It is now possible to follow on the nanometer and millisecond scales the individual trajectory of a single enzyme as it catalyzes a reaction, a molecular motor as it translocates, or a single polypeptide or nucleic acid molecule as it unfolds and refolds (18, 110, 171, 189). In each case, this trajectory consists of a sequence of molecular events—transitions between the distinct kinetic states of the system—which are stochastic in nature. Single-molecule methods have the ability to measure not only the average trajectory, but also the fluctuations around this average; thus, the statistical analysis of single-molecule trajectories can provide crucial insight into the underlying sequence of events that leads to the behavior of a biological system.

Measurement of fluctuations about the average rate—such as the diffusion constant D or the related randomness parameter $r = 2D/vd$ (112, 125), a dimensionless measure of fluctuations—can lend significantly more information about the underlying kinetics of a system, as discussed in Chapter 1. The latter, specifically, is related to another kinetic parameter, n_{\min} , which has proven particularly powerful as it provides a lower limit on the number of rate-limiting kinetic transitions in a reaction cycle under given experimental conditions (112, 127, 190). Measurements of the randomness parameter or related quantities (191) have been used in the study of molecular motors

such as kinesin (126, 192, 193), topoisomerase II (191), the bacterial DNA translocase FtsK (194), and, as we saw in Chapter 4, the packaging motor of the bacteriophage φ 29 (20, 21).

One advantage of the randomness parameter is that it is possible to measure it even when the individual steps of the motor are obscured by experimental noise (190, 191, 194). Indeed, in cases where certain features of the kinetic scheme are known *a priori*, the randomness parameter can be used to determine the step size of a motor without direct observation (190). However, if the individual steps are resolvable, then it is possible to measure the exact time between events and compile the distribution of first passage or dwell times, $\psi(t)$, in addition to the distribution of step sizes, $\rho(x)$. In a rigorous sense, the first two moments of the dwell time distribution, the mean and the variance, are directly related to the mean reaction rate and its fluctuations, respectively. However, since these distributions can in principle generate every moment, they contain the maximal amount of kinetic information than can be extracted from the data. Dwell time distributions have been measured for molecular motors such as myosin V (123, 195), kinesin (196, 197), the rotary motor F1-ATPase (198), and enzymes such as β -galactosidase (199), to name only a few.

However, it is becoming increasingly clear that many molecular motors or other enzymes are capable of more complicated behavior that cannot be captured in a single dwell time distribution or step size distribution. In particular, motors such myosin (122), kinesin (115), and dynein (116, 117, 120) have been observed to take backward steps in addition to the normal forward steps. Moreover, both myosin and dynein have been observed to take forward steps of varying sizes (115-117, 120). In parallel, we observe

that while the packaging motor takes steps of uniform size, 2.5-bp, these steps are clustered in time in a fashion not consistent with the simple, single outcome kinetic models. When an enzyme displays multiple possible outcomes, such as steps of various sizes and directions, there is a possibility that the kinetic mechanisms that generate these different kinetic outcomes are different; and, thus the statistics of the dwell times may be different depending on the reaction outcome. And it is clear that a dwell time distribution built from dwells taken from different kinetic mechanisms will say very little about the kinetic pathways of the enzyme. In this Chapter, we address this problem by developing the basic classes of statistics that govern enzymes with multiple outcomes. These classes will provide an understanding of how one should sort the dwells of a multi-outcome enzyme to avoid these problems.

In parallel, most kinetic modeling involves the comparison of the properties of candidate kinetic models to actual experimental data, properties such as the mean velocity v , randomness parameter r , and the dwell time distribution $\psi(t)$ (or distributions). However, deriving these properties from the basic kinetic rates of a candidate kinetic model is not trivial even for simple kinetic schemes. And as the behavior of the enzyme becomes more complicated, the complexity of this task grows quickly. While analytical and numerical methods for performing these types of calculation have already been developed and described previously (112, 114, 200-208), no single method has been used to calculate exact analytical expressions for all of these kinetic properties. In particular, the calculation of dwell time distributions for systems with multiple stepping outcomes has been limited (112, 205, 207, 208). The basic statistical properties we develop for kinetic models can be used to extend previous

methods (203, 204), providing a simple and straightforward method for calculating these experimental measures from the arbitrary model. We conclude this Chapter with a discussion of these techniques.

6.2: Theoretical Results

6.2.1: Basic Formalism

We model enzyme dynamics as a first passage process through a series of discrete kinetic states each of which has an exponential lifetime and probabilities of transitioning to any of the states to which it is connected that are independent of the previous history of the enzyme (114). Many of these kinetic transitions produce motions that are not detectable via the experimental method, and, thus, these transitions are hidden. However, we assume that members of a subset of these transitions do produce clear experimental signals. These are the events which will define the beginning and end of individual cycles of the enzyme, i.e. *dwell* times. For simplicity, we will assume that these signals are the physical motion of the enzyme along a one-dimensional track. However, in general the formalism we will develop can apply equally well to motion in multiple dimensions, such as along or around microtubules or actin filaments (209), to internal motions, perhaps revealed by fluorescence resonant energy transfer (110), or even to chemical product release (199).

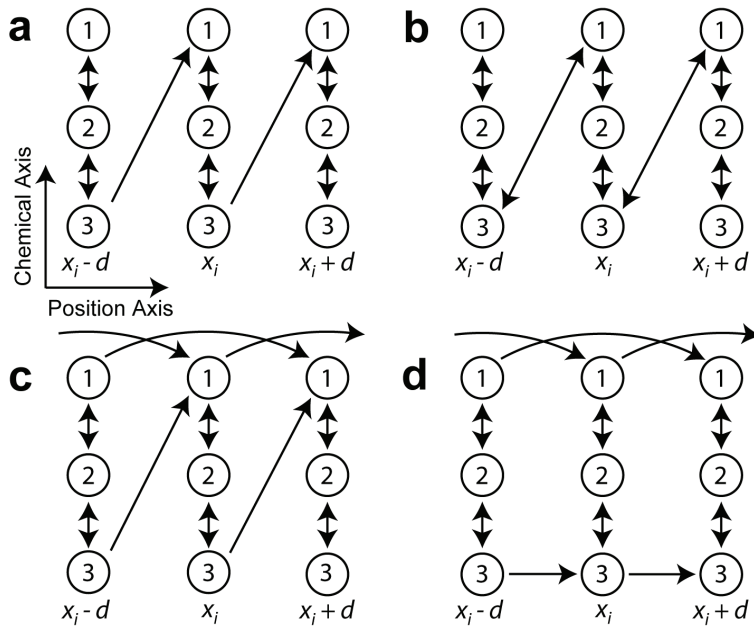


Figure 6.1. Example Kinetic Models

Abstract representation of a variety of three-state kinetic models. Circles represent discrete kinetic states of the enzyme. Arrows represent possible transitions between these states. Vertical transitions correspond to pure chemical transitions which are hidden from detection while horizontal transitions generate a physical movement from spatial position x_i to $x_i \pm d$, which is detectable. (a) A kinetic scheme in which the motor only takes forward steps. (b) A kinetic scheme in which the motor can take forward and backward steps, and backward steps are generated from the reverse transition that generates forward steps. (c) A kinetic scheme in which the motor can take two different steps of different sizes, generated via different kinetic transitions but in which the steps bring the motor to the same initial kinetic state. (d) A kinetic scheme in which the motor can take steps of different sizes but each type of step injects the motor into a different kinetic scheme. The scheme depicted in (c) will display non-conditional stepping statistics while the schemes in (b) and (d) will display conditional statistics. Adapted with permission, © 2008 American Chemical Society.

To help develop an understanding of the different classes of behaviors that can arise in different kinetic schemes, we adopt an abstract way of representing kinetic models, as depicted in Figure 6.1. Individual kinetic states are connected via transitions that can have a component along an abstract chemical axis (vertical in Figure 1.6), which is not detected, or along the actual position axis (horizontal in Figure 1.6), which is

detected. In Figure 6.1a, we represent a standard, single outcome kinetic model in which the system transitions from the first kinetic state to the third and then in resetting back to the first state generates a single observable step. (This is the kinetic model considered in Chapter 1.) In panels b-d we consider more complicated kinetic schemes which display multiple types of steps: forward and backward steps (panel b), steps of multiple sizes which return the system to the original kinetic state (panel c), and steps of multiple sizes that do not return the system to the original kinetic states (panel d). Physically, multiple transitions paths that do not satisfy detailed balance are possible as long as there is an energy source to keep the system out of equilibrium. And such energy sources, e.g. bond hydrolysis, are typical for molecular motors (114).

6.2.2: Classes of Enzyme Statistics

Though it may not be obvious at first glance, the kinetic models displayed in the different panels of Figure 6.1 have fundamentally different statistical fluctuations. For example, because the kinetic scheme in panel a generates only a single outcome—a single step of a uniform size—it must pass through the same kinetic mechanism each time to produce this step; thus, its fluctuations can be described by a single dwell time distribution, $\psi(t)$. However, this is not the case for the schemes in panels b-d. The kinetic scheme in panel c requires *two* distinct dwell time distributions while panels b and d actually require *four* dwell time distributions to fully characterize their fluctuations.

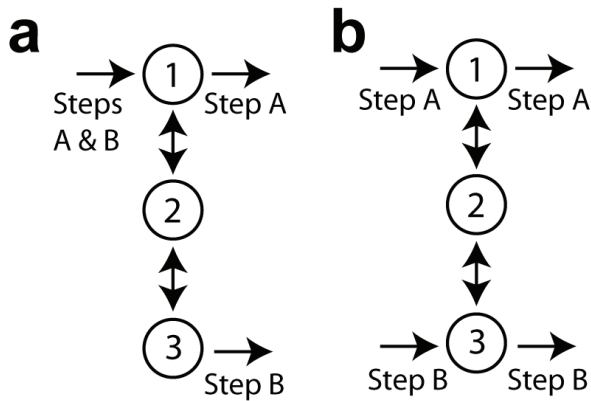


Figure 6.2. Examples of Conditional and Non-Conditional Statistics

Example kinetic schemes with two distinct types of detectable steps, A and B. (a) Both steps return the system to the same kinetic state, so there is no memory of the previous step type. Thus, the statistics of this scheme are *non-conditional*. (b) Each step takes the system to a different kinetic state, so there is some memory of the previous type of step. Thus, the statistics of this scheme are *conditional*.

Figure 6.2 illustrates the essential distinctions between the behaviors in kinetic schemes in panels b-d. We consider an arbitrary kinetic scheme which can generate two different and distinct types of steps, A and B. These steps could vary in size, in direction, or in more subtle, but detectable ways. Moreover, these don't need to both be physical steps. For example, event type A could be a physical step while event type B might be a long-lived off-pathway pause. The crucial point is that these are enzymatic events which can be clearly identified and distinguished.

In Figure 6.2a, both of the two types of steps return the enzyme to the same kinetic state, in this case state 1. Based on our assumption that kinetic states have no memory of the previous kinetic state—i.e. the movement through a discrete kinetic model is a Markov process—this implies that the enzyme no longer remembers the identity of the previous type of step. Thus, the time it takes to generate each of the different types of steps will not depend on the identity of the previous step, and the fluctuations in this system will be completely described by two dwell time distributions $\psi_A(t)$ and $\psi_B(t)$.

(These two dwell times will be distinct because the kinetic pathways to generate each step type are different.) In combination with the branching probabilities p_A and p_B —the probability that the system will choose step type A or step type B—these quantities fully characterize the fluctuations in this system. We will term this class of statistics *non-conditional* because the dwell time distributions and branching probabilities depend only on the type of step that the system *will* take, i.e. this choice is not conditional on the previous step type. Note that both types of steps in the system in Figure 6.1c return the system to the same kinetic state; thus, this system will display non-conditional statistics.

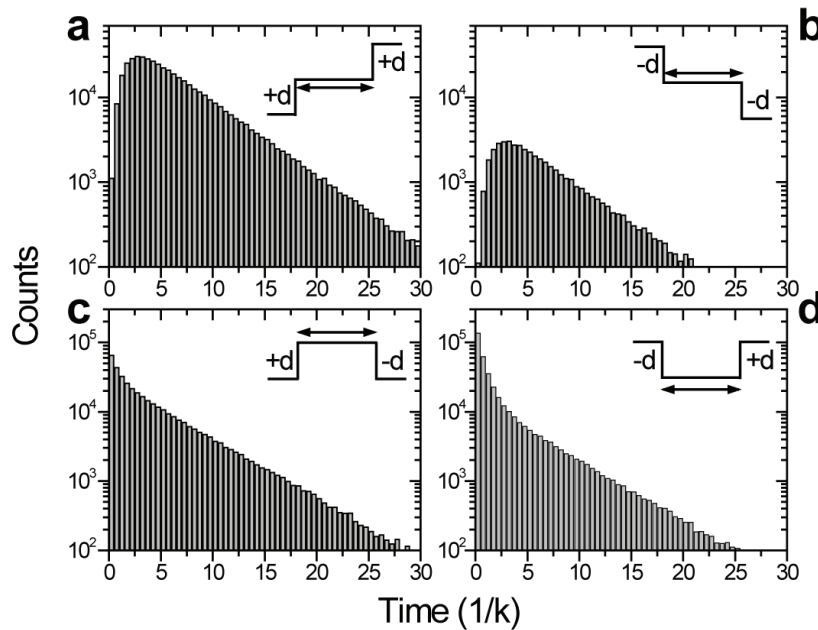


Figure 6.3. Dwell Time Distributions for a Reversible System

Dwell time distributions from a Monte-Carlo simulation of a 4-state fully reversible linear kinetic scheme as in Figure 6.1d. Panels (a) – (d) show the different dwell time histograms for forward steps that were preceded by a forward step (a) or a backward step (d), or backward steps which were preceded by a backward step (b) or a forward step (c). Despite the apparent simplicity of the reversible linear scheme, its dynamics are described by multiple dwell time distributions that depend on the type of physical step taken both before and after the dwell. All forward and backward rates are equal in this simulation, except for the rate at which backwards steps are taken which is $k/5$. Time is measured in units of the inverse of this common rate, i.e. $1/k$. Adapted from Ref. (17) with permission, © 2008 American Chemical Society.

This is not true of the general system considered in Figure 6.2b and Figures 6.1b&d. Rather, each type of step returns the system to a different kinetic state. Returning to the example system in Figure 6.2b, if the system takes step A, it will start its next dwell in kinetic state 1. And, all of the possible enzymatic trajectories that end with another step of type A (or B) must, therefore, start in state 1. In contrast, if the system took a step of type B, then it will start the next dwell in kinetic state 3. And again all trajectories leading to a step of type A or B must start in state 3. The different starting state, even if the final result is the same, implies that the dwell time distribution and the branching probability will most likely be different. It is in this sense that the enzyme gains a memory of its previous step type. Systems that display this property will be termed *conditional* systems and their fluctuations must be described by dwell time distributions and branching probabilities that depend not only on the following step type but on the *preceding* step type as well, i.e. $\psi_{AA}(t)$, $\psi_{AB}(t)$, $\psi_{BA}(t)$, and $\psi_{BB}(t)$ and p_{AA} , p_{AB} , p_{BA} , and p_{BB} . Here the first index indicates the preceding step type while the second index represents the succeeding step. Because each type of step injects the system into a different kinetic state, the schemes in panels b & d in Figure 6.1 will display conditional statistics. Figure 6.3 illustrates the four classes of events that occur in the scheme in Figure 6.1b. Conditional statistics in models of molecular motor dynamics were first recognized by Tsygankov, Lindén, Fisher, and Wallin among others (206, 207). With certain restrictions, Lindén and Wallin (207) have shown that the forward and reverse dwell time distributions are actually identical, i.e. $\psi_{AA}(t)=\psi_{BB}(t)$, a property termed *dwell time symmetry*. Thus, in certain cases only three distinct dwell time distributions are needed.

6.2.3: Identifying Classes in Experimental Data

The above discussion indicates that if the system follows conditional statistics one should sort dwell times by the identity of both the preceding and succeeding event, whereas if the system follows non-conditional statistics one should sort dwell times by the identity of the succeeding event only. Sorting dwell times in this fashion will ensure that dwells generated by different kinetic pathways are analyzed separately. However, how does one know which type of statistics are displayed by the enzyme, and, thus, how to sort dwells? What features of the experimental data indicate the appropriate class of statistics?

There are several methods for determining the statistical class to which a given set of experimental data belongs. The simplest method is to calculate the conditional and non-conditional branching probabilities, e.g. the probability of observing a step of type A independent of the identity of previous step, p_A , and the probability of observing a step of type A conditional on the type of the previous step, p_{AA} and p_{BA} . These probabilities are calculated by simply counting the fraction of steps or step pairs that are of each type (206, 207). If the statistics of the system are *non-conditional*, then the probability of observing a given combination of steps, e.g. A followed by A or B followed by A, will simply be the product of the single step probabilities. Explicitly, the conditional probability of observing a step of type A followed by another A step will be $p_{AA} = p_A^2$. Similarly, a step of type B followed by a step of type A will occur with a probability $p_{BA} = p_A p_B$. However, if the statistics of the system are *conditional*, then these equalities will not be true, i.e. $p_{AA} \neq p_A^2$ and $p_{BA} \neq p_A p_B$. Thus, as long as these probabilities can be measured with sufficient certainty to determine equality or inequality

as in these relations, the specific statistical class of fluctuations of a given enzyme can be easily identified.

Sometimes it is not so trivial to properly classify steps of a given type. For example, when experimental noise broadens a step size distribution, it is possible that two distinct populations may have regions that overlap. See Figure 4.3. Thus, it is sometimes more useful to calculate related conditional distributions. For example, in Chapter 4 we calculated the step size distribution conditional on the type of a succeeding step. If the statistics of the system are non-conditional, then the distributions will be independent of the choice of step type whereas if the statistics are conditional, the distributions will change based on the choice of step type. This is essentially the continuous version of the discrete inequalities described above.

In addition, the classification of step types can be extended to include distinct step durations as well. For example, in Chapter 4 we argued that the dwell time distribution observed for the ~5-bp events (Figure 4.3) was composed of the weighted sum of two different dwell time distributions, which we could partially discriminate by drawing a threshold and labeling 5-bp steps with durations shorter than this threshold as one step type and 5-bp steps with durations longer than this threshold as an additional step type. Once these labels are assigned, the same analysis suggested above can be done with two different classes of 5-bp steps. One could imagine further extending this analysis to include many additional temporal classifications, i.e. three temporal divisions, four divisions, etc. The limit of this analysis is a full two-dimensional dwell time distribution in which the duration of pairs of dwells (of subsequent steps) is plotted. If this distribution is identical along both axes, then there is only one type of dwell time that

produces the step of that given type (in this case likely size) whereas if the distribution is different along each of the axis, then it is clear that there are multiple kinetic pathways which can generate the same size of step. (The implication of such two-dimensional distributions has been worked out extensively for the statistics of single ion channels (210).) Thus, the system may be non-conditional in step size, but when the steps are classified in a new way, say by duration, the statistics will be conditional. This is a general property—the events that you can observe largely determine the class of statistics to which an enzyme exists.

6.2.4: The Position Probability Density

An understanding of the class of statistics that govern the behavior of a given enzyme does more than determine how the data should be treated, it also greatly limits the possible choices for candidate kinetic models for the enzymatic mechanism. And given that the number of candidate kinetic models is, in principle, *infinite*, this is an important point in the analysis of multi-outcome enzymes. Simply put, the discrete kinetic models must share the same statistical class as the enzymatic data. For the simplest kinetic models, inspection of the model is typically sufficient to determine the statistical class. However, for more complicated cases, it is not always so trivial to identify the statistical class of a candidate model. To aid in this process, and calculations discussed further below, we develop a mathematical formulation of what it means to be conditional or non-conditional.

We start by defining a quantity, which we term the *position probability density*, which describes the probability of an enzyme being at lattice state x at time t . This expression is in general a complicated function of space and time; however, because it is

the step size distributions which generate the spatial dependence of the motor and the dwell time distributions which determine the temporal dependence, we expect that the space and time dependence of the position probability density should be a function of these distributions. And it should be possible to separate these dependencies. Namely, we expect that the position probability density, $P(x,t)$, should be a function of the step size distributions, dwell time distributions, and the relative weights of each of these distributions, i.e. the branching probabilities. Explicitly,

$$P(x,t) = f(p_A, p_B; \psi_A(t), \psi_B(t), \rho_A(x), \rho_B(x)) \quad (6.1)$$

where we consider here a non-conditional system with two types of steps distributed via functions ρ_A and ρ_B . If the system displays conditional statistics, then this expression would be a function of all of the conditional probabilities and dwell time distributions.

The derivation of these expressions is described in the Appendix in Section 6.5.1. Before we present the results, there is one important complication to discuss. When one considers multiple possible pathways from one kinetic state to another, the mathematical expression which calculates the final time is the convolution over all possible durations in each of the kinetic states (112). Since our final expressions will involve sums over an infinite number of paths, they will include infinite convolutions—which cannot be expressed in a closed-form fashion. To avoid this problem we will move from real space to a related space, Fourier-Laplace space, in which we measure position not with a real distance x but with a Fourier variable q and time not with t but with the Laplace variable s . In Fourier-Laplace space, convolutions are replaced by products, greatly simplifying our analysis. If we need to move back to real space and time, we can always inverse our transformations. As we will see below, it is often not necessary to move back to the

space and time domain. Thus, our final position probability density will be a function of q and s , and we will relate this to the Fourier transform of the step size distributions, $\tilde{\rho}_A(q)$ and $\tilde{\rho}_B(q)$ and the Laplace transform of the dwell time distributions, $\tilde{\psi}_A(s)$ and $\tilde{\psi}_B(s)$ (or with double indices for conditional systems.)

In Fourier-Laplace space, we find that for a simple one outcome system the position probability density is related to the single step size distribution and single dwell time distribution via

$$P(q,s) = \frac{1}{s} \frac{\tilde{\psi}(s)}{1 - \tilde{\rho}(q)\tilde{\psi}(s)} \quad (6.2)$$

a result that has been derived previously (211). For a multi-outcome system that displays non-conditional statistics, this expression is modified slightly. For a system with only two outcomes, steps of type A and B, then the position probability density is related to the dwell time distributions, step size distributions, and branching probabilities via

$$P(q,s) = \frac{1}{s} \frac{p_A \tilde{\psi}_A(s) + p_B \tilde{\psi}_B(s)}{1 - p_A \tilde{\rho}_A(q) \tilde{\psi}_A(s) - p_B \tilde{\rho}_B(q) \tilde{\psi}_B(s)}. \quad (6.3)$$

If there are more than two outcomes, this expression can be modified appropriately. See Eq. (6.54) in Section 6.5.1.

The expression for a system that displays conditional statistics is more complicated and must be expressed in matrix notation. It is

$$\tilde{P}(q,s) = \mathbf{p}_0^T (\mathbf{I} - \tilde{\Psi}(s) \mathbf{p}(q))^{-1} \tilde{\Psi}(s) \quad (6.4)$$

where \mathbf{p}_0^T is the vector of initial conditions, i.e. the type of step taken before the experiment started, $\mathbf{p}(q)$ is a diagonal matrix of the step type distributions, $\tilde{\Psi}(s)$ is the matrix of dwell time distributions and branching probabilities, $\tilde{\Psi}(s)$ is a vector of

branching probabilities and dwell time distributions, and \mathbf{I} is the identity matrix. For the two outcome system, these matrices and vectors are

$$\mathbf{p}(q) = \begin{pmatrix} \tilde{\rho}_A(q) & 0 \\ 0 & \tilde{\rho}_B(q) \end{pmatrix}, \quad (6.5)$$

$$\tilde{\Psi}(s) = \begin{pmatrix} p_{AA}\tilde{\psi}_{AA}(s) & p_{AB}\tilde{\psi}_{AB}(s) \\ p_{BA}\tilde{\psi}_{BA}(s) & p_{BB}\tilde{\psi}_{BB}(s) \end{pmatrix}, \quad (6.6)$$

and

$$\tilde{\Psi}(s) = \frac{1}{s} \begin{pmatrix} 1 - p_{AA}\tilde{\psi}_{AA}(s) - p_{AB}\tilde{\psi}_{AB}(s) \\ 1 - p_{BA}\tilde{\psi}_{BA}(s) - p_{BB}\tilde{\psi}_{BB}(s) \end{pmatrix}. \quad (6.7)$$

If we imagine that the previous system started with a step of type A, then the initial condition would be $\mathbf{p}_0^T = (1 \ 0)$. Additional outcomes can be added by increasing the dimension of these matrices.

6.2.5: Identifying Classes in Theoretical Models

To better understand the distinction between the conditional and non-conditional statistics, it is useful to expand equation (6.4) for the two state system. Using state A as the initial condition, we find that

$$\tilde{P}_A(q, s) = \frac{1}{s} \frac{1 - p_{AA}\tilde{\psi}_{AA} - p_{AB}\tilde{\psi}_{AB} - \tilde{\rho}_B(p_{AB}\tilde{\psi}_{AB}(p_{BA}\tilde{\psi}_{AB} - 1) + p_{BB}\tilde{\psi}_{BB}(1 - p_{AA}\tilde{\psi}_{AA}))}{1 - \tilde{\rho}_A p_{AA}\tilde{\psi}_{AA} - \tilde{\rho}_B p_{BB}\tilde{\psi}_{BB} - \tilde{\rho}_A \tilde{\rho}_B (p_{AB}\tilde{\psi}_{AB} p_{BA}\tilde{\psi}_{BA} - p_{AA}\tilde{\psi}_{AA} p_{BB}\tilde{\psi}_{BB})}. \quad (6.8)$$

This expression illustrates two points. First, conditional statistics are more complicated than non-conditional statistics. And, second, conditional statistics have unique signatures in the algebraic structure of the position probability density relative to non-conditional statistics. To be exact, this expression has terms that are proportional to the product of the step size distributions, see the final term in the denominator. This is not the case for

non-conditional systems, Eq. (6.4). Thus, if we can calculate the position probability density for a given kinetic model, its class of statistics can easily be determined by identifying this distinguishing term. We will show this explicitly in the example calculation below.

It turns out that the position probability density, once calculated, can generate a series of useful experimental measures, the velocity, the randomness parameter, the branching probabilities, and all of the distributions. And we will discuss a method to calculate the position probability density and these useful experimental measures in the next section.

6.2.6: Connection to the Velocity and the Randomness Parameter

Finally, the fact that enzymes can have multiple outcomes has implications for the relationship between macroscopic measures of the behavior of an enzyme, such as the mean velocity and the randomness parameter, and the moments of the underlying distributions, step size and type and the different dwell times. And in many cases, the informative power of the velocity and the randomness parameter arise because of the connections that are typically assumed between these parameters and the moments of these distributions. The basic statistical properties that we derived above, relating the step size and dwell time distributions to the positional probability density, allow us to calculate the relationship between the velocity and the randomness parameter for all kinetic schemes that are a member of each of the different statistical classes.

In Section 6.5.2 we derive these relations, and we summarize them here for convenience. For all multi-outcome systems, we find that the mean dwell time $\langle t \rangle$ and the mean step size $\langle d \rangle$ determine the average velocity, exactly as is expected

$$v = \frac{\langle d \rangle}{\langle t \rangle}. \quad (6.9)$$

However, when there are multiple outcomes, these first moments $\langle t \rangle$ and $\langle d \rangle$ become composite moments and are functions of the moments of all of the individual distributions and the branching probabilities. In particular, the moments of the step size distribution and dwell time distribution are determined by

$$\langle d^n \rangle = p_A \langle d_A^n \rangle + p_B \langle d_B^n \rangle, \quad (6.10)$$

$$\langle t^n \rangle = p_A \langle t_A^n \rangle + p_B \langle t_B^n \rangle, \quad (6.11)$$

where for a conditional system the single index probabilities are determined from the conditional probabilities via

$$p_A = \frac{p_{BA}}{p_{AB} + p_{AB}} \quad (6.12)$$

and similarly for the other index (17, 206). Similarly for a conditional system the single index moments of the dwell time are

$$\langle t_A^n \rangle = p_{AA} \langle t_{AA}^n \rangle + p_{AB} \langle t_{AB}^n \rangle \quad (6.13)$$

with the other moment is determined by switching indices (17, 206).

While the velocity has a simple form, this does not appear to be true for the randomness parameter. For a system that displays conditional statistics (and two types of step types) the randomness parameter is

$$\begin{aligned}
r = & \frac{\langle d^2 \rangle - \langle d \rangle^2}{\langle d \rangle^2} + \frac{\langle t^2 \rangle - \langle t \rangle^2}{\langle t \rangle^2} + 2 \frac{\langle d \rangle^2 - p_A \langle d_A \rangle^2 - p_B \langle d_B \rangle^2}{\langle d \rangle^2} \\
& + 2 p_A \langle d_A \rangle \frac{p_{BB} \langle t_{BB} \rangle \langle d_A \rangle - p_{AB} \langle t_{AB} \rangle \langle d_B \rangle}{(p_{AB} + p_{BA}) \langle d \rangle^2 \langle t \rangle} + 2 p_B \langle d_B \rangle \frac{p_{AA} \langle t_{AA} \rangle \langle d_B \rangle - p_{BA} \langle t_{BA} \rangle \langle d_A \rangle}{(p_{AB} + p_{BA}) \langle d \rangle^2 \langle t \rangle} \\
& - 2 \frac{p_{AA} p_{BB} \langle t_{AA} \rangle \langle t_{BB} \rangle - p_{AB} p_{BA} \langle t_{AB} \rangle \langle t_{BA} \rangle}{(p_{AB} + p_{BA}) \langle t \rangle^2}
\end{aligned} \quad (6.14)$$

which is a rather complicated expression of the different moments. This expression simplifies significantly when the statistics are non-conditional:

$$r = \frac{\langle d^2 \rangle - \langle d \rangle^2}{\langle d \rangle^2} + \frac{\langle t^2 \rangle - \langle t \rangle^2}{\langle t \rangle^2} + 2 \frac{\langle d \rangle \langle t \rangle - p_A \langle d_A \rangle \langle t_A \rangle - p_B \langle d_B \rangle \langle t_B \rangle}{\langle d \rangle \langle t \rangle}. \quad (6.15)$$

In all of its reported uses (112, 126, 190, 191, 193, 194) the randomness parameter is assumed to reduce to a simple function of the dwell times only, i.e.

$$r = \frac{\langle t^2 \rangle - \langle t \rangle^2}{\langle t \rangle^2}. \quad (6.16)$$

which, as the above expressions show, is valid only when the steps are uniform in size and there is only one reaction outcome.

In this form, it is clear that the inverse of the randomness parameters is the related kinetic parameter n_{\min} , which, as has been discussed in Chapter 1 and 4, places strict limits on the number of kinetic events in a given cycle. It is this ability to relate the randomness parameter—which does not require the direct observation of steps—to n_{\min} which makes the randomness parameter a useful and powerful measure of enzymatic fluctuations. However, as we have shown here if there are multiple outcomes in an enzymatic cycle, then the randomness parameter is no longer simply related to n_{\min} and it seems likely that it loses much of its informative power. While it is possible to partially

account for multiple outcomes (208), it seems more likely that the only way to know if the simple form of the randomness parameter is applicable is to observe the discrete steps of the enzyme directly (126, 208). And if these steps can be seen, much more can be learned by sorting them based on the statistical class of the fluctuations, and then calculating n_{\min} or related properties for each of the types of dwell times, as is shown here.

6.3: Exact Solutions for Discrete Kinetic Models

A crucial process in the modeling of kinetic data is the calculation of the analytical properties of a candidate kinetic model, properties such as the statistical class of the model, and how the various experimentally measurable quantities—the branching probabilities, the dwell time distributions, and even the mean velocity and the randomness parameter—depend on the different kinetic parameters of the system. However, as it becomes increasingly clear that many molecular motors are capable of a variety of complicated behaviors, the needed complexity of the candidate models increases. And, unfortunately, the difficulty of calculating analytical solutions increases dramatically as the candidate models increase in size and complexity. To address this problem, we have developed a simple method, which exploits the position probability density relations derived above, to calculate the basic properties of different kinetic models with relative ease. In this Section we present this method.

6.3.1: Calculating the Position Probability Density

We start by recognizing that the probability of being at any given kinetic state at any lattice position x at time t is governed by a set of coupled differential equations:

$$\frac{dP_i(x,t)}{dt} = -\sum_{j=1}^N k_{ij} P_j(x,t) + \sum_{j=1}^N k_{ji} P_j(x,t) + \sum_{l=1}^M \int_{-\infty}^{\infty} \sum_{j=1}^N k_{ji}^l P_j(\eta, t) \rho_l(x-\eta) d\eta \quad (6.17)$$

where $P_i(x,t)$ is the probability of being in the i th kinetic state at lattice position x and time t . The first term is the rate at which probability flows out this state—the sum of all of the transition rates out of state i —where k_{ij} is the rate at which probability flows from state i to state j . The second term is the sum of all of the probability flowing out of other kinetic states at the *same* lattice position and into state i . Again k_{ji} is the rate at which probability flows from the j th state to the i th state. Finally, the complicated final term is simply the sum of the flow of probability into state i from kinetic states at *different* lattice positions via all possible steps of type l . Here $\rho_l(\eta)$ is the step size distribution for each step type l , i.e. the probability of taking a step of type l of size η . The first summation in this final term includes all possible step types, in total M . The following integral captures all of the possible sizes of each step type. If the lattice is discrete this integral becomes a sum and the step size distribution becomes a delta function. The final sum captures all of the different kinetic rates k_{ji}^l which can generate each of these step types. If there is only one transition which generates a step of a given type, then there will only be one term in this final sum, i.e. all other k_{ji}^l will be zero.

In an N state kinetic model, there are N distinct expression of the form in Eq. (6.17)—one for each kinetic state—at every lattice position. And since there are an infinite number of lattice positions, this system is governed by an *infinite* number of coupled, first-order differential equations. In this form this problem is particularly intractable. However, we can Fourier transform these probabilities, compressing this

infinite lattice into a finite representation, to generate a more manageable description of the system. Fourier transforming Eq. (6.17) yields

$$\frac{dP_i(q,t)}{dt} = -\sum_{j=1}^N k_{ij} P_i(q,t) + \sum_{j=1}^N k_{ji} P_j(q,t) + \sum_{l=1}^M \sum_{j=1}^N k_{ji}^l P_j(q,t) \rho_l(q). \quad (6.18)$$

Notice that the integral has been replaced by a simple product, via the convolution theorem (182), and that all probabilities now occur at a single value q . Thus, the differential equations at different values of the Fourier variable have been *uncoupled*.

We can further simplify this expression by transforming from the time domain to the related Laplace domain. The advantage is that in Laplace space derivatives in time are replaced with algebraic expressions. Thus, we can change the problem from solving a set of differential equations to a set of coupled algebraic expressions. Namely, performing the Laplace transform yields

$$s\tilde{P}_i(q,s) - P_i(q,t=0) = -\sum_{j=1}^N k_{ij} \tilde{P}_i(q,s) + \sum_{j=1}^N k_{ji} \tilde{P}_j(q,s) + \sum_{l=1}^M \sum_{j=1}^N k_{ji}^l \tilde{P}_j(q,s) \rho_l(q) \quad (6.19)$$

where $\tilde{P}_i(q,s)$ is the Fourier-Laplace transform of the probability $P_i(x,t)$, and $P_i(q,t=0)$ is the initial condition of state i —the probability of being in this state at time zero.

This set of N linear, algebraic equations can now be expressed in compact notation. We define the rate matrix \mathbf{M} which contains all of the transition rates from one state to another. The ii th components—diagonal components—determine the rate at which probability leaves state i for other states. The ij th components—off-diagonal components—determine the rate at which probability flows from state j to state i . Finally, every rate that transports the system to a new lattice position by a step of type l is weighted by the Fourier transform of the step size distribution for this step type, $\rho_l(q)$.

We also define the position probability vector $\tilde{\mathbf{P}}(q,s)$ whose components correspond to the individual $\tilde{P}_i(q,s)$ and the initial condition vector $\mathbf{P}(q,t=0)$ whose components are the initial conditions $P_i(q,t=0)$. With this formalism Eq. (6.19) can be expressed as

$$s\tilde{\mathbf{P}}(q,s) - \mathbf{P}(q,t=0) = \mathbf{M}(q)\tilde{\mathbf{P}}(q,s). \quad (6.20)$$

And we can solve exactly for the position probability vector, yielding

$$\tilde{\mathbf{P}}(q,s) = (s\mathbf{I} - \mathbf{M}(q)\tilde{\mathbf{P}}(q,s))^{-1} \mathbf{P}(q,t=0). \quad (6.21)$$

Since we can only observe the lattice position of a given system, not the individual probabilities of being in a given kinetic state, the individual components of $\tilde{\mathbf{P}}(q,s)$ are undetectable. Thus, we sum over these components to form the *position probability density* $\tilde{P}(q,s)$, i.e.

$$\tilde{P}(q,s) = \sum_{i=1}^N \tilde{P}_i(q,s). \quad (6.22)$$

This is the same position probability density that we discussed in the above sections and which, more importantly, we related to the specific experimental observables—the branching probabilities and the dwell time distributions. Because we have shown how to calculate the position probability density directly from the rate matrix \mathbf{M} , we have now connected these experimental measures to features of a given kinetic model. And, as we will show below, it is straightforward to construct this matrix from a diagrammatic model such as those shown in Figures 6.1 and 6.2. Thus, it should be straightforward to extract analytical expressions for the important parameters of any kinetic model.

6.3.2: Dwell Time Distributions and Branching Probabilities

To extract the dwell time distributions and branching probabilities it is first necessary to determine the statistical class of the candidate kinetic model, i.e. conditional or non-conditional. This can be done easily, as described above. Once the statistical class has been identified, then the position probability density calculated as above, can be related to the dwell time distributions and branching probabilities via the appropriate statistical relations described in Eq. (6.3) or (6.4). A few algebraic manipulations of the position probability density is all that is needed to yield the experimental measures, i.e. the dwell time distributions and step size distributions.

Starting with the non-conditional statistics in Eq. (6.3), if we set all step size distributions to zero except for the distribution for state i , we find that

$$\left(s\tilde{P}(q,s)\right)^{-1}\Big|_{\rho_B \rightarrow 0} = \frac{1 - p_A \psi_A(s) \rho_A(q)}{1 - p_A \psi_A(s) - p_B \psi_B(s)} = a_0(s) + a_A(s) \rho_A(q) \quad (6.23)$$

Notice that this expression has one term that is independent of a step size distribution, a_0 and a second term that is proportional to this distribution, a_A . Careful comparison of the identity of these terms reveals that

$$p_A \psi_A(s) = -\frac{a_A(s)}{a_0(s)}. \quad (6.24)$$

To separate these two expressions we use that fact that dwell time distributions must be normalized such that the integral over all time is equal to one. In Laplace space this condition translates into the condition that the dwell time distribution evaluated at $s = 0$ must be 1, i.e. $\psi_A(0) = 1$. Thus, the branching probability is

$$p_A = -\frac{a_A(s=0)}{a_0(s=0)}. \quad (6.25)$$

This can then be combined with Eq. (6.24) to extract the Laplace transform of the dwell time distribution for a step of type A. This procedure can be repeated to find all of the branching probabilities and dwell time distributions for all step types by systematically setting all of the different step size distributions to zero.

A similar procedure can be applied when the system displays conditional statistics. In particular, consider the relationship between the position probability density for a two state system evaluated with state A as the initial condition and the individual distributions, Eq. (6.8). Inspection of this expression reveals that if one sets the step size distribution for step B to zero, the inverse of the position probability distribution is

$$\left(s\tilde{P}_A(q,s)\right)^{-1} \Big|_{\rho_B \rightarrow 0} = \frac{1 - p_{AA}\psi_{AA}(s)\rho_A(q)}{1 - p_{AA}\psi_{AA}(s) - p_{AB}\psi_{AB}(s)} = a_0(s) + a_A(s)\rho_A(q). \quad (6.26)$$

Again, the product of one of the branching probabilities and dwell time distributions can be extracted from the terms independent of $\rho_A(q)$ and proportional to $\rho_A(q)$. Namely,

$$p_{AA}\psi_{AA}(s) = -\frac{a_{AA}(s)}{a_0(s)}. \quad (6.27)$$

Additional inspection of Eq. (6.26) reveals that we can also extract another branching probability and dwell time distribution from these coefficients. In particular,

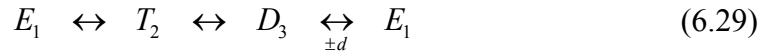
$$p_{AB}\psi_{AB}(s) = \frac{a_{AA}(s) + a_0(s) - 1}{a_0(s)}. \quad (6.28)$$

The branching probabilities and the dwell time distributions can be separated by again setting $s = 0$.

The other two branching probabilities and dwell time distributions can be extracted by first recalculating the position probability density but using state B as the initial condition, and then performing the same manipulations as above.

6.3.3: Example Calculation: A Reversible 3 State System

To illustrate this technique, let's consider an example kinetic model widely applicable to simple molecular motors but which displays conditional statistics. In particular, we consider the system



in which the motor binds ATP to an empty motor (E) forming an ATP bound motor (T), the ATP is hydrolyzed to form a product bound state (D) and then upon the release of hydrolysis products (reset to E) the motor generates a physical step of size d . If the hydrolysis products are in reasonable concentration in the buffer, then we allow the motor to rebind these products and generate a backward step, $-d$. Thus, in principle, the motor can occasionally run backwards, moving in the reverse direction and recatalyzing the gamma bond of ATP from its hydrolysis products.

The rate matrix for this system is

$$\mathbf{M}(q) = \begin{pmatrix} -(k_{21} + k_{31}) & k_{12} & k_{13}\rho_+(q) \\ k_{21} & -(k_{12} + k_{32}) & k_{23} \\ k_{31}\rho_-(q) & k_{32} & -(k_{13} + k_{23}) \end{pmatrix} \quad (6.30)$$

where the step size distributions for forward steps are $\rho_+(q)$ and $\rho_-(q)$ respectively. Inspection of this matrix shows that it is straightforward to construct it from the diagram in Eq. (6.29). First, all rates are indexed with the subscript of the states in Eq. (6.29) where k_{ij} refers to the rate at which probability flows from state j to state i . The diagonal

terms in the rate matrix are simply the negative of the sum of all of the rates out of the corresponding state (the i th component corresponds to the i th state) whereas the off-diagonal terms correspond to the rate at which probability flows from one state to the next (the ij th component corresponds to the transition rate from state j to state i .) When the transition generates a physically detectable motion—a step—this transition is weighted with the Fourier transform of the step size distribution for that step type.

In principle, the rates that correspond to binding of substrate molecules should have a concentration dependence; however, we will ignore this complication for simplicity. It is trivial to add these concentrations to the appropriate terms in Eq. (6.30) and all of the subsequent results if desired, i.e. $k_{21} \rightarrow k_{21}[ATP]$ and $k_{31} \rightarrow k_{31}[ADP][P_i]$.

Taking the initial condition as the kinetic state to which the positive step takes the system, state 1, we can calculate the position probability density via the matrix manipulations in Eqs. (6.21) and (6.22). This expression is

$$\begin{aligned}\tilde{P}_+(q, s) = & \{k_{12}(k_{13} + k_{23} + s) + k_{13}(k_{21} + k_{32} + s) + (k_{21} + s)(k_{23} + k_{32} + s) \\ & + (k_{12}k_{31} + k_{31}(k_{23} + k_{32} + s))\rho_-(q)\}/\{k_{12}(k_{13} + k_{23} + s)(k_{31} + s) \\ & + (k_{21} + k_{31} + s)(k_{13}(k_{32} + s) + s(k_{23} + k_{32} + s)) \\ & - (k_{13}k_{21}k_{32})\rho_+(q) - (k_{12}k_{23}k_{31})\rho_-(q) \\ & - k_{13}k_{31}(k_{12} + k_{32} + s)\rho_+(q)\rho_-(q)\}\end{aligned}. \quad (6.31)$$

Taking the other initial condition, after a back step, i.e. starting in state 3, we calculate the other position probability density as above. This yields

$$\begin{aligned}
\tilde{P}_-(q, s) = & \{k_{12}(k_{31} + k_{23} + s) + (k_{21} + k_{31} + s)(k_{23} + k_{32} + s) \\
& + (k_{12}k_{13} + k_{13}(k_{23} + k_{32} + s))\rho_+(q)\}/\{k_{12}(k_{13} + k_{23} + s)(k_{31} + s) \\
& + (k_{21} + k_{31} + s)(k_{13}(k_{32} + s) + s(k_{23} + k_{32} + s)) \\
& - (k_{13}k_{21}k_{32})\rho_+(q) - (k_{12}k_{23}k_{31})\rho_-(q) \\
& - k_{13}k_{31}(k_{12} + k_{32} + s)\rho_+(q)\rho_-(q)\}
\end{aligned} \quad . \quad (6.32)$$

It is interesting to note that these expressions have terms in the denominator that are the multiple of the two step size distributions; thus, our intuition that this system belongs to the conditional class of statistics is correct. This is exactly how one would determine the statistical class for arbitrary kinetic models.

With the position probability densities, we can now perform the algebraic manipulations listed in Eqs. (6.26)-(6.28) to extract the branching probabilities and Laplace transform of the dwell time distributions. Inspection of Eq. (6.31) reveals that the necessary coefficients are

$$a_0 = \frac{1}{s} \frac{k_{12}(k_{13} + k_{23} + s)(k_{31} + s) + (k_{21} + k_{31} + s)(k_{13}(k_{32} + s) + s(k_{23} + k_{32} + s))}{k_{12}(k_{13} + k_{23} + s) + k_{13}(k_{21} + k_{32} + s) + (k_{21} + s)(k_{23} + k_{32} + s)} \quad (6.33)$$

and

$$a_+ = \frac{1}{s} \frac{-(k_{13}k_{21}k_{32})}{k_{12}(k_{13} + k_{23} + s) + k_{13}(k_{21} + k_{32} + s) + (k_{21} + s)(k_{23} + k_{32} + s)}. \quad (6.34)$$

For the position probability density with a negative step as the initial condition, we find that

$$a'_0 = \frac{1}{s} \frac{k_{12}(k_{13} + k_{23} + s)(k_{31} + s) + (k_{21} + k_{31} + s)(k_{13}(k_{32} + s) + s(k_{23} + k_{32} + s))}{k_{12}(k_{31} + k_{23} + s) + (k_{21} + k_{31} + s)(k_{23} + k_{32} + s)} \quad (6.35)$$

and

$$a_- = \frac{1}{s} \frac{-(k_{12}k_{23}k_{31})}{k_{12}(k_{31} + k_{23} + s) + (k_{21} + k_{31} + s)(k_{23} + k_{32} + s)}. \quad (6.36)$$

Using these expressions we can now derive the four conditional branching probabilities

$$p_{++} = \frac{k_{13}k_{21}k_{32}}{k_{12}k_{31}(k_{13} + k_{23}) + k_{13}k_{32}(k_{21} + k_{31})}, \quad (6.37)$$

$$p_{+-} = \frac{k_{31}(k_{12}k_{13} + k_{12}k_{23} + k_{13}k_{32})}{k_{12}k_{31}(k_{13} + k_{23}) + k_{13}k_{32}(k_{21} + k_{31})}, \quad (6.38)$$

$$p_{-+} = \frac{k_{13}(k_{12}k_{31} + k_{21}k_{32} + k_{31}k_{32})}{k_{12}k_{31}(k_{13} + k_{23}) + k_{13}k_{32}(k_{21} + k_{31})}, \quad (6.39)$$

and

$$p_{--} = \frac{k_{12}k_{23}k_{31}}{k_{12}k_{31}(k_{13} + k_{23}) + k_{13}k_{32}(k_{21} + k_{31})}. \quad (6.40)$$

And we can derive the Laplace transforms of the four conditional dwell time distributions:

$$p_{++}\psi_{++}(s) = \frac{k_{13}k_{32}k_{21}}{k_{12}(k_{13} + k_{23} + s)(k_{31} + s) + (k_{21} + k_{31} + s)(k_{13}(k_{32} + s) + s(k_{23} + k_{32} + s))}, \quad (6.41)$$

$$p_{+-}\psi_{+-}(s) = \frac{k_{31}(k_{12}(k_{13} + k_{23} + s) + k_{13}(k_{32} + s) + s(k_{23} + k_{32} + s))}{k_{12}(k_{13} + k_{23} + s)(k_{31} + s) + (k_{21} + k_{31} + s)(k_{13}(k_{32} + s) + s(k_{23} + k_{32} + s))}, \quad (6.42)$$

$$p_{-+}\psi_{-+}(s) = \frac{k_{13}(k_{12}(k_{31} + s) + (k_{32} + s)(k_{21} + k_{31} + s))}{k_{12}(k_{13} + k_{23} + s)(k_{31} + s) + (k_{21} + k_{31} + s)(k_{13}(k_{32} + s) + s(k_{23} + k_{32} + s))}, \quad (6.43)$$

and

$$p_{--}\psi_{--}(s) = \frac{k_{12}k_{23}k_{31}}{k_{12}(k_{13} + k_{23} + s)(k_{31} + s) + (k_{21} + k_{31} + s)(k_{13}(k_{32} + s) + s(k_{23} + k_{32} + s))}. \quad (6.44)$$

As we discussed above, the dwell time distributions we have calculated here are in Laplace space; however, measured distributions are in real time. If desired, we can

produce the dwell time distributions in real time by performing an inverse Laplace transformation on these expressions. However, such an operation is not always possible for kinetic schemes larger than five states. (This is because the inverse Laplace transformation requires finding the roots of the distribution, an eigenvalue problem for which there is no formal solution for systems above five kinetic states.)

Fortunately, this is typically not necessary because the Laplace transform of the dwell time distributions can be used to generate the moments of the distribution, i.e. the mean, the variance, etc. And the moments of the distribution are often more informative than the distribution itself—as we will show in Chapter 7. It can be shown that the moments of this distribution are related to the derivative of the transform at $s = 0$. Mathematically,

$$\langle t^n \rangle = (-1)^n \left. \frac{d^n \psi(s)}{ds^n} \right|_{s=0}. \quad (6.45)$$

A similar relation holds true for the step size distribution and the moments of the distribution—the average step size, its variance, etc. Namely,

$$\langle d^n \rangle = (-i)^n \left. \frac{d^n \rho(q)}{dq^n} \right|_{q=0}. \quad (6.46)$$

While there are alternative techniques for calculating the velocity and the randomness parameter directly from the position probability density (17, 203, 204), these expression relating the moments to the transform of the distributions, Eqs. (6.45) and (6.46), can be used to calculate the velocity and the randomness parameter for any system using the appropriate relationship between the velocity and randomness parameter for the statistical class discussed above, Eqs. (6.14) – (6.16).

Finally, the complexity of these expressions is one indication of why more robust techniques for calculating these properties is needed. The matrix formalism that we introduce here is particularly conducive to computer algebra programs, which makes automation of this process trivial. A set of computer algebra code to generate these expressions is provided in the Appendix, Section 6.5.3. The power of computer algebra in the analysis of candidate kinetic models should not go unappreciated.

6.4: Summary and Conclusions

In this Chapter, we have considered the different types of statistical fluctuations that can be displayed by enzymatic systems which have multiple reaction outcomes. We found that multi-outcome systems can have two distinct types of statistical fluctuations, conditional and non-conditional. And the type of statistical class to which an enzyme belongs determines how the individual dwell times and steps should be sorted and analyzed in order to avoid mixing dwells from distinct kinetic pathways. We further showed that the statistical class of an enzyme is trivial to determine from the data itself. Namely, conditional and non-conditional branching probabilities are compared to determine if the conditional probabilities are a simple function of the non-conditional probabilities. As long as there are sufficient data to constrain these probabilities, it should be trivial to distinguish the two statistical classes. In parallel, we showed that the position probability density for kinetic models have clear signatures that allow the statistical class of the model to be easily determined.

Finally, by providing a connection between the position probability density and the different dwell time distributions and branching probabilities, and by providing a simple method for calculating the position probability, we have developed a method that

allows these complicated properties to be calculated with relative ease from kinetic models of arbitrary complexity. In recent years, it has become clear that the statistics of enzymatic dynamics with multiple outcomes is not a mathematical curiosity. Rather several systems that display multiple outcomes have now been observed. The formalism we develop here not only provides the theoretical framework to classify and analyze the complicated data from these systems, it also provides the ability to calculate the analytical solutions for important experimental measures with relative ease from candidate kinetic models that include the complexity now mandated by experimental data.

6.5: Appendices

6.5.1: Deriving the Position Probability Density

Consider a kinetic system in which there is the possibility of taking m different types of steps, each of which is preceded by a distinct kinetic pathway. We allow the dwell time for each step to depend not only on the type of step that succeeds the dwell, but the type of step that precedes it as well. Thus, there are m^2 distinct dwell time distributions, which in Laplace space we denote by $\tilde{\psi}_{ij}(s)$ where i is the index of the type of step preceding the dwell and j is the type of step following it. There will also be m different step size distributions, denoted in Fourier space by $\rho_i(q)$.

The probability to be at a position, x , at a given time, t , is the sum of the probability to arrive at x by taking exactly N steps in the duration, t , for all N . In Fourier-Laplace space this can be written as

$$\tilde{P}(q,s) = \sum_{N=0}^{\infty} \tilde{P}(q,s,N), \quad (6.47)$$

where $\tilde{P}(q,s,N)$ is the Fourier-Laplace transform of the probability of arriving at position x in a duration t by exactly N steps. We will determine the general form for $\tilde{P}(q,s,N)$ by extrapolating a pattern from explicit values for low N .

Consider first the case that the motor has not taken a step in time t , i.e. $N=0$. Physically, the motor starts in the kinetic state corresponding to a preceding step of type i with some initial probability p_{0i} , chooses the path corresponding to a step of type j with some probability p_{ij} , and then does not complete it. The final probability is the sum over all initial conditions and possible choices for the different kinetic paths:

$$\tilde{P}(q,s,0) = \sum_{i=1}^m \sum_{j=1}^m p_{0i} p_{ij} \frac{1 - \tilde{\psi}_{ij}(s)}{s}, \quad (6.48)$$

where we have used the fact that if the dwell time distribution is given by $\tilde{\psi}(s)$, the probability of not taking a step within a given time t is given by $(1 - \tilde{\psi}(s))/s$. For the $N=1$ case, the motor starts in its initial state i with probability p_{0i} , chooses a path out of that state j with probability p_{ij} , completes this path generating a step of type j the size and duration of which are governed in Fourier-Laplace space by $\rho_j(q)\psi_{ij}(s)$, chooses another path k with a probability p_{jk} , and then does not complete this path with probability $(1 - \tilde{\psi}_{jk}(s))/s$. Again, the total probability is the sum over all possible combinations of paths

$$\tilde{P}(q,s,1) = \sum_{i=1}^m \sum_{j=1}^m \sum_{k=1}^m p_{0i} p_{ij} \tilde{\psi}_{ij}(s) \rho_j(q) p_{jk} \frac{1 - \tilde{\psi}_{jk}(s)}{s}. \quad (6.49)$$

The $N = 2$ case adds one more completed step; thus, the probability is

$$\tilde{P}(q,s,2) = \sum_{i=1}^m \sum_{j=1}^m \sum_{k=1}^m \sum_{l=1}^m p_{0i} (p_{ij} \tilde{\psi}_{ij}(s) \rho_j(q)) (p_{jk} \tilde{\psi}_{jk}(s) \rho_k(q)) p_{kl} \frac{1 - \tilde{\psi}_{kl}(s)}{s}. \quad (6.50)$$

Eqs. (6.48)-(6.50) can be simplified greatly by defining two matrices $\tilde{\Psi}(s)$ and $\mathbf{p}(q)$ whose ij th elements equal $p_{ij} \tilde{\psi}_{ij}(s)$ and $\rho_i(q) \delta_{ij}$, respectively. In addition, we define the vectors \mathbf{p}_0 and $\tilde{\Psi}(s)$ whose i th elements equal the initial probability p_{0i} and the sum $\sum_{j=1}^m p_{ij} (1 - \tilde{\psi}_{ij}(s)) / s$. Because the sum of the probability of taking all steps j given the previous step i must be 1, the latter simplifies to $\tilde{\Psi}_i(s) = \frac{1}{s} \left(1 - \sum_{j=1}^m p_{ij} \tilde{\psi}_{ij}(s) \right)$.

With these definitions, Eqs. (6.48)-(6.50) can be written compactly as

$$\tilde{P}(q,s,0) = \mathbf{p}_0^T (\tilde{\Psi}(s) \mathbf{p}(q))^0 \tilde{\Psi}(s), \quad (6.51)$$

$$\tilde{P}(q,s,1) = \mathbf{p}_0^T (\tilde{\Psi}(s) \mathbf{p}(q))^1 \tilde{\Psi}(s), \quad (6.52)$$

and

$$\tilde{P}(q,s,2) = \mathbf{p}_0^T (\tilde{\Psi}(s) \mathbf{p}(q))^2 \tilde{\Psi}(s). \quad (6.53)$$

Extrapolating for all N ,

$$\tilde{P}(q,s,N) = \mathbf{p}_0^T (\tilde{\Psi}(s) \mathbf{p}(q))^N \tilde{\Psi}(s), \quad (6.54)$$

and the position probability density is

$$\tilde{P}(q,s) = \sum_{N=0}^{\infty} \mathbf{p}_0^T (\tilde{\Psi}(s) \mathbf{p}(q))^N \tilde{\Psi}(s). \quad (6.55)$$

Evaluating the infinite sum produces the final relation, Eq. (6.4) in the Section 6.2.4,

$$\tilde{P}(q, s) = \mathbf{p}_0^T (\mathbf{I} - \tilde{\Psi}(s)\mathbf{p}(q))^{-1} \tilde{\Psi}(s) \quad (6.56)$$

where \mathbf{I} is the identity matrix.

For a system in which there is no memory of the previous step, all distributions and probabilities have only one index, i.e. $p_{ij} \rightarrow p_j$ and $\psi_{ij} \rightarrow \psi_j$, reflecting the fact that the choice of a given step and the preceding dwell time do not depend on the previous step. The above relation for the position probability density can be simplified for such a system by noting that the elements of each column of the matrix product $\tilde{\Psi}(s)\mathbf{p}(q)$ are now identical, i.e. the elements of the j th column are $p_j \tilde{\psi}_j(s) \rho_j(q)$. Since the elements of \mathbf{p}_0^T must sum to 1, the product $\mathbf{p}_0^T \tilde{\Psi}(s)\mathbf{p}(q)$ is thus a vector with elements $p_j \tilde{\psi}_j(s) \rho_j(q)$. Moreover, the vector $\tilde{\Psi}(s)$ consists of identical elements $\frac{1}{s} \left(1 - \sum_{j=1}^m p_j \tilde{\psi}_j(s)\right)$, which can be compactly written as $(1 - \text{Tr}(\tilde{\Psi}(s))) / s$, where $\text{Tr}(\tilde{\Psi}(s))$ is the trace of $\tilde{\Psi}(s)$. It thus follows that

$$\mathbf{p}_0^T (\tilde{\Psi}(s)\mathbf{p}(q)) \tilde{\Psi}(s) = \text{Tr}(\tilde{\Psi}(s)\mathbf{p}(q)) \frac{1}{s} (1 - \text{Tr}(\tilde{\Psi}(s))). \quad (6.57)$$

It can be shown by direct matrix multiplication that powers of the matrix product $\tilde{\Psi}(s)\mathbf{p}(q)$ are given by the relation $(\tilde{\Psi}(s)\mathbf{p}(q))^N = (\text{Tr}(\tilde{\Psi}(s)\mathbf{p}(q)))^{N-1} \tilde{\Psi}(s)\mathbf{p}(q)$. Thus,

$$\tilde{P}(q, s) = \sum_{N=0}^{\infty} \mathbf{p}_0^T (\tilde{\Psi}(s)\mathbf{p}(q))^N \tilde{\Psi}(s) = \sum_{N=0}^{\infty} (\text{Tr}(\tilde{\Psi}(s)\mathbf{p}(q)))^N \frac{1}{s} (1 - \text{Tr}(\tilde{\Psi}(s))), \quad (6.58)$$

which, summing over N , simplifies to

$$\tilde{P}(q, s) = \frac{1}{s} \frac{1 - \text{Tr}(\tilde{\Psi}(s))}{1 - \text{Tr}(\tilde{\Psi}(s)\mathbf{p}(q))}, \quad (6.59)$$

which is Eq. (6.3) in Section 6.4.2.

6.5.2: Connecting the Moments of ϕ_{ij} and ρ_i to v and r

Eqs. (6.2)-(6.4) in Section 6.4.2 connect the Fourier-Laplace transform of the position probability density $\tilde{P}(q,s)$ to the Laplace transform of the dwell time distributions $\tilde{\psi}(s)$ and the Fourier transform of the step size distributions $\rho(q)$. These expressions allow us to express the moments of $\tilde{P}(q,s)$ —more specifically, the related velocity v and randomness parameter r —in terms of the moments of the dwell time distributions and step size distributions. We adopt here the definition $r = 2D/v\langle d \rangle$ so that the final expressions are completely general (208).

We first consider a system that displays correlated stepping statistics in which Laplace transforms of the dwell time distributions $\tilde{\psi}_{\pm\pm}(s)$ and the Fourier transforms of the step size distributions $\rho_{\pm}(q)$ are related to the position probability density $\tilde{P}(q,s)$ via Eq. (6.4). We consider a system with only two types of steps, labeled with + or -, but this calculation can be extended to systems with m step distributions. The mean velocity v is determined from the average position in Laplace space, obtained by calculating the derivative of Eq. (6.4) at $q = 0$:

$$\langle \tilde{x}(s) \rangle = i \frac{\partial \tilde{P}(q,s)}{\partial q} \Big|_{q=0}. \quad (6.60)$$

With no loss in generality we can assume that the initial step is a forward step, and evaluating the derivative in Eq. (6.60), we find

$$\langle \tilde{x}(s) \rangle = \frac{(p_{++}\tilde{\psi}_{++} + p_{+-}\tilde{\psi}_{+-}p_{-+}\tilde{\psi}_{-+} - p_{++}\tilde{\psi}_{++}p_{--}\tilde{\psi}_{--})\langle d_+ \rangle + p_{+-}\tilde{\psi}_{+-}\langle d_- \rangle}{s(1 - p_{++}\tilde{\psi}_{++} - p_{--}\tilde{\psi}_{--} + p_{++}\tilde{\psi}_{++}p_{--}\tilde{\psi}_{--} - p_{+-}\tilde{\psi}_{+-}p_{-+}\tilde{\psi}_{-+})}. \quad (6.61)$$

Expanding the Laplace transform of the dwell time distributions around $s = 0$ and relating the derivatives to the moments of these distributions yields

$$\tilde{\psi}_{\pm\pm}(s) = \tilde{\psi}_{\pm\pm}(0) + s \frac{d\tilde{\psi}_{\pm\pm}}{ds} \Big|_{s=0} + \frac{1}{2}s^2 \frac{d^2\tilde{\psi}_{\pm\pm}}{ds^2} \Big|_{s=0} + \dots = 1 - s\langle t_{\pm\pm} \rangle + \frac{1}{2}s^2\langle t_{\pm\pm}^2 \rangle + \dots \quad (6.62)$$

Inserting these expressions into Eq. (6.62) and expanding in powers of $1/s$ yields

$$\begin{aligned} \langle \tilde{x}(s) \rangle &= \frac{\langle d \rangle}{s^2\langle t \rangle} - \langle d \rangle \frac{p_{++}p_{--}\langle t_{++} \rangle\langle t_{--} \rangle - p_{+-}p_{-+}\langle t_{+-} \rangle\langle t_{-+} \rangle}{s\langle t \rangle^2(p_{+-} + p_{-+})} \\ &\quad + \frac{\langle d \rangle\langle t^2 \rangle}{2s\langle t \rangle^2} - \frac{p_{+-}\langle t_{+-} \rangle\langle d_- \rangle - p_{--}\langle t_{--} \rangle\langle d_+ \rangle}{s\langle t \rangle(p_{+-} + p_{-+})} - \frac{\langle d_+ \rangle}{s} + O(s^0), \end{aligned} \quad (6.63)$$

where we have defined composite step size and dwell time moments via

$$\langle d^n \rangle = p_+\langle d_+^n \rangle + p_-\langle d_-^n \rangle \text{ and } \langle t^n \rangle = p_+\langle t_+^n \rangle + p_-\langle t_-^n \rangle, \text{ where } p_{\pm} \text{ is the probability of}$$

taking a given step and $\langle t_{\pm}^n \rangle$ is the n th moment of the distribution of all dwells preceding

a forward or backward step. These expressions can be related to the individual branching probabilities and dwell time moments via $p_{\pm} = p_{\mp\pm}/(p_{+-} + p_{-+})$ and

$$\langle t_{\pm}^n \rangle = p_{\pm\pm}\langle t_{\pm\pm}^n \rangle + p_{\pm\mp}\langle t_{\pm\mp}^n \rangle, \text{ expressions derived by Tsygankov et al.(206). Only terms}$$

with negative powers of s are needed since they are the only terms that will survive the inverse Laplace transform.

Evaluating the inverse transform and limit of Eq. (6.63):

$$\lim_{t \rightarrow \infty} \langle x(t) \rangle = \frac{\langle d \rangle}{\langle t \rangle} t - \langle d \rangle \frac{p_{++} p_{--} \langle t_{++} \rangle \langle t_{--} \rangle - p_{+-} p_{-+} \langle t_{+-} \rangle \langle t_{-+} \rangle}{\langle t \rangle^2 (p_{+-} + p_{-+})},$$

$$+ \frac{\langle d \rangle \langle t^2 \rangle}{2 \langle t \rangle^2} - \frac{p_{+-} \langle t_{+-} \rangle \langle d_{-} \rangle - p_{-+} \langle t_{-+} \rangle \langle d_{+} \rangle}{\langle t \rangle (p_{+-} + p_{-+})} - \langle d_{+} \rangle, \quad (6.64)$$

Taking the time derivative required yields the expected relation between the velocity and the composite moments (17),

$$v = \frac{\langle d \rangle}{\langle t \rangle}. \quad (6.65)$$

To derive the diffusion constant D and thus the randomness parameter r , we need the second moment of the position, which is derived via

$$\langle \tilde{x}^2(s) \rangle = - \left. \frac{\partial^2 \tilde{P}(q, s)}{\partial q^2} \right|_{q=0}. \quad (6.66)$$

Applying this to the position probability density, Eq. (6.42), expanding the dwell time distributions as above, and expanding around $s = 0$ yields,

$$\begin{aligned} \langle \tilde{x}(s)^2 \rangle &= \frac{2 \langle d \rangle^2}{s^3 \langle t \rangle^2} + \frac{\langle d^2 \rangle - 2 p_{+} \langle d_{+} \rangle^2 - 2 p_{-} \langle d_{-} \rangle^2 - 2 \langle d_{+} \rangle \langle d_{-} \rangle}{s^2 \langle t \rangle} + \frac{2 \langle d \rangle^2 \langle t^2 \rangle}{s^2 \langle t \rangle^3} \\ &+ 2(\langle d \rangle + p_{+} \langle d_{+} \rangle) \frac{p_{--} \langle t_{--} \rangle \langle d_{+} \rangle - p_{+-} \langle t_{+-} \rangle \langle d_{-} \rangle}{s^2 \langle t \rangle^2 (p_{+-} + p_{-+})} \\ &+ 2 p_{-} \langle d_{-} \rangle \frac{p_{++} \langle t_{++} \rangle \langle d_{-} \rangle - p_{-+} \langle t_{-+} \rangle \langle d_{+} \rangle}{s^2 \langle t \rangle^2 (p_{+-} + p_{-+})} \\ &- 4 \langle d \rangle^2 \frac{p_{++} p_{--} \langle t_{++} \rangle \langle t_{--} \rangle - p_{+-} p_{-+} \langle t_{+-} \rangle \langle t_{-+} \rangle}{s^2 \langle t \rangle^3 (p_{+-} + p_{-+})} + O(s^{-1}) \end{aligned}, \quad (6.67)$$

Transforming to the time domain and taking the appropriate time derivative and limit,

$$\begin{aligned} \lim_{t \rightarrow \infty} \frac{\partial}{\partial t} \langle x(t)^2 \rangle &= \frac{\langle d^2 \rangle - 2p_+ \langle d_+ \rangle^2 - 2p_- \langle d_- \rangle^2 - 2\langle d_+ \rangle \langle d_- \rangle}{\langle t \rangle} + \frac{2\langle d \rangle^2}{\langle t \rangle^2} t + \frac{2\langle d \rangle^2 \langle t^2 \rangle}{\langle t \rangle^3} \\ &+ 2(\langle d \rangle + p_+ \langle d_+ \rangle) \frac{p_{--} \langle t_{--} \rangle \langle d_+ \rangle - p_{+-} \langle t_{+-} \rangle \langle d_- \rangle}{\langle t \rangle^2 (p_{+-} + p_{-+})} \\ &+ 2p_- \langle d_- \rangle \frac{p_{++} \langle t_{++} \rangle \langle d_- \rangle - p_{-+} \langle t_{-+} \rangle \langle d_+ \rangle}{\langle t \rangle^2 (p_{+-} + p_{-+})} \\ &- 4\langle d \rangle^2 \frac{p_{++} p_{--} \langle t_{++} \rangle \langle t_{--} \rangle - p_{+-} p_{-+} \langle t_{-+} \rangle \langle t_{-+} \rangle}{\langle t \rangle^3 (p_{+-} + p_{-+})} \end{aligned}, \quad (6.68)$$

Eq. (6.68) can now be used with (6.63) to solve for the diffusion constant and for the randomness parameter (17), $r = 2D/v\langle d \rangle$, yielding

$$\begin{aligned} r &= \frac{\langle d^2 \rangle - \langle d \rangle^2}{\langle d \rangle^2} + \frac{\langle t^2 \rangle - \langle t \rangle^2}{\langle t \rangle^2} + 2 \frac{\langle d \rangle^2 - p_+ \langle d_+ \rangle^2 - p_- \langle d_- \rangle^2}{\langle d \rangle^2} \\ &+ 2p_+ \langle d_+ \rangle \frac{p_{--} \langle t_{--} \rangle \langle d_+ \rangle - p_{+-} \langle t_{+-} \rangle \langle d_- \rangle}{(p_{+-} + p_{-+}) \langle d \rangle^2 \langle t \rangle} + 2p_- \langle d_- \rangle \frac{p_{++} \langle t_{++} \rangle \langle d_- \rangle - p_{-+} \langle t_{-+} \rangle \langle d_+ \rangle}{(p_{+-} + p_{-+}) \langle d \rangle^2 \langle t \rangle} \\ &- 2 \frac{p_{++} p_{--} \langle t_{++} \rangle \langle t_{--} \rangle - p_{+-} p_{-+} \langle t_{-+} \rangle \langle t_{-+} \rangle}{(p_{+-} + p_{-+}) \langle t \rangle^2} \end{aligned} \quad (6.69)$$

As detailed above, while the particular choice of initial conditions affects the specific values of $\langle \tilde{x}(s) \rangle$ and $\langle \tilde{x}(s)^2 \rangle$, it does not affect either the mean velocity or randomness parameter. This can be verified directly by repeating this calculation with a backward step as the initial condition.

We can now derive the same relations for a system with uncorrelated stepping pathways by dropping the first index of every term in Eqs. (6.64) and (6.68). With some algebra, we find that the velocity obeys Eq. (6.65) and that the randomness reduces to

$$r = \frac{\langle d^2 \rangle - \langle d \rangle^2}{\langle d \rangle^2} + \frac{\langle t^2 \rangle - \langle t \rangle^2}{\langle t \rangle^2} + 2 \frac{\langle d \rangle \langle t \rangle - p_+ \langle d_+ \rangle \langle t_+ \rangle - p_- \langle d_- \rangle \langle t_- \rangle}{\langle d \rangle \langle t \rangle} \quad (6.70)$$

where it can be verified that the above expressions for composite moments of the step size and dwell times reduce to the expected $\langle d^n \rangle = p_+ \langle d_+^n \rangle + p_- \langle d_-^n \rangle$ and $\langle t^n \rangle = p_+ \langle t_+^n \rangle + p_- \langle t_-^n \rangle$.

Finally, we can derive the velocity and randomness for a system with only one stepping pathway by setting one of the branching probabilities to zero. We find that the velocity continues to obey Eq. (6.65) as expected and that the randomness parameter becomes

$$r = \frac{\langle d^2 \rangle - \langle d \rangle^2}{\langle d \rangle^2} + \frac{\langle t^2 \rangle - \langle t \rangle^2}{\langle t \rangle^2}, \quad (6.71)$$

a result derived previously (208).

6.5.3: Mathematica Code for Example System

With increasingly complex kinetic models, the position probability density, the dwell time distributions, and the branching probabilities become extraordinarily complicated. For example, in one candidate model considered for the packaging data in Chapter 4, the mean dwell time as a function of the individual kinetic rates filled an entire page of text when fully simplified. By hand such calculations would be tedious and highly error prone. One solution is to move to numerical simulations, avoiding this complexity (or rather hiding it). However, analytical solutions offer an ability to infer properties of a model that simply cannot be achieved from numerical simulations, where one can never be sure that the full parameter space has been searched.

The formalism that we present here offers an alternative: leave the complicated and tedious algebra to computers. All of the matrix manipulations described above can be easily done, and a computer program, such as *Mathematica* (Wolfram Research, Champaign, IL), has no problem with algebraic solutions that are one page or longer. Here we include the *Mathematica* code required to calculate the different properties of the example kinetic model above.

We start by entering the rate matrix **M**:

```
M = {{-k21 - k31, k12, k13 ρp}, {k21, -k12 - k32, k23}, {k31 ρm, k32, -k13 - k23} };
```

With this matrix, we can calculate the position probability density with a positive step as the first step (**ρ_p** is the step size distribution for this step in the above expression). This can be done with the code:

```
Pp = Sum[Inverse[s IdentityMatrix[3] - M] . {{1}, {0}, {0}}] [[i]], {i, 1, 3}] [[1]] // Simplify
```

and the position probability density with the other initial condition—a backwards step—can be calculated with

```
Pm = Sum[Inverse[s IdentityMatrix[3] - M] . {{0}, {0}, {1}}] [[i]], {i, 1, 3}] [[1]] // Simplify
```

With these expressions, we can now extract the coefficients needed to calculate the branching probabilities and dwell time distributions:

$$\text{ap} = \text{CoefficientList}\left[\frac{1}{s P_p} / . \rho_m \rightarrow 0, \rho_p\right]$$

$$\psi_{pp} = \text{FullSimplify}[-ap[2] / ap[1]]$$

$$\psi_{pm} = \text{FullSimplify}\left[\frac{(ap[2] + ap[1] - 1)}{ap[1]}\right]$$

$$pp = \psi_{pp} / . s \rightarrow 0 // \text{FullSimplify}$$

$$ppm = \psi_{pm} / . s \rightarrow 0 // \text{FullSimplify}$$

$$\psi_{ppnorm} = \frac{\psi_{pp}}{pp} // \text{FullSimplify}$$

$$\psi_{\text{pmnorm}} = \frac{\psi_{\text{pm}}}{\text{ppm}} // \text{FullSimplify}$$

where **ppp** is the branching probability for two positive steps (pp), **ppm** is the branching probability for a positive step followed by a negative step, and **oppnorm** and **opmnorm** are the normalized Laplace transform of the dwell time distributions for two positive steps and a positive and a negative step, respectively. Similar code can be used to calculate the other branching probabilities and distributions. By setting the rate of a backward step to zero, and taking an inverse Laplace transform, the dwell time distribution for the example system in Chapter 1 can be calculated analytically from the dwell time distribution for two forward steps.

Chapter 7. A Michaelis-Menten Expression for Enzymatic Fluctuations

Driven by thermal fluctuations, the dynamics of enzyme-catalyzed reactions are inherently stochastic and the time to complete a given reaction is a fluctuating quantity. Methods to measure and quantify these fluctuations now exist, as we have seen throughout this thesis. However, it is still unclear exactly what information is contained in these fluctuations and what fluctuations imply about mechanism.

In this Chapter, we extend our understanding of the informative power of fluctuations by deriving the general substrate dependence of n_{\min} —an important measure of fluctuations. In strong analogy to the Michaelis-Menten expression, we show that the substrate dependence of an entire class of important kinetic models is described by a simple closed-form expression and that all of the complexities and individuality of different kinetic models are captured in just three new “macroscopic” kinetic parameters, in analogy to the Michaelis constants k_{cat} and K_M . We use this expression to formalize many of the kinetic arguments made in Chapter 4. And, by developing a detailed understanding of how properties of the underlying kinetic model influence these new parameters, we extend our understanding of the packaging motor by providing quantitative restrictions on the way in which ATP loads to the individual subunits. The discovery that binding properties can be inferred solely from properties of the fluctuations in the dwell time, despite the fact that the binding of ATP was never

observed directly, indicates the surprising degree of mechanistic information contained in enzymatic fluctuations.

Materials for this Chapter have been taken, in part, from a manuscript coauthored by Yann Chemla and Carlos Bustamante that has not yet been submitted for publication.

7.1: Introduction

7.1.1: Previous Inferences from Fluctuations

In Chapter 4, we were able to measure the full distribution of pause or dwell durations before the 10-bp packaging bursts as a function of [ATP]. We argued that the fact that the dwell time distributions were peaked functions for all [ATP] indicated that the dwell time was governed by multiple rate-limiting kinetic events for all [ATP]. Moreover, we were able to formalize the degree to which a distribution is peaked using a new kinetic parameter, n_{\min} , defined as

$$n_{\min} = \frac{\langle \tau \rangle^2}{\langle \tau^2 \rangle - \langle \tau \rangle^2} \quad (7.1)$$

where $\langle \tau \rangle$ is the mean dwell time and $\langle \tau^2 \rangle - \langle \tau \rangle^2$ is the variance in the dwell times. This parameter and the related randomness parameter (112) are particularly powerful since it is widely believed that they provide a lower bound on the actual number of kinetic states in a given cycle (112, 127). Mathematically, if n_{actual} is the number of kinetic states in the enzymatic cycle, then it appears that for all kinetic models

$$n_{\min} \leq n_{actual}. \quad (7.2)$$

We argued in Chapter 4 that when one works at “limiting” or “saturating” concentrations of substrate, this inequality is replaced by inequalities related to the number of substrate binding events or the number of non-substrate binding events in each cycle. Thus, by investigating the value of this parameter at low and high concentrations of [ATP], we were able to argue that each dwell must contain the binding of no less than 2 ATP molecules and no less than four additional non-ATP-binding kinetic events.

Finally, by combining the observed substrate dependence of the mean dwell time—which we were able to show is well described by a Michaelis-Menten expression—with the inference that multiple ATP molecules must load each dwell, we were able to greatly limit the mechanisms by which ATP loads to the ring. In particular, we were able to argue that the binding of each ATP must be followed by an irreversible, “tight” binding transition and that one and only one subunit at a time can be competent for the binding of ATP. Remarkably these restrictions came from the simple observation that the mean dwell time as a function of [ATP] could be well described by a simple, closed-form expression.

7.1.2: Limitations to these Arguments

Overall, there are aspects of the above arguments which are not particularly formal. First, the definitions of “saturating” and “limiting” concentrations of ATP are not strict; thus, it is not clear that we probed conditions that were *sufficiently* “saturating” or “limiting” for our measured values of n_{\min} to be a reasonable or accurate estimate of the true asymptotic behavior. Second, even if we did probe an appropriate concentration range, we have not rigorously proven that the asymptotic limits of n_{\min} actually restrict

the number of binding or non-binding events as we have assumed they do; thus, it is not clear that our previous conclusions are truly strict limits on the number of kinetic events.¹² Finally, we argued that reversibility or different binding rates could change the value of n_{\min} from the expected value of four, the binding of four ATPs, to a lower value, ~ 2 . However, while this has been suggested previously by analysis of a few example systems (112), it has not be proven formally, limiting our ability to infer properties of the packaging motor from these measurements.

These are all practical concerns associated with the proper interpretation of our data. Notice, however, that none of these concerns can be raised about our interpretations of the mean dwell time versus the substrate concentration. Did we go to sufficiently “limiting” or “saturating” ATP? The fit to the Michaelis-Menten expression gives us all the information we need to provide a *quantitative* answer to this question. Can we interpret our measured k_{cat} and K_M in terms of properties of the underlying kinetic model? No, but we know this that we cannot because we understand the types of kinetic models that lead to this substrate dependence well enough to know that these properties say little about the specifics of the individual kinetic rates or dissociation constants (128). These observations beg the question: what could we learn from our measured values of n_{\min} if we had a similar expression that captures the general substrate dependence for a wide range of models, i.e. a Michaelis-Menten expression for fluctuations?

¹² For example, one might consider a particularly insidious possibility in which the binding of ATP is so reversible in a hypothetical kinetic scheme that a single subunit must bind ATP multiple times on average per dwell. This might give the impression that multiple rate-limiting events must occur in a single dwell without the need for multiple ATPs to bind to multiple subunits.

7.1.3: Analogy to Measurements of the Mean

To address this question, let's first consider, in detail, exactly how one classifies the substrate dependence of the mean dwell and what practical value this classification has for the researcher. In the typical experiment, the concentration of the enzymatic substrate will be varied and the rate of reaction measured, and then this data will be fit with a few different functions which relate the reaction rate to the substrate concentration. The function which provides the best fit will be considered the general substrate dependence of the enzyme. In general, there are essentially two types of substrate dependencies (128): the Michaelis-Menten expression

$$v = \frac{k_{cat}[S]}{K_M + [S]} \quad (7.3)$$

and the more general (but approximate¹³) Hill equation

$$v = \frac{k_{cat}[S]^n}{K_M^n + [S]^n} \quad (7.4)$$

where v is the average rate of a reaction, $[S]$ is the substrate concentration, k_{cat} is the maximum rate of the reaction, K_M —the Michaelis constant—is the substrate concentration at which the reaction proceeds at half-maximum speed, and finally n is the Hill coefficient, a number which characterizes the “shape” of the substrate dependence.

In practice, these basic substrate dependencies are of tremendous utility to the experimenter. First and foremost, they allow simple curve fitting to discriminate between classes of enzymatic behaviors—Michaelis-Menten or sigmoidal/Hill. This is

¹³ The general substrate dependence of the mean velocity is the ratio of two polynomials in substrate concentration where the form of these polynomials is very sensitive to the specifics of the kinetic scheme, i.e. the number of substrate binding states and the way in which these binding events are kinetically connected. Formally, the Hill expression is rarely the correct polynomial expression, yet it provides a useful way to determine if the substrate dependence is *not* described by the Michaelis-Menten expression.

particularly powerful because a large body of theoretical work (128) has established the basic kinetic properties that can lead to these behaviors—e.g. the binding of a single substrate molecule or the cooperative binding of multiple molecules. Thus, this classification provides the first round of restrictions on candidate kinetic models. These were the arguments that allowed us to so thoroughly restrict the mechanism by which ATP binds to the packaging motor in Chapter 4.

In addition, the parameters of these “macroscopic” substrate dependencies allow the properties of the enzyme to be concisely measured and listed, e.g. the k_{cat} and K_M . This allows the properties of different enzymes to be quickly compared and contrasted, and changes to the enzymatic behavior, due perhaps to the application of force or the introduction of inhibitors, to be easily reported. For example, the specific dependence of the k_{cat} and K_M as a function of force was what allowed Chemla et al. (59) to argue that the packaging motor translocates the DNA on product release as opposed to ATP binding. Moreover, because these expressions provide a clear relationship between rates at different substrate concentrations, one can infer the asymptotic values, i.e. the velocity at low and high substrate concentration, from measurements over a finite range. This allows a formal definition of what it means to be “saturating” or “limiting” in substrate concentration, exactly what was missing in our measurements of n_{min} discussed above.

Finally, and more subtly, these expressions provide a firm limit on the information content of these measurements. One could imagine measuring the average rate of a reaction at many different substrate concentrations, but the fact that Eq. (7.3) is completely determined by two parameters implies that once these parameters are specified, measurements at new concentrations will yield no new information.

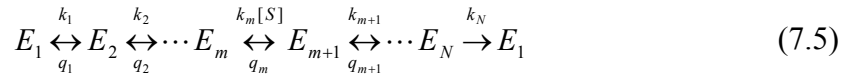
Additional measurements can only serve to better constrain the values of the k_{cat} and K_M . This knowledge is particularly useful in the construction of candidate kinetic models since it determines the number of free kinetic rates which experimental measurements can constrain. (A fact that appears to be often forgotten in the most advanced modeling work.)

In contrast, no such expression exists for enzymatic fluctuations. Yet it is clear that if such expressions existed, they would be quite useful in the interpretation of the type of data presented in Chapter 4. In this Chapter, we provide such an expression for the general substrate dependence of n_{min} . We derive a Michaelis-Menten-like expression for enzymatic fluctuations.

7.2: Theoretical Results

7.2.1: Assumptions and Schematic Proof

We model enzymatic dynamics as a first passage process through a series of discrete kinetic states, each of which has an exponentially distributed lifetime and transition rates which depend only on the current kinetic state, not the past trajectory of the enzyme (114). We restrict our analysis to an important class of kinetic models: the nearest neighbor or linear kinetic schemes which we can express symbolically as



where E_i represents the i th kinetic state of the enzyme, k_i is the forward transition rate from E_i to E_{i+1} , q_i is the reverse transition rate from E_{i+1} back to E_i , and N is the total number of kinetic states in the cycle. At one or multiple points in the cycle, one of these

transitions corresponds to the binding of a substrate molecule, S . We label the binding state m and the substrate bound state $m+1$. The transition rate for substrate binding is proportional to the substrate binding rate, $k_m[S]$, thus the forward rate, k_m is a pseudo-first-order binding constant.

This class of models contains all kinetic mechanisms in which every kinetic state is on-pathway, i.e. the mechanism contains no branches and no parallel pathways. We further restrict our analysis to all such models that demonstrate a Michaelis-Menten¹⁴ substrate dependence for the mean cycle completion time (see Figure 7.1a);

$$\langle \tau \rangle = \frac{1}{k_{cat}} + \frac{K_M}{k_{cat}} \frac{1}{[S]} , \quad (7.6)$$

where $[S]$ is the substrate concentration (128, 212). It is generally assumed that a Michaelis-Menten substrate dependence indicates that only a single substrate molecule binds each cycle. However, as has been argued before (Chapter 4), multiple substrate molecules may bind each cycle, and the mean dwell time will still obey Eq. (7.6), as long as each binding event is separated by an irreversible kinetic transition. We provide a formal proof of this in Section 7.5.2 below.

Finally, we require that at some point in time the enzyme produce a clear signal that marks the end of one cycle and the beginning of the next. For the case of a molecular motor, this transition could correspond to a physical movement such as a discrete step or rotation. However, for more general enzymes, this transition might correspond to an internal conformational change or the formation of the enzymatic product. All other kinetic transitions are hidden from detection, and it is the sum of the

¹⁴ Practically, we will refer to the substrate dependence of the mean dwell time as the Michaelis-Menten equation throughout this Chapter though technically the expected substrate dependence is actually the inverse of Eq. (7.3).

individual lifetimes of these hidden states that composes the time for the enzyme to complete one full cycle. Finally, we will assume, for simplicity, that this detectable transition is irreversible, e.g. if the detectable transition is the physical motion of the enzyme, then we require that it cannot step backwards. All other transitions can be reversible. Such an assumption is not necessary if backwards steps or reverse events can be clearly identified and cycles that begin or end with such events are separately analyzed (17, 206, 207) (as discussed in Chapter 6).

Given these assumptions, our proof of the general form for the substrate dependence of n_{\min} proceeds as follows: we start with the closed form, analytic solutions for the mean cycle completion time and the variance in these times as a function of the individual rate constants for *all* kinetic models of the form in Eq. (7.5), results which we derived in Chapter 6 and which have been derived previously (202). We then derive the necessary and sufficient restrictions to the kinetic rates required to produce a Michaelis-Menten substrate dependence for the mean dwell time, as in Eq. (3). In particular, we require that if each cycle involves the binding of multiple substrate molecules, these binding transitions be separated by additional irreversible transitions. We then apply these restrictions to the closed-form expression for the variance in the cycle times. With expressions for the substrate dependence of the mean and the variance of the dwell time, we then derive the general substrate dependence of n_{\min} in terms of three new kinetic parameters, and the specific combinations of rate constants that compose these new parameters. For interested readers, the full proof is provided in the Appendices in Section 7.5.

7.2.2: The General Substrate Dependence of n_{\min}

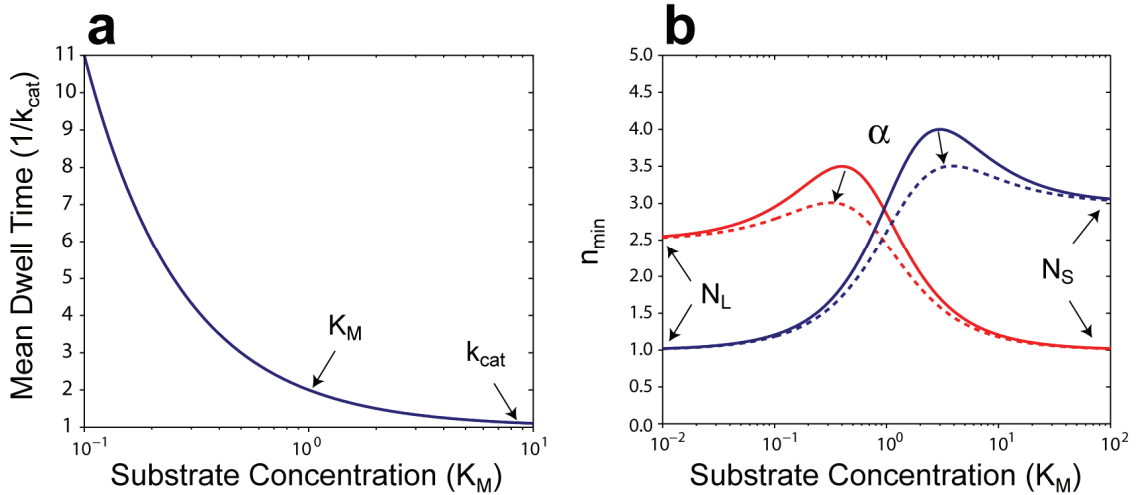


Figure 7.1. Dwell Time Statistics versus Substrate Concentration

(a) Mean dwell time versus substrate concentration. The mean dwell time is measured in units of its smallest duration, $1/k_{\text{cat}}$, and the substrate concentration is measured in units of K_M . (b) Possible behaviors for n_{\min} as a function of substrate concentration as determined by Eq. (7.7). N_L determines the asymptotic limit at low substrate concentrations while N_S determines the asymptotic limit at saturating substrate concentrations. The parameter α determines the height of the peak between these two asymptotic limits. For $\alpha > 0$ the peak is less than the sum of the two limits. The solid red curve corresponds to $N_L = 2.5$, $N_S = 1$, and $\alpha = 0$. The solid blue curve corresponds to $N_L = 1$, $N_S = 3$, and $\alpha = 0$. The dashed lines correspond to the same parameter values as the colored curves but with $\alpha = 0.3$.

Under the above assumptions, we find that the general substrate dependence of n_{\min} is given by

$$n_{\min} = \frac{N_L N_S \left(1 + \frac{[S]}{K_M}\right)^2}{N_S + 2\alpha \frac{[S]}{K_M} + N_L \left(\frac{[S]}{K_M}\right)^2}, \quad (7.7)$$

where K_M is the same parameter that sets the natural substrate scale in the mean dwell time, Eq (7.6). This expression defines a family of curves governed by three new parameters: N_L , N_S , and α . See Figure 7.1b. The fact that the substrate dependence of

any kinetic model of the form in Eq. (7.5) which has a substrate dependence of the mean which follows Eq. (7.6) is captured by such a simple expression may be surprising given the large number of kinetic rates which compose these models. However, this complexity is hidden in the functional dependence of these three new parameters on both the number of kinetic states and the individual kinetic rates. We provide these functional forms in Section 7.5.6, Eqs. (42) - (45).

7.2.3: Geometric Interpretation of New Kinetic Parameters

The three new parameters which capture the substrate dependence of n_{\min} have simple geometric interpretations. See Figure 7.1b. N_L is the value of n_{\min} at asymptotically low $[S]$, or “*Limiting*” substrate concentrations, i.e.

$$N_L = \lim_{[S]/K_M \rightarrow 0} n_{\min}. \quad (7.8)$$

N_S , on the other hand, is the value of n_{\min} at asymptotically high $[S]$, or “*Saturating*” substrate concentrations, i.e.

$$N_S = \lim_{[S]/K_M \rightarrow \infty} n_{\min}. \quad (7.9)$$

Between these two asymptotic values, n_{\min} often peaks to a value greater than either of the two limits. The third parameter, α , controls the properties of this peak if it exists. In particular, the maximum value attained by n_{\min} is

$$\max(n_{\min}) = \frac{N_L + N_S - 2\alpha}{1 - \frac{\alpha^2}{N_L N_S}}, \quad (7.10)$$

which for small α is $\sim N_L + N_S - 2\alpha$; thus, α determines the degree to which the peak value of n_{\min} is less than the sum of the two asymptotic limits, $N_L + N_S$. Finally, the peak occurs at a substrate concentration of

$$[S]_{\max} = K_M \frac{N_S - \alpha}{N_L - \alpha}. \quad (7.11)$$

If $\alpha = 0$, then n_{\min} peaks to a value of $N_L + N_S$ at $[S]_{\max} = K_M N_S / N_L$. The substrate concentration at which this maximum can occur can be either below or above the K_M depending on the larger of N_S or N_L . See Figure 7.1b.

Finally, inspection of Eq. (7.7) indicates that there will be a peak in n_{\min} if and only if

$$\alpha < \min(N_L, N_S). \quad (7.12)$$

For values of α between N_S or N_L there is no peak at finite substrate concentration whereas for values of α larger than N_S or N_L , n_{\min} does not peak, but rather drops to a local minima. Since a minimum in n_{\min} seems unphysical—this would imply that *both* increasing or decreasing the substrate concentration from this minimum would produce more rate-limiting kinetic events—it seems unlikely that a specific kinetic model can generate an α in this range. However, formally, we can only limit α such that

$$0 \leq \alpha < N_L N_S. \quad (7.13)$$

The proof of this limit is provided in Section 7.5.9.

7.2.4: Physical Meaning of the New Parameters

The three new parameters that characterize the substrate dependence of n_{\min} have clear interpretations with respect to the underlying kinetic mechanism of the enzyme. In particular, if the underlying kinetic model has $N = N_B + N_{\text{other}}$ kinetic states, where N_B is the number of substrate binding states and N_{other} is the number of other, non-substrate binding states, then the asymptotic limits of n_{\min} place restrictions on these quantities.

In particular, N_S provides a strict lower limit on the actual number of non-substrate-binding kinetic states in the cycle

$$N_S \leq N_{\text{other}}. \quad (7.14)$$

Moreover, $N_S = N_{\text{other}}$ if and only if the system visits each kinetic state once and only once and the lifetimes of each kinetic state are equal, i.e. all non-binding transitions are irreversible and have the same transition rate. Thus, any difference in the transition rates between kinetic steps or any reversibility in the cycle necessarily will result in a value of $N_S < N_{\text{other}}$. We prove these properties in Section 7.5.8.

The value of n_{\min} at asymptotically low substrate, N_L , has a similar interpretation. If the enzyme only binds one substrate molecule, i.e. $N_B = 1$, then $N_L = 1$. However, if the enzyme binds multiple substrate molecules, N_L provides a strict lower limit on the number of molecules that bind each cycle

$$N_L \leq N_B. \quad (7.15)$$

In general, N_L is a complicated function of the individual kinetic rates that are involved in the binding and commitment of each substrate molecule. However, if we define the ratio $\beta_i = k_{\text{cat},i}/K_{M,i}$ where $k_{\text{cat},i}$ and $K_{M,i}$ are the Michaelis-Menten

constants—a ratio often termed the catalytic efficiency¹⁵ (128, 213)—then it turns out that N_L is determined by a simple function of these ratios:

$$N_L = \frac{\left(\sum_{i=1}^{N_B} \frac{1}{\beta_i} \right)^2}{\sum_{i=1}^{N_B} \frac{1}{\beta_i^2}} = \frac{\left(\frac{1}{\beta_1} + \frac{1}{\beta_2} + \dots + \frac{1}{\beta_{N_B}} \right)^2}{\frac{1}{\beta_1^2} + \frac{1}{\beta_2^2} + \dots + \frac{1}{\beta_{N_B}^2}}. \quad (7.16)$$

This specific functional form implies several important properties of N_L . First, $N_L = N_B$ if and only if the catalytic efficiencies for binding each of the substrate molecules are identical. In contrast to N_S , this equality does not require that the binding of substrate molecules be irreversible or even that each binding process involves exactly the same kinetic states with the same kinetic rates. Rather, multiple substrate molecules may be bound to the enzyme via very different mechanisms, yet if the catalytic efficiencies of these processes are the same, N_L will be equal to the number of substrate molecules that bind. Second, the form of Eq. (7.16) implies that $N_L \geq 1$. This result indicates that an observed value of $N_L < 1$ implies that the enzymatic mechanism must have features not treated here, e.g. parallel catalytic pathways. This conclusion is supported by theoretical studies (199-201) on enzymatic systems that display dynamic disorder—i.e. a larger or infinite set of parallel catalytic pathways—in which it is shown that $n_{\min} < 1$. Finally, this remarkable result allows one to infer properties of the catalytic efficiencies of each of the separate subunits from the measured value of N_L without

¹⁵ The term catalytic efficiency is potentially misleading. In practice, the individual β_i are functions of only the kinetic rates reversibility connected to the binding transition—i.e. every kinetic rate starting with the first irreversible transition before binding proceeding to the first irreversible transition after binding. And these rates need not include important catalytic events; thus, a better term might be *binding propensity*.

knowledge or specific assumptions about the underlying kinetic transitions that are involved in the binding and commitment of substrate molecules to the catalytic cycle.

Finally, the value of the parameter α places some physical restrictions on the enzymatic mechanism. In particular, $\alpha = 0$ *if and only if* 1) the binding of substrate molecules is strictly irreversible and 2) the binding state is not in equilibrium with the previous kinetic state. In other words, a measured value of $\alpha = 0$ indicates that the local structure of the substrate-binding scheme is of the following form:



where E' is the kinetic state that proceeds the binding state, E is the substrate binding state, S is the substrate docked state, and the arrows represent irreversible transitions. If the enzyme binds multiple substrate molecules, then condition (7.17) must be true for each binding transition. This is a particularly remarkable conclusion as it indicates that measurements of the substrate dependence of dwell time fluctuations in which substrate binds reversibly or binds irreversibly via the mechanism in Eq. (7.17) have fundamentally different statistical properties.

7.3: Application to the Packaging Motor

7.3.1: Fitting the Measured Data

To illustrate the type of analysis possible with the general substrate dependence for enzymatic fluctuations derived here and the general information contained in its associated parameters, we have applied this analysis to the data collected on the packaging motor of the bacteriophage $\varphi 29$. In Chapter 4 we showed that we can observe the discrete steps of this motor and compile the exact time between steps—the dwell

times. We calculated both the average dwell time (Figure 7.2a) and the variance in these times as a function of [ATP], and used these values to calculate n_{\min} for all [ATP] (Figure 7.2b).

As described in Chapter 4, the mean dwell time is well described by a Michaelis-Menten [ATP] dependence (Figure 7.2a). Thus, we expect that the substrate dependence of the measured n_{\min} should be well described by the general substrate dependence derived here, Eq. (7.7). To test this hypothesis, we first fit the n_{\min} data in Figure 7.2b with Eq. (7.7) allowing all four parameters to float. Figure 7.2b shows that the resulting fit describes well the substrate dependence of the data (solid black line), producing a $K_M = 36 \pm 18 \mu\text{M}$, consistent with the value measured directly from the mean dwell time, $K_M = 23 \pm 7 \mu\text{M}$. The agreement between the K_M measured from $\langle \tau \rangle$ and from n_{\min} lends support to both the data and the theoretical treatment considered above. Given this support, we then refit the n_{\min} values using the K_M measured from the mean dwell time, which is better constrained than the value measured from a fit to n_{\min} directly, to produce better constraints on the parameters of n_{\min} . Again, Figure 7.2b shows that the data are well fit by Eq. (7.7) (dashed black line). Table 7.1 lists the resulting values of N_L , N_S , and α and their uncertainties from these fits.

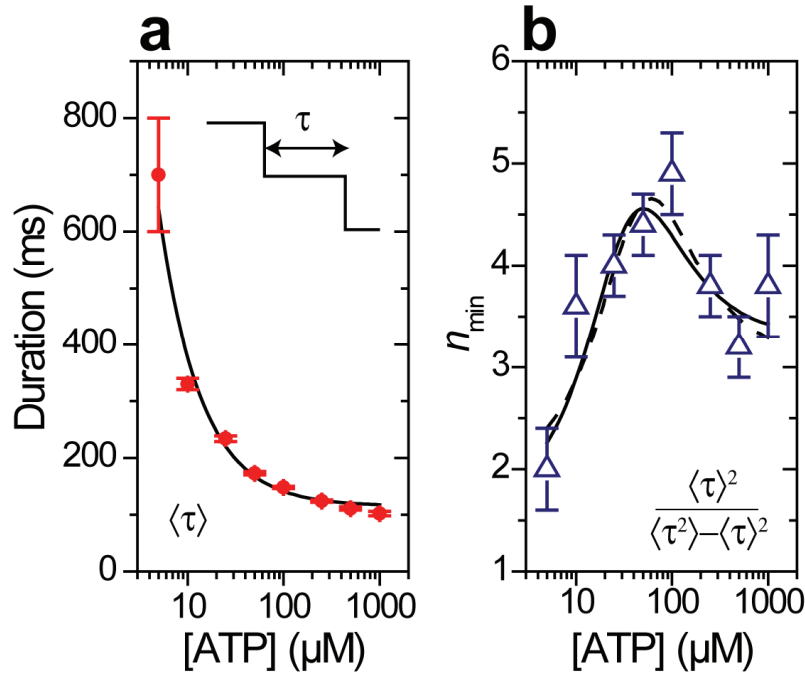


Figure 7.2. Fitting the Measured Data

(a) Mean dwell time as a function of [ATP] with a Michaelis-Menten fit (solid black). (b) n_{\min} as a function of [ATP]. The dashed black line corresponds to a fit to Eq. (7.7) with K_M free and the solid black line corresponds to the fit with the K_M fixed to the value determined by the Michaelis-Menten fit in (b). Fit values are listed in Table 7.1. Adapted with permission from Macmillan Publishers Ltd: Nature, Ref. (20), © 2009.

Table 7.1. Parameter Fits to Packaging Data

Parameter	Michaelis-Menten	n_{\min} (Floating K_M)	n_{\min} (Fixed K_M)
k_{cat}	$8.7 \pm 0.2 \text{ s}^{-1}$	N/A	N/A
K_M	$23 \pm 7 \mu\text{M}$	$36 \pm 18 \mu\text{M}$	$23 \mu\text{M}$
N_L	N/A	1.9 ± 0.4	1.6 ± 0.3
N_S	N/A	3.1 ± 0.3	3.3 ± 0.2
α	N/A	0.2 ± 0.3	0.2 ± 0.3

7.3.2: Asymptotic Limits

The specific fit values of the new kinetic parameters associated with n_{\min} have several implications for the kinetic mechanism of the packaging motor. First, a value of N_L of

1.6 ± 0.3 indicates that no less than 2 ATP molecules must bind to the motor each cycle, confirming our previous conclusions. In Chapter 4, we drew this conclusion from the measured value of n_{\min} under conditions in which ATP was limiting for the mean dwell time ($5 \mu\text{M} [\text{ATP}]$). However, as mentioned above, it is not obvious that “sufficiently limiting” for the mean dwell time implies that [ATP] is low enough that n_{\min} has reached its asymptotic value. The fit value of N_L confirms that the lowest value of [ATP] used in these studies is sufficiently limiting with respect to n_{\min} and that the previous use of the lower value as an estimate of the asymptotic limit was valid. More importantly, by fitting these data with Eq (7.7), we need not estimate the asymptotic limit from a single measurement, but rather we can constrain this asymptotic limit using all of the measurements of n_{\min} over the finite range of [ATP] probed. The result is a better constrained estimate for the asymptotic value (compare the uncertainty in the single measurement at $5 \mu\text{M}, \pm 0.4$, to the fit value, ± 0.3).

Second, a value of N_S of 3.3 ± 0.2 , indicates that no less than 4 additional, non-ATP-binding states, must compose the kinetic cycle. Again, this result confirms the previous conclusions which were made by interpreting the measured value of n_{\min} at the highest [ATP] measured, 1 mM. As above, the assumption implicit in the arguments in Chapter 4 was that 1 mM [ATP] was sufficiently saturating so that n_{\min} measured at high [ATP] would be a good approximation for the asymptotic limit. The fit value of N_S confirms that this was in fact the case for the previous measurements. And, as above, the use of Eq. (7.7) allows us to estimate the true asymptotic limit from values measured over a finite range of [ATP], resulting in a better estimate for this parameter (± 0.5 for the measurement at 1 mM versus ± 0.2 for the fit value).

Finally, the measured value of α is very small, nearly zero, suggesting that the binding of ATP is not likely to be highly reversible. This result is consistent with the ATP binding mechanism proposed in Chapter 4, in which ATP is quickly committed to hydrolysis by a tight binding reaction. However, the relatively large uncertainty on this parameter prohibits drawing extensive conclusions from its value.

7.3.3: Restricting the Catalytic Efficiencies of Binding

The specific relationship between N_L and the catalytic efficiencies of the individual subunits also allows us to draw novel conclusions about the binding properties of the individual subunits. In particular, under the assumption that four ATPs load each cycle, we can use the specific functional relationship between the individual catalytic efficiencies of each subunit and N_L , as displayed in Eq. (7.16), to place quantitative restrictions on the binding properties of the individual subunits.

First, the measured value of $N_L \neq 4$ immediately allows us to conclude that even though the individual ATPase subunits are chemically identical, they *cannot* have identical catalytic efficiencies. From previous work (112), it was known that reversibility in a kinetic transition would lower n_{\min} . Thus, it was assumed that a value of N_L less than four could be explained by four identical subunits, binding ATP with identical catalytic efficiencies, but with some reversibility in the binding of ATP (20). However, Eq. (7.16) indicates that this is not the case; only differences in the catalytic efficiencies can lower N_L from the actual number of binding substrate molecules, not reversibility in binding alone. Thus, we must conclude that because $N_L \neq 4$ the individual and identical

subunits in the packaging motor cannot bind ATP with identical kinetic rates and identical catalytic efficiencies.

This result immediately implies symmetry breaking among the otherwise identical subunits of the pentameric ring, i.e. the individual subunits, or a subset of the subunits, must “know” their relative position within the ring. Physically, this implies that the catalytic efficiency of a given subunit must depend on the chemical state of its neighbors, e.g. empty, ATP bound, etc. We can use Eq. (7.16) and the measured value of N_L to place quantitative limits on the relative relationships between the catalytic efficiencies of the different subunits. First, we parameterize the system in the following way: the subunits are ordered from smallest catalytic efficiency to largest and the catalytic efficiency of each subunit is described as function of the previous subunit, i.e.

$$\begin{aligned} k_{cat,1}/K_{M,1} &= a_1 k_{cat,0}/K_{M,0} \\ k_{cat,2}/K_{M,2} &= a_2 k_{cat,1}/K_{M,1}, \\ k_{cat,3}/K_{M,3} &= a_3 k_{cat,2}/K_{M,2} \end{aligned} \quad (7.18)$$

as depicted in Figure 7.3a. By restricting $a_1, a_2, a_3 \geq 1$, we maintain the specific ordering of the subunits and insure that a specific combination of efficiencies is not considered twice. This ordering should not be confused with the physical ordering of the subunits in the ring. Because the binding dynamics of each subunit are not observed directly, the measured dwell time would have the same statistics if the smallest catalytic efficiency corresponded to the first ATP binding per dwell or the last ATP binding, or anything in between.

Under this parameterization, Eq. (7.16) becomes

$$N_L = \left(1 + a_1^{-1} + a_1^{-1}a_2^{-1} + a_1^{-1}a_2^{-1}a_3^{-1}\right)^2 / \left(1 + a_1^{-2} + a_1^{-2}a_2^{-2} + a_1^{-2}a_2^{-2}a_3^{-2}\right). \quad (7.19)$$

Combined with the measured value of $N_L = 1.6$, this expression defines a unique three dimensional surface that constrains the possible catalytic efficiencies in the ring. This surface is shown in Figure 7.3b and has several interesting features. First, not all combinations of a_1 and a_2 are permissible, rather a_1 and a_2 must be within a narrow range of values to produce the measured N_L (colored region in Figure 7.3b). In particular, a_1 is bounded by 3.0 ± 1.9 and 10.7 ± 5.2 , implying that even if the catalytic efficiencies of the third and fourth subunits are very large, the second subunit must have a catalytic efficiency at least ~ 3 times larger but not more than ~ 11 times larger than the first subunit to produce the measured N_L . (Error bars are propagated from the error in N_L)

Within these permissible values, there are two interesting cases which are worth specific attention. These cases are highlighted in Figure 7.3b. First, if one and only one subunit is distinct from the others, i.e. the other three have identical catalytic efficiencies ($a_2 = a_3 = 1$), then this “special” subunit must have a catalytic efficiency 10.7 ± 5.2 times smaller than the other three. In such a model, one might imagine that the first or, perhaps, last subunit to bind ATP within a cycle would sense the asymmetry in the ring and have a distinct catalytic efficiency for binding that ATP.

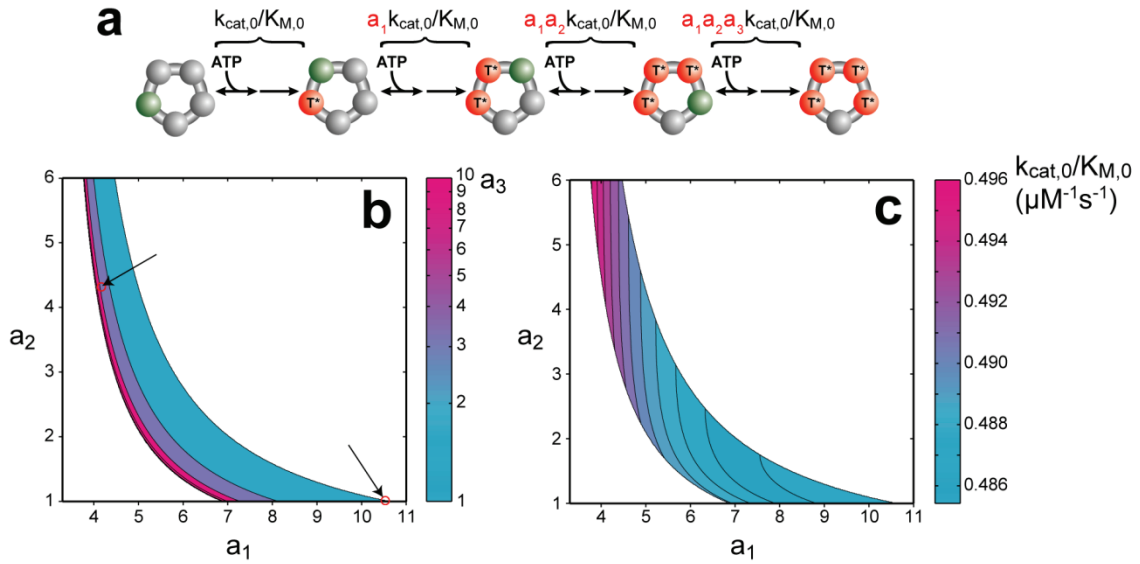


Figure 7.3. Restricting the Catalytic Efficiencies of the Different Subunits

(a) A cartoon depiction of the loading cycle of the pentameric ring ATPase that drives genome compaction in the bacteriophage $\varphi 29$. We parameterize the differences between the catalytic efficiencies of each subunit, $k_{cat,i}/K_{M,i}$, with the multiplicative parameters a_1 , a_2 , and a_3 . The parameters are restricted to values of $a_1, a_2, a_3 \geq 1$. The order depicted here need not be the actual order within the ring. (b) Contour plot of the possible combinations of a_1 , a_2 , and a_3 which generate an $N_L = 1.6$. White regions correspond to combinations of a_1 and a_2 for which there is no a_3 which will produce the measured value of N_L . Arrows highlight specific combinations of a_1 , a_2 , and a_3 mentioned in the text. (c) Contour plot of the smallest catalytic efficiency in the ring given the plotted values of a_1 and a_2 and the corresponding value of a_3 from (b).

Alternatively, each subunit might “know” its relative position within a catalytic cycle—i.e. 1st, 2nd, etc—and the catalytic efficiency at which each subunit binds ATP might depend on its relative position. In this case, it is useful to consider a model in which the catalytic efficiency of each subunit increases with respect to the previous subunit by the same “average” geometric amount, i.e. $a_1 = a_2 = a_3$. Figure 7.3b shows that to produce the measured value of N_L , this geometric factor must be 4.3 ± 1.7 . Thus, on average, the catalytic efficiencies between the different subunits in the packaging motor must increase (or decrease) by a factor ~ 4 as each ATP loads.

This later model, in which each subunit increases its catalytic efficiency with respect to the previous subunit, is essentially the text-book definition of allostery (128), and in general would be expected to produce a sigmoidal substrate dependence for the mean dwell time. However, the binding events are decoupled by the irreversible transitions between them, producing the simple Michaelis-Menten [ATP] dependence observed in Figures 7.1a and 7.2a. Are such irreversible events physically reasonable? In general, it is thought that one of the intermediate kinetic states in the binding of ATP or other nucleotide triphosphates involves the formation of a large number of hydrogen bonds (59, 166). The formation of these bonds is thought to release enough free energy to make the reverse reaction, breaking these bonds, highly unlikely. Thus, it is not unreasonable to think that such irreversible binding transitions might be a general part of the binding mechanism for ATPases.

Once the specific relationships between the catalytic efficiencies has been determined by Eq. (7.19) and the surface in Figure 7.3b, it is possible to calculate the initial catalytic efficiency by using the fact that the measured catalytic efficiency for the entire binding process, the binding and catalysis of all four ATPs, is the sum of the individual catalytic efficiencies (Eq. 7.35) below; thus, using the parameterization above, we find that

$$k_{cat,0}/K_{M,0} = k_{cat}/K_M \left(1 + a_1^{-1} + a_1^{-1}a_2^{-1} + a_1^{-1}a_2^{-1}a_3^{-1}\right). \quad (7.20)$$

The specific values for the smallest catalytic efficiency in the system, $k_{cat,0}/K_{M,0}$, as a function of a_1 and a_2 are shown in Figure 7.3c.

7.4: Discussion and Conclusions

Enzymatic dynamics are dominated by fluctuations, and techniques for quantifying these fluctuations directly are becoming increasingly routine (18, 107, 110). In this Chapter, we extend fluctuation analysis by proving that for a wide range of kinetic models the substrate dependence of a useful measure of fluctuations, n_{\min} , is governed by a single general expression. Moreover, we show that this expression is parameterized by just three new kinetic parameters: N_L which sets the value of n_{\min} at asymptotically limiting substrate concentrations, N_S which sets the value of n_{\min} at asymptotically saturating substrate concentrations, and α which parameterizes the difference between the maximum value of n_{\min} and the sum of the two asymptotic limits, $N_L + N_S$. Moreover, we prove that these parameters provide powerful, model-independent constraints on the underlying kinetic mechanism of the enzyme. In particular, N_L and N_S provide strict lower bounds on the number of substrate binding events and non-substrate binding events, respectively, while the specific value of α provides information on the degree to which the docking of substrate is strictly irreversible. Finally, we illustrate the power of this analysis by using it to capture the substrate dependence of the fluctuations observed for the packaging motor of the bacteriophage $\varphi29$. The values we derive from fits to previous data not only rigorously confirm previous conclusions by providing the true asymptotic values of n_{\min} at low and high substrate concentration, they also allow us to greatly restrict the possible values of the catalytic efficiencies for the different subunits.

What is the advantage of a general expression for the substrate dependence of n_{\min} ? Extensive theoretical studies of the mean enzymatic behavior as a function of

different experimental conditions have revealed that there are only a small number of basic substrate dependencies for the mean velocity, the Michaelis-Menten expression and the more general, yet approximate, Hill expression (128). Knowing these general forms allows experimentalists to classify the behavior of their enzyme and to extract the relevant kinetic parameters, such as k_{cat} and K_M . In this sense, the general substrate dependence for n_{min} that we provide here is the first step in providing the necessary tools to perform similar classification of enzymes based on fluctuations. Dynamics can now be classified based the measured values of N_L , N_S , and α in addition to the values of k_{cat} , K_M , and k_{cat}/K_M .

In addition, a general substrate dependence, as provided by Eq. (7.7), provides experimentalists with a way to quantitatively determine if truly “saturating” or “limiting” conditions have been probed. Given that much of the informative power of n_{min} comes from its values at asymptotically low and high substrate concentrations, an understanding of what signifies a saturating or limiting concentration of substrate is crucial to extracting information from fluctuations. Of course, truly saturating or limiting substrate concentrations can never be probed, but by specifying the specific relationship between n_{min} at different substrate concentrations, Eq. (7.7) allows the asymptotic limits of n_{min} to be inferred from measurements over a finite range of substrate concentrations.

More fundamentally, a general substrate dependence for n_{min} provides an understanding of the information content of such measurements. Measurements of the mean dwell time or n_{min} can be made at many different substrate concentrations, yet these measurements are not independent of one another. For example, a mean dwell time that is described by the Michaelis-Menten expression is completely determined by just

two independent parameters, k_{cat} and K_M . No matter how many different substrate concentrations are probed, these measurements only serve to better constrain these two parameters. This is an important realization since a general kinetic model may have many more than two independent kinetic rates; thus, measurements of the mean dwell time as a function of substrate concentration *do not* uniquely constrain even the simplest kinetic model. In this light, the results we provide here reveal the information content of the second moment of the fluctuations. Specifically, if the n_{min} of a given system has a substrate dependence described by Eq (7.7), then these measurements will provide only three additional constraints on the underlying kinetic mechanism. Once these parameters are specified, additional measurements at new substrate concentrations will only better constrain these parameters, not yield new constraints on the system. Moreover, it is now clear that there is a large degree of degeneracy in the types of kinetic models which produce a given substrate dependence for both the mean dwell time and n_{min} ; thus, care should be taken before touting the validity of specific kinetic models because they can be fit to the experimental data. Rather, experimental data should be used to dictate features of the kinetic scheme, not specifics.

Despite the seemingly limited information content of measurements of the substrate dependence of n_{min} , the constraints provided by these measurements are fundamentally different than those provided by the mean dwell time. In practice, the specific values of k_{cat} or K_M say very little about the individual kinetic rates or binding affinities of the underlying kinetic model. In contrast, the parameters of n_{min} provide fundamental limits on the enzymatic mechanism. For example, a measured value of N_S places a strict limit on the number of kinetic states that must exist in the underlying

kinetic model. Any kinetic model which has more states is a potential model, but any kinetic model with fewer states simply cannot represent the mechanism of the enzyme. The ability to make such statements is a reflection of the fact that there are fundamental differences between the statistics of different kinetic models—properties which are now amenable to direct measurement.

Finally, this work represents an additional step in the continued development of the exciting field of statistical kinetics—the theoretical tools which allow the extraction of mechanistic information from the inherent fluctuations in enzymatic dynamics. But, there are several additional advances one could imagine. For example, it is still unclear if the correspondence between the substrate dependence derived here for n_{\min} and the Michaelis-Menten expression is strict. We have proven it for an important class of kinetic models, yet there may be a more fundamental relationship between these two expressions, which dictates that they always occur together. In parallel, a complete classification of enzymatic dynamics based on fluctuations will require that additional, more general forms of the substrate dependence of n_{\min} are known. One might imagine natural extensions to this analysis aimed at deriving analogs to the Hill expression. Finally, n_{\min} involves only the first and second moment of the distribution of cycle completion times, yet there are a large number of independent higher moments, each of which likely contain additional mechanistic information and constraints. While there have been some recent advances in using more general features of the shape of these dwell time distributions to extract limits on underlying kinetic model (214), the use of higher moments of these distributions or general shape parameters remains largely unexplored. With experimental capabilities to extract and quantify the full distribution of

enzymatic fluctuations and their dependence on various experimental parameters almost routine, the challenge now lies in the development of the theoretical tools necessary to extract mechanistic information from these fluctuations. These experimental abilities issue a challenge to theorists: provide the comprehensive theoretical tools necessary to interpret this new data. The work we present here is one step towards addressing this challenge.

7.5: Appendices

7.5.1: General Closed Form Solutions for the Mean and Variance

In this Chapter, we consider kinetic models of the form in Eq. (7.5). Remarkably, the mean dwell time and the variance in the dwell time for *all* models of this form have been solved, and analytic, closed-form solutions exist which relate the individual kinetic rates to these moments. In particular, as was shown first by Derrida (202) and adapted by Chemla (17), the mean cycle completion time, or dwell time, for this kinetic scheme is

$$\langle \tau \rangle = \sum_{i=1}^N \frac{1}{k_i} \Gamma(i+1, N) \quad (7.21)$$

where we define the useful function (not to be confused with the incomplete gamma function)

$$\Gamma(i, n) = 1 + \sum_{j=i}^n \prod_{l=i}^j \Lambda_l \quad (7.22)$$

and the useful ratio of backward and forward rates, $\Lambda_l = q_{l-1}/k_l$.

In addition, Chemla et al. (17) adopt results derived by Derrida (202) to show that the variance in the cycle completion times is

$$\langle \tau^2 \rangle - \langle \tau \rangle^2 = \left(\sum_{i=1}^N \frac{1}{k_i} \Gamma(i+1, N) \right)^2 - 2 \sum_{i=2}^N \sum_{j=1}^{i-1} \frac{1}{k_i} \frac{1}{k_j} \Gamma(j+1, i-1) \Gamma(i+1, N). \quad (7.23)$$

Eqs. (7.21) - (7.23) define the functional dependence of the mean and variance of the cycle completion times on the individual rate constants for *all* possible kinetic schemes of the form in Eq. (7.5). We will use these forms to derive the general substrate dependence of n_{\min} .

7.5.2: Necessary and Sufficient Conditions for Michaelis-Menten

Let's start by considering a cycle in which only a single substrate molecule binds during the transition from state m to state $m+1$. Notice that the specific form of the mean dwell time, Eq. (7.21), does not involve the product of a given rate constant with itself. This implies that the mean dwell time will have two types of terms, terms proportional to the inverse of the substrate concentration, which we can combine into the factor η and terms independent of the substrate concentration which we can combine into the factor ξ , yielding

$$\langle \tau \rangle = \xi + \eta \frac{1}{[S]}. \quad (7.24)$$

Inspection of the terms in Eq. (7.21) reveals that

$$\xi = \sum_{i=1}^{m-1} \frac{1}{k_i} \Gamma(i+1, m-1) + \sum_{i=m+1}^N \frac{1}{k_i} \Gamma(i+1, N) \quad (7.25)$$

and

$$\eta = \Gamma(m+1, N) \sum_{i=1}^m \frac{1}{k_i} \prod_{l=i+1}^m \Lambda_l. \quad (7.26)$$

where in deriving the final property we have used that fact that

$$\Gamma(i, n) = \Gamma(i, j-1) + \Gamma(j+1, n) \prod_{l=i}^j \Lambda_l \quad (7.27)$$

to split the portions of the $\Gamma(i, n)$ functions which are proportional to or independent of $[S]^{-1}$. Eq. (7.27) is an extremely useful property of these $\Gamma(i, n)$ functions which we will use throughout this section.

Comparison of Eq. (7.24) with the Michaelis-Menten expression, Eq. (7.6) in the main text, implies that

$$\frac{1}{k_{cat}} = \xi \quad (7.28)$$

and

$$\frac{K_M}{k_{cat}} = \eta . \quad (7.29)$$

Now, let's consider the case that multiple substrate molecules bind in a single cycle. In particular, let's assume that these binding events occur during the transitions from state m to state $m+1$ and from state m' to state $m'+1$. In this case, the algebraic structure of the mean dwell time, Eq. (7.21), implies that there will be terms that involve the product of the pseudo-first-order binding constants for each of these binding events; thus, there will be terms proportional to $[S]^{-2}$ and the general substrate dependence for the mean dwell time will not follow the Michaelis-Menten expression, Eq. (7.6).

Note, however, that the general form of each of the terms in the mean dwell time $k_i^{-1}\Gamma(i+1, N)$ depends only on rate constants between states i and N . More importantly, these terms *always* depend on *all* of the rate constants between these states. This implies

that the terms proportional to $[S]^{-2}$ will involve not just the pseudo first order rate constants k_m and $k_{m'}$ but also the following term

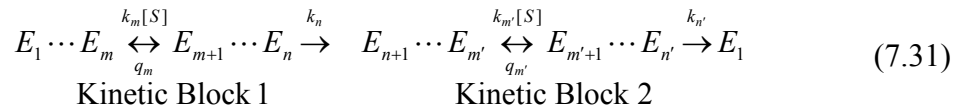
$$\prod_{l=m+1}^{m'-1} \Lambda_l = \Lambda_{m+1} \Lambda_{m+2} \cdots \Lambda_{m'-2} \Lambda_{m'-1} = \frac{q_m q_{m+1} \cdots q_{m'-3} q_{m'-2}}{k_{m+1} k_{m+2} \cdots k_{m'-2} k_{m'-1}} \quad (7.30)$$

Because all of the non-Michaelis-Menten terms are proportional to this common factor, if it is zero, then all non-Michaelis-Menten terms will be zero. In this case, the system will display the simple substrate dependence for the mean dwell time, Eq. (7.6), despite the fact that each cycle *requires* the binding of multiple substrate molecules.

For finite forward rates, this term can only be zero if one or more of the reverse rates q_m through $q_{m'-2}$ is zero. This implies that starting with the first binding event, an irreversible transition anywhere between the first and the second binding event will set the expression in Eq. (7.30) to zero. Thus, it is both *necessary* and *sufficient* for every binding event to be separated by an irreversible transition for a kinetic scheme of the form in Eq. (7.5) to display a Michaelis-Menten-like substrate dependence, Eq. (7.6).

7.5.3: Kinetic Blocks

Irreversible transitions separate the kinetic scheme in Eq. (7.5) into distinct *kinetic blocks*—different sets of reversibly connected kinetic states. For example,



where states m and m' are substrate binding states and the forward transitions out of states n and n' are irreversible transitions.

Since the dynamics in one kinetic block are separated from another block by an irreversible transition, the statistics of these blocks are distinct. And, the statistical

properties of the full cycle will be built from the statistical properties of these isolated blocks. For example, if $\langle t_b \rangle$ is the mean dwell time of the b th kinetic block and $\langle t_b^2 \rangle - \langle t_b \rangle^2$ is the variance of this block, then

$$\langle \tau \rangle = \sum_{b=1}^{N_B} \langle t_b \rangle \quad (7.32)$$

and

$$\langle \tau^2 \rangle - \langle \tau \rangle^2 = \sum_{b=1}^{N_B} \langle t_b^2 \rangle - \langle t_b \rangle^2, \quad (7.33)$$

where N_B is the number of kinetic blocks. The validity of Eqs. (7.32) and (7.33) can be checked by using the fact that $\Lambda_{n+1} = 0$ for all irreversible transitions, which implies that if a state index i is in a specific kinetic block, i.e. $n < i \leq n'$, then $\Gamma(i+1, N) = \Gamma(i+1, n')$. Using this fact, it is possible to show that Eqs. (7.21) and (7.23) reduce to Eqs. (7.32) and (7.34).

7.5.4: Michaelis-Menten Parameters for Multi-Block Cycles

In principle, the number of kinetic blocks in a given cycle is equal to the number of irreversible transitions. However, for our purposes, we will group kinetic blocks such that each block contains *one and only one* substrate binding event. In this fashion, N_B will also be the number of substrate binding events in each cycle. Then because each kinetic block is a smaller version of the nearest neighbor kinetic cycle considered in Eq. (7.5), i.e. an n state system with one binding state located at state m , the expressions for the mean dwell time derived above are valid for each kinetic block. In other words, $\xi \rightarrow \xi_b$ and $\eta \rightarrow \eta_b$. The indexes in these terms, η_b and ξ_b , are now particular to the

individual kinetic block, i.e. index 1 corresponds to the first state in the block, m corresponds to the position of the binding state within that block, and n , or N in Eqs. (7.25) and (7.26), corresponds to the last state within that block. The numerical value of these indices need not match the position of the state in the overall cycle.

Because the mean dwell time is the sum of the mean for each kinetic block, it will have the same Michaelis-Menten form as in Eqs. (7.6) and (7.24). However, the Michaelis constants will be the sum of the individual parameters of each kinetic block

$$\frac{1}{k_{cat}} = \sum_{b=1}^{N_B} \xi_b = \sum_{b=1}^{N_B} \frac{1}{k_{cat,b}} \quad (7.34)$$

and

$$\frac{K_M}{k_{cat}} = \sum_{b=1}^{N_B} \eta_b = \sum_{b=1}^{N_B} \frac{K_{M,b}}{k_{cat,b}}, \quad (7.35)$$

where $k_{cat,b}$ and $K_{M,b}$ are the Michaelis constants for the b th kinetic block. Since the binding of multiple substrate molecules per cycle likely involves the action of multiple subunits in the enzyme, these parameters can just as easily be thought of as the Michaelis constants of the b th subunit.

It is worth noting that the catalytic efficiency of the b th subunit is $k_{cat,b}/K_{M,b} = \eta_b^{-1}$. Eq. (7.26) shows that the η_b only depend on the kinetic rates of states reversibly connected to the substrate binding state in a given kinetic block. Moreover, if that block has additional irreversible transitions, then η_b will only depend on the subset of kinetic rates that correspond to the transitions that are reversibly connected to binding. Any transitions within that kinetic block but after the irreversible transition (or before it) will not appear in η_b . It is in this sense that the term *catalytic efficiency* is a misnomer.

Irreversible transitions may separate binding from subsequent catalysis states; thus, the catalytic efficiency may not depend on the specific rates of catalysis. Perhaps a better term would be *binding propensity* since the rates that do appear in η_b will determine the rate at which substrate is bound to the cycle and committed to catalysis.

7.5.5: Substrate Dependence of the Variance

Since we have shown that the variance of the individual kinetic blocks add to produce the total variance for the system, we need only consider the variance for a single kinetic block. In this case,

$$\langle t_b^2 \rangle - \langle t_b \rangle^2 = \left(\sum_{i=1}^n \frac{1}{k_i} \Gamma(i+1, n) \right)^2 - 2 \sum_{i=2}^n \sum_{j=1}^{i-1} \frac{1}{k_i} \frac{1}{k_j} \Gamma(j+1, i-1) \Gamma(i+1, n) \quad (7.36)$$

The first term is simply the mean squared, so its coefficients have already been determined above. Thus, we focus our attention on the second term. Notice again that this term does not involve the product of a given rate with itself. This implies that there will only be two types of terms: terms proportional to $[S]^{-1}$ and terms independent of $[S]^{-1}$. Thus,

$$2 \sum_{i=2}^n \sum_{j=1}^{i-1} \frac{1}{k_i} \frac{1}{k_j} \Gamma(j+1, i-1) \Gamma(i+1, n) = \chi_b + \sigma_b \frac{1}{[S]}, \quad (7.37)$$

where we have combined all terms proportional to the inverse of the substrate concentration or independent of this concentration into σ_b and χ_b , respectively. The subscript b represents the fact that there will be a similar term for each kinetic block in the cycle.

By expanding Eq. (7.37) and collecting terms proportional or independent of $[S]^{-1}$

, it is possible to show that

$$\begin{aligned}\chi_b = & \sum_{i=2}^{m-1} \sum_{j=1}^{i-1} \frac{1}{k_i} \frac{1}{k_j} \Gamma(i+1, m-1) \Gamma(j+1, i-1) \\ & + \sum_{i=m+1}^n \sum_{j=1}^{m-1} \frac{1}{k_i} \frac{1}{k_j} \Gamma(i+1, n) \Gamma(j+1, m-1) \\ & + \sum_{i=m+1}^n \sum_{j=m+1}^n \frac{1}{k_i} \frac{1}{k_j} \Gamma(i+1, n) \Gamma(j+1, i-1)\end{aligned}\quad (7.38)$$

and

$$\begin{aligned}\sigma_b = & \sum_{i=2}^{m-1} \sum_{j=1}^{i-1} \frac{1}{k_i} \frac{1}{k_j} \Gamma(m+1, n) \Gamma(j+1, i-1) \prod_{l=i+1}^m \Lambda_l \\ & + \sum_{i=m+1}^n \sum_{j=1}^m \frac{1}{k_i} \frac{1}{k_j} \Gamma(i+1, n) \Gamma(m+1, i-1) \prod_{l=j+1}^m \Lambda_l\end{aligned}\quad (7.39)$$

When combined with Eqs. (7.21), (7.22), (7.36), and (7.37), these complicated sums of products of rate constants completely determine the way in which the individual rate constants of a specific kinetic model combine to form the variance of the cycle completion time.

7.5.6: General Form for the Substrate Dependence of n_{\min}

With the substrate dependence of the mean and the variance of the individual kinetic blocks, Eqs. (7.24)-(7.26) and (7.37)-(7.39), and an understanding of how these statistical properties of the individual blocks compose the statistical properties of the full cycle, we can now calculate the general substrate dependence of n_{\min} . Using the definition of n_{\min} and the expressions derived above, it can be shown that

$$n_{\min} = \frac{\left(\sum_{b=1}^{N_B} \langle t_b \rangle \right)^2}{\sum_{b=1}^{N_B} \langle t_b^2 \rangle - \langle t_b \rangle^2} = \frac{\left(\sum_{b=1}^{N_B} (\xi_b + \eta_b [S]^{-1}) \right)^2}{\sum_{b=1}^{N_B} (\xi_b + \eta_b [S]^{-1})^2 - 2 \sum_{b=1}^{N_B} (\chi_b + \sigma_b [S]^{-1})}. \quad (7.40)$$

With some additional algebra it is possible to further show that this expression reduces to

$$n_{\min} = \frac{N_L N_S \left(1 + \frac{[S]}{K_M} \right)^2}{N_L \left(\frac{[S]}{K_M} \right)^2 + 2\alpha \frac{[S]}{K_M} + N_S} \quad (7.41)$$

which is Eq. (7.7) above. In this process we have used Eqs. (7.34) and (7.35) to define the Michaelis constant for the full cycle,

$$K_M = \frac{\sum_{b=1}^{N_B} \eta_b}{\sum_{b=1}^{N_B} \xi_b} \quad (7.42)$$

and we have defined the following new “macroscopic” constants

$$N_L = \frac{\left(\sum_{b=1}^{N_B} \eta_b \right)^2}{\sum_{b=1}^{N_B} \eta_b^2}, \quad (7.43)$$

$$N_S = \frac{\left(\sum_{b=1}^{N_B} \xi_b \right)^2}{\sum_{b=1}^{N_B} (\xi_b^2 - 2\chi_b)}, \quad (7.44)$$

and

$$\alpha = \frac{\sum_{b=1}^{N_B} (\xi_b \eta_b - \sigma_b)}{\sum_{b=1}^{N_B} \eta_b \sum_{b=1}^{N_B} \xi_b} N_L N_S . \quad (7.45)$$

The final expressions, Eqs. (7.42)-(7.45), completely determine the macroscopic parameters of the general substrate dependence of n_{\min} from the individual kinetic rates that compose the cycle. Notice that while these parameters are in general complicated functions of the individual rate constants, this complexity is effectively hidden within these parameters.

7.5.7: Properties of N_L

Starting with Eq. (7.43), which relates N_L to the specific kinetic rates in the underlying kinetic cycle, we now derive the properties of N_L provided in the sections above. In particular, we use the Cauchy Schwarz inequality to prove that N_L is bounded from above by the number of substrate molecules that are bound each cycle and from below by

1. The Cauchy Schwarz inequality states that for all real numbers x_i and y_i

$$\left(\sum_{i=1}^N x_i y_i \right)^2 \leq \sum_{i=1}^N x_i^2 \sum_{i=1}^N y_i^2 . \quad (7.46)$$

If we let $x_i = \eta_b$ and $y_i = 1$ for all i , then this expression becomes

$$\left(\sum_{b=1}^{N_B} \eta_b \right)^2 \leq \sum_{b=1}^{N_B} \eta_b^2 \sum_{b=1}^{N_B} 1 = N_B \sum_{b=1}^{N_B} \eta_b^2 \quad (7.47)$$

which proves the bound

$$\frac{\left(\sum_{b=1}^{N_B} \eta_b\right)^2}{\sum_{b=1}^{N_B} \eta_b^2} = N_L \leq N_B \quad (7.48)$$

which is Eq. (7.15) in the main text.

A corollary of the Cauchy Schwarz inequality is that the equality only holds if all x_i are proportional to all y_i with the same proportionality constant for all i , i.e. $x_i = ay_i$ for all i . Since the $y_i = 1$ in our argument above, this implies $N_L = N_B$ if and only if the η_b for each kinetic block are identical. Interestingly, Eq. (7.26) indicates that in general the η_b are a complicated function of the number of kinetic states and their rates, yet Eq. (7.48) does not depend on these details, only the numerical value of η_b . Thus, one might imagine a case in which the binding events are quite different in each kinetic block, but the η_b happen to be identical, in which case, $N_L = N_B$. It is worth further emphasizing that $N_L = N_B$ if all η_b are the same, even if the kinetic events involved in binding are reversible. Thus, reversibility in binding or other connected kinetic transitions *need not* lower N_L from N_B . (This is in sharp contrast to what we will prove below for N_S .)

Eq. (7.48) also indicates that N_L is bounded from below from 1. If the kinetic scheme involves the binding of only a single substrate molecule, then Eq. (7.48) shows trivially that $N_L = 1$. However, even if multiple substrate molecules are bound, Eq. (7.48) requires that $1 \leq N_L$ with N_L only approaching 1 in the limit that one of the η_b is much larger than all other η_b . Thus, a measured value of N_L less than 1 indicates that one of our assumptions must not apply to the kinetic mechanism of the specific enzyme. The

most likely assumption would be that the kinetic mechanism has more complicated catalytic pathways than included in Eq. (7.5).

Finally, it is worth noting that by Eq. (7.29), the individual η_b correspond to the ratio of the K_M to the k_{cat} for each kinetic block. This ratio is the inverse of what is commonly known as the catalytic efficiency of the enzyme for a given substrate molecule (128). Given the complexity of the different kinetic constants observed above, it is perhaps remarkable that N_L would depend in a simple fashion on such an important kinetic parameter.

7.5.8: Properties of N_S

Starting with Eq. (7.44) we can derive the properties of N_S provided above. The general approach to proving that N_S is bounded from above by the number of non-substrate binding states is the same for N_L , i.e. we will manipulate Eq. (7.44) to show that the Cauchy Schwarz inequality applies. However, one complication to this derivation compared to that above is that the denominator in N_S has a negative term; thus, it is not obvious *a priori* that the denominator cannot be arbitrarily small, making N_S arbitrarily large.

We start by combining the terms in the denominator of N_S , $\xi_b^2 - 2\chi_b$, to show that this term is always positive. We first expand ξ_b^2 so that the terms are indexed in a fashion similar to those in χ_b :

$$\begin{aligned}
\xi_b^2 &= \left(\sum_{i=1}^{m-1} \frac{1}{k_i} \Gamma(i+1, m-1) + \sum_{i=m+1}^n \frac{1}{k_i} \Gamma(i+1, n) \right)^2 \\
&= \sum_{i=1}^{m-1} \left(\frac{1}{k_i} \Gamma(i+1, m-1) \right)^2 + 2 \sum_{i=2}^{m-1} \sum_{j=1}^{i-1} \frac{1}{k_i} \frac{1}{k_j} \Gamma(i+1, m-1) \Gamma(j+1, m-1) \\
&\quad + \sum_{i=m+1}^n \left(\frac{1}{k_i} \Gamma(i+1, n) \right)^2 + 2 \sum_{i=m+2}^n \sum_{j=m+1}^{i-1} \frac{1}{k_i} \frac{1}{k_j} \Gamma(i+1, n) \Gamma(j+1, n) \\
&\quad + 2 \sum_{i=1}^{m-1} \sum_{j=m+1}^n \frac{1}{k_i} \frac{1}{k_j} \Gamma(i+1, m-1) \Gamma(j+1, n)
\end{aligned} \tag{7.49}$$

Here we have explicitly separated the square of individual terms and the cross-terms. The indexing of these sums is now identical to the terms χ_b , allowing us to combine these two expressions. This yields

$$\begin{aligned}
\xi_b^2 - 2\chi_b &= \sum_{i=1}^{m-1} \left(\frac{1}{k_i} \Gamma(i+1, m-1) \right)^2 + \sum_{i=m+1}^n \left(\frac{1}{k_i} \Gamma(i+1, n) \right)^2 \\
&\quad + 2 \sum_{i=2}^{m-1} \sum_{j=1}^{i-1} \frac{1}{k_i} \frac{1}{k_j} \Gamma(i+1, m-1) \{\Gamma(j+1, m-1) - \Gamma(j+1, i-1)\}, \\
&\quad + 2 \sum_{i=m+2}^n \sum_{j=m+1}^{i-1} \frac{1}{k_i} \frac{1}{k_j} \Gamma(i+1, n) \{\Gamma(j+1, n) - \Gamma(j+1, i-1)\}
\end{aligned} \tag{7.50}$$

which can be further simplified by using the identity in Eq. (7.27). The result is a compact form for the terms from each kinetic block in the denominator of N_s ,

$$\begin{aligned}
\xi_b^2 - 2\chi_b &= \sum_{i=1}^{m-1} \left(\frac{1}{k_i} \Gamma(i+1, m-1) \right)^2 + \sum_{i=m+1}^n \left(\frac{1}{k_i} \Gamma(i+1, n) \right)^2 \\
&\quad + 2 \sum_{i=2}^{m-1} \frac{1}{k_i} \Gamma(i+1, m-1)^2 \sum_{j=1}^{i-1} \frac{1}{k_j} \prod_{l=j+1}^i \Lambda_l \\
&\quad + 2 \sum_{i=m+2}^n \frac{1}{k_i} \Gamma(i+1, n)^2 \sum_{j=m+1}^{i-1} \frac{1}{k_j} \prod_{l=j+1}^i \Lambda_l
\end{aligned} \tag{7.51}$$

This expression demonstrates that the denominator of N_s is always positive (since all rate constants and their ratios must be positive); thus, N_s has a finite bound. To further

prove that this bound is N_{other} , the total number of non-substrate binding states in the cycle, we must investigate the specific terms in this expression. In particular, note that the first two terms are simply the sum of the squares of the terms that compose ξ_b . Thus, we can define a related quantity

$$N' = \frac{\left(\sum_{i=1}^{N_{\text{other}}} x_i \right)^2}{\sum_{i=1}^{N_{\text{other}}} x_i^2} \leq N_{\text{other}}, \quad (7.52)$$

where each x_i can be identified with a term in each of the ξ_b from each of the different kinetic blocks. The sum is over N_{other} terms since for each kinetic block there is a term in ξ_b for each of the kinetic states other than the substrate binding state, m , (see the bounds on the sum in Eqs. (7.49) and (7.51)). Finally, using the Cauchy Schwarz inequality exactly as above, we can show that N' is bounded from above by N_{other} , the number of terms in the sum.

Since the only difference between N_s and N' is that the denominator of N_s contains additional positive terms, then $N_s \leq N'$; thus, we can immediately conclude that

$$N_s \leq N_{\text{other}} \quad (7.53)$$

the bound stated in Eq. (7.14) in the main text.

In addition, $N_s = N'$ only in the limit that the additional terms in the denominator, the final two terms in Eq. (7.51), are zero. Note that these terms are proportional to products of Λ_l ; thus, if all of the transitions are irreversible, these terms will be zero, and $N_s = N'$. Furthermore, using the same argument as above, $N' = N_{\text{other}}$,

if and only if all of the transition rates are identical. Thus, we can conclude that $N_S = N_{other}$ if and only if 1) all non-binding transitions are irreversible and 2) all forward transition rates are identical.

7.5.9: Properties of α

The general form of α in Eq. (7.45) provides several limits on the possible values of α . We start by showing that α is bounded from above by $N_S N_L$. In particular, we will show that

$$\frac{\sum_{b=1}^{N_B} (\xi_b \eta_b - \sigma_b)}{\sum_{b=1}^{N_B} \eta_b \sum_{b=1}^{N_B} \xi_b} \leq 1. \quad (7.54)$$

To prove this, we first recognize that since σ_b is non-negative (again it is a function of rate constants which must all be non-negative) this implies that

$$\frac{\sum_{b=1}^{N_B} (\xi_b \eta_b - \sigma_b)}{\sum_{b=1}^{N_B} \eta_b \sum_{b=1}^{N_B} \xi_b} \leq \frac{\sum_{b=1}^{N_B} (\xi_b \eta_b)}{\sum_{b=1}^{N_B} \eta_b \sum_{b=1}^{N_B} \xi_b} \quad (7.55)$$

Reindexing the bottom products yields

$$\sum_{b=1}^{N_B} \eta_b \sum_{b=1}^{N_B} \xi_b = \sum_{b=1}^{N_B} \eta_b \sum_{j=1}^{N_B} \xi_j = \sum_{b=1}^{N_B} \eta_b \xi_b + 2 \sum_{i=2}^{N_B} \sum_{j=1}^{i-1} \eta_i \xi_j \quad (7.56)$$

The first term in the final expression is simply the numerator and the additional terms must be positive; thus,

$$\frac{\sum_{b=1}^{N_B} (\xi_b \eta_b)}{\sum_{b=1}^{N_B} \eta_b \sum_{b=1}^{N_B} \xi_b} \leq 1 \quad (7.57)$$

which implies that

$$\alpha \leq N_S N_L . \quad (7.58)$$

To show that α is bounded from below by zero, we must prove that $\xi_b \eta_b - \sigma_b$ is non-negative. Using Eqs. (7.25) and (7.26) we can expand $\xi_b \eta_b$

$$\begin{aligned} \xi_b \eta_b &= \left(\sum_{i=1}^{m-1} \frac{1}{k_i} \Gamma(i+1, m-1) + \sum_{i=m+1}^n \frac{1}{k_i} \Gamma(i+1, n) \right) \left(\Gamma(m+1, n) \sum_{i=1}^m \frac{1}{k_i} \prod_{l=i+1}^m \Lambda_l \right) \\ &= \sum_{i=1}^{m-1} \sum_{j=1}^m \frac{1}{k_i} \frac{1}{k_j} \Gamma(i+1, m-1) \Gamma(m+1, n) \prod_{l=j+1}^m \Lambda_l \\ &\quad + \sum_{i=m+1}^n \sum_{j=1}^m \frac{1}{k_i} \frac{1}{k_j} \Gamma(i+1, n) \Gamma(m+1, n) \prod_{l=j+1}^m \Lambda_l \end{aligned} \quad (7.59)$$

where we have again carefully changed the indexing to match the indexing of terms in σ_b , Eq. (7.39). Combining terms yields

$$\begin{aligned} \xi_b \eta_b - \sigma_b &= \frac{1}{k_1} \prod_{l=2}^m \Lambda_l \Gamma(m+1, n) \sum_{j=1}^{m-1} \frac{1}{k_j} \Gamma(j+1, m-1) \\ &\quad + \sum_{i=2}^m \frac{1}{k_i} \Gamma(m+1, n) \prod_{l=i+1}^m \Lambda_l \left\{ \sum_{j=i}^{m-1} \frac{1}{k_j} \Gamma(j+1, m-1) + \Gamma(i+1, m-1) \sum_{j=1}^{i-1} \frac{1}{k_j} \prod_{l=j+1}^i \Lambda_l \right\} \\ &\quad + \sum_{i=m+1}^n \frac{1}{k_i} \Gamma(i+1, n)^2 \prod_{l=m+1}^i \Lambda_l \sum_{j=1}^m \frac{1}{k_j} \prod_{l=j+1}^m \Lambda_l \end{aligned} \quad (7.60)$$

where we have separated the first term of the sum in $\xi_b \eta_b$, $i = 1$, to match the initial index in σ_b , and we have used the property in Eq. (7.27) several times. This expression is extremely cumbersome and relatively unintuitive; however, it is positive, indicating that α is bounded from below by zero. Thus, we have proven

$$0 \leq \alpha \leq N_S N_L \quad (7.61)$$

the bound stated in the main text, Eq. (7.13).

Inspection of the combined form for $\xi_b \eta_b - \sigma_b$ in Eq. (7.60) reveals that all of the terms are proportional to two common factors, Λ_m and Λ_{m+1} . Thus, if these two terms are zero, then $\xi_b \eta_b - \sigma_b = 0$, and if this term is zero for all of the kinetic blocks that compose the full cycle, then $\alpha = 0$. Setting Λ_m and Λ_{m+1} equal to zero corresponds to setting two reverse rates to zero, q_{m-1} and q_m . q_m is the rate at which substrate molecules unbind from the enzyme while q_{m-1} is the rate at which the substrate binding state transitions into a previous non-substrate binding states. Thus, setting these rates equal to zero, implies that the local structure of the kinetic mechanism as substrate loads is



Remarkably, since all of the terms in Eq. (7.60) must be non-negative, and the only common factors between all of these terms is Λ_m and Λ_{m+1} , the only way that this expression can be zero is if the local structure of binding transition is that seen in Eq. (7.62). The implication of this result is that kinetic schemes in which the binding competent state is not in equilibrium with any other state have fundamentally different fluctuations than other systems, and, more importantly, careful measurements of the substrate dependence of n_{\min} can reveal these unique fluctuations.

7.5.10: Proof of n_{\min} Bound

Koza (127) was the first to prove that $n_{\min} \leq N$ for all kinetic models of the form in Eq. (7.5), i.e. nearest neighbor or linear kinetic schemes. Here we provide an alternative proof that utilizes the specific form of the mean and the variance included in Eqs. (7.21) and (7.23). We start by rewriting the first term in the variance,

$$\begin{aligned} \left(\sum_{i=1}^N \frac{1}{k_i} \Gamma(i+1, N) \right)^2 &= \sum_{i=1}^N \sum_{j=1}^N \frac{1}{k_i} \frac{1}{k_j} \Gamma(i+1, N) \Gamma(j+1, N) \\ &= \sum_{i=1}^N \left(\frac{1}{k_i} \Gamma(i+1, N) \right)^2 + 2 \sum_{i=2}^N \sum_{j=1}^{i-1} \frac{1}{k_i} \frac{1}{k_j} \Gamma(i+1, N) \Gamma(j+1, N) \end{aligned} . \quad (7.63)$$

The second term in this expression can now be combined with the second term in the variance

$$\begin{aligned} &2 \sum_{i=2}^N \sum_{j=1}^{i-1} \frac{1}{k_i} \frac{1}{k_j} \Gamma(i+1, N) [\Gamma(j+1, N) - \Gamma(j+1, i-1)] \\ &= 2 \sum_{i=2}^N \sum_{j=1}^{i-1} \frac{1}{k_i} \frac{1}{k_j} \Gamma(i+1, N) \Gamma(i+1, N) \prod_{l=j+1}^i \Lambda_l , \\ &= 2 \sum_{i=2}^N \frac{1}{k_i} \Gamma(i+1, N)^2 \sum_{j=1}^{i-1} \frac{1}{k_j} \prod_{l=j+1}^i \Lambda_l \end{aligned} , \quad (7.64)$$

where we used the identity in Eq. (7.27) in going from the first line to the second line. Combining these final terms gives the variance

$$\langle \tau^2 \rangle - \langle \tau \rangle^2 = \sum_{i=1}^N \left(\frac{1}{k_i} \Gamma(i+1, N) \right)^2 + 2 \sum_{i=2}^N \frac{1}{k_i} \Gamma(i+1, N)^2 \sum_{j=1}^{i-1} \frac{1}{k_j} \prod_{l=j+1}^i \Lambda_l , \quad (7.65)$$

and combining this expression with the mean dwell time yields

$$n_{\min} = \frac{\langle \tau \rangle^2}{\langle \tau^2 \rangle - \langle \tau \rangle^2} = \frac{\left(\sum_{i=1}^N \frac{1}{k_i} \Gamma(i+1, N) \right)^2}{\sum_{i=1}^N \left(\frac{1}{k_i} \Gamma(i+1, N) \right)^2 + 2 \sum_{i=2}^N \frac{1}{k_i} \Gamma(i+1, N)^2 \sum_{j=1}^{i-1} \frac{1}{k_j} \prod_{l=j+1}^i \Lambda_l}. \quad (7.66)$$

Now, consider the following quantity

$$n' = \frac{\left(\sum_{i=1}^N \frac{1}{k_i} \Gamma(i+1, N) \right)^2}{\sum_{i=1}^N \left(\frac{1}{k_i} \Gamma(i+1, N) \right)^2}. \quad (7.67)$$

Because the second term in the denominator of n_{\min} is non-negative, this new quantity n' is an upper bound for n_{\min} , i.e. $n_{\min} \leq n'$. Using the Cauchy Schwarz inequality as above, it is possible to show that

$$\frac{\left(\sum_{i=1}^N \frac{1}{k_i} \Gamma(i+1, N) \right)^2}{\sum_{i=1}^N \left(\frac{1}{k_i} \Gamma(i+1, N) \right)^2} = n' \leq N. \quad (7.68)$$

Thus, n' is bounded from above by the number of kinetic states in the system. Since $n_{\min} \leq n'$, this implies that

$$n_{\min} \leq N. \quad (7.69)$$

Given the form of the second term in the denominator of n_{\min} , $n_{\min} = n'$ if and only if all $\Lambda_l = 0$. Thus, $n_{\min} = n'$ if and only if all of the transitions in the kinetic scheme are irreversible, i.e. all $q_i = 0$. In this case, $\Gamma(i+1, N) = 1$ for all i , and $x_i = k_i^{-1}$. And as above the equality $n' = N$ only holds when all terms are equal. Thus, $n_{\min} = N$, if and only if 1) all transitions are irreversible and 2) all transition rates are identical.

Chapter 8. Work in Progress and Conclusions

The novel experimental techniques described in this thesis now permit a variety of targeted experiments aimed at deciphering additional questions about the packaging motor mechanism. And our new understanding of the motor opens new questions. In this Chapter, we describe a variety of experiments, currently underway, that will address several novel features of the packaging motor dynamics. We start by describing experiments aimed at understanding the importance of phosphates in the motor-DNA interaction. We then turn our attention to experiments aimed at placing the remaining chemical transitions, ATP hydrolysis and ADP release, in the context of the new mechanochemical cycle. Finally, we describe some unexpected motor dynamics which occur as the capsid fills with DNA at the end of the packaging process—dynamics which may reveal a novel mechanism for the connector.

Materials for this Chapter represent research in progress that either has or will be submitted for publication elsewhere. Portions of the work described here have been conducted with Aathavan Karunakaran, Adam Politzer, Ariel Kaplan, Gheorghe Chistol, Chris Tae Hyung Lee, Craig Hetherington, Yann Chemla, Shelley Grimes, Paul Jardine, Dwight Anderson, and Carlos Bustamante and are discussed with their permission.

8.1: DNA Contacts in the Packaging Motor

In Chapter 4 we used the high resolution optical tweezers to decipher the detailed coordination between the individual subunits of the packaging motor, revealing many of the features of the mechanochemical cycle of the packaging motor. This information goes a long way in addressing the fundamental question we posed in Chapter 1: how does this motor transduce chemical energy into the mechanical work necessary to package the genome? However, an understanding of the mechanochemical cycle provides only a portion of the full picture. To truly understand the mechanochemical transduction in this system, we must also understand how these conformational changes are transferred to the DNA. We must understand the motor-DNA contacts: what chemical moieties are important, whether these contacts change throughout the cycle, and if these contacts, in turn, affect the chemical rates of the motor?

In this section, we discuss a series of experiments aimed at directly addressing these questions. This work represents, largely, the efforts of Aathavan Karunakaran, Adam Politzer, and Ariel Kaplan (140).

8.1.1: Mapping the Phosphate Contacts

Of all of the different chemical moieties in dsDNA, an ionic interaction with the charge on the phosphate backbone is widely believed to be one of the most likely motor-DNA contacts. This opinion is supported by mutational work in several related ASCE motors in which disrupting a single charge (either on the motor or on the DNA) can completely abrogate translocation (77, 215-218). To probe the role of the phosphate charge in the motor-DNA interaction in the packaging motor, we inserted short regions of methylphosphonate (MEP) DNA into the center of ~8kb dsDNA molecules. The MEP

modification replaces the charged oxygen in the phosphate backbone with an isosteric methyl group (inset Figure 8.1b), preserving the B-form helix (219-221). We then followed the ability of single prohead-motor complexes to package these modified substrates using the standard, single trap optical tweezers assay. See Figure 8.1a.

In Figure 8.1b we show two sample traces for packaging 10 bp of double stranded MEP (dsMEP) under saturating [ATP] (1 mM) and 5 pN of optically applied load. The motor packages at a normal velocity until it encounters the modification at ~4 kb at which point the motor pauses for a variable duration and either (i) successfully traverses the insert and continues packaging or (ii) dissociates from the DNA and is pulled from the tether under the applied force. Due to a large variability in attachment position on the polystyrene bead affixed to the micropipette (Figure 8.1a), the insert induced pauses appear to occur over a wide range of positions, as seen in the residency time histogram inset in Figure 8.1b. However, the background probability of pausing on normal DNA (59) is low enough (blue regions) that insert induced events can be easily distinguished (red).

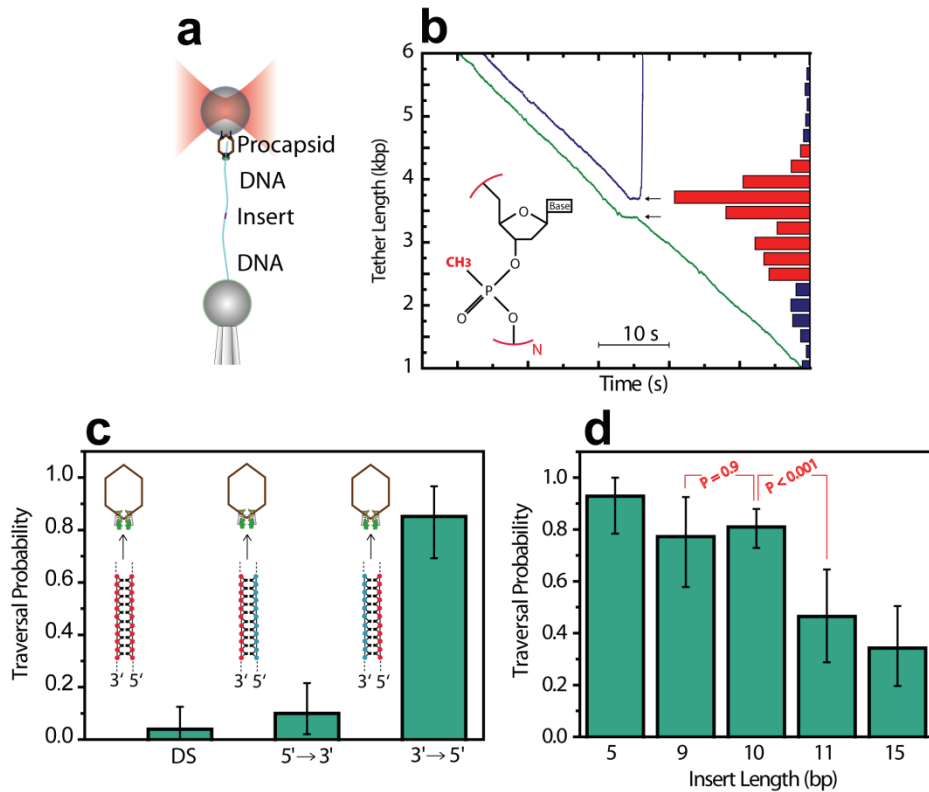


Figure 8.1. Mapping the Phosphate Contacts

(a) Experimental geometry used to map the important phosphate-motor contacts. A single prohead-motor complex affixed to an optically trapped bead packages a ~8 kb DNA tether which contains a short region of chemically modified DNA in the middle (insert). (b) Packaging traces (DNA length as a function of time) for these DNA constructs with 10 bp of double stranded methylphosphonate (MEP) DNA (inset), a charge neutral structural mimic of DNA. Packaging proceeds normally until the motor reaches the modified insert at which point it pauses for a measurable duration and either successfully packages the insert (green) or slips from the insert, terminating the experiment (blue). The vertical histogram represents the relative duration of the motor at each length along the DNA in different experimental runs. The red bars represent statistically significant deviations from the background pauses (blue bars) and, thus, pauses in these regions were analyzed. (c) Probability of traversing an insert with two strands of 30 bp of MEP (DS), 30 bp of MEP on the 5'-3' strand in the direction of packaging ($5' \rightarrow 3'$), or 30 bp of MEP on the 3'-5' strand ($3' \rightarrow 5'$). (d) Traversal probability for different lengths of dsMEP inserts. P values between given lengths are listed in the plot. All error bars represent 95% confidence intervals determined by the adjusted Wald method (222). Figure adapted from a manuscript in submission with permission from the coauthors (140).

Because the MEP modification does not distort the DNA from a B-form structure, this modification allows us to probe the specific role of the phosphate charge in a *native*

structural context. By varying the length and strand on which we place the MEP modifications, we can map out the spatial relationship of the motor-phosphate interactions. Figure 8.1c shows the traversal probability (the fraction of prohead-motor complexes which were capable of successfully packaging the modified insert) for 30 bp of MEP on either strand. The motor has a difficult time packaging 30 bp of neutral DNA when both strands are neutral (DS); however, if we restore the charge to the 5'-3' strand selectively (MEP 3'→5'), we rescue the ability of the motor to package the insert. In contrast, restoring the charge to the 3'-5' (MEP 5'→3') has little effect on the ability of the motor to package the modified insert. See Figure 8.1c. This result indicates that the important motor-phosphates interactions occur primarily on the 5'-3' strand in the direction of packaging.

To probe the length dependence of the phosphate interactions, we varied the length of the dsMEP inserts. Figure 8.1c shows that as the length of the MEP region is increased from 5 bp to 10 bp, the ability of the motor to package the modification is largely unchanged. However, when the length of the insert is increased by just one base pair, from 10 bp to 11 bp, the traversal probability drops by a statistically-significant factor of two. Increasing the length of the insert to 15 bp does little to further degrade the ability of the motor to package the DNA. A drop between 10 and 11 bp is remarkably consistent with the 10-bp burst size observed in Chapter 4. However, a drop in traversal probability between 10 and 11 bp as opposed to between 9 and 10 bp suggests that the motor makes contact with adjacent phosphate charges with a single charge contact sufficient to support packaging. Similar contacts between adjacent phosphate charges

have been observed (223) and a similar periodicity of phosphate charges has been proposed for related motors (224).

8.1.2: High Resolution Packaging Experiments

This data suggests that important contacts are made only with adjacent phosphate charges every 10 bp on the 5'-3' strand. The agreement between this distance scale and the burst size of the packaging motor, 10 bp, suggests that these important contacts are made primarily during the dwell phase of the motor. However, this inference does not rule out important interactions with the phosphate charges during the burst phase, when the DNA is actually translocated.

To confirm this interpretation and to probe the relative important of phosphate interactions within the burst, we packaged 5-bp-long dsMEP inserts. Circumstantial evidence from the high resolution experiments suggests that the burst size has a limited degree of variability (as suggested by the slight decrease in the peak height of the PWD for the 10-bp bursts, Figure 4.1c); thus, we expect the motor to effectively randomize its trajectory on the DNA during the packaging of the initial ~4 kb of DNA. Assuming a random positioning of the dwell phase for the motor, roughly 50% of the motors should dwell less than 5 bp from the beginning of the modified insert; thus, the 10-bp burst will carry them across the insert placing them on charged DNA for the subsequent dwell. See Figure 8.2a. However, in the other ~50% of the motors, the 10-bp burst will position the next dwell phase within the neutral DNA. See Figure 8.2b. If the phosphates are important during both the dwell and burst, then we expect to see a modified packaging phenotype for all prohead-motor complexes since the step size is smaller than the neutral region. However, if the phosphates are only important during the dwell phase and are not

needed during the burst phase, we would expect only the motors that dwell in the neutral region, Figure 8.2a, to display a modified packaging phenotype.

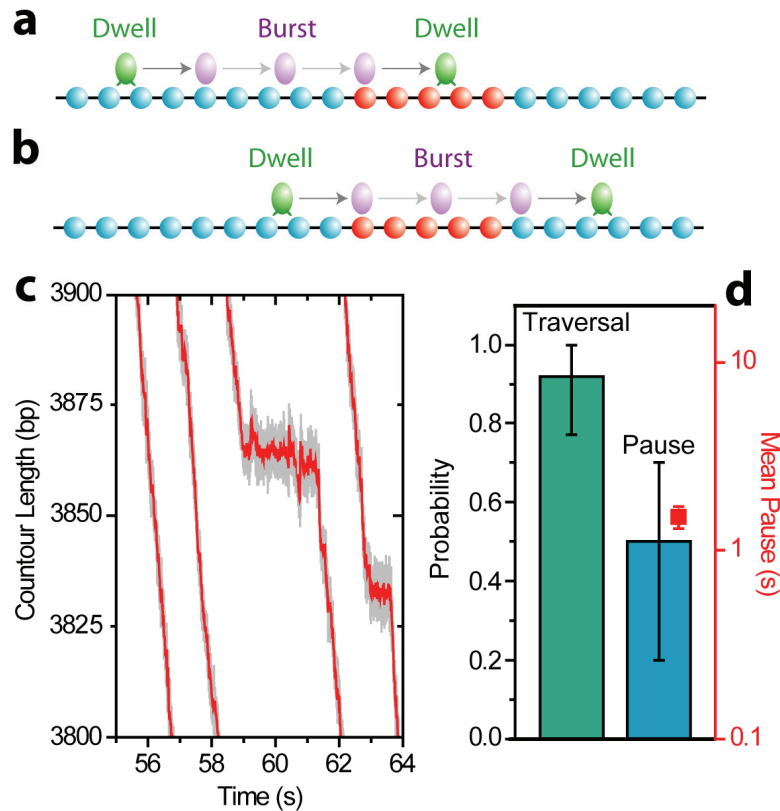


Figure 8.2. High Resolution Experiments with 5 bp of dsMeP

(a) Motors that start the dwell phase more than 5 bp upstream of the 5 bp neutral insert will burst into the neutral DNA and must dwell within it during the subsequent ATP-loading dwell. (b) Motors that start the dwell phase less than 5 bp upstream of the 5 bp insert will burst across this insert, and the subsequent dwell will be on charged DNA. (c) Example high resolution packaging traces of 5 bp of ds MeP. Note that some traces show no clear modification to the packaging phenotype. (d) Traversal probability (green), probability of observing a pause (blue), and the mean pause duration (red). Probabilities estimated with the Laplace estimator with 95% confidence intervals using the Adjusted Wald Method. The error on the mean pause duration is the standard error of the mean.

To probe small modifications to the packaging phenotype that might not be observable with the lower resolution optical tweezers, we used the high resolution optical tweezers discussed in Chapters 2 and 3. We packaged 11 prohead-motor complexes

against an average opposing load of ~15 pN. Of these complexes, 5 motors displayed a clear pause, distinct from the normal dwell-phase pauses, while 6 motors crossed the insert with no apparent modification in the packaging phenotype. See Figure 8.2c. This implies a probability of pausing at the 5-bp insert of 50% as shown in Figure 8.2d. This probability is remarkably consistent with the 50% chance of randomly positioning a 10-bp contact within a 5-bp insert, suggesting that the phosphate charges are not as important during the burst phase as they are during the dwell phase. This result supports the interpretation of the drop in traversal probability between 10 and 11 bp discussed above. In addition, it is important to note that these measurements do not rule out a role for the phosphates in the burst phase. They only indicate that the removal of this charge has a small effect.

Having established the spatial geometry of the contacts made with the phosphates, we investigated their specific role in the mechanochemical cycle by probing the base-pair-scale dynamics of the motor at an uncharged insert. Phosphate contacts may serve several possible roles in the mechanochemical cycle. For example, they may provide the long-lived contacts required to keep the enzyme attached to the DNA and increase its processivity. Alternatively, motor-DNA contacts need not be load-bearing, but may serve purely regulatory or sensory roles, accelerating a chemical rate such as ATP hydrolysis upon sensing that the DNA is bound and properly oriented or tightly coupling the chemical cycle to the mechanical cycle. These alternative roles of the phosphate charge predict different behaviors of the motor as it traverses the modified insert. For example, if the phosphate is needed to provide load-bearing contacts, its absence will increase the dissociation rate of the motor, and the insert-induced pause will consist of a

series of attempts to package followed by small slips. Alternatively, if the role of the phosphate charge is regulatory, translocation will proceed normally with no slips, but the time between packaging steps will be greatly lengthened, due to the decreased rate of catalytic turnover or the loose coupling of turnover to translocation.

At the spatial resolution of the measurements above, the pauses appear as single events. Thus, to reveal the dynamics of the motor as it crosses a neutral insert (10 bp of ds-MeP), we followed packaging using the high resolution optical tweezers described in Chapters 2 and 3. Figure 8.3a shows that the pauses observed at low resolution (Figure 8.1b) are actually remarkably dynamic events, containing two types of sub-pauses at distinct locations along the DNA and with distinct lifetimes. The first type of sub-pause, which we term an *upstream pause*, occurs at longer DNA tether lengths clustering at the same position with a variation of only 1.0 bp (Figure 8.3d) and has longer average durations (Figure 8.3b). These sub-pauses are followed by either brief disengagement (slips) of the motor or packaging attempts. These attempts are themselves followed by a second class of sub-pauses, which we term *downstream* pauses. These sub-pauses occur over a larger range of positions (Figure 8.3e) and have very short durations (Figure 8.2c). These sub-pauses are terminated either with slips or with the successful packaging of the insert. After slips from either the upstream or downstream pauses the motor typically recovers and repackages the DNA to the original position of the upstream pause. Occasionally the motor does not recover from a slip, and the slip becomes a terminal slip. Figure 8.3f contains the branching probabilities for these events.

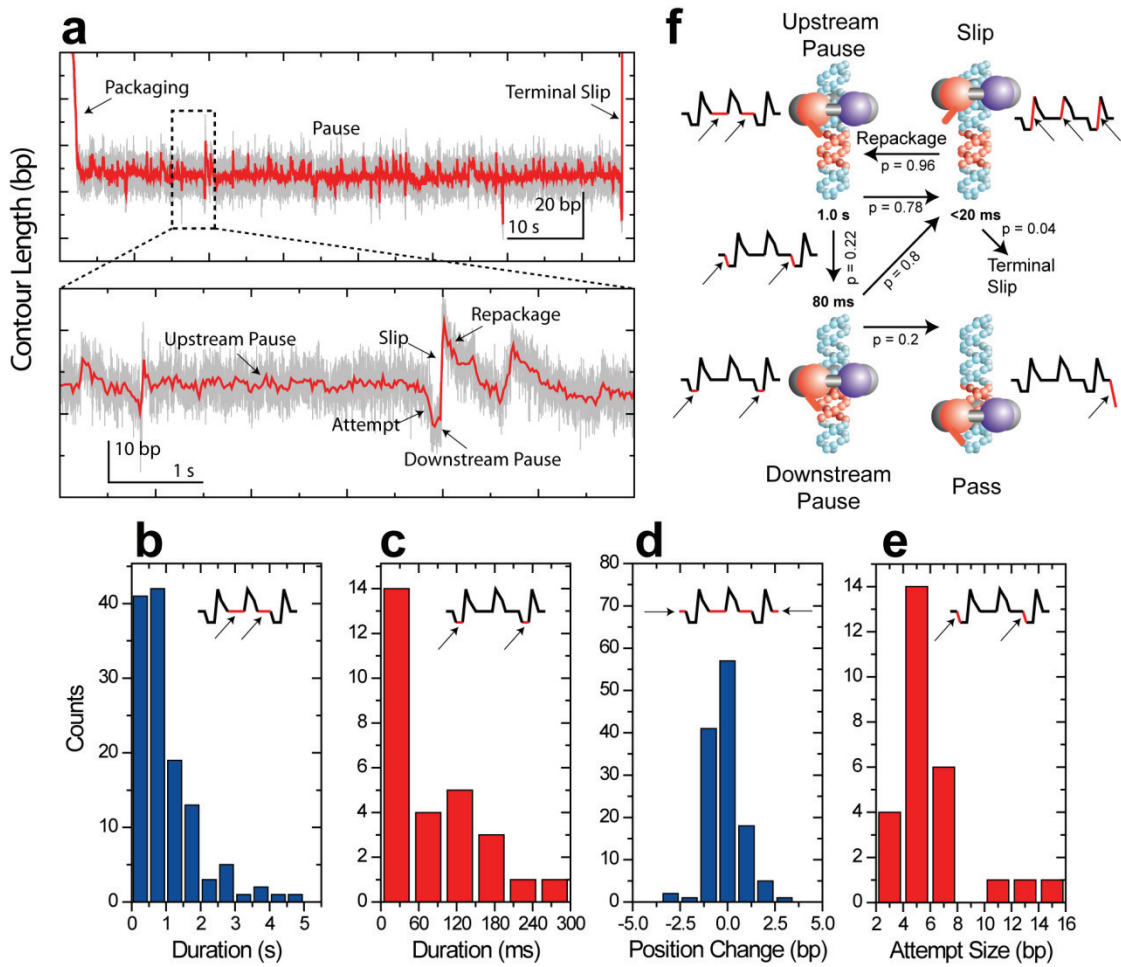


Figure 8.3. High Resolution Dynamics at Neutral DNA

(a) Top: representative high resolution trace of the base-pair-scale dynamics at an insert composed of 10 bp of dsMEP. Bottom: close up of a segment of this pause which shows that the dynamics consist of two classes of sub-pauses, upstream and downstream pauses, separated by attempts and punctuated by slips and repackaging events. (b) Histogram of upstream pause durations. (c) Histogram of downstream pause durations. (d) Histograms of position changes in the upstream pause. (e) Histogram of distance between upstream and downstream pauses. (f) A cartoon model of the dynamics of these pauses with average lifetimes and interconversion probabilities. Figure adapted from a manuscript in submission with permission from the coauthors (140).

The multiple slip/attempts phenotype observed in Figure 8.3a clearly indicates that the absence of the phosphate charge results in a loss in the processivity of the motor; thus, the phosphate is responsible for providing stable, load-bearing contacts with the

DNA. However, the average rate at which the motor attempts to package is also 10-fold smaller than the rate at which it normally steps on charged DNA, i.e. the upstream pauses are on average 1.00 ± 0.08 s (s.e.m.) in duration compared to the dwells on normal DNA under the same experimental conditions, 100 ± 4 ms (s.e.m.). Thus, we conclude that the rate of the chemical cycle is slowed when the phosphate charge is removed, revealing an additional sensory role for this interaction. The dwell time distribution of the upstream pauses has an n_{\min} value of 1.1 ± 0.1 (s.e.m.); thus, a single kinetic event dominates the upstream pause duration. This is in sharp contrast to the ~ 4 kinetic events that are known to be rate-limiting for the ATP-loading dwell phase on charged DNA (Chapter 4). Thus, not only does the phosphate contact play a sensory role in the dwell phase, this role appears to be largely important during only *one* kinetic event. This event may act as a kinetic checkpoint—a process which halts the chemical cycle until the DNA is correctly positioned. The relatively long duration of the downstream pauses, ~ 80 ms, compared to our measurement dead-time, 10 ms, rules out the alternative possibility—that the motor attempts at a normal rate but we fail to detect most of these attempts.

These data suggest a microscopic interpretation of the data, as displayed in Figure 8.3f, which provides a mechanism by which the motor can package long regions of modified DNA. Since the motor displays a dramatic increase in the rate of slipping over a ~ 10 bp length scale, i.e. at both the locations of the upstream and the downstream sub-pauses, we conclude that the upstream pauses likely involve contacts near the junction of the charged and neutral DNA and that the downstream pauses involve contacts within the insert. Moreover, since the important phosphate contacts are made with a 10-bp periodicity, the same spatial separation as the ATP-loading dwell phases, we conclude

that the upstream pause, with the largest modifications to the normal packaging phenotype, likely corresponds to the dwell phase of the motor. This implies that the downstream pauses correspond to the occasional micro-dwells before a 2.5-bp step. This is supported by the fact that the average duration of the downstream pauses, 80 ± 10 ms (s.e.m.), is consistent with the micro-dwells observed before 2.5-bp steps on charged DNA under similar conditions. The fact that the observed attempt sizes are not 10 bp (Figure 8.3e) indicates that there is an increased off-rate for the motor on the DNA during the burst phase, revealing a minor role for the phosphates during the burst. These dynamics indicate that the successful traversal of the neutral inserts is due to a kinetic competition between the increased off-rate of the motor during the dwell and burst and the time it takes to complete these phases. As illustrated by the probabilities in Figure 8.3f, the successful completion of a burst and dwell typically is out competed by the slipping of the motor. However, the fact that the probability of recovering from a slip is very high allows the motor to attempt many times, effectively amplifying the small success rate for individual attempts to the relatively large total traversal probability. This kinetic competition also explains the dramatic decrease in the ability of the motor to package the 30 bp of neutral DNA since this requires the successive occurrence of two unlikely events—the successful loading of ATP and generation of a burst before the motor slips from the neutral DNA.

8.1.3: Implications for the Mechanism

These observations have several important implications for the mechanism of the motor. First, the 10-bp periodicity of the important phosphate contacts strongly suggests that these contacts occur primarily during the dwell phase. This implies that the nature of the

motor-DNA contact *changes* between the two phases of the mechanochemical cycle, i.e. its interaction with the phosphates is different depending on whether it is loading ATP or stepping. A phase-dependent contact is sensible from energetic and kinetic arguments. During the long duration of the dwell phase, when the motor must stay stably bound to the DNA as it loads multiple ATP and performs other chemical tasks, a strong ionic interaction with the phosphate charge may be necessary to provide the stable, long-lived interaction needed to withstand high forces for the relatively long duration of the dwell phase. In contrast, during the burst phase, stable, strong contacts might actually inhibit the progress of the motor since it needs to make and break DNA contacts in a few milliseconds in order to quickly translocate the DNA. Thus, strong ionic interactions may not be favored during the actual translocation phase.

A phase dependent motor-DNA contact further strengthens the degree to which the symmetry of the pentameric packaging motor is broken during active operation. In Chapter 4, we showed that only four of the five subunits bind ATP and generate steps each cycle. In Chapter 7, we showed that the fluctuations of the packaging motor indicate that the identical subunits *cannot* bind ATP in an identical fashion. And now we show that the motor-DNA interactions, how each subunit engages the DNA, are themselves dependent on the local context of the ring—the chemical state of each of the different subunits. The clear conclusion is that allostery rules the dynamics of the packaging motor. The local context of the motor is *more important* than its global symmetry. How this dynamic symmetry breaking arises—how local changes are induced by conformational changes in different subunits—is the new pressing question.

8.2: Completing the Mechanochemical Cycle

We concluded Chapter 4 with a detailed mechanochemical picture of the packaging motor. Four ATPs load to the motor in a two step process, i.e. docking followed by tight binding and commitment to the cycle. Only a single subunit is capable of docking ATP at a time, and it is likely the tight binding of one ATP that activates the binding pocket of the next subunit. Once this process finishes, the first step is taken and the burst phase begins. This phase proceeds with the likely release of product phosphate (59) and the generation of three additional, 2.5-bp steps. Once completed the burst phase ends, and the next dwell phase begins.

It is clear that this picture leaves out several key kinetic events such as the hydrolysis of bound ATP molecules and the release of product ADP molecules. An understanding of where these events occur and if they are as tightly coordinated as the binding of ATP is crucial for a full understanding of the mechanochemical cycle of the motor. In this section, we propose several experiments aimed at determining the location of the missing kinetic events, describe the work in progress, and end by speculating on our “favored” location for these events. This work has been conducted in collaboration with Gheorghe Chistol and is discussed with his permission.

8.2.1: Experimental Strategy

To gain experimental control over the process of ATP hydrolysis or ADP release we will follow the base-pair-scale dynamics of the packaging motor as in Chapter 4 but with trace amounts of non-natural nucleotide analogs that are known to disrupt packaging. For example, by introducing non-hydrolyzable or slowly-hydrolyzable ATP analogs that bind to the motor, we can slow the portion of the kinetic cycle that involves hydrolysis. By

determining which phase of the mechanochemical cycle is affected by these analogs, we can limit the possible locations of ATP hydrolysis. In parallel, by introducing metallic complexes that are known to complex with ADP and form phosphate analogs or transition state analogs, we can stabilize ADP on the ring, slowing release and slowing the phase of the cycle that involves this important kinetic event.

Figure 8.4 diagrams the possible locations of ATP hydrolysis in the dwell-burst structure of the mechanochemical cycle of the packaging motor. Within a single subunit ATP hydrolysis must obviously occur after it is bound but before its hydrolysis products are released. Because it is believed that product release, in particular inorganic phosphate, proceeds or occurs with stepping (59), this implies that hydrolysis by a given subunit must occur after binding but before stepping. These restrictions leave four basic scenarios for the location of ATP hydrolysis within the context of the full mechanochemical cycle. In the first scenario, ATP hydrolysis occurs immediately after tight binding of ATP and is a necessary trigger of the binding of ATP to the next subunit (case 1 in Figure 8.4.) Alternatively, all four ATPs may be bound and then hydrolyzed either in a collective burst or a sequential “wave” around the ring. Once all ATPs are hydrolyzed the first step would be triggered. This is case 2 in Figure 8.4 or the “trigger” process in Figure 4.12. In addition, ATP hydrolysis might immediately precede translocation by each subunit with the previous step of an adjacent subunit triggering hydrolysis of the ATP in the adjacent pocket (case 3 in Figure 8.4.) Finally, there is the possibility that ATP hydrolysis is not strictly coordinated within the ring. In other words, each ATP can hydrolyze at any point after being tightly bound but before that subunit can generate a step, and the rate of this hydrolysis would be largely independent of the

chemical state of the rest of the ring. This scenario is captured in the light red regions in Figure 8.4.

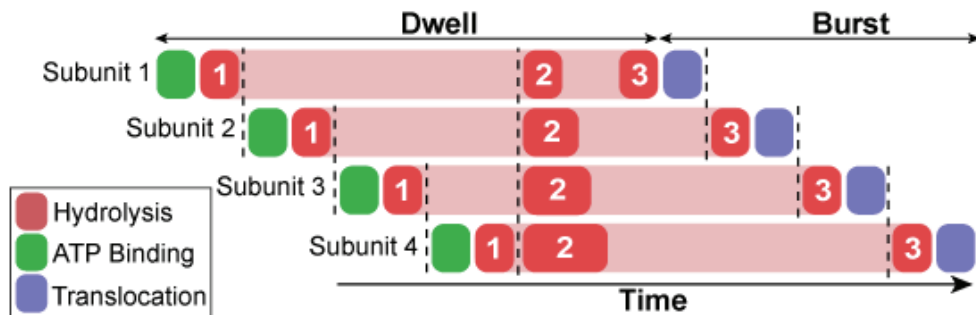


Figure 8.4. Possible Locations for ATP Hydrolysis

A schematic diagram of the possible locations of ATP hydrolysis for each subunit relative to the mechanochemical state of the other subunits. In case 1, hydrolysis of each ATP (red) occurs immediately after binding (green) and must occur before the next subunit can bind its ATP. In case 2, hydrolysis of each ATP occurs only after all four ATPs are bound but before any of the subunits can translocate the DNA (blue). In case 3, hydrolysis of each ATP occurs immediately before that subunit translocates the DNA and only after the previous subunit has translocated the DNA. The final possibility is that ATP hydrolysis is uncoordinated between the subunits, occurring at any point after binding but before translocation (light red). Figure courtesy of G. Chistol.

Notice that these four scenarios place ATP hydrolysis at different phases of the cycle. Thus, if we could arrest or slow ATP hydrolysis, the dwell phase would be modified in scenarios 1 and 2 while in scenarios 3 and 4 the dwell phase would proceed at a normal rate but the burst phase would be slowed. If the off-rate or the hydrolysis rate of the analog is slow, then we will likely see long analog-induced pauses. By determining if this pause occurs in the dwell phase or the burst phase, we can determine the phase of the cycle sensitive to the hydrolysis state of ATP. The location of these pauses should be easy to identify: dwell-phase pauses will occur in register with the surrounding 10-bp dwells while burst-phase pauses will occur out of register with these surrounding dwells. If the analog has a fast off-rate, then we will see individual cycles

slowed by the presence of the analog rather than distinct pauses. By following the concentration-dependent increase in the duration of the dwell or the burst phase, we will determine which phase is sensitive to the hydrolysis state of ATP, and, thus, limit the possible locations for this important kinetic event. ADP release can occur in a similar set of four scenarios as in Figure 8.3 and similar experiments with the transition state or phosphate analogs should be able to limit its location.

8.2.2: Preliminary Results

We have conducted a variety of bulk screens to identify candidate ATP, phosphate, and transitions state analogs. We use bulk nuclease protection assays (180) to probe the effect of the analog on the packaging process. By packaging in the presence of only the analog, we can determine if the motor is capable of powering translocation with the analog—i.e. the analog is capable of binding and being hydrolyzed. In addition, by packaging in the presence of ATP but trace amounts of analog, we can determine if the analog can act as an inhibitor of packaging, implying that it can bind to the motor. Our preliminary screens of ATP- γ -S, AMP-PNP, and ATP- α -S indicate that these analogs can bind to the motor whereas ATP-PCP and ATP-CPP cannot. In addition, ATP- α -S alone can drive the packaging of DNA, indicating that it is a hydrolysable analog.

In parallel, we have screened several known phosphate and transition state analogs in bulk. We find that sodium sulfate has no effect on packaging, consistent with the lack of inhibition by inorganic phosphate (59). In addition, we find that sodium orthovanadate inhibits packaging as does a mixture of aluminum chloride and sodium fluoride. Orthovanadate and aluminum fluoride are thought to act as transition-state or nucleotide analogs when complexed with ADP (225-227). However, control experiments

with aluminum chloride and sodium fluoride indicate that these compounds each inhibit packaging independently, which significantly complicates the interpretation of the inhibitory effect of the mixture of the two. For this reason, we have not screened another common analog, beryllium fluoride, since it also involves the mixture of sodium fluoride and beryllium salts. Thus, of the transition state or phosphate analogs, our only potential candidate so far is sodium orthovanadate.

Preliminary optical tweezers experiments indicate that we can observe the single pauses introduced by the non-hydrolyzable ATP analogs: ATP- γ -S and AMP-PNP. Data is still limited and the analysis is still preliminary, but it appears that the steps before and after the analog-induced pause add to \sim 20-bp, consistent with two 10-bp bursts before and after the pause. This result, in turn, suggests that the pause occurs within the dwell phase only. Thus, ATP hydrolysis is coordinated and likely occurs via scenarios 1 or 2 in Figure 8.3.

Orthovanadate experiments in the tweezers have proven much more difficult. Concentrations of orthovanadate which inhibit packaging in bulk do not produce clear pauses or modifications to the packaging behavior of single prohead-motor complexes. Increasing the concentration of orthovanadate only decreases the efficiency at which we can form packaging complexes in the tweezers. There are a few potential explanations for this behavior. First, it is possible that orthovanadate binds with extremely low efficiency to the packaging motor, but when it does bind, it does so *irreversibly*, effectively inactivating that packaging complex. If the binding events were particularly rare, we may not see them in the brief time during active packaging in the tweezers. Alternatively, it is known that orthovanadate salts in solution can multimerize, forming

structures which may not act as inhibitors (225). In the tweezers, but not in bulk studies, we use an oxygen scavenging system which can slightly affect our pH if the buffer is not carefully controlled (which it typically is). Thus, it might be possible, though unlikely, that our preliminary experiments favored the formation of these inactive forms. Further control experiments are obviously necessary before conclusions can be drawn.

Finally, slowly hydrolysable ATP analogs such as ATP- α -S have proven to be promising in single-molecule experiments. Preliminary low resolution screens of packaging driven solely by ATP- α -S indicate that the K_M of the motor and the V_{max} are both lowered in the presence of this analog, but remarkably the ratio of these constants is unchanged (data not shown). A similar ratio of V_{max} to K_M for ATP and ATP- α -S suggests that the binding of the analog is similar to that of ATP; thus, the lower V_{max} must arise from another kinetic event. Since the sulfur atom likely affects the electronegativity of the γ -phosphate bond, it is tempting to assume that the slowed rate is ATP hydrolysis. However, since the hydrolyzed product is ADP- α -S, we cannot rule out the possibility that a slower release of this ADP analog is what produces the lower V_{max} . Ultimately, high resolution packaging experiments will be conducted to determine whether it is the dwell or the burst phase which are slowed with this analog. Additional, hydrolysable analogs will also prove useful, and we are actively screening candidate compounds. Of particular interest are analogs which have modifications to the γ phosphate since the modification will unbind with the phosphate, leaving a normal ADP bound to the ring. Since the rate of ADP release should, thus, be unaffected, the interpretation of our data will be greatly simplified.

8.2.3: Speculation

It is tempting to speculate on the position of these important kinetic events. In the case of ADP release, energetic and kinetic arguments lead us to favor a model in which ADP release occurs in the dwell. For example, the required tight binding of ATP—the zippering of hydrogen bonds around the phosphate backbone which makes this transition largely irreversible—raises energetic issues when product ADP must be released. Namely, these same hydrogen bonds must be broken to release ADP, and this should make the release of ADP slow and energetically unfavorable. In parallel, the requirement that only a single subunit can actively dock ATP at a time also raises potential problems. What kind of conformational change can inactive all of the binding pockets but one?

These issues can be resolved if we require that ADP release occurs during the dwell phase. We imagine that all of the pockets in the ring, save one, are filled with product ADP from the previous burst phase. As the empty subunit tightly binds an ATP, the hydrogen bonds zipper around the phosphate backbone, and this conformational change is coupled to an adjacent subunit which simultaneously unzippers the hydrogen bonds around the bound ADP. In this fashion, the binding energy gained upon tight binding of one ATP can be used to eject ADP from the adjacent pocket. Once the adjacent ADP undergoes this “un-tight” binding reaction, that ADP would be loosely bound and free to undock via thermal fluctuations. One elegant feature of this scenario is that it nicely explains why only a single subunit can dock ATP at a time—all other subunits are filled with ADP (or tightly-bound ATP). Moreover, if the undocking of four ADPs provides the ~four rate-limiting kinetic events observed at saturating [ATP], this would also explain why these events are so highly coordinated and why the dwell-burst

structure is maintained at high force (uncoordinated events would blur the distinction between the dwell and burst phase under the application of force.) The coordination in ADP release comes from the coordination in ATP binding, and the sequential, coordinated binding of ATP comes from the need to sequentially eject ADP molecules from the previous cycle.

We can also speculate on the location of ATP hydrolysis based on measurements on related ring ATPases. In particular, pre-steady-state, stopped-flow measurements on the *E. coli* Rho (72) helicase and T7 gp4 (73) helicase have shown that ADP production in these systems precedes the release of inorganic phosphate by multiple subunits, greater than 2 for T7 gp4 (73) and ~3.5 for Rho (72). This delay in ATP hydrolysis and product release was explained in these original papers by invoking the requirement that the motor maintain 3-4 hydrolyzed ATP molecules on the ring. Translocation is still accomplished via a sequential mechanism, i.e. one ATP—one step, but the motor simply carries multiple product molecules for a few mechanochemical cycles before they are released. Though not explicitly stated, this model implies that the delay between ADP production and inorganic phosphate release is an *artifact* of the experiment. Since Rho and T7 gp4 are prepared in the absence of ATP, the experiment starts with an empty ring; thus, multiple mechanochemical cycles are required to build up this “reservoir” of hydrolyzed ATPs before the first inorganic phosphate is released. Thus, the delay originates in this *off-pathway* loading process. If the pre-steady state measurements could have been started with rings paused during active translocation, this delay would not have appeared since one inorganic phosphate would be released for each ADP produced. It just

wouldn't be the inorganic phosphate from that ADP, but the phosphate from the ATP used to power translocation four steps previous.

However, our dwell-burst model can also explain a delay in the formation of ADP and the release of inorganic phosphate, as long as we assume that ATP hydrolysis occurs in the dwell phase. In this case, the ring would bind four ATPs, hydrolyze them in either scenario 1 or 2 above, forming four ADPs during the dwell phase. The phosphates would then be released in the burst phase as part of the stepping mechanism. Thus, the natural dwell-burst structure would produce a delay in ADP production and inorganic phosphate release of exactly four molecules. Moreover, in a dwell-burst model, the delay in phosphate release is not an artifact of an off-pathway loading process, but rather represents a fundamental property of the mechanochemical cycle of the entire ring.

Clearly these arguments are speculative, and the definitive answer for the location of ATP hydrolysis and ADP release will come, in part, from the detailed experiments we describe above. An understanding of where these events occur and how they are coordinated will provide the crucial remaining details in the mechanochemistry of the packaging motor.

8.3: Dissecting a Molecular Throttle

In the original studies of the packaging motor, it was discovered that as the capsid fills with DNA, the packaging velocity slows, presumably due to the increasing resistance of the packaged DNA (58). In our initial efforts to slow the packaging motor with force, we tested the ability of such an “internal” force to reveal the steps within the packaging bursts. The idea was to use this internal force to supplement the rather weak forces provided by our first optical tweezers. As we will show in this section, it turns out that it

was not possible to use this internal force to slow the bursts because the presence of packaged DNA does not appear to slow the packaging process in a fashion equivalent to the application of external force. Rather, the presence of the packaged DNA has unique and unexpected effects on the motor dynamics. In this section, we will describe experiments aimed at characterizing these effects, discuss the current progress, and, finally, end with some speculation on the origin of these dynamics.

This work has been done in collaboration with Craig Hetherington, Gheorghe Chistol, and most of the experimental data has been collected by Chris Tae Hyung Lee. We discuss this work here with their permission.

8.3.1: The Effect of Packaged DNA

In the original single-molecule experiments in 2001, Smith and Tans (58) showed that the average packaging velocity of a single prohead-motor complex decreased with increasing opposing load with a force dependence that varied with the amount of genome that had already been packaged. See Figure 8.5a. The authors noticed that, remarkably, the shape of the force-dependent velocity appeared very similar for different amounts of prepackaged DNA. The only difference was that the force-velocity curves were separated by a constant force offset that was a function of the amount of packaged genome. They hypothesized that this “additional” force offset was due to the packaged genome, and that this “internal” force affected the packaging motor in a fashion *equivalent* to forces applied externally via the optical tweezers. Under this assumption, Smith and Tans were able to use the force dependence of the packaging velocity to calibrate this internal force directly from the packaging velocity as a function of internal filling of the capsid. See Figure 8.5b.

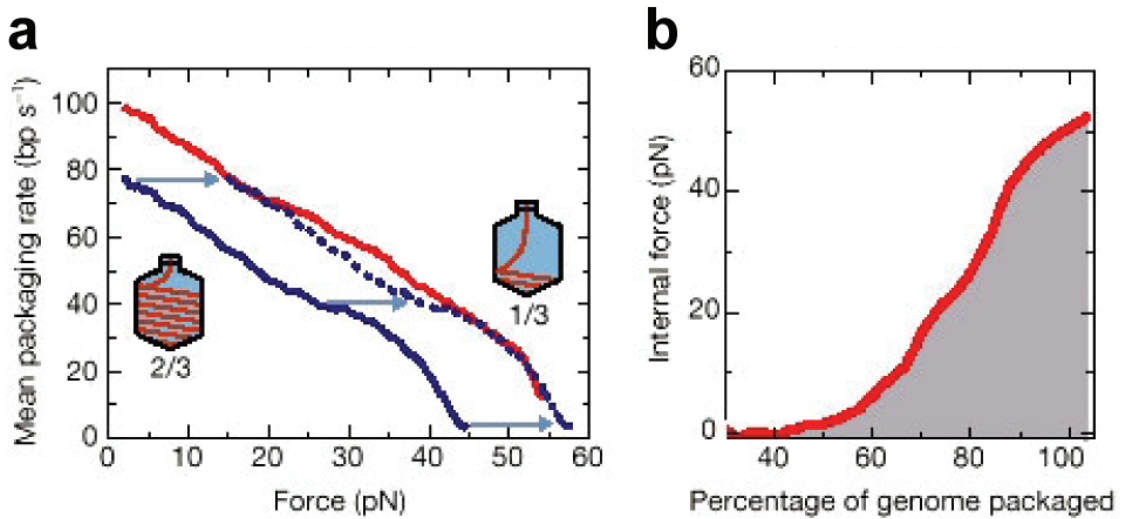


Figure 8.5. Effect of Packaged DNA on Packaging Velocity

(a) The average packaging velocity for two different prohead-motor complexes (red and blue) which differ only in the amount of DNA prepackaged: $\frac{1}{3}$ of the 19kb genome in red and $\frac{2}{3}$ of the genome in blue. The dashed blue line is the force dependence of the prohead when a single force offset is added to account for the prepackaged genome. This suggests that the effect of internalized DNA is to act only as an opposing load on the packaging motor. (b) The effective internal force as a function of the percentage of the genome packaged estimated via the additive force determined as in panel (a). Reprinted with permission from Macmillan Publishers Ltd: Nature, Ref. (58), © 2001.

8.3.2: High Resolution Observations

We have revisited these experiments using the high resolution optical tweezers. Given the dwell-burst model that we describe in Chapter 4, we expect that the effect of packaged DNA will be to slow, primarily, the burst phase since this is the force sensitive phase. Thus, we would expect that at high internal fillings the packaging dynamics would be equivalent to what was observed under high opposing loads in Chapter 4, i.e. the 2.5-bp steps would be the dominant feature of the packaging dynamics as in Figure 4.5a.

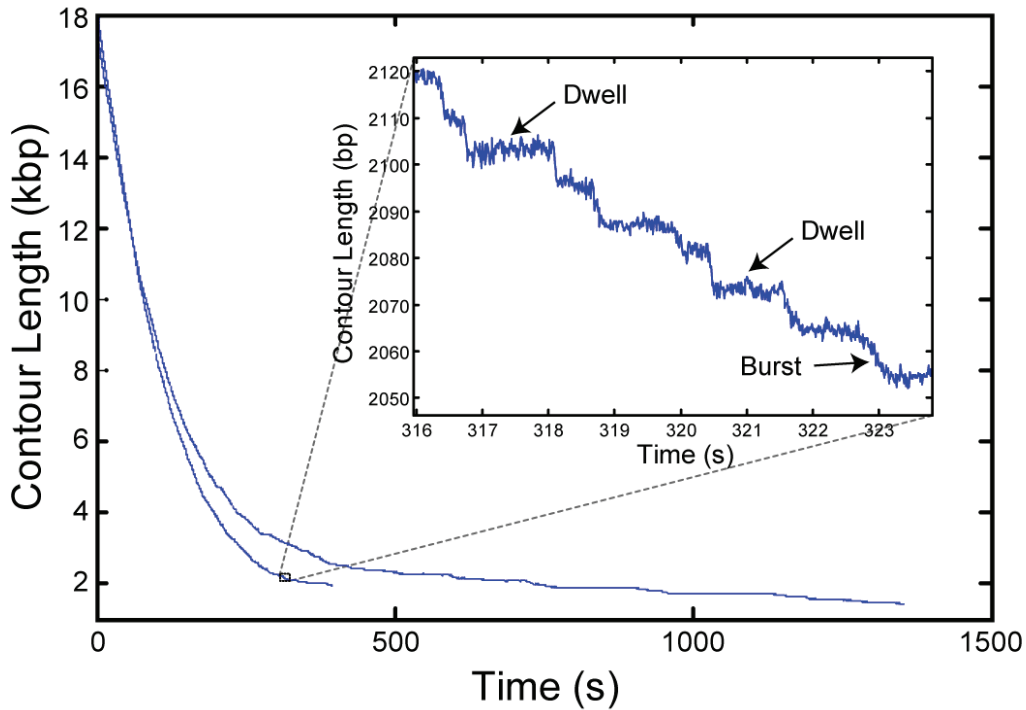


Figure 8.6. High Resolution Dynamics at High Internal Filling

Two single molecule packaging traces of 21 kb DNA under \sim 10 pN opposing load and saturating [ATP]. The rate of packaging decreases dramatically when a full 19 kb genome is nearly packaged, \sim 2 kb in remaining tether length. Inset: the base-pair-scale dynamics when the capsid is nearly filled. The dominant feature is a slowed dwell phase as opposed to the slow burst phase previously predicted. Note the 1 s pauses, nearly 10 times the duration under low filling. However, there is some evidence that the burst is also slowed. Data are averaged to 100 Hz.

In Figure 8.6 we show the observed high resolution dynamics of a packaging motor towards the end of packaging a 21 kb DNA molecule, \sim 2 kb longer than the full genome, under conditions of low opposing load, \sim 10 pN, and saturating [ATP], \sim 500 μ M. We observe a dramatic decrease in the average packaging velocity as expected from the measurements of Smith and Tans (58), Figure 8.5a. Yet, the high resolution dynamics are not at all similar to the dynamics under high external forces, Figure 4.5a. Instead of seeing the 2.5-bp steps, i.e. slowed bursts, we continue to see clear 10-bp bursts but with much longer dwells before these bursts. Thus, the dramatic decrease in

the packaging velocity arises not because of a slowdown in the force-sensitive burst phase, but a dramatic slowdown in the force-*insensitive* dwell phase.

Preliminary experiments are now underway to fully characterize this phenomenon. We have constructed DNA molecules of various lengths, ~11, 15, 17, 19, and 21 kb in length. The optical tweezers resolution is optimal when the unpackaged tether is ~1 kb in length; thus, these molecules will allow us to probe ~50%, 75%, 85%, 95%, and 105% filling with optimal resolution. These experiments are being conducted exactly as described in Chapters 4 and 5 using the *in situ* method of initiating the packaging process. Once sufficient data are collected, we will characterize the statistics of the dwells as in Chapter 4, to determine how the mean dwell time varies with internal filling. In parallel, the shape of this distribution will reveal how the number of rate-limiting kinetic events varies as a function of internal filling, providing insight into the number of kinetic events which are affected by internal filling. Finally, additional control experiments to determine how the K_M varies with internal filling will be conducted to insure that the concentration of [ATP] is saturating for all internal fillings.

In parallel, Figure 8.6 suggests that there is an additional increase in the duration of the burst phase in addition to the dominant effects in the dwell phase. Since this is the force-sensitive phase of the cycle, this effect is likely due to an actual resisting force from the packaged DNA. (The presence of such a pressure has now been suggested by a variety of experimental techniques (228-233), so it is likely that such an effect will be observed.) Thus, in addition to characterizing the change in the average duration in the dwell phase, we will also determine the average duration of the burst phase as a function of internal force. By measuring the force dependence of this phase under conditions of

low filling, we can again use the burst duration to calibrate the “effective internal” force felt by the motor. In this fashion we can correct the original estimates of the internal force using only the force-sensitive portion of the cycle, providing a more precise estimate of the internal pressure of the packaged genome.

8.3.3: A Speculative Explanation

If the dwell phase is the force-*insensitive* phase of the cycle, then how can the presence of packaged DNA slow this phase? There are essentially two ways for information about the internalized DNA to be transmitted to the motor. First, it can be transmitted along the DNA itself, acting as a force that opposes packaging. This is the simplest method of transmitting this information and is essentially what was proposed by Smith and Tans (58). However, there is an alternative: this information might be passed via conformational changes in the packaging motor, i.e. through the connector, to the pRNA, and then to the ATPase ring. Thus, the connector might act as an allosteric “pressure sensor”, sending information about the packaged state of the DNA within the capsid to the distal ATPase.

Methods for passing information from the capsid to the packaging motor have already been observed for other bacteriophages (234-240). For example, in related bacteriophages the ATPase-ring contains an additional endonuclease domain not present in gp16. The role of these endonuclease domains is to terminate the packaging process by cutting a concatenated genome. Mutation experiments (236, 237, 241) and structural studies (235) suggest that conformational changes in the connector, induced by the presence of packaged DNA, are what trigger the action of this endonuclease—three protein and nucleic acids rings distant from the packaged DNA. This form of termination

is known as the “head-full” mechanism and represents the molecular analog of a pressure sensor or a pressure induced switch. While gp16 does not have an endonuclease domain nor does φ 29 terminate packaging via a head-full mechanism, the connector of φ 29 shares significant sequence (55) and structural features (34, 240, 242) with the connectors of these related packaging motors. Thus, it may not be unreasonable to imagine that the dynamics that we observe as the capsid fills is cued by a similar connector-mediated conformational change in the packaging motor. In such a hypothetical scheme the connector would act as a molecular throttle, slowing the progress of the core ATPase in response to changes in the local concentration or pressure of the packaged DNA. One can speculate on a variety of reasons why a packaging motor might evolve such a function—slowing packaging to allow the packaged DNA to relax to a more stable configuration, for example—yet even if this is not the ultimate origin of these dynamics, it is clear that the dynamics of the motor are modified by the presence of the packaged DNA in a unexpected fashion. Determining the origin of this behavior will shed insight into the mechanism by which the function of ring ATPases can be regulated—a biological task which has clear implications for the mechanism of a variety of cellular ATPases.

8.4: Concluding Thoughts

In the Introduction, we raised the possibility that because of its relation to a broad and diverse set of cellular ATPases, our studies of the packaging motor might lend insight into the general mechanisms of this ATPase superfamily. Now that we have presented our data and developed our models, does this supposition hold true? What can we learn about the ASCE superfamily from the studies in this thesis? In parallel, the

measurements presented here were only possible due to the developments in high resolution optical trapping techniques we described in Chapters 2 and 3. In Chapter 3, we demonstrate that the resolution of an optical tweezers has a fundamental limit, and we argued that our instruments reach this limit for a wide range of experimental parameters. Thus, we have built instruments nearly as quiet as they can physically be. Does this conclusion imply that there is no future in high resolution optical trapping instrumentation and development? Are there no more advances that are possible? We conclude this thesis by commenting on these questions.

8.4.1: Implications of the Two-Phase Mechanism for the ASCE Family

In Chapter 4, we followed the packaging motor dynamics at base-pair resolution, and we discovered that DNA is packaged in bursts of 10 bp with preceding dwells that contain the binding of multiple ATP molecules and at least four additional kinetic events. By pulling to high force, we determined that this 10-bp burst is composed of four 2.5-bp steps. The action of four steps per cycle strongly argues that the motor binds four ATPs during each dwell. These measurements revealed that the mechanism of the packaging motor is governed by a novel form of inter-subunit coordination more intricate and detailed than expected. In parallel, a step size that is a non-integer repeat of the chemical periodicity of the DNA is completely unexpected and demands a subtle shift in our thinking on the geometry of the motor or how it engages the DNA. Our models can maintain symmetric DNA contacts, but at the cost of asymmetry in the structure of the motor, or vice versa.

In Chapter 7, we formalized many of our kinetic arguments about the packaging motor and by deriving a Michaelis-Menten-like expression for a useful measure of

enzymatic fluctuations, we were able to argue that even though the subunits in the packaging motor are chemically identical, they cannot bind ATP identically. Finally, as discussed above, work in progress has revealed many features of the motor-DNA interaction, in particular the spatial distribution of the important phosphate contacts. These results strongly suggest that the type of motor-DNA contact changes during the phase of the cycle.

The final message of all of these experiments is that there is *extensive* asymmetry in the mechanism of what is widely depicted as symmetric motor, and if any of our conclusions have wide-reaching implications for ringed members of the ASCE family, it is this: asymmetry dominates the dynamics of the packaging motor. Of course the idea of asymmetry within ringed motors is not novel. Crystal structures of many related motors—Rho (74, 167), BPV E1 (75, 169), T7 gp4 (76), and ϕ 8 P4 (77, 243), to name a few—display structural asymmetry in some form. While such static, structural asymmetry can explain many of the features of our data—including a non-integer step size—our dynamic measurements indicate a more fundamental, a more extensive *dynamic* asymmetry. The asymmetry implicit in the sequential models of inter-subunit coordination is a local asymmetry, set perhaps by the chemical state of the adjacent pockets, yet the inter-subunit coordination we observe in the package motor suggests a more global asymmetry—each motor subunit likely “knows” the chemical state of the other subunits. Extensive allostery of this form would explain the use of only four subunits per cycle, the different catalytic efficiencies of the different subunits, and a motor-DNA contact which depends on the chemical phase of the entire ring. It is not hard to imagine such extensive allostery in a homomeric ring—crystal structures of

related ring ATPases capture such states (75, 169)—but this would be the first time that it has been observed in dynamic measurements.

Thus, the major mechanistic lesson for the general ASCE family as a whole is that such dynamic asymmetry is possible. In other words, our measurements have expanded the repertoire of structural dynamics we now know to be possible within this superfamily. And this observation raises several exciting questions: is a φ 29-like inter-subunit coordination mechanism widespread in the ASCE family or are there mechanistic features that differ between clades within this superfamily or between larger divisions, RecA-like versus AAA; if there are differences, what are the structural features which drive these differences? The detailed mechanism we provide for the packaging motor in this thesis is the first step in addressing these questions, but such comparative questions clearly require comparative studies. While biochemical and structural studies provide tantalizing hints to these questions, they are no substitution for the direct observation of the dynamics of a single copy of the motor. Unfortunately, our measurements represent the first single-molecule, high resolution interrogation of a homomeric ASCE ring ATPase; thus, a true comparative study will have to wait until similar studies have been conducted on related ring ATPases. However, the ability to address the fundamental origin of the functional diversity in the ASCE family—whether this diversity arises in the core ATPase dynamics or if the core structural dynamics are the same, with the diversity arising from adaptor or modulator domains—should be more than ample motivation for these studies. As illustrated by this thesis, the necessary experimental and theoretical tools for such measurements are now in place.

8.4.2: The Future of High Resolution Optical Trapping

In Chapters 2 and 3 we discussed the construction of an optical tweezers capable of observing atomic-scale motions of single molecular motors. We began in Chapter 2 by addressing the various extraneous noise sources that can couple to an optical tweezers measurement and limit its spatial and temporal resolution. We then continued in Chapter 3 by addressing a more fundamental source of noise—the fluctuating Brownian forces of the surrounding thermal bath—a noise source which cannot be removed via careful instrumentation. In this Chapter, we developed a detailed theory of the effects of these fluctuations and derived expressions for the fundamental limits that these fluctuations place on the spatial resolution of optical tweezers. We concluded these Chapters by demonstrating that the instruments that we have constructed actually reach this fundamental limit over an important range of experimental parameters.

If these instruments are as quiet as they can be, then are there further advances that can be made in optical trapping techniques? The signal-to-noises ratios in Chapter 3 and the noise-power spectra in Chapter 2 indicate that there are indeed ways that the resolution of our instruments can be improved. The first improvements can be made in the low frequency, long-time regime. Spatial resolution can often be improved by slowing the biological system to permit as much temporal averaging as possible. However, this strategy pushes important temporal scales to lower frequencies where, despite our best efforts, extraneous noise sources again become dominant. See Figure 2.13. In this regime, better instrumentation is the solution. In particular, quieter lasers are needed, as discussed in the conclusions of Chapter 2. The advantage of this regime is that there is *a priori* no inherent limitation to the spatial resolution that is possible,

assuming that the biological system can be slowed appropriately. Thus, measurements of slow, sub-Ångstrom motions are not out of reach if additional attention is paid to extraneous sources of noise.

Unfortunately, it is often the case that a given molecular motor *cannot* be slowed arbitrarily. Off-pathway events, such as disassembly, often increasingly occur at the low concentration of substrate or the high forces needed to slow a motor. Thus, it is also important to consider techniques to improve the spatial resolution when additional temporal averaging is not possible. In this regime, the noise power spectra in Chapter 2 strongly suggest that our measurements are *only* limited by Brownian noise. Thus, to improve the resolution of our measurements in this regime, we must change properties of the experiment—the size of the beads, the length of the DNA, etc—in order to decrease the thermal fluctuations in the measurement. This is where the signal-to-noise ratios derived in Chapter 3 become extremely informative. Inspection of these expressions, such as Eq. (3.22), indicate that the use of smaller beads and shorter DNA handles—which increase the stiffness of the DNA—decrease the effect of Brownian fluctuations on our measurement, increasing the spatial resolution for a given amount of temporal averaging.

In our opinion, this is where the greatest advances in high resolution optical trapping should be possible. Current optical trapping techniques require relatively large beads, 100s of nanometers in diameter, and relatively long molecules of DNA, typically 1 kb or larger, to allow efficient trapping and manipulation (16). However, a careful examination of the signal-to-noise ratios in Chapter 3 indicates that there is no fundamental reason why optical trapping techniques cannot detect sub-Ångstrom motions

on the millisecond timescale if smaller molecular handles could be used—handles such as nanoparticles with diameters of 10s of nanometers. It is possible to trap particles of this size with conventional optical trapping techniques (244) though the relative size of these particles compared to the natural size of the traps, ~500 nm, makes it much more difficult to manipulate such small particles. However, if advances in trapping techniques can be made that permit the application of large forces to nanoparticles, it should be possible to detect Ångstrom-scale motions on the millisecond or shorter time scale. Resolution on this scale promises the ability to detect directly the small conformational changes that drive enzymatic dynamics in a wide range of proteins—not just molecular motors where evolution has favored a large, detectable conformational change, i.e. the step. This is the future of high resolution trapping techniques—the use of smaller molecular handles and shorter molecules. While these improvements may involve complicated instrumentation, novel optical geometries, or even novel manipulation methods, the variety of molecular motions that such resolution would bring into focus should provide ample motivation for these efforts.

That being said, we should not forget that the resolution that is now possible with the advances described in this thesis, several Ångstroms on the 10s of millisecond time scale, now opens the door to direct measurement of the fundamental motions of a wide variety of nucleic acid translocases. Thus, before we invest the time to improve optical trapping techniques, there is a tremendous amount of biology that can be learned with the techniques we have described here.

From the very large to the very small, life is inherently mechanical, and, on the cellular level, many crucial biological tasks are carried out by enzymes which transduce

chemical energy into mechanical work—enzymes which truly are nanomachines. In this thesis we have provided the experimental and theoretical tools necessary to dissect, directly and in detail, the mechanism of these key players in the cellular world. Exciting discoveries await the widespread use of these techniques.

Bibliography

1. Bustamante, C., Chemla, Y. R., Forde, N. R. & Izhaky, D. (2004) *Annu Rev Biochem* **73**, 705-48.
2. Lemon, K. P. & Grossman, A. D. (1998) *Science* **282**, 1516-1519.
3. Dekker, J. (2008) *Science* **319**, 1793-1794.
4. Fraser, P. & Bickmore, W. (2007) *Nature* **447**, 413.
5. Herbert, K. M., Greenleaf, W. J. & Block, S. M. (2008) *Annual Review of Biochemistry* **77**, 149-176.
6. Bustamante, C., Macosko, J. C. & Wuite, G. J. (2000) *Nat Rev Mol Cell Biol* **1**, 130-6.
7. Bai, L., Santangelo, T. J. & Wang, M. D. (2006) *Annual Review of Biophysics and Biomolecular Structure* **35**, 343-360.
8. Bustamante, C. & Moffitt, J. R. (2009) *RNA Polymerases as Molecular Motors* (The Royal Society of Chemistry, Cambridge, UK).
9. Cheng, W., Dumont, S., Tinoco, I., Jr. & Bustamante, C. (2007) *Proc Natl Acad Sci U S A* **104**, 13954-9.
10. Dumont, S., Cheng, W., Serebrov, V., Beran, R. K., Tinoco, I., Jr., Pyle, A. M. & Bustamante, C. (2006) *Nature* **439**, 105-8.
11. Wen, J. D., Lancaster, L., Hodges, C., Zeri, A. C., Yoshimura, S. H., Noller, H. F., Bustamante, C. & Tinoco, I. (2008) *Nature* **452**, 598-603.
12. Kinoshita, K., Adachi, K. & Itoh, H. (2004) *Annual Review of Biophysics and Biomolecular Structure* **33**, 245-268.
13. Nollmann, M., Crisponi, N. J. & Arimondo, P. B. (2007) *Biochimie* **89**, 490.

14. Stone, M. D., Bryant, Z., Crisona, N. J., Smith, S. B., Vologodskii, A., Bustamante, C. & Cozzarelli, N. R. (2003) *Proceedings of the National Academy of Sciences of the United States of America* **100**, 8654-8659.
15. Gore, J., Bryant, Z., Stone, M. D., Nollmann, M., Cozzarelli, N. R. & Bustamante, C. (2006) *Nature* **439**, 100-4.
16. Bustamante, C., Chemla, Y. R. & Moffitt, J. R. (2008) in *Single-Molecule Techniques: A Laboratory Manual*, eds. Selvin, P. R. & Ha, T. (Cold Spring Harbor Laboratories, Cold Spring Harbor, New York), pp. 297 - 324.
17. Chemla, Y. R., Moffitt, J. R. & Bustamante, C. (2008) *J. Phys. Chem. B* **112**, 6025-6044.
18. Moffitt, J. R., Chemla, Y. R., Smith, S. B. & Bustamante, C. (2008) *Annu Rev Biochem* **77**, 205-228.
19. Moffitt, J. R., Chemla, Y. R., Izhaky, D. & Bustamante, C. (2006) *Proceedings of the National Academy of Sciences* **103**, 9006-9011.
20. Moffitt, J. R., Chemla, Y. R., Aathavan, K., Grimes, S., Jardine, P. J., Anderson, D. L. & Bustamante, C. (2009) *Nature* **457**, 446-50.
21. Bustamante, C. & Moffitt, J. R. (2009) in *Proceedings of the Nobel Symposium: Single Molecule Spectroscopy in Chemistry, Physics, and Biology*, ed. Thyberg, P., Sanga Saby).
22. Black, L. W. (1989) *Annual Review of Microbiology* **43**, 267-292.
23. Grimes, S., Jardine, P. J. & Anderson, D. (2002) *Adv Virus Res* **58**, 255-94.
24. Jardine, P. J. & Anderson, D. (2006) in *The Bacteriophages*, ed. Calendar, R. (Oxford University Press, Oxford), pp. 49-65.

25. Meijer, W. J. J., Horcajadas, J. A. & Salas, M. (2001) *Microbiol. Mol. Biol. Rev.* **65**, 261-287.
26. Xiang, Y., Morais, M. C., Battisti, A. J., Grimes, S., Jardine, P. J., Anderson, D. L. & Rossmann, M. G. (2006) *Embo Journal* **25**, 5229-5239.
27. Tang, J., Olson, N., Jardine, P. J., Grimes, S., Anderson, D. L. & Baker, T. S. (2008) *Structure* **16**, 935-43.
28. Garcia, H. G., Grayson, P., Han, L., Inamdar, M., Kondev, J., Nelson, P. C., Phillips, R., Widom, J. & Wiggins, P. A. (2007) *Biopolymers* **85**, 115-30.
29. Purohit, P. K., Inamdar, M. M., Grayson, P. D., Squires, T. M., Kondev, J. & Phillips, R. (2005) *Biophys J* **88**, 851-66.
30. Petrov, A. S. & Harvey, S. C. (2008) *Biophys. J.* **95**, 497-502.
31. Petrov, A. S. & Harvey, S. C. (2007) *Structure* **15**, 21-7.
32. Locker, C. R., Fuller, S. D. & Harvey, S. C. (2007) *Biophys. J.* **93**, 2861-2869.
33. Morais, M. C., Koti, J. S., Bowman, V. D., Reyes-Aldrete, E., Anderson, D. L. & Rossmann, M. G. (2008) *Structure* **16**, 1267.
34. Simpson, A. A., Tao, Y. Z., Leiman, P. G., Badasso, M. O., He, Y. N., Jardine, P. J., Olson, N. H., Morais, M. C., Grimes, S., Anderson, D. L., Baker, T. S. & Rossmann, M. G. (2000) *Nature* **408**, 745-750.
35. Simpson, A. A., Leiman, P. G., Tao, Y., He, Y., Badasso, M. O., Jardine, P. J., Anderson, D. L. & Rossmann, M. G. (2001) *Acta Crystallogr D Biol Crystallogr* **57**, 1260-9.
36. Hendrix, R. W. (1978) *Proceedings of the National Academy of Sciences* **75**, 4779-4783.

37. Hugel, T., Michaelis, J., Hetherington, C. L., Jardine, P. J., Grimes, S., Walter, J. M., Falk, W., Anderson, D. L. & Bustamante, C. (2007) *PLoS Biol* **5**, e59.
38. Baumann, R. G., Mullaney, J. & Black, L. W. (2006) *Mol Microbiol* **61**, 16-32.
39. Koti, J. S., Morais, M. C., Rajagopal, R., Owen, B. A., McMurray, C. T. & Anderson, D. L. (2008) *J Mol Biol* **381**, 1114-32.
40. Guo, P. X., Erickson, S. & Anderson, D. (1987) *Science* **236**, 690-4.
41. Grimes, S. & Anderson, D. (1990) *J Mol Biol* **215**, 559-66.
42. Lee, T. J. & Guo, P. (2006) *J Mol Biol* **356**, 589-99.
43. Chen, C. & Guo, P. (1997) *J Virol* **71**, 3864-71.
44. Guo, P., Zhang, C., Chen, C., Garver, K. & Trottier, M. (1998) *Mol Cell* **2**, 149-55.
45. Shu, D. & Guo, P. (2003) *J. Biol. Chem.* **278**, 7119-7125.
46. Kitamura, A., Jardine, P. J., Anderson, D. L., Grimes, S. & Matsuo, H. (2008) *Nucl. Acids Res.* **36**, 839-848.
47. Shu, D., Zhang, H., Jin, J. & Guo, P. (2007) *Embo J* **26**, 527-37.
48. Morais, M. C., Choi, K. H., Koti, J. S., Chipman, P. R., Anderson, D. L. & Rossmann, M. G. (2005) *Mol Cell* **18**, 149-59.
49. Morais, M. C., Tao, Y., Olson, N. H., Grimes, S., Jardine, P. J., Anderson, D. L., Baker, T. S. & Rossmann, M. G. (2001) *J Struct Biol* **135**, 38-46.
50. Fang, Y., Shu, D., Xiao, F., Guo, P. & Qin, P. Z. (2008) *Biochem Biophys Res Commun* **372**, 589-94.
51. Zhang, H., Shu, D., Huang, F. & Guo, P. (2007) *Rna* **13**, 1793-802.
52. Xiao, F., Zhang, H. & Guo, P. (2008) *Nucleic Acids Res* **36**, 6620-32.

53. Moll, W. D. & Guo, P. (2007) *J Nanosci Nanotechnol* **7**, 3257-67.
54. Guo, P., Peterson, C. & Anderson, D. (1987) *J Mol Biol* **197**, 229-36.
55. Burroughs, A. M., Iyer, L. M. & Aravind, L. (2007) in *Gene and Protein Evolution*, ed. Volff, J.-N. (Karger, Basel), Vol. 3, pp. 48-65.
56. Iyer, L. M., Makarova, K. S., Koonin, E. V. & Aravind, L. (2004) *Nucleic Acids Res* **32**, 5260-79.
57. Grimes, S. & Anderson, D. (1997) *J Mol Biol* **266**, 901-14.
58. Smith, D. E., Tans, S. J., Smith, S. B., Grimes, S., Anderson, D. L. & Bustamante, C. (2001) *Nature* **413**, 748-52.
59. Chemla, Y. R., Aathavan, K., Michaelis, J., Grimes, S., Jardine, P. J., Anderson, D. L. & Bustamante, C. (2005) *Cell* **122**, 683-692.
60. Rickgauer, J. P., Fuller, D. N., Grimes, S., Jardine, P. J., Anderson, D. L. & Smith, D. E. (2008) *Biophys J* **94**, 159-67.
61. Fuller, D. N., Rickgauer, J. P., Jardine, P. J., Grimes, S., Anderson, D. L. & Smith, D. E. (2007) *Proc Natl Acad Sci U S A* **104**, 11245-50.
62. Smith, D. E., Fuller, D. N., Raymer, D. M., Rickgauer, P., Grimes, S., Jardine, P. J., Anderson, D. L., Catalano, C. E., Kottadiel, V. & Rao, V. B. (2007) in *Optical Trapping and Optical Micromanipulation IV* (SPIE, San Diego, CA, USA), Vol. 6644, pp. 664404.
63. Smith, S. B., Cui, Y. & Bustamante, C. (2003) *Methods Enzymol* **361**, 134-62.
64. Finer, J. T., Simmons, R. M. & Spudich, J. A. (1994) *Nature* **368**, 113.
65. Smith, S. B., Cui, Y. & Bustamante, C. (1996) *Science* **271**, 795-9.

66. Cluzel, P., Lebrun, A., Heller, C., Lavery, R., Viovy, J.-L., Chatenay, D. & Caron, F. (1996) *Science* **271**, 792-794.
67. Keller, D. & Bustamante, C. (2000) *Biophys J* **78**, 541-56.
68. Kainov, D. E., Tuma, R. & Mancini, E. J. (2006) *Cell Mol Life Sci* **63**, 1095-105.
69. Hopfner, K.-P. & Michaelis, J. (2007) *Current Opinion in Structural Biology* **17**, 87.
70. Galletto, R., Jezewska, M. J. & Bujalowski, W. (2004) *Journal of Molecular Biology* **343**, 83.
71. Bujalowski, W. & Jezewska, M. J. (2000) *Journal of Molecular Biology* **295**, 831.
72. Adelman, J. L., Jeong, Y.-J., Liao, J.-C., Patel, G., Kim, D.-E., Oster, G. & Patel, S. S. (2006) *Molecular Cell* **22**, 611.
73. Liao, J.-C., Jeong, Y.-J., Kim, D.-E., Patel, S. S. & Oster, G. (2005) *Journal of Molecular Biology* **350**, 452.
74. Skordalakes, E. & Berger, J. M. (2006) *Cell* **127**, 553-64.
75. Enemark, E. J. & Joshua-Tor, L. (2006) *Nature* **442**, 270.
76. Singleton, M. R., Sawaya, M. R., Ellenberger, T. & Wigley, D. B. (2000) *Cell* **101**, 589-600.
77. Mancini, E. J., Kainov, D. E., Grimes, J. M., Tuma, R., Bamford, D. H. & Stuart, D. I. (2004) *Cell* **118**, 743-55.
78. Massey, T. H., Mercogliano, C. P., Yates, J., Sherratt, D. J. & Lowe, J. (2006) *Mol Cell* **23**, 457-69.
79. Crampton, D. J., Mukherjee, S. & Richardson, C. C. (2006) *Mol Cell* **21**, 165-74.

80. Gai, D., Zhao, R., Li, D., Finkielstein, C. V. & Chen, X. S. (2004) *Cell* **119**, 47-60.
81. Martin, A., Baker, T. A. & Sauer, R. T. (2005) *Nature* **437**, 1115.
82. Moreau, M. J., McGeoch, A. T., Lowe, A. R., Itzhaki, L. S. & Bell, S. D. (2007) *Molecular Cell* **28**, 304.
83. Erzberger, J. P. & Berger, J. M. (2006) *Annu Rev Biophys Biomol Struct* **35**, 93-114.
84. Thomsen, N. D. & Berger, J. M. (2008) *Mol Microbiol* **69**, 1071-90.
85. Iyer, L. M., Leipe, D. D., Koonin, E. V. & Aravind, L. (2004) *J Struct Biol* **146**, 11-31.
86. Ogura, T. & Wilkinson, A. J. (2001) *Genes to Cells* **6**, 575-597.
87. Latterich, M. & Patel, S. (1998) *Trends in Cell Biology* **8**, 65.
88. Ye, J., Osborne, A. R., Groll, M. & Rapoport, T. A. (2004) *Biochim Biophys Acta* **1659**, 1-18.
89. Ogura, T., Whiteheart, S. W. & Wilkinson, A. J. (2004) *Journal of Structural Biology* **146**, 106-112.
90. Ashkin, A., Dziedzic, J. M., Bjorkholm, J. E. & Chu, S. (1986) *Optics Letters* **11**, 288-290.
91. Ashkin, A. (1970) *Physical Review Letters* **24**, 156-&.
92. Neuman, K. C. & Block, S. M. (2004) *Review of Scientific Instruments* **75**, 2787.
93. Svoboda, K. & Block, S. M. (1994) *Annu Rev Biophys Biomol Struct* **23**, 247-85.
94. Ashkin, A. (1997) *Proceedings of the National Academy of Sciences* **94**, 4853-4860.

95. Perkins, T. T. (2009) *Laser & Photonics Review* **3**, 203-220.
96. Berg-Sorensen, K. & Flyvbjerg, H. (2004) *Review Of Scientific Instruments* **75**, 594-612.
97. Bustamante, C., Finzi, L., Sebring, P. & Smith, S. (1991) *SPIE Proc. Ser.* **1435**, 179-87.
98. Smith, S. B., Finzi, L. & Bustamante, C. (1992) *Science* **258**, 1122-6.
99. Bustamante, C., Marko, J. F., Siggia, E. D. & Smith, S. (1994) *Science* **265**, 1599-600.
100. Wang, M. D., Yin, H., Landick, R., Gelles, J. & Block, S. M. (1997) *Biophys J* **72**, 1335-46.
101. Bustamante, C., Smith, S. B., Liphardt, J. & Smith, D. (2000) *Curr Opin Struct Biol* **10**, 279-85.
102. Bustamante, C., Bryant, Z. & Smith, S. B. (2003) *Nature* **421**, 423.
103. Cecconi, C., Shank, E. A., Bustamante, C. & Marqusee, S. (2005) *Science* **309**, 2057-2060.
104. Li, P. T., Vieregg, J. & Tinoco, I., Jr. (2008) *Annu Rev Biochem* **77**, 77-100.
105. Liphardt, J., Onoa, B., Smith, S. B., Tinoco, I., Jr. & Bustamante, C. (2001) *Science* **292**, 733-737.
106. Woodside, M. T., Garcia-Garcia, C. & Block, S. M. (2008) *Curr Opin Chem Biol* **12**, 640-6.
107. Greenleaf, W. J., Woodside, M. T. & Block, S. M. (2007) *Annu Rev Biophys Biomol Struct* **36**, 171-190.

108. Gittes, F. & Schmidt, C. F. (1998) *European Biophysics Journal With Biophysics Letters* **27**, 75-81.
109. Wynveen, A., Lee, D. J., Kornyshev, A. A. & Leikin, S. (2008) *Nucleic Acids Res* **36**, 5540-51.
110. Cornish, P. V. & Ha, T. (2007) *Acs Chemical Biology* **2**, 53-61.
111. Shaevitz, J. W., Block, S. M. & Schnitzer, M. J. (2005) *Biophys. J.* **89**, 2277-2285.
112. Schnitzer, M. J. & Block, S. M. (1995) *Cold Spring Harbor Symposia on Quantitative Biology* **60**, 793-802.
113. Qian, H. (2008) *Biophys J* **95**, 10-7.
114. Kolomeisky, A. B. & Fisher, M. E. (2007) *Annual Review of Physical Chemistry* **58**, 675-695.
115. Carter, N. J. & Cross, R. A. (2005) *Nature* **435**, 308.
116. Mallik, R., Carter, B. C., Lex, S. A., King, S. J. & Gross, S. P. (2004) *Nature* **427**, 649-652.
117. Reck-Peterson, S. L., Yildiz, A., Carter, A. P., Gennerich, A., Zhang, N. & Vale, R. D. (2006) *Cell* **126**, 335-348.
118. Gennerich, A. & Vale, R. D. (2009) *Curr Opin Cell Biol* **21**, 59-67.
119. Yildiz, A., Tomishige, M., Gennerich, A. & Vale, R. D. (2008) *Cell* **134**, 1030-41.
120. Gennerich, A., Carter, A. P., Reck-Peterson, S. L. & Vale, R. D. (2007) *Cell* **131**, 952-65.
121. Cappello, G., Pierobon, P., Symonds, C., Busoni, L., Gebhardt, J. C., Rief, M. & Prost, J. (2007) *Proc Natl Acad Sci U S A* **104**, 15328-33.

122. Clemen, A. E., Vilfan, M., Jaud, J., Zhang, J., Barmann, M. & Rief, M. (2005) *Biophys J* **88**, 4402-10.
123. Rief, M., Rock, R. S., Mehta, A. D., Mooseker, M. S., Cheney, R. E. & Spudich, J. A. (2000) *Proc Natl Acad Sci U S A* **97**, 9482-6.
124. Zhou, Y. & Zhuang, X. (2006) *Biophys J* **91**, 4045-53.
125. Svoboda, K., Mitra, P. P. & Block, S. M. (1994) *PNAS* **91**, 11782-11786.
126. Schnitzer, M. J. & Block, S. M. (1997) *Nature* **388**, 386-390.
127. Koza, Z. (2002) *Physical Review E* **65**, 031905.
128. Segel, I. H. (1975) *Enzyme Kinetics* (John Wiley & Sons, Inc., Hoboken, NJ).
129. Nugent-Glandorf, L. & Perkins, T. T. (2004) *Opt Lett* **29**, 2611-3.
130. Carter, A. R., King, G. M., Ulrich, T. A., Halsey, W., Alchenberger, D. & Perkins, T. T. (2007) *Applied Optics* **46**, 421-427.
131. Shaevitz, J. W., Abbondanzieri, E. A., Landick, R. & Block, S. M. (2003) *Nature* **426**, 684.
132. Abbondanzieri, E. A., Greenleaf, W. J., Shaevitz, J. W., Landick, R. & Block, S. M. (2005) *Nature* **438**, 460-5.
133. Mejia, Y. X., Mao, H., Forde, N. R. & Bustamante, C. (2008) *J Mol Biol* **382**, 628-37.
134. Galburd, E. A., Grill, S. W., Wiedmann, A., Lubkowska, L., Choy, J., Nogales, E., Kashlev, M. & Bustamante, C. (2007) *Nature* **446**, 820-823.
135. Greenleaf, W. J., Woodside, M. T., Abbondanzieri, E. A. & Block, S. M. (2005) *Phys Rev Lett* **95**, 208102.

136. Woodside, M. T., Anthony, P. C., Behnke-Parks, W. M., Larizadeh, K., Herschlag, D. & Block, S. M. (2006) *Science* **314**, 1001-1004.
137. Woodside, M. T., Behnke-Parks, W. M., Larizadeh, K., Travers, K., Herschlag, D. & Block, S. M. (2006) *Proc Natl Acad Sci U S A* **103**, 6190-5.
138. Greenleaf, W. J., Frieda, K. L., Foster, D. A., Woodside, M. T. & Block, S. M. (2008) *Science* **319**, 630-3.
139. Fuller, D. N., Raymer, D. M., Rickgauer, J. P., Robertson, R. M., Catalano, C. E., Anderson, D. L., Grimes, S. & Smith, D. E. (2007) *J Mol Biol* **373**, 1113-22.
140. Aathavan, K., Politzer, A. T., Kaplan, A., Moffitt, J. R., Chemla, Y. R., Grimes, S., Jardine, P. J., Anderson, D. & Bustamante, C. (2009), Submitted to Nature.
141. Gordon, C. G. (1992) in *Vibration Control in Microelectronics, Optics, and Metrology* (SPIE, San Jose, CA, USA), Vol. 1619, pp. 71.
142. Beranek, L. L., Blazier, J. W. E. & Figwer, J. J. (1971) *The Journal of the Acoustical Society of America* **50**, 96.
143. Settles, G. S. (2001) *Schlieren and Shadowgraph Techniques* (Springer-Verlag, New York).
144. Hecht, E. (2001) *Optics* (Addison Wesley, Reading, MA).
145. Gittes, F. & Schmidt, C. F. (1998) *Optics Letters* **23**, 7-9.
146. Pralle, A., Prummer, M., Florin, E. L., Stelzer, E. H. K. & Hörber, J. K. H. (1999) *Microscopy Research and Technique* **44**, 378-386.
147. Wuite, G. J., Davenport, R. J., Rappaport, A. & Bustamante, C. (2000) *Biophys J* **79**, 1155-67.
148. Brewer, L. R. & Bianco, P. R. (2008) *Nat Methods* **5**, 517-25.

149. Allersma, M. W., Gittes, F., deCastro, M. J., Stewart, R. J. & Schmidt, C. F. (1998) *Biophys. J.* **74**, 1074-1085.
150. Press, W., Flannery, B., Teukolsky, S. & Vetterling, W. (1992) *Numerical Recipes in C* (Cambridge University Press, Port Melbourne, Australia).
151. Faxén, H. (1923) *Ark. Mat. Astron. Fys.* **17**, 1.
152. Meiners, J. C. & Quake, S. R. (1999) *Physical Review Letters* **82**, 2211-2214.
153. Henderson, S., Mitchell, S. & Bartlett, P. (2002) *Phys Rev Lett* **88**, 088302.
154. Rouse, P. E. (1953) *Journal Of Chemical Physics* **21**, 1272-1280.
155. Zimm, B. H. (1956) *The Journal of Chemical Physics* **24**, 269.
156. Batchelor, G. K. (1976) *Journal Of Fluid Mechanics* **74**, 1-29.
157. Uhlenbeck, G. E. & Ornstein, L. S. (1930) *Physical Review* **36**, 823.
158. Visscher, K. & Block, S. M. (1998) *Methods Enzymol* **298**, 460-89.
159. Meiners, J. C. & Quake, S. R. (2000) *Phys Rev Lett* **84**, 5014-7.
160. Massey, T. H., Mercogliano, C. P., Yates, J., Sherratt, D. J. & Löwe, J. (2006) *Molecular Cell* **23**, 457.
161. Guo, P., Grimes, S. & Anderson, D. (1986) *Proc Natl Acad Sci U S A* **83**, 3505-9.
162. Simpson, A. A., Tao, Y., Leiman, P. G., Badasso, M. O., He, Y., Jardine, P. J., Olson, N. H., Morais, M. C., Grimes, S., Anderson, D. L., Baker, T. S. & Rossmann, M. G. (2000) *Nature* **408**, 745-50.
163. Kellner, L. (1937) *Proceedings of the Royal Society of London Series a-Mathematical and Physical Sciences* **159**, 0410-0415.
164. Mao, H. B., Arias-Gonzalez, J. R., Smith, S. B., Tinoco, I. & Bustamante, C. (2005) *Biophysical Journal* **89**, 1308-1316.

165. Ha, S. C., Lowenhaupt, K., Rich, A., Kim, Y.-G. & Kim, K. K. (2005) *Nature* **437**, 1183.
166. Eide, J. L., Chakraborty, A. K. & Oster, G. F. (2006) *Biophys J* **90**, 4281-94.
167. Skordalakes, E. & Berger, J. M. (2003) *Cell* **114**, 135-46.
168. Lisal, J., Lam, T. T., Kainov, D. E., Emmett, M. R., Marshall, A. G. & Tuma, R. (2005) *Nat Struct Mol Biol* **12**, 460-6.
169. Sanders, C. M., Kovalevskiy, O. V., Sizov, D., Lebedev, A. A., Isupov, M. N. & Antson, A. A. (2007) *Nucl. Acids Res.* **35**, 6451-6457.
170. Rickgauer, J. P., Fuller, D. N. & Smith, D. E. (2006) *Biophys J* **91**, 4253-7.
171. Greenleaf, W. J., Frieda, K. L., Abbondanzieri, E. A., Woodside, M. T. & Block, S. M. (2007) in *Optical Trapping and Optical Micromanipulation IV* (SPIE, San Diego, CA, USA), Vol. 6644, pp. 664406.
172. Berg-Sorensen, K., Oddershede, L., Florin, E. L. & Flyvbjerg, H. (2003) *Journal of Applied Physics* **93**, 3167-3176.
173. Tolic-Norrelykke, S. F., Schaffer, E., Howard, J., Pavone, F. S., Julicher, F. & Flyvbjerg, H. (2006) *Review of Scientific Instruments* **77**, 103101.
174. Berg-Sorensen, K., Peterman, E. J. G., Weber, T., Schmidt, C. F. & Flyvbjerg, H. (2006) *Review of Scientific Instruments* **77**, 063106.
175. Huisstede, J. H., van Rooijen, B. D., van der Werf, K. O., Bennink, M. L. & Subramaniam, V. (2006) *Opt Lett* **31**, 610-2.
176. Seol, Y., Li, J., Nelson, P. C., Perkins, T. T. & Betterton, M. D. (2007) *Biophys J* **93**, 4360-73.

177. Mangeol, P. & Bockelmann, U. (2008) *Review of Scientific Instruments* **79**, 083103.
178. Lide, D. (2007) (Taylor and Francis, Boca Raton, FL).
179. Sambrook, J. (2001) *Molecular Cloning: A Laboratory Manual* (Cold Spring Harbor Laboratory Press, Cold Spring Harbor, NY).
180. Grimes, S. & Anderson, D. (1989) *Journal of Molecular Biology* **209**, 91.
181. Baumann, C. G., Smith, S. B., Bloomfield, V. A. & Bustamante, C. (1997) *Proceedings of the National Academy of Sciences* **94**, 6185-6190.
182. Korn, G. A. & Korn, T. M. (2000) *Mathematical Handbook for Scientists and Engineers: Definitions, Theorems, and Formulae for Reference and Review* (Courier Dover Publications.
183. Gelles, J., Schnapp, B. J. & Sheetz, M. P. (1988) *Nature* **331**, 450-3.
184. Kuo, S. C., Gelles, J., Steuer, E. & Sheetz, M. P. (1991) *J Cell Sci Suppl* **14**, 135-8.
185. Svoboda, K., Schmidt, C. F., Schnapp, B. J. & Block, S. M. (1993) *Nature* **365**, 721-7.
186. Block, S. M. & Svoboda, K. (1995) *Biophys. J.* **68**, 2305S-2415.
187. Carter, B. C., Vershinin, M. & Gross, S. P. (2008) *Biophys. J.* **94**, 306-319.
188. Parzen, E. (1962) *Annals of Mathematical Statistics* **33**, 1065-&.
189. Ritort, F. (2006) *Journal of Physics-Condensed Matter* **18**, R531-R583.
190. Neuman, K. C., Saleh, O. A., Lionnet, T., Lia, G., Allemand, J. F., Bensimon, D. & Croquette, V. (2005) *Journal of Physics: Condensed Matter* **17**, S3811.
191. Charvin, G., Bensimon, D. & Croquette, V. (2002) *Single Molecules* **3**, 43-48.

192. Fisher, M. E. & Kolomeisky, A. B. (2001) *PNAS* **98**, 7748-7753.
193. Valentine, M. T., Fordyce, P. M., Krzysiak, T. C., Gilbert, S. P. & Block, S. M. (2006) *Nat Cell Biol* **8**, 470-6.
194. Saleh, O. A., Perals, C., Barre, F. X. & Allemand, J. F. (2004) *Embo J* **23**, 2430-9.
195. Yildiz, A., Forkey, J. N., McKinney, S. A., Ha, T., Goldman, Y. E. & Selvin, P. R. (2003) *Science* **300**, 2061-2065.
196. Asbury, C. L., Fehr, A. N. & Block, S. M. (2003) *Science* **302**, 2130-2134.
197. Yildiz, A., Tomishige, M., Vale, R. D. & Selvin, P. R. (2004) *Science* **303**, 676-678.
198. Yasuda, R., Noji, H., Kinoshita, K. & Yoshida, M. (1998) *Cell* **93**, 1117-1124.
199. English, B. P., Min, W., van Oijen, A. M., Lee, K. T., Luo, G. B., Sun, H. Y., Cherayil, B. J., Kou, S. C. & Xie, S. N. (2006) *Nature Chemical Biology* **2**, 168-168.
200. Min, W., Gopich, I. V., English, B. P., Kou, S. C., Xie, X. S. & Szabo, A. (2006) *Journal of Physical Chemistry B* **110**, 20093-20097.
201. Kou, S. C., Cherayil, B. J., Min, W., English, B. P. & Xie, X. S. (2005) *Journal of Physical Chemistry B* **109**, 19068-19081.
202. Derrida, B. (1983) *Journal of Statistical Physics* **31**, 433-450.
203. Koza, Z. (2000) *Physica A* **285**, 176-186.
204. Koza, Z. (1999) *Journal of Physics a-Mathematical and General* **32**, 7637-7651.
205. Liao, J.-C., Spudich, J. A., Parker, D. & Delp, S. L. (2007) *Proceedings of the National Academy of Sciences* **104**, 3171-3176.

206. Tsygankov, D., Linden, M. & Fisher, M. E. (2007) *Phys Rev E Stat Nonlin Soft Matter Phys* **75**, 021909.
207. Linden, M. & Wallin, M. (2007) *Biophys. J.* **92**, 3804-3816.
208. Shaevitz, J. W., Block, S. M. & Schnitzer, M. J. (2005) *Biophysical Journal* **89**, 2277-2285.
209. Gennerich, A. & Vale, R. D. (2009) *Current Opinion in Cell Biology* **21**, 59.
210. Qin, F. & Li, L. (2004) *Biophysical Journal* **87**, 1657.
211. Weiss, G. H. (1994) *Aspects and Applications of the Random Walk* (Elsevier Science B. V., North-Holland).
212. Michaelis, L. & Menten, M. L. (1913) *Biochemische Zeitschrift* **49**, 333-369.
213. Koshland, D. E. (2002) *Bioorganic Chemistry* **30**, 211.
214. Zhou, Y. & Zhuang, X. (2007) *J Phys Chem B* **111**, 13600-10.
215. Kawaoka, J., Jankowsky, E. & Pyle, A. M. (2004) *Nat Struct Mol Biol* **11**, 526-30.
216. Eoff, R. L., Spurling, T. L. & Raney, K. D. (2005) *Biochemistry* **44**, 666-74.
217. SenGupta, D. J. & Borowiec, J. A. (1992) *Science* **256**, 1656-61.
218. Dillingham, M. S., Soultanas, P. & Wigley, D. B. (1999) *Nucleic Acids Res* **27**, 3310-7.
219. Strauss, J. K. & Maher, L. J., 3rd (1994) *Science* **266**, 1829-34.
220. Strauss-Soukup, J. K., Vaghefi, M. M., Hogrefe, R. I. & Maher, L. J., 3rd (1997) *Biochemistry* **36**, 8692-8.
221. Thiyianathan, V., Vyazovkina, K. V., Gozansky, E. K., Bichenchova, E., Abramova, T. V., Luxon, B. A., Lebedev, A. V. & Gorenstein, D. G. (2002) *Biochemistry* **41**, 827-38.

222. Agresti, A. & Coull, B. (1998) *The American Statistician* **52**.
223. Enemark, E. J. & Joshua-Tor, L. (2006) *Nature* **442**, 270-5.
224. Saleh, O. A., Bigot, S., Barre, F. X. & Allemand, J. F. (2005) *Nat Struct Mol Biol* **12**, 436-40.
225. Goodno, C. C. (1982) *Methods Enzymol* **85 Pt B**, 116-23.
226. Sharma, S. & Davidson, A. L. (2000) *J Bacteriol* **182**, 6570-6.
227. Yang, Q. & Catalano, C. E. (2004) *Biochemistry* **43**, 289-99.
228. Grayson, P. & Molineux, I. J. (2007) *Current Opinion in Microbiology* **10**, 401.
229. Grayson, P., Han, L., Winther, T. & Phillips, R. (2007) *Proc Natl Acad Sci U S A* **104**, 14652-7.
230. Grayson, P., Evilevitch, A., Inamdar, M. M., Purohit, P. K., Gelbart, W. M., Knobler, C. M. & Phillips, R. (2006) *Virology* **348**, 430-6.
231. Nurmamedov, I., Castelnovo, M., Catalano, C. E. & Evilevitch, A. (2007) *Quarterly Reviews of Biophysics* **40**, 327-356.
232. Castelnovo, M. & Evilevitch, A. (2007) *The European Physical Journal E - Soft Matter* **24**, 9.
233. Evilevitch, A., Lavelle, L., Knobler, C. M., Raspaud, E. & Gelbart, W. M. (2003) *Proc Natl Acad Sci U S A* **100**, 9292-5.
234. Catalano, C. E. (2000) *Cell Mol Life Sci* **57**, 128-48.
235. Lander, G. C., Tang, L., Casjens, S. R., Gilcrease, E. B., Prevelige, P., Poliakov, A., Potter, C. S., Carragher, B. & Johnson, J. E. (2006) *Science* **312**, 1791-1795.
236. Casjens, S., Wyckoff, E., Hayden, M., Sampson, L., Eppler, K., Randall, S., Moreno, E. T. & Serwer, P. (1992) *J Mol Biol* **224**, 1055-74.

237. Tavares, P., Santos, M. A., Lurz, R., Morelli, G., de Lencastre, H. & Trautner, T. A. (1992) *J Mol Biol* **225**, 81-92.
238. Isidro, A., Henriques, A. O. & Tavares, P. (2004) *Virology* **322**, 253-63.
239. Isidro, A., Santos, M. A., Henriques, A. O. & Tavares, P. (2004) *Mol Microbiol* **51**, 949-62.
240. Lebedev, A. A., Krause, M. H., Isidro, A. L., Vagin, A. A., Orlova, E. V., Turner, J., Dodson, E. J., Tavares, P. & Antson, A. A. (2007) *Embo J* **26**, 1984-94.
241. Oliveira, L., Henriques, A. O. & Tavares, P. (2006) *J Biol Chem* **281**, 21914-23.
242. Agirrezabala, X., Martín-Benito, J., Valle, M., González, J. M., Valencia, A., Valpuesta, J. M. & Carrascosa, J. L. (2005) *Journal of Molecular Biology* **347**, 895.
243. Kainov, D. E., Mancini, E. J., Telenius, J., Lisal, J., Grimes, J. M., Bamford, D. H., Stuart, D. I. & Tuma, R. (2008) *J Biol Chem* **283**, 3607-17.
244. Svoboda, K. & Block, S. M. (1994) *Optics Letters* **19**, 930-932.